Bruit de raie des ventilateurs axiaux : Estimation des sources aéroacoustiques par modèles inverse et Méthodes de contrôle

Anthony Gérard

THESE

pour l'obtention du Grade de

Docteur de l'Université de Poitiers

ECOLE SUPERIEURE d'INGENIEURS DE POITIERS
(Diplôme National - Arrêté du 7 août 2006)
Ecole Doctorale : Sciences pour l'Ingénieur

SPECIALITE
Acoustique et Dynamique des Ecoulements Instationnaires

Présentée par

Anthony GÉRARD

Bruit de raie des ventilateurs axiaux : Estimation des sources aéroacoustiques par modèles inverses et Méthodes de contrôle

Directeur de thèse : **Alain BERRY**
Co-directeur de thèse : **Patrice MASSON**
Co-directeur de thèse : **Yves GERVAIS**
Co-directeur de thèse : **Jacky TARTARIN**

Soutenue le 15 décembre 2006

JURY

Rapporteurs	
S. LEWY	Directeur de recherche, ONERA, Chatillon
M. ROGER	Professeur, Ecole Centrale de Lyon
Examinateurs	
Y. GERVAIS	Professeur, Université de Poitiers
J. TARTARIN	Maître de Conférences, Université de Poitiers
A. BERRY	Professeur, Université de Sherbrooke
P. MASSON	Professeur, Université de Sherbrooke
Y. CHAMPOUX	Professeur, Université de Sherbrooke
J.B. PIAUD	PhD, Conseiller technologique, Venmar, Drummondville
S.A. MESLIOUI	Docteur, Senior Staff Specialist, Pratt and Whitney Canada, Montréal

À mon père, Albert
À ma mère, Jeannine
À ma soeur, Alexandra
À mon frère, Stéven

"La science ne sert qu'à vérifier les découvertes de l'instinct."

Jean Cocteau

"Quelli che s'innamora di pratica saza scietia, so come 'l nocchiere che e tra navilio sanza timone o bussola, che mai à certezza dove si vada."

"Ceux qui sont en amour avec la pratique sans connaissance sont comme le marin qui part en mer sans gouvernail ou sans boussole et qui n'est jamais sûr de l'endroit où il va."

Leonardo da Vinci

ABSTRACT

Despite the efforts made during the last decades to control noise from subsonic fans, low frequency tonal noise is still of major concern. For those frequencies, passive techniques are bulky and inefficient but active techniques are better adapted and have a great potential for a control at the source. The contributions of this PhD work are 1) the estimation of tonal aeroacoustic sources using inverse models, 2) an acoustic noise control method using a single loudspeaker and 3) an adaptive passive control method using flow control obstructions. Theoretical developments provided in the thesis are valid for subsonic axial fans and experiments were carried out for an automotive engine cooling fan.

RÉSUMÉ

L'inaptitude des solutions passives à contrôler le bruit de raie basse fréquence des ventilateurs pousse de nombreux industriels à s'intéresser à la mise au point de nouvelles méthodes de contrôle. Pour répondre à ces besoins, trois volets ont été explorés durant ce doctorat : 1) Estimation des sources de bruit de raie par modèle aéroacoustique inverse, 2) Contrôle actif acoustique du bruit de raie à l'aide d'un haut-parleur et 3) Contrôle passif adaptatif du bruit de raie à l'aide d'obstructions dans l'écoulement.

L'intensité et la directivité du bruit de raie dépendent de la non uniformité stationnaire de l'écoulement entrant dans le rotor. Le modèle analytique de Blake, et dans une moindre mesure celui de Morse et Ingard, décrivent très bien les mécanismes de génération et de propagation du bruit de raie en champ libre. Ils permettent, en effet, de relier les forces instationnaires périodiques exercées sur les pales du rotor dans le domaine spectral circonférentiel au champ de pression acoustique rayonné en champ libre et en champ lointain à la FPP (Fréquence de Passage des Pales) et ses harmoniques. À l'inverse, la partie stationnaire et non uniforme de l'écoulement et les forces instationnaires périodiques qu'elle induit sur les pales du rotor peuvent être estimées à partir du champ acoustique rayonné. Toutefois, la discrétisation des modèles analytiques, requise pour cette inversion, mène à des systèmes linéaires mal conditionnés. Nous avons utilisé la régularisation de Tikhonov pour les inverser. Pour assurer une bonne reconstruction des forces instationnaires exercées sur les pales, il faut choisir avec précaution le paramètre de régularisation de Tikhonov. Le paramètre associé au dernier maximum local de la courbure de la courbe en L est choisi si la condition de stabilité de Picard est respectée. Des expériences menées sur un ventilateur de radiateur d'automobile ont ainsi permis de localiser les zones où le rotor subit des fluctuations de portance, à partir de mesures de pressions acoustiques en champ lointain. Des mesures anémométriques ont partiellement validé les profils de vitesse reconstruits à l'aide de l'inversion d'une formulation en vitesse du modèle de Blake. En plus de fournir une méthode d'estimation sans contact des sources de bruit de raie, utile pour estimer le potentiel d'un contrôle à la source, les modèles inverses offrent un outil d'extrapolation du champ acoustique rayonné à la FPP et ses harmoniques, à partir d'un nombre limité de mesure, utile pour des simulations de contrôle actif.

Nous avons ensuite développé une stratégie de contrôle actif du bruit de raies des ventilateurs en champ libre. Pour un ventilateur de radiateur d'automobile, des simulations ont montré qu'un contrôle global des deux premières raies est possible avec un petit haut-parleur non bafflé de directivité dipolaire, situé devant le moyeu du ventilateur. Ce choix était justifié par la nature aussi dipolaire du bruit de raie en basse fréquence (quelques centaines de Hz). L'implémentation

d'un contrôleur par anticipation FX-LMS monocanal a mené à des atténuations de niveau de pression acoustique de 28 dB et 18 dB au microphone d'erreur à la FPP et son premier harmonique respectivement.

Pour des ventilateurs subsoniques, le mode circonférentiel de l'écoulement possédant un nombre de périodes égal à un multiple entier n du nombre de pales contribue significativement au rayonnement de l'harmonique de rang n de la FPP. Le contrôle de ce mode, réalisé grâce à l'ajout d'obstructions dans l'écoulement, permet une atténuation globale du champ acoustique rayonné, en créant un champ acoustique secondaire d'égale intensité mais en opposition de phase avec le champ acoustique primaire. La distance axiale rotor/obstructions et l'orientation angulaire des obstructions permettent d'ajuster respectivement l'amplitude et la phase de l'onde acoustique secondaire. Nous avons conceptualisé et mis en œuvre cette méthode pour contrôler les deux premières raies, grâce à l'ajout d'obstructions en amont du rotor. Une formulation analytique de l'approche de contrôle a d'abord été élaborée à partir du modèle de Blake. Une modélisation analytique de l'interaction rotor/obstructions a été développée à partir du modèle de Sears pour concevoir des obstructions permettant de contrôler sélectivement une raie sans régénération d'harmoniques. Expérimentalement, ces obstructions ont ensuite été positionnées pour minimiser la pression acoustique rayonnée par un ventilateur de radiateur d'automobile pour diverses charges et diverses conditions de rayonnement. La superposition de deux séries d'obstructions a permis d'atténuer simultanément la FPP de 21 dB et 15 dB en conduit. Finalement, des mesures ont montré que l'impact des obstructions de contrôle est mineur (inférieur à 1 %) sur l'efficacité aéraulique du ventilateur.

REMERCIEMENTS

Je tiens tout d'abord à remercier chaleureusement et amicalement le professeur Alain Berry qui m'a accueilli au GAUS, pour son soutien dans les moments difficiles et pour sa rigueur scientifique.

Je remercie tout aussi chaleureusement et amicalement Patrice Masson, professeur à l'Université de Sherbrooke et Yves Gervais, professeur à l'université de Poitiers. Leur aide a permis d'enrichir et de diversifier la nature des sujets traités durant ce doctorat.

Merci aussi à Jacky Tartarin, professeur à l'Université de Poitiers et Sylvain Nadeau, ingénieur chez Siemens VDO, pour leurs précieux conseils et le temps qu'ils m'ont consacré.

Merci à Christian Clavet, Marc Quiquerez, Marc-André Duval, Brian Driscoll, Pascal Biais, Laurent Philippon, Philippe Szeger, Jean-Christophe Vergez et Yann Pasco pour leur soutien technique.

Je tiens aussi à remercier tous les membres du jury qui m'ont fait l'honneur d'évaluer mon travail avec objectivité.

Un clin d'œil et une tape dans le dos à Pierrot, à Philou, au Camille, la Ilia, la Claire fontaine, au Marc, à Phil, au Pascal, au Richer, la Audrey, le Grand Fred, au Pierre Olivier, à Manu, le Philippe-Aubert, la Tania, aux Stéphanie, la Solenn, la Caroline, le Morvan, le Fañch, les Nico, le Arnaud, le Franck, le Benj, la Béa, le Michel, la Marie, la Marion, la Carole, le Whalid, le François, au Florent, au grand Cyrille, au petit pousset , allez Stéphane, au Cédric, à Éric, le Romu, le JCioù, le Fabioù, aux Valérie, à Monique et à tous les musiciens d'IMG, de l'Azylis, d'Hysteresis, du Onze Swing et des Gars Trans...

Une pensée particulière à mes parents, ma soeur (et Franck, ne t'énerve pas), mon frère et à Emmanuelle.

TABLE DES MATIÈRES

LISTE DES TABLEAUX

LISTE DES FIGURES

CHAPITRE 1

INTRODUCTION

Les travaux de cette thèse, financée par le Réseau des Centres d'Excellence AUTO21 (projets F03 "Interior Noise Environment of Future Automobile" et F204 "Smart technologies for improved acoustic environment in future automobiles"), s'inscrivent dans le cadre d'une cotutelle entre le GAUS (Groupe d'Acoustique de l'Université de Sherbrooke) et le LEA (Laboratoire d'Études Aérodynamiques) de l'Université de Poitiers.

1.1 Contexte

L'exigence de confort des consommateurs et les normes environnementales de plus en plus strictes poussent de nombreux industriels à s'intéresser à l'enjeu majeur qu'est la réduction du bruit des hélices, ventilateurs, turbomachines et autres machines tournantes. Ainsi, dans le secteur de l'automobile, le bruit des ventilateurs de radiateur est un critère de vente important dans un marché de plus en plus concurrentiel (Réseau Auto 21, Siemens VDO). Dans le secteur aéronautique, les entreprises s'engagent dans la lutte contre le bruit des turboréacteurs : les projets européen Silence(R) et RESOUND [1] et les programmes de la NASA [2] attestent des efforts réalisés. Dans le secteur de la climatisation, il est important de lutter contre le bruit pour augmenter le confort d'utilisation (York). Les plaintes de particuliers habitant à proximité d'usines ou de fermes utilisant des ventilateurs démontrent aussi le besoin de fournir des solutions simples, robustes et économiques pour contrôler le bruit de raie basse fréquence, qui se propage très bien (ferme de Compton, Québec, Canada).

Deux types de bruit sont à distinguer, le bruit large bande, aléatoire par nature, et le bruit de raie à la fréquence de passage des pales (FPP) et ses harmoniques, périodique par nature. Des solutions passives, basées sur la géométrie des pales du rotor et sur l'environnement immédiat du ventilateur, ont déjà permis la réduction du bruit rayonné. Il s'agit de "mesures préventives". Cependant, lorsque l'écoulement traversant le ventilateur demeure spatialement non uniforme, un bruit de raie peut fortement émerger du bruit large bande. Ce bruit est souvent basse fréquence ; dans ce cas, l'ajout de matériaux absorbants est inefficace et les silencieux encombrants et coûteux. Il faut alors faire appel à des "mesures curatives", comme le contrôle actif acoustique

ou le contrôle actif à la source.

1.2 Objectifs

Le bruit de raie sera étudié théoriquement et expérimentalement pour un ventilateur de radiateur d'automobile mais ces travaux sont applicables à tous les ventilateurs axiaux subsoniques.

D'un point de vue scientifique, le problème du bruit de raie soulève des questions sur ses mécanismes de génération, sur la méthode expérimentale de mesure de ces mécanismes et sur les méthodes de contrôle efficaces en terme d'atténuation acoustique. D'un point de vue technologique, se posent des questions sur le choix des actionneurs, des capteurs et des contrôleurs à utiliser pour assurer un contrôle robuste, peu coûteux et facile à mettre en oeuvre. Pour répondre à ces questions, multi-physiques par nature, et combler certains manques relevés dans la littérature, trois volets ont été explorés :

A. Estimation des sources de bruit de raie par modèle aéroacoustique inverse

B. Contrôle actif acoustique du bruit de raie à l'aide d'un haut-parleur

C. Contrôle passif adapté du bruit de raie à l'aide d'obstructions dans l'écoulement

Ces trois volets se basent sur le développement d'outils analytiques modélisant les phénomènes de façon simple mais réaliste ainsi que sur la mise en oeuvre de dispositifs expérimentaux permettant leur validation. Plus spécifiquement, les objectifs sont :

A. Premièrement, le développement d'un modèle inverse basé sur les modèles analytiques du bruit de raie des rotors en champ libre de Morse et Ingard [3] et de Blake [4].

B. Deuxièmement, la mise en oeuvre d'une stratégie de contrôle actif par anticipation en champ libre pour contrôler globalement le bruit de raie à l'aide d'un petit haut-parleur non bafflé (fixé sur le moyeu du ventilateur).

C. Troisièmement de conceptualiser et de mettre oeuvre une méthode de contrôle passif adaptative du bruit de raie grâce à l'ajout d'obstruction(s) de contrôle dans l'écoulement (en amont du rotor) pour contrôler le mode de l'écoulement le plus rayonnant pour chaque raie. Comme les raies ont généralement une amplitude décroissante avec la fréquence, seules les deux premières raies feront l'objet d'une attention particulière.

1.3 Organisation du mémoire

Tout d'abord, le chapitre 2 récapitule l'**état de l'art** sur la question du bruit de raie des ventilateurs. Y sont présentées des généralités sur le bruit aérodynamique des ventilateurs puis une revue de bibliographie sur l'utilisation de modèles inverses en aéroacoustique. Enfin, les techniques de contrôle existantes seront décrites et classées.

Ensuite, ce mémoire propose un recueil de cinq articles (dont deux publiés, un accepté et deux à soumettre). Les nomenclatures sont présentées pour chaque article. Nous faisons aussi un bilan en français à la fin des articles afin d'articuler les différents chapitres de la thèse.

Le chapitre 3 est la première partie d'un article en deux parties paru dans le Journal of Sound and Vibration en 2005 [5], intitulé : "***Active control of tonal noise from subsonic axial fan. Part 1 : Reconstruction of aeroacoustic sources from far-field sound pressure***" (*Contrôle du bruit de raie des ventilateurs axiaux subsoniques. Partie 1 : Reconstruction des sources aéroacoustiques à partir du champ acoustique rayonné en champ lointain*). Il concerne le développement d'un modèle inverse basé sur le modèle analytique de Morse et Ingard sur le bruit de raie des rotors en champ libre. Une synthèse bibliographique sur les modèles de bruit de raie et des problèmes inverses, reliés à l'acoustique des rotors, commence cet article. Il se poursuit par la description du modèle de Morse et Ingard, reliant les forces instationnaires périodiques exercées sur les pales au champ de pression acoustique. Dans la section suivante, l'inversion du modèle de Morse et Ingard est détaillée et la technique de régularisation de Tikhonov est proposée pour surmonter les difficultés inhérentes au mauvais conditionnement des systèmes linéaires à inverser. L'inversion est premièrement testée sur quelques cas simples pour analyser l'influence de certains paramètres sur le conditionnement du modèle inverse. Ensuite, un cas numérique supposant une non-uniformité de l'écoulement amont est étudié pour démontrer la capacité du modèle inverse à reconstruire les composantes rayonnantes des forces agissant sur les pales (dues à la non-uniformité de l'écoulement). Finalement, des résultats expérimentaux préliminaires sont présentés pour un ventilateur de radiateur d'automobile et le modèle inverse est utilisé comme outil d'extrapolation de champ acoustique rayonné à la FPP et son premier harmonique.

Le chapitre 4 est la deuxième partie de l'article paru dans le Journal of Sound and Vibration en 2005 [6], intitulé : "***Active control of tonal noise from subsonic axial fan. Part 2 : Active control simulations and experiments in free field***" (*Contrôle du bruit de raie des ventilateurs axiaux subsoniques. Partie 2 : Simulations et expériences de contrôle actif en champ libre*). Il commence par une revue de bibliographie sur les différentes techniques de contrôle actif du bruit de raie. Un modèle analytique simplifié est ensuite proposé pour décrire l'interférence entre le bruit de raie du ventilateur et la source acoustique secondaire (haut-parleur non bafflé). Cet article définit aussi des critères de contrôle global en champ libre. Le modèle inverse présenté dans le premier chapitre est utilisé pour décrire plus précisément les sources équivalentes du rotor

évoluant dans un écoulement non uniforme réaliste. Des simulations de contrôle actif basées sur l'extrapolation du champ acoustique primaire à partir des sources reconstruites par le modèle inverse sont ensuite exposées. Ces simulations sont finalement comparées aux directivités mesurées dans des expériences avec et sans contrôle.

Le modèle de Morse et Ingard sur le bruit de raie des rotors a été utilisé dans les deux premiers chapitres. Dans les chapitres suivants, le modèle de Blake sera au coeur des analyses. Ce choix a été justifié par la commodité qu'offre le modèle de Blake pour passer du modèle de Sears (permettant de calculer les forces aérodynamiques à partir de vitesses d'écoulement) au rayonnement acoustique des rotors. Ce modèle constitue ainsi un outil plus versatile pour traiter les problèmes d'interaction rotor/obstruction de contrôle proposés aux chapitres 6 et 7. Un modèle inverse basé sur le modèle de Blake (similaire à l'inversion du modèle de Morse et Ingard) sera aussi formulé au chapitre 5. Il permettra alors de comparer les vitesses d'écoulement estimées par le modèle inverse à des mesures anémométriques préliminaires de l'écoulement. Dans ces chapitres, les notations changeront pour se conformer à celles de Blake, procurant ainsi plus de cohésion entre le modèle de Sears et celui de Blake.

Le chapitre 5 est un article accepté pour publication dans le journal de l'American Institute of Aeronautics and Astronautics en juin 2006 [7], intitulé "***Evaluation of tonal aeroacoustic sources in subsonic fans using inverse models*** (*Évaluation des sources aéroacoustiques de bruit de raie des ventilateurs subsoniques par modèles inverses*). La bibliographie présentée dans cet article reprend en partie celle du premier article. La première section détaille le modéle de Blake. Ensuite, la technique de régularisation de Tikhonov est décrite et une méthode originale pour choisir le paramètre de régularisation est exposée. La dernière section présente des résultats expérimentaux reprenant une expérience similaire aux simulations du chapitre 3 pour montrer la capacité des modèles inverses à localiser des zones de fluctuation de portance ou de vitesse d'écoulement. Les reconstructions de vitesse d'écoulement sont aussi comparées à des mesures anémométriques à fil chaud dans cette section. Tout au long de cet article, une attention particulière est portée au choix du paramètre de régularisation.

Le chapitre 6 est le premier article soumis d'une série de deux articles [8], intitulé "***Control of tonal toise from subsonic axial fans using flow control obstructions. Part 1 : Interaction between the flow control obstructions and the rotor***" (*Contrôle du bruit de raie des ventilateurs axiaux subsoniques à l'aide d'obstructions de contrôle dans l'écoulement. Partie 1 : Interaction entre les obstructions de contrôle et le rotor*). Ce chapitre est consacré à la conception d'obstructions permettant de contrôler la FPP sans régénération d'harmoniques d'ordres supérieurs. L'approche de contrôle du bruit de raie avec des obstructions est premièrement formalisée en s'appuyant sur le modèle de Blake. Ensuite, la théorie analytique de Sears est associée à la décomposition des pales en bandes selon l'envergure ("strip theory") pour calculer la portance instationnaire générée par l'interaction entre le rotor et les obstructions. Puis l'article expose quelques spectres de portance instationnaire des pales du rotor pour différentes géométries

d'obstructions (obstructions trapezoïdales, sinusoïdales et cylindriques). Une analyse de contenance harmonique est menée pour optimiser l'angle des obstructions trapézoïdales et évaluer la capacité des obstructions à contrôler sélectivement un mode de portance instationnaire.

Le chapitre 7 est la deuxième partie de l'article soumis dans le Journal of Sound and Vibration [9], intitulé "***Control of tonal noise from subsonic axial fans using flow control obstructions. Part 2 : Acoustic performance of the control approach***" (*Contrôle du bruit de raie des ventilateurs axiaux subsoniques à l'aide d'obstructions de contrôle dans l'écoulement. Partie 2 : Performance acoustique de l'approche de contrôle*). L'objectif de ce chapitre est de caractériser acoustiquement les obstructions présentées au chapitre précédent et de montrer expérimentalement que la conception d'obstructions menant à un faible taux de contenance harmonique est possible. Il commence par quelques bases théoriques sur le contrôle du bruit de ventilateur. Il décrit ensuite un banc d'essai permettant de valider les résultats du chapitre 6. Des résultats de contrôle de la non-uniformité de l'écoulement, due à l'interaction rotor/stator, à l'aide d'une obstruction sinusoïdale en champ libre sont ensuite présentés. Puis, l'approche de contrôle est validée en conduit avec une obstruction trapezoïdale, pour différentes charges. Finalement, les performances aérauliques du ventilateur sont évaluées avec et sans ajout des obstructions de contrôle dans l'écoulement.

L'annexe A présente une stratégie de **positionnement automatique des obstructions de contrôle par contrôle optimal**. Une analogie avec le contrôle actif de l'équilibrage dynamique des rotors est d'abord présentée. La théorie du contrôle optimal est ensuite rappelée. Finalement, des résultats expérimentaux préliminaires de positionnement automatique des obstructions de contrôle sont montrés.

CHAPITRE 2

ÉTAT DE L'ART

2.1 Généralités sur le bruit aérodynamique des ventilateurs subsoniques

2.1.1 Principe de fonctionnement d'un ventilateur de radiateur d'automobile

Un ventilateur est un appareil destiné à transférer de l'énergie mécanique au fluide qui le traverse, en vue d'en accroître la pression et/ou de créer un débit d'air. Il existe deux grandes familles de ventilateurs : les ventilateurs centrifuges, se prêtant mieux à des taux de compression élevés, et les ventilateurs axiaux pour des débits plus grands. C'est ce dernier type de ventilateur qui est utilisé dans le système de refroidissement des moteurs d'automobile. Le rôle du ventilateur de radiateur d'automobile est d'assurer un débit d'air suffisant à travers les échangeurs thermiques et de compenser les pertes de charge à travers le système de refroidissement (Fig. 2.1). Les pertes de charge étant causées par la calandre, les échangeurs et le bloc moteur.

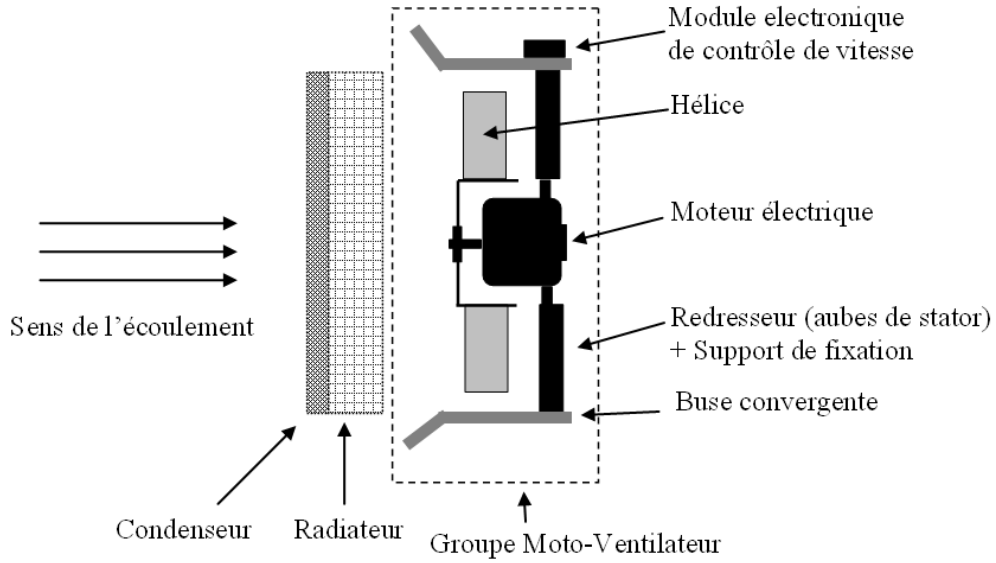

Figure 2.1 Éléments constitutifs d'un groupe moto-ventilateur

Lorsque la vitesse de l'automobile est suffisamment grande, les échanges thermiques sont assurés par l'écoulement naturel de l'air à travers les ailettes du radiateur et du condenseur. Par contre, lorsque le véhicule est au ralenti, le ventilateur est actionné pour fournir un débit d'air suffisant à travers les échangeurs thermiques. Les ventilateurs peuvent être soufflants (en amont des échangeurs), aspirants (en aval des échangeurs) ou les deux en même temps (ventilateur situé entre le radiateur et le condenseur). L'utilisation de deux ventilateurs est de plus en plus courante.

Le ventilateur est inséré dans un ensemble appelé Groupe Moto-Ventilateur (GMV) constitué de plusieurs éléments (Fig. 2.1) :

- Une hélice
- Un moteur électrique entraînant l'hélice
- Une buse divergente ou convergente avec ou sans redresseur guidant l'écoulement
- Un support de fixation
- Un module électronique de contrôle de vitesse du moteur électrique

D'après les éléments constitutifs du GMV, le bruit généré peut être de trois natures : aérodynamique (interaction entre l'hélice et le redresseur ou le support par exemple), vibratoire (vibration du support de fixation) ou électro-magnétique (moteur électrique). Cependant, la majeure partie du bruit rayonné est souvent d'origine aérodynamique. Les caractéristiques fréquentielles de ce bruit sont de deux types : le bruit de raie, engendré par des phénomènes périodiques, et le bruit large bande, engendré par des phénomènes aléatoires. Ce projet de doctorat ne s'intéresse qu'au bruit de raie d'origine aérodynamique.

2.1.2 Analogie de Lighthill et de Ffowcs Williams et Hawkings

L'idée originale de Lighthill a été de manipuler l'équation d'Euler et l'équation de continuité, pour l'espace libre, en isolant dans le membre de gauche l'opérateur de propagation et en regroupant les termes de turbulence dans le membre de droite de façon à le considérer comme une source analogue à un quadripôle : une double dérivée du tenseur de Lighthill. La région d'écoulement turbulent est considérée relativement petite et la propagation se fait dans un milieu fluide homogène au repos.

Le développement de Curle (1955) [15] a ensuite permis d'introduire le cas d'un écoulement en présence de surfaces solides fixes. Les sources ainsi créées sont équivalentes à une répartition de dipôles sur la surface. Enfin, Ffowcs Williams et Hawkings (1969) [16] ont introduit le cas des surfaces solides en mouvement, donnant ainsi l'équation la plus utilisée en aéroacoustique [15] :

$$\frac{\partial^2 \rho'}{\partial \tau^2} - c_0^2 \frac{\partial^2 \rho'}{\partial y_i^2} = \frac{\partial^2 T_{ij}}{\partial y_i \partial y_j} - \frac{\partial f}{\partial y_i}(P_{ij}\delta(f)\frac{\partial f}{\partial y_j}) + \frac{\partial}{\partial \tau}(\rho_0 V_{Sj}\delta\frac{\partial f}{\partial y_j}) \tag{2.1}$$

L'équation d'onde classique est facilement reconnaissable dans la partie gauche de l'équation (2.1) où ρ' est la partie fluctuante de la masse volumique, c_0 la vitesse du son dans le milieu au repos, y_i la variable d'espace et τ la variable temporelle. Quant au terme de droite, il fait apparaître la somme de trois termes sources analogues à des quadripôles (double dérivée spatiale), des dipôles (simple dérivée spatiale) et des monopôles :

- Le premier terme fait intervenir le tenseur de Lighthill $T_{ij} = \rho_0 u_i u_j + (p - c_0^2\rho_0) - \tau_{ij}$ où ρ_0 est la partie moyenne de la masse volumique, u_i la vitesse de l'écoulement et τ_{ij} le tenseur des contraintes de viscosité. Ce terme est la contribution de l'écoulement seul au rayonnement acoustique.
- Le deuxième terme est une distribution surfacique de sources dipolaires dues à l'interaction fluide-structure (bruit de charge). P_{ij} est le tenseur des contraintes et $f(\mathbf{y}, \tau)$ définit la position de la surface en fonction de l'espace $\mathbf{y}$ et du temps τ.
- Le troisième terme prend en compte les effets de déplacement du fluide résultant du mouvement des surfaces, où V_{Si} représente la vitesse des points constituant les surfaces. Ce terme est représenté par une distribution surfacique de monopôles (bruit d'épaisseur).

D'une manière générale, le bruit de charge d'une hélice ou d'un rotor est dominant à vitesse modérée tandis que le bruit d'épaisseur devient prépondérant pour un régime transsonique. Le bruit quadripolaire devient plus intense pour des vitesses supersoniques [10] [15] [4]. Dans le cas des ventilateurs de radiateur d'automobile, c'est donc le bruit de charge qui prévaut sur les autres types de bruit, étant donné un nombre de Mach en bout de pale toujours inférieur à 0,25. Ce régime de rotation subsonique se rencontre couramment dans de nombreuses applications : ventilateurs de climatisation, petits compresseurs, ventilateurs de refroidissement de composants électroniques...

2.1.3 Mécanismes de génération du bruit aérodynamique des ventilateurs axiaux

Neise [10] fournit un bon résumé des mécanismes fondamentaux de génération du bruit aérodynamique des ventilateurs industriels subsoniques ainsi que des principales techniques de réduction du bruit. Wright [17], quant à lui, présente une synthèse des travaux antérieurs à 1976 sur le spectre acoustique des rotors de machines à flux axial allant de vitesses subsoniques à transsoniques. Ses travaux concernent aussi bien les hélices d'avions que les rotors d'hélicoptères en passant par les compresseurs ou bien les ventilateurs utilisés dans l'industrie ou dans l'automobile. Plus théorique, dans son livre intitulé " Aeroacoustics ", Goldstein [15] présente aussi des modèles du bruit de rotors de vitesses subsoniques, transsoniques ou supersoniques. Dans

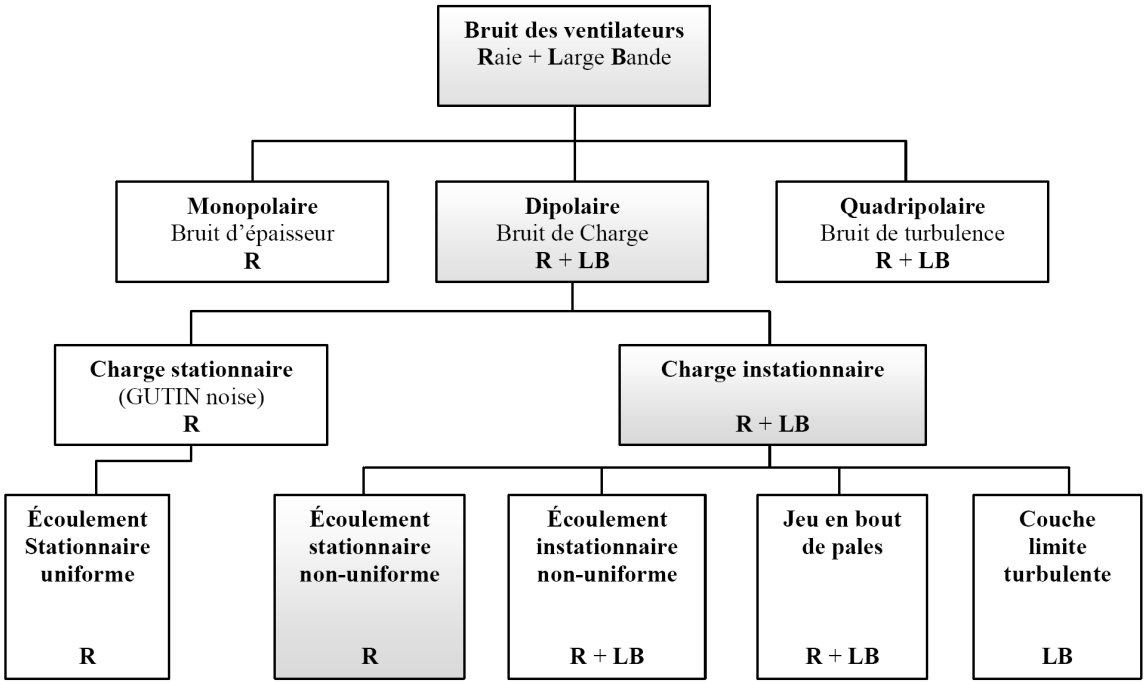

Figure 2.2 Résumé des mécanismes de génération du bruit aéroacoustique d'un ventilateur (adapté de [10])

un article de 1961, Tyler et Sofrin [18] proposent un modèle des mécanismes de génération, de transmission et de rayonnement des compresseurs à flux axial, idéal pour traiter du rayonnement des rotors dans un conduit. Les analyses théoriques de Lowson [19] et Morse et Ingard [3] fournissent aussi de précieux renseignements sur le bruit de raie de ventilateurs en champ libre ou en conduit. Plus récemment, Blake [4] a proposé des modèles similaires de bruit de raie de rotor en champ libre et en conduit, très bien adaptés aux modèles de type Sears [20].

La figure 2.2 présente un résumé des différents mécanismes de génération du bruit aéroacoustique des ventilateurs, brièvement décrits dans cette section. Comme nous nous intéressons aux rotors de vitesses subsoniques, nous allons uniquement nous attarder sur le bruit dipolaire, dit de charge.

Écoulement uniforme stationnaire

Historiquement, Gutin (1936) [21] a été le premier à avoir développé un modèle valide du bruit d'hélice et a reconnu son caractère principalement dipolaire. Il a calculé le rayonnement acoustique causé par une hélice tournant dans un écoulement uniforme (Fig. 2.3) en considérant des forces tournantes d'intensité constante exercées sur les pales du rotor. Un observateur dans un référentiel fixe observera des fluctuations de pressions à la FPP et ses harmoniques. En pratique, ce bruit est négligeable pour des ventilateurs subsoniques car la vitesse de phase angulaire des forces d'intensité constante est égale à la vitesse de rotation du rotor.

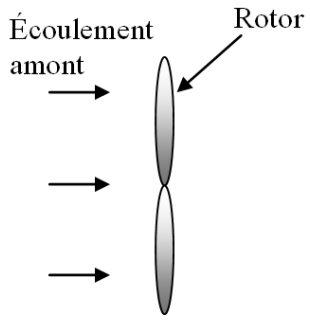

Figure 2.3 Écoulement uniforme

Écoulement non uniforme stationnaire

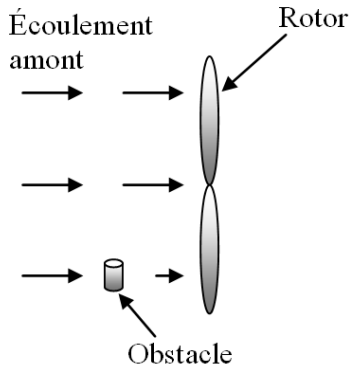

Figure 2.4 Écoulement non uniforme

Quand une hélice évolue dans un écoulement stationnaire mais non uniforme (Fig. 2.4), chaque pale est sujette à des forces dont l'amplitude varie périodiquement au cours de la rotation, à cause du changement circonférentiel d'amplitude et d'angle d'attaque de l'écoulement entrant. Ces forces instationnaires périodiques sont à l'origine de tons purs à la FPP et ses harmoniques, beaucoup plus intenses que dans le cas d'un écoulement uniforme (bruit en excès) [10] [17] [19]. En effet, les vitesses de phase angulaires de ces forces sont habituellement largement supérieures à la vitesse de rotation du rotor. Elles peuvent même devenir supersoniques pour certains modes de la décomposition en série de Fourier circonférentielle des forces instationnaires périodiques exercées par les pales sur le fluide [3] [4] [15].

C'est ce type de bruit qui fera l'objet de toute l'attention de cette thèse. Des études plus approfondies sont proposées dans les parties théoriques des chapitres 2, 4 et 5.

Écoulement non uniforme instationnaire

Quand l'écoulement devient instationnaire (Fig. 2.5), les forces ne sont plus périodiques et le spectre n'est plus discret. L'ingestion de structures turbulentes suffisamment petites pour n'être

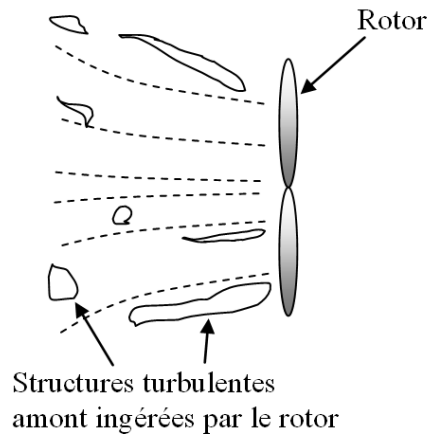

Figure 2.5 Ingestion de turbulences par un rotor

interceptées qu'une seule fois lors de leur passage dans le rotor génèrent un bruit large bande. Par contre, l'ingestion de turbulences plus étirées, pouvant être interceptées plusieurs fois par les pales du rotor, peuvent causer un élargissement de la fréquence de passage des pales et ses harmoniques.

Couche limite et bruit d'instabilité

Même en l'absence d'ingestion de turbulences, les couches limites turbulentes se développant sur les pales peuvent rayonner un bruit large bande, en particulier au bord de fuite. Cependant, le bruit provoqué par les turbulences ingérées par l'hélice (bruit en excès), domine souvent le bruit de couche limite [10].

Un bruit d'instabilité peut aussi résulter d'une rétroaction aérodynamique-acoustique. Des ondes instables dans la couche limite laminaire sur l'extrados forment un dipôle acoustique en arrivant au bord de fuite de la pale, qui se propage ensuite et renforce la perturbation aérodynamique originale, créant ainsi une boucle de rétroaction aérodynamique-acoustique sous certaines conditions de fréquence [10] [17]. Dans certaines études, le spectre engendré par de telles perturbations peut être distribué sur une grande bande fréquentielle ou bien être localisé sur une bande étroite (quelques références bibliographiques sont données dans [10]). Ce type de bruit ne fait pas partie des objectifs de contrôle de cette thèse.

Jeu en bout de pales

Des forces instationnaires peuvent aussi être provoquées par des décollements en bout de pale, créés par la différence de pression entre l'intrados et l'extrados des pales [10]. Ce bruit ne devient important que pour des jeux en bout de pale suffisamment grands. Une virole limite l'apparition de ce phénomène. Les composantes spectrales de ce bruit peuvent être large bande ou à bande

étroite à des fréquences non-harmoniques de la FPP [22]. Ce type de bruit ne fait pas non plus l'objet d'attention particulière dans cette thèse.

Interaction rotor/stator

Les perturbations de l'écoulement introduites par un obstacle situé en amont du rotor (des aubes par exemple) se composent d'une distorsion stationnaire due aux vitesses moyennes des sillages et d'une distorsion instationnaire due aux tourbillons lâchés par l'obstacle et ingérés par le rotor. Les charges induites sur le rotor par ces sillages sont respectivement périodiques et aléatoires, rayonnant ainsi respectivement des bruits de raies et large bande. Dans le cas d'un rotor évoluant en amont d'un obstacle, deux mécanismes peuvent rayonner du bruit de raie et large bande, les interactions potentielles et les interactions de sillage [23] [24] :

- L'obstacle aval peut être le siège de fluctuations de charge dues à l'interception de sillages visqueux issus du rotor.
- Les distorsions de l'écoulement situées au voisinage de l'obstacle peuvent provoquer des charges instationnaires sur le rotor amont. On parle alors d'interaction potentielle, du nom de la théorie des écoulements à potentiel, utilisée pour calculer les distorsions.

L'étude analytique fondamentale permettant de relier les distorsions d'écoulement entrant aux charges instationnaires (en terme de portance) fut menée par Sears en 1941 [20] et Kemp et Sears [25] [26] dans le cadre de l'interaction rotor-stator d'un étage de compresseur à flux axial. Amiet [27] a ensuite permis d'étendre ce modèle pour des fluides compressibles. Les résultats principaux sont répertoriés dans [15], [4] ou [28]. Une revue de bibliographie plus détaillée sera fournie au chapitre 6.

Des études numériques aéroacoustiques plus récentes sur l'interaction rotor/stator ont été menées pour des ventilateurs de radiateur d'automobile [29] [30] [31] [32] [33] ou pour d'autres types de rotors [34] [35]. L'étude de Korakianatis [36] [37] a apporté des résultats sur la contribution relative des interactions de sillage et potentielles dans les turbines.

La littérature est riche de travaux expérimentaux sur l'interaction rotor/stator ou l'interaction entre un rotor et un écoulement non uniforme. Quelques exemples sont donnés dans cette section. Mugridge [38] a examiné le bruit rayonné par un ventilateur d'automobile fonctionnant derrière un radiateur. Il a mesuré les distorsions de l'écoulement entrant avec un anémomètre à fil chaud attaché sur une pale ainsi que le bruit rayonné. Des profils de vitesse d'écoulement plus raffinés ont été mesurés plus récemment par Morris *et al.* [39]. Raffy *et al.* [40] ont quant à eux mesuré les fluctuations de pression directement sur les pales d'une maquette de soufflante subsonique grâce à des transducteurs à films minces. Staiger [41] a mené une étude expérimentale très complète sur des compresseurs axiaux à faible vitesse. Les travaux exposés dans [41] présentent un grand intérêt

pour la validation de modèle permettant de relier les variations de vitesse d'écoulement aux forces agissant à divers emplacement sur les pales. Des mesures d'écoulement par anémométrie laser à effet Doppler ainsi que des mesures d'intensimétrie acoustique ont été effectuées par Akaike *et al.* [42] sur des ventilateurs de radiateur d'automobile. Washburn [43] et Wong [44] ont quant à eux regardé empiriquement l'influence d'obstructions en amont dans la génération du bruit de raie de petits ventilateurs utilisés pour refroidir les composants électroniques. Des mesures de fluctuations de pression sur des pales de rotor de ventilateurs centrifuges sont présentées dans [45] et [46] pour une roue à aubes. Enfin, une étude intéressante pour le contrôle du bruit de raie à l'aide d'obstructions dans l'écoulement a été menée par Subramanian [47] sur le rayonnement en champ libre d'une hélice à quatre pales interagissant avec une distorsion à trois ou quatre cycles circonférentiels.

Nous finirons cette section sur le bruit aérodynamique des ventilateurs subsoniques par deux remarques sur la contribution relative du bruit de rotor et de stator. La première est formulée par Fournier [48] : "*les forces, donc le bruit, sont d'autant plus grands que la vitesse relative entre l'aube* (ou la pale) *et le fluide est élevée ; le bruit de rotor domine donc en général le bruit de stator*". La deuxième remarque, de Huang [49], va aussi dans ce sens pour les ventilateurs utilisés dans les ordinateurs : "*Typical struts are circular or triangular cylinders of small size, and the unsteady forces experienced by the struts are normally much smaller than on the rotor blades which are, after all, so profiled to generate large lift*". Pour ces raisons, nous orienterons aussi les travaux de cette thèse en émettant l'hypothèse que le bruit de rotor domine le bruit de stator dans le cas des ventilateurs de radiateur d'automobile. Tempérons ces propos pour un ventilateur soumis à un écoulement peu distordu. Dans un tel cas, le bruit de stator peut devenir non négligeable par rapport au bruit de rotor.

La lourdeur de la mise en œuvre d'une modélisation aérodynamique numérique et la difficulté technologique des méthodes expérimentales pour accéder aux sources de bruit que sont les forces exercées sur les pales, nous ont orienté vers une solution expérimentale alternative : un modèle aéroacoustique inverse.

2.2 Modèle inverse

Un problème inverse consiste à déterminer des causes connaissant des effets. Ainsi, ce problème est l'inverse de celui appelé problème direct, consistant à déduire les effets, les causes étant connues. En aéroacoustique, les sources (les causes) rayonnant du bruit (l'effet) peuvent par exemple provenir d'un écoulement turbulent (source quadripolaire), de fluctuation de pression sur une paroi (source dipolaire) ou de fluctuation de débit (source monopolaire).

Holste *et al.* [50] ont ainsi proposé une méthode inverse pour retrouver les mécanismes sources

responsables du bruit de raie à partir de l'analyse des modes acoustiques tournants générés par un modèle de turbopropulseur dans un conduit. Un peu plus tard, Holste a mis en œuvre une méthode des sources équivalentes toroïdales pour le calcul du bruit rayonné par les moteurs d'avion [51].

Cependant, ces études ne s'intéressent pas au caractère fondamentalement mal posé de nombreux problèmes inverses. Les difficultés d'inversion, dues par exemple au mauvais conditionnement des matrices de transfert à inverser, ne sont pas traitées. Le modèle lui-même repose sur une idéalisation de la réalité physique et repose sur des hypothèses simplificatrices, il est donc également une source d'incertitudes [52]. Le problème inverse peut alors n'avoir aucune solution au sens strict mais beaucoup de solutions approchées [52]. Des critères additionnels comme la vraisemblance physique peuvent permettre de choisir une solution parmi l'ensemble des solutions possibles. Dans les cas qui suivent, les solutions existent et sont uniques, ce qui satisfait les deux premières conditions d'un problème bien posé selon Hadamard [52]. Par contre, les problèmes qui suivent ne satisfont pas la troisième et dernière condition de Hadamard, de par leurs fortes sensibilités aux erreurs de mesure.

En pratique, plusieurs méthodes d'investigation des problèmes inverses existent mais nous nous limiterons aux techniques de régularisation. Régulariser un problème mal posé, c'est le "remplacer" par un autre, proche du premier et bien posé, de sorte que l'erreur commise soit compensée par un gain de stabilité [52]. La méthode de régularisation de Tikhonov est la plus courante [14]. Pour un problème direct linéaire discrétisé de la forme $\mathbf{p} = \mathbf{Hq}$, elle consiste à trouver une solution $\mathbf{q_0}$ qui minimise la fonction coût suivante :

$$J = \mathbf{e^H e} + \beta \mathbf{q^H q} \tag{2.2}$$

où $\mathbf{e} = \hat{\mathbf{p}} - \mathbf{p}$ est l'erreur entre les mesures réelles $\hat{\mathbf{p}}$ et les "mesures synthétiques" $\mathbf{p}$ (c'est-à-dire la solution du problème direct) plus un terme pondérant la solution produite $\mathbf{q}$. Le choix d'un paramètre de régularisation β, basé sur des critères physiques, s'impose alors. Un outil pratique pour choisir ce paramètre est la courbe en L. Cette courbe, représente la norme de la solution régularisée $\| \mathbf{q} \|$ en ordonnées en fonction de la norme de l'erreur résiduelle $\| \mathbf{e} \|$ en abscisses, correspondant aux différentes valeurs du paramètre de régularisation. Un compromis entre une solution de norme faible (physiquement acceptable) et une norme résiduelle petite peut ainsi permettre de choisir le paramètre de régularisation "optimal" [53] [54] [55] [56]. Un autre outil fondamental dans l'analyse des problèmes inverses est la décomposition en valeurs singulières [14] et en particulier la condition de Picard, permettant d'étudier la stabilité des inversions. Plus de détails sur les techniques de régularisation sont donnés dans les chapitres 3 et 5.

En acoustique, une revue de quelques problèmes inverses est donnée par Nelson [57]. Des

études fondamentales menées par Yoon [58] *et al.* et Nelson *et al.* [59] montrent les possibilités et les limites des reconstructions de sources acoustiques par des techniques inverses, basées sur la régularisation de Tikhonov. Des travaux menés par Kim *et al.* [60] montrent en particulier que la résolution spatiale des sources acoustiques reconstruites peut être inférieure à la demi longueur d'onde du rayonnement acoustique mesuré pour certains arrangements géométriques de capteurs en champ lointain.

Des exemples d'application des méthodes de régularisation se retrouvent dans de nombreux domaines de l'acoustique. Gauthier *et al.* [61] appliquent cette technique à la reproduction de champ sonore. Kim *et al.* [62] l'utilisent pour l'estimation de sources acoustiques à l'intérieur d'un conduit cylindrique. Schuhmacher *et al.* [63] utilisent la méthode de régularisation de Tikhonov pour reconstruire les sources de bruit d'un pneu roulant ou excité par un pot vibrant à l'aide d'un calcul par éléments de frontière inverse. Ils remarquent notamment que, dans une situation expérimentale, la courbe en L est un critère plus robuste que l'approche conventionnelle de la validation croisée généralisée (Generalized Cross-Validation) pour choisir le paramètre de régularisation.

Toutefois, très peu de références sont disponibles sur les modèles inverses appliqués au bruit de ventilateur. Les travaux menés par Patrick *et al.* [64] ont posé les bases des problèmes inverses en aérodynamique instationnaire et en aéroacoustique. Ils ont montré la possibilité de reconstruire une perturbation de vorticité dans un écoulement approchant un profil aérodynamique à partir du champ acoustique rayonné. Grace *et al.* [65] [66] ont repris les travaux de Patrick *et al.* [64] et analysé plus en détail la reconstruction des pressions instationnaires le long d'une surface portante plate et rigide soumise à un écoulement subsonique instationnaire. Une étude similaire a été menée par Wood *et al.* [67] sur un profil d'aile rectangulaire. Luo *et al.* [68] ont quant à eux étudié numériquement un problème aéroacoustique inverse sur l'interaction entre les sillages lâchés par un rotor et interceptés par un stator. Le champ de pression acoustique est relié à la distribution de pression sur la surface du stator par une intégrale de Fredholm de première espèce, qui est un problème mal posé bien connu. Li *et al.* [69] ont également proposé d'utiliser un modèle inverse, basé sur une équation intégrale obtenue par Farassat, pour extrapoler le champ acoustique rayonné par une hélice à partir d'un ensemble limité de points de mesure.

Citons enfin Lewy [70], qui a estimé la structure modale du champ acoustique engendré par une soufflante de turboréacteur carénée à partir de mesures de directivité en champ lointain (hors conduit), en se basant sur un modèle analytique. Un nombre limité de modes a été sélectionné, à partir d'informations connues a priori sur les sources, pour rendre le système d'équations déterminé. Cependant aucune méthode de régularisation n'a été mise en œuvre dans cet article.

Malgré les quelques études sur les modèles inverses en aéroacoustique des profils aérodynamiques et leur résolution par des méthodes de régularisation, aucune étude expérimentale n'a été publiée. Cette thèse propose donc de combler ce manque dans les chapitres 3 et 5. Les forces

tournantes instationnaires périodiques agissant sur les pales du rotor seront estimées expérimentalement à partir de mesures du champ acoustique rayonné en champ lointain à la FPP et ses harmoniques, à l'aide de l'inversion des modèles analytiques de Morse et Ingard et de Blake.

2.3 Techniques de contrôle

2.3.1 Généralités

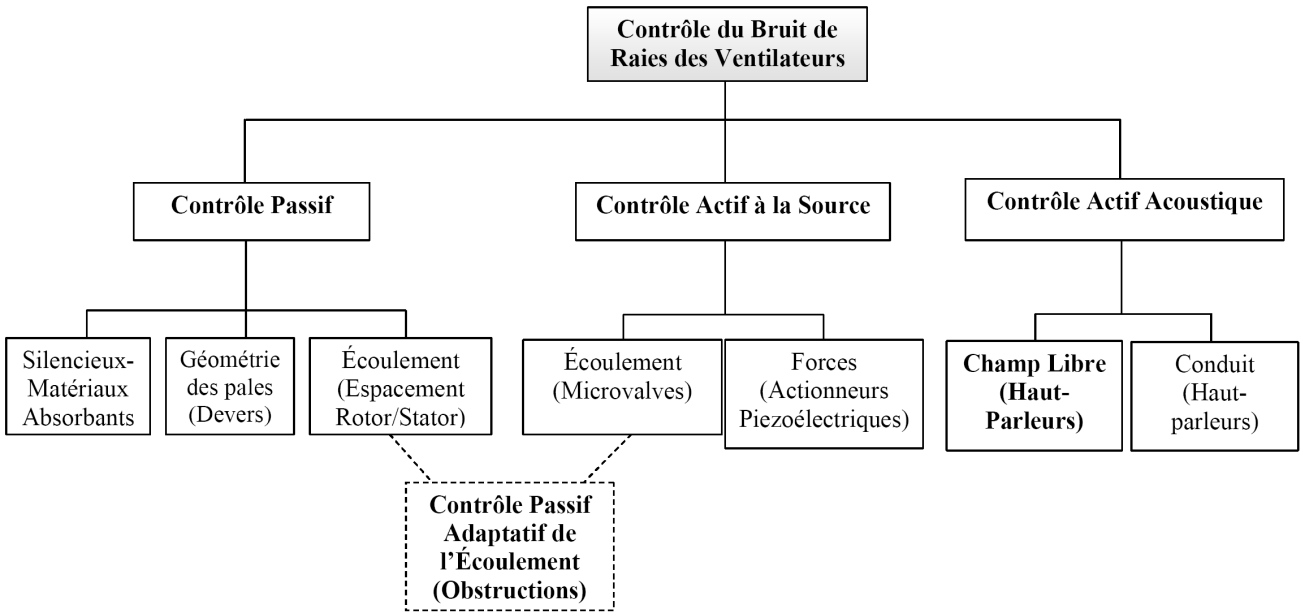

Figure 2.6 Résumé des techniques de contrôles du bruit de raie de ventilateur

Les techniques de contrôle du bruit peuvent généralement être classées en deux grandes familles : les méthodes passives et les méthodes actives (figure 2.6). Les premières ont fait l'objet de beaucoup d'attention et ont permis de réduire très largement le bruit total rayonné par les ventilateurs. Neise [10] propose une synthèse des méthodes de contrôle passif pour des ventilateurs à flux axial et centrifuge et Maling [71] présente une large revue de littérature sur le contrôle passif du bruit généré par des petits ventilateurs. Alizadeh *et al.* [72] présentent aussi quelques solutions pour réduire le bruit des groupes moto-ventilateurs d'une automobile. Les techniques passives s'intéressent surtout à la géométrie du rotor, à ses conditions d'utilisation et à son environnement, afin de réduire le plus de mécanismes de génération de bruit possible (diminuer les fluctuations de forces en homogénéisant l'écoulement) ou minimiser leurs effets acoustiques (ajout de matériaux absorbants ou utilisation de silencieux). Cependant, lorsque l'écoulement traversant le ventilateur demeure spatialement non uniforme, un bruit de raie peut fortement émerger du bruit large bande. Ce bruit est souvent basse fréquence ; dans ce cas, l'ajout de matériaux absorbants est inefficace et l'emploi de silencieux passif encombrant et coûteux. De plus, la place

disponible pour ces ajouts est souvent limitée, comme dans le cas des ventilateur de radiateur d'automobile. La même problématique est rencontrée dans le secteur aéronautique où, comme le mentionne Envia [2], les nouvelles nacelles de turboréacteurs sont de plus en plus courtes, ce qui diminue la place disponible pour l'ajout de matériaux absorbants diminue.

Quand les méthodes passives ont échoué, des méthodes actives peuvent être utilisées. Nous distinguerons contrôle actif acoustique et contrôle actif à la source (figure 2.6).

2.3.2 Contrôle actif acoustique

Principe

Le principe de base du contrôle actif est présenté sur la figure 2.7. Cette technique est basée sur la superposition de deux ondes, l'onde acoustique secondaire (S2) générée au point L venant annuler l'onde perturbatrice primaire (S1) générée au point A. La perturbation primaire est captée par un microphone M ; et la source secondaire est pilotée par un contrôleur V, introduisant un déphasage entre l'onde primaire et l'onde secondaire, Lueg (1936).

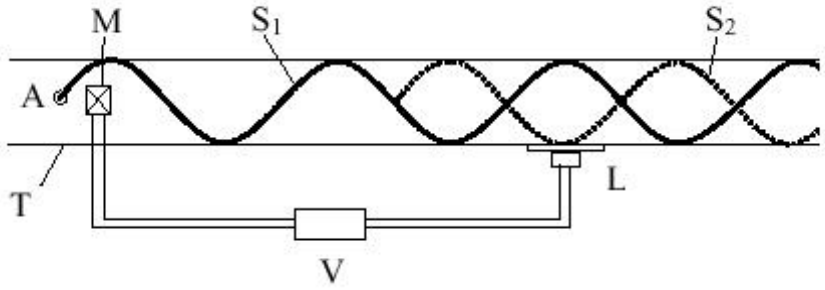

Figure 2.7 Brevet de Lueg sur le contrôle actif, 1936

Cette technique a été rendue possible et commercialement viable par la puissance sans cesse croissante et le prix sans cesse décroissant des microprocesseurs dédiés au traitement du signal (ou DSP pour " Digital Signal Processor "). Dans les ouvrages de référence [73] sur le contrôle actif des vibrations, [74] sur le contrôle actif acoustique et [75] sur les techniques de traitement du signal qui y sont associées, les techniques de contrôle actif sont classées de différentes façons selon le type de bruit à contrôler : 1) Contrôle par rétroaction (feedback) ou Contrôle par anticipation (feedforward), 2) Contrôle entrée simple/sortie simple (SISO) ou Contrôle entrées multiples/sorties multiples (MIMO), 3) Contrôle linéaire ou contrôle non linéaire.

Les applications du contrôle actif sont généralement basses fréquences. Des techniques de contrôle linéaire par anticipation monocanal sont alors suffisantes dans bien des cas. Pour les plus hautes fréquences, les stratégies de contrôle actif sont limitées par la complexité des champs

acoustiques rayonnés, nécessitant l'usage de contrôleurs multicanaux, ainsi que par le besoin d'une fréquence d'échantillonnage plus haute [75], limitant la charge de calcul des DSP entre chaque pas de temps.

Contrôle actif en conduit

Beaucoup d'applications de contrôle actif du bruit de ventilateur sont orientées vers le contrôle d'onde acoustique plane en conduit, donc typiquement pour des fréquences associées à des longueurs d'onde au moins deux fois plus grandes que le diamètre du conduit. Un seul haut-parleur affleurant le conduit sur le chemin de propagation de l'onde acoustique est alors nécessaire. Par exemple, Erikson *et al.* [76] ont obtenu des atténuations du bruit de l'ordre d'une dizaine de dB dans un conduit de ventilation sur une plage fréquentielle allant de 20 Hz à 300 Hz à l'aide d'un contrôleur monocanal par anticipation. Yeung *et al.* [77] confirment aussi le potentiel d'application de techniques commerciales de contrôle actif monocanal pour réduire le bruit des systèmes de ventilation. Kostek [78] a quant à lui proposé un système hybride, combinant le contrôle actif et l'utilisation d'un résonateur de Helmholtz adaptatif. Wong [44] a mis en œuvre une solution hybride passive/active pour contrôler le bruit d'un ventilateur de climatisation dans un hall d'entrée. Il a disposé des matériaux absorbants et un haut-parleur sur un court conduit volontairement ajouté, procurant ainsi une atténuation du bruit large bande haute fréquence et des atténuations de la FPP (85 Hz) de l'ordre d'une quinzaine de dB en divers endroits du hall. Cette technique nécessite un minimum de place pour introduire un petit conduit. Citons aussi Besombes [79] pour le contrôle actif du bruit de ventilateurs centrifuges avec des capteurs et actionneurs integrés. Enfin, Howard *et al.* [80] ont repris le brevet de Harada [81] qui consiste à ajuster la position angulaire relative de deux ventilateurs dans un conduit afin de réduire l'amplitude d'une seule raie. Ils ont ainsi obtenu une atténuation de 10 dB à la FPP. L'inconvénient du système est que l'atténuation de la FPP et une de ses harmoniques n'exige pas nécessairement la même "synchronisation de phase" des deux ventilateurs.

C'est dans le domaine de l'aéronautique que nous trouvons les systèmes de contrôle actif en conduit les plus évolués, capables de contrôler plusieurs modes de conduit simultanément. Des rangées circonférentielles de sources acoustiques affleurant le conduit sont, par exemple, utilisées pour contrôler les modes générés par des soufflantes de turboréacteurs [82] [83] [84] [85] [86] [87]. Cependant, le coût, le poids et les contraintes de mise en œuvre rendent ces techniques pratiquement peu viables pour l'instant [88].

Contrôle actif en champ libre

Peu de résultats de contrôle actif en champ libre sont disponibles dans la littérature et encore moins sur le bruit de ventilateur.

Dans une étude sur le contrôle actif de bruit environnemental, Wright *et al.* [89] montrent la possibilité de créer des dipôles, tripôles et quadripôles de faibles amplitudes en champ libre à partir d'un monopôle primaire ponctuel et d'un monopôle secondaire ponctuel en fonction de la distance les séparant et de la fréquence de l'onde acoustique à contrôler. Qiu *et al.* [90] arrivent à la conclusion que : si la taille de la source primaire est petite devant la longueur d'onde acoustique, si la source primaire est stable et si le champ acoustique est bien défini, alors l'utilisation d'un multipôle très proche de la source primaire est plus adéquate qu'un réseau de monopôles en terme de nombre de canaux de sortie du contrôleur et de sensibilité au positionnement des sources secondaires. Cette conclusion a étayé a posteriori le choix, présenté au chapitre 4, d'un petit haut-parleur non-bafflé, de directivité dipolaire, pour contrôler le bruit de raie basse fréquence, quasi dipolaire, rayonné par un ventilateur de radiateur d'automobile en champ libre.

Bschorr [91] a analysé théoriquement la possibilité de contrôler le bruit de raie généré par une hélice d'avion en champ libre à l'aide d'une ou plusieurs sources acoustiques monopolaires situées près de l'hélice. Il remarquait alors que l'utilisation d'une seule source monopolaire n'était pas suffisante pour atténuer les harmoniques de la FPP dans tout l'espace mais que l'utilisation de plusieurs sources monopolaires pouvait rendre le contrôle quasi omnidirectionnel. Une autre expérience, menée par Quinlan [92], a consisté à modifier l'impédance de rayonnement vue par un petit ventilateur axial inséré dans un baffle rigide plan grâce à un haut-parleur en opposition de phase situé à coté du ventilateur. En présence de la source secondaire, l'impédance de rayonnement devient faiblement résistive et hautement réactive, ce qui permet de considérablement réduire l'énergie capable de se propager en champ lointain. Il obtient ainsi une atténuation de puissance acoustique de 12 dB et de 7 dB dans un demi-espace à la FPP et son premier harmonique respectivement. La même stratégie de contrôle a été utilisée par Wang *et al.* [93] pour un ventilateur possédant autant d'aubes de stator que de pales de rotor, facilitant ainsi le contrôle de la FPP en privilégiant son rayonnement dans l'axe. Finalement, Gee *et al.* [94] ont conçu un système de contrôle actif multi-canaux pour contrôler globalement le bruit de raie de petits ventilateurs à flux axial typiquement utilisés dans les ordinateurs. La puissance acoustique des quatre premières raies a ainsi été réduite de 9 à 19 dB dans un demi-espace en champ libre avec deux microphones d'erreur et quatre petits haut-parleurs. L'utilisation de petits haut-parleurs (de 28 mm de diamètre) de faible puissance en basse fréquence limite l'atténuation de la FPP (370 Hz).

Le chapitre 4 de cette thèse contribue à l'avancement des connaissances dans ce domaine. Une stratégie de contrôle actif monocanal, utilisant un petit haut-parleur pour contrôler le bruit de raie généré par un ventilateur de radiateur d'automobile en champ libre, sera simulée et mise en œuvre expérimentalement. L'originalité de cette stratégie réside dans l'utilisation d'un seul petit haut-parleur non bafflé situé devant le moyeu du ventilateur. Sa directivité dipolaire permet le contrôle d'une grande partie du rayonnement acoustique à la FPP et son premier harmonique.

2.3.3 Contrôle actif à la source

En contrôle actif acoustique conventionnel, des haut-parleurs sont utilisés pour générer un bruit en opposition de phase avec le bruit à contrôler. Certaines études ont aussi montré qu'un contrôle actif du bruit de raie à la source est possible, soit en contrôlant les forces sur les pales (génération magnétique ou vibratoire), soit en contrôlant directement l'écoulement à l'origine des forces (aspiration de la couche limite ou soufflage au bord de fuite). Elles présentent un grand intérêt pour l'intégration des systèmes de contrôle actif.

Contrôle des forces

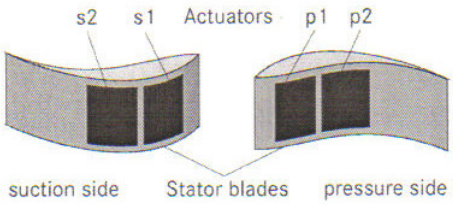

Figure 2.8 Vue schématique d'une aube de stator active (d'après Zillmann *et al.* [11])

Lauchle *et al.* [95] ont par exemple utilisé un ventilateur de refroidissement électronique (lui-même) comme source secondaire, en l'actionnant axialement par un pot vibrant pour générer un bruit secondaire en opposition de phase avec le bruit primaire grâce à un contrôleur par anticipation. Des atténuations globales de 13 dB à la FPP et de 8 dB pour son premier harmonique ont été obtenues dans le demi-espace amont, pour un ventilateur bafflé. Cette étude prouve expérimentalement que le bruit de raie peut être réduit en injectant des forces secondaires périodiques en opposition de phase avec les forces primaires générant le bruit à contrôler. Piper *et al.* [96] ont ensuite poussé plus loin le concept de Lauchle *et al.* [95] en faisant usage de roulements magnétiques pour se servir du rotor comme source secondaire. Ils ont démontré expérimentalement le principe en connectant le ventilateur à un arbre supporté radialement et axialement par des roulements. Ils ont ensuite piloté ces roulements pour injecter des vibrations au rotor, afin qu'il rayonne un bruit en opposition de phase avec le bruit de raie primaire. Grâce à un contrôleur par rétroaction, des atténuations de pression acoustique de 4 dB ont été obtenues à la FPP (100 Hz) au microphone d'erreur.

Par une approche analytique et numérique, Kousen *et al.* [97] ont montré que le contrôle du déplacement des aubes de stator permettrait d'atténuer le champ acoustique rayonné par l'interaction du sillage des pales du rotor sur les aubes du stator. Kousen *et al.* montrent que si le nombre d'aubes indépendamment actionnées était égal au nombre de modes acoustiques de propagation à contrôler dans un conduit, alors l'atténuation du champ acoustique serait complète avec des amplitudes de déplacement de l'ordre de 1/1000 à 1/10000 de la corde. Les résultats sont

très encourageants. Dans le même ordre d'idées, un arrangement de sources dipolaires disposées sur les aubes de stator a permis à Myers et Fleeter [98] d'atténuer quelques modes se propageant dans le conduit d'un turboréacteur à double flux simplifié de 16 pales de rotor et soit une soit trois aubes de stator. Sawyers et Fleeter [34] ont mesuré des atténuations de 10 dB en utilisant des cavités perforées dans les aubes du stator et en les actionnant par des compresseurs. Finalement, Zillmann *et al.* [11] ont utilisé deux paires d'actionneurs piezoélectriques (2 sur l'intrados et 2 sur l'extrados, Fig. 2.8) comme sources dipolaires sur les 10 aubes de stator équipant un compresseur monoétage. Des atténuations de puissance acoustique de 7 dB ont été obtenues à la FPP.

Contrôle de l'écoulement

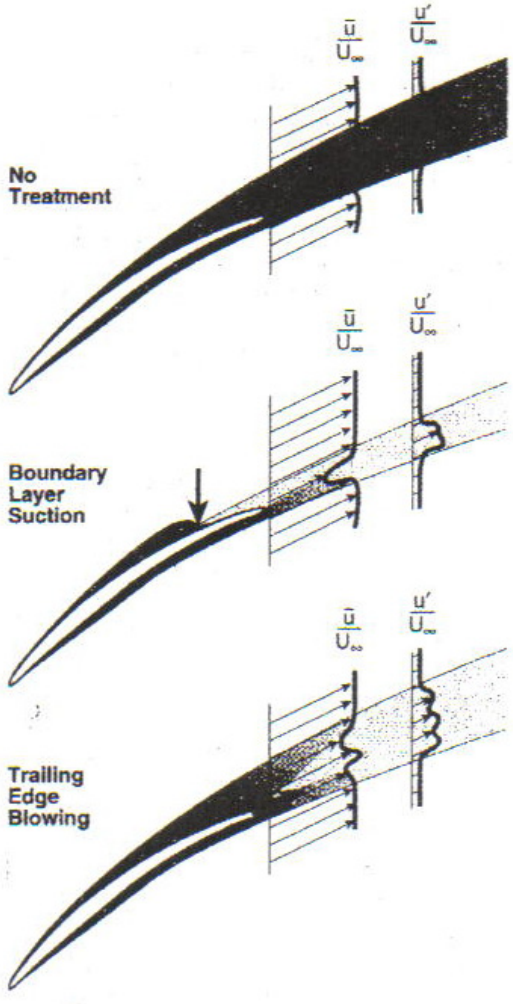

Figure 2.9 Principe du contrôle de l'écoulement autour d'une pale (d'après Waitz *et al.* [12])

Waitz *et al.* [12] on montré le potentiel du contrôle de l'écoulement autour des pales d'un rotor (amont) de turbocompresseur pour rendre l'écoulement traversant le stator (aval) plus uniforme et donc réduire les charges instationnaires sur le stator (et ainsi réduire le bruit rayonné). Des modèles numériques 2D et des mesures de sillage leur ont permis de conclure qu'une technique

d'injection de fluide au bord de fuite des pales du rotor avait un plus grand potentiel de réduction de bruit qu'une technique d'aspiration de la couche limite des pales du rotor. La figure 2.9 illustre le principe des deux techniques.

Rao *et al.* [99] ont ensuite réussi à contrôler activement les interactions entre les sillages lâchés par les aubes de stator (amont) et interceptés par le rotor (aval) sur un modèle réduit de turboréacteur à double flux en se servant de microvalves intégrées pour injecter du fluide au bord de fuite de chaque aube de stator. Un contrôleur PID (Proportionnel Integral Dérivé) a été utilisé pour envoyer le signal aux microvalves en fonction des déficits de vitesses mesurés dans les sillages du bord de fuite des 4 aubes de stator à l'aide de tubes de Pitot. Des atténuations de pression acoustique de plus de 3 dB (avec un maximum de 8,2 dB) ont été obtenues en champ lointain. Neuhaus *et al.* [100] ont enfin utilisé des buses réparties circonférentiellement pour injecter des petits jets d'air comprimés en aval du rotor pour homogénéiser l'écoulement arrivant sur un stator situé en aval. La position axiale des buses et la direction du jet étaient variables. L'injection de jets correctement orientés a permis l'atténuation de la FPP de 20,5 dB en aval et de 5 dB en amont mais a aussi généré des harmoniques de la FPP.

2.3.4 Contrôle passif adaptatif de l'écoulement

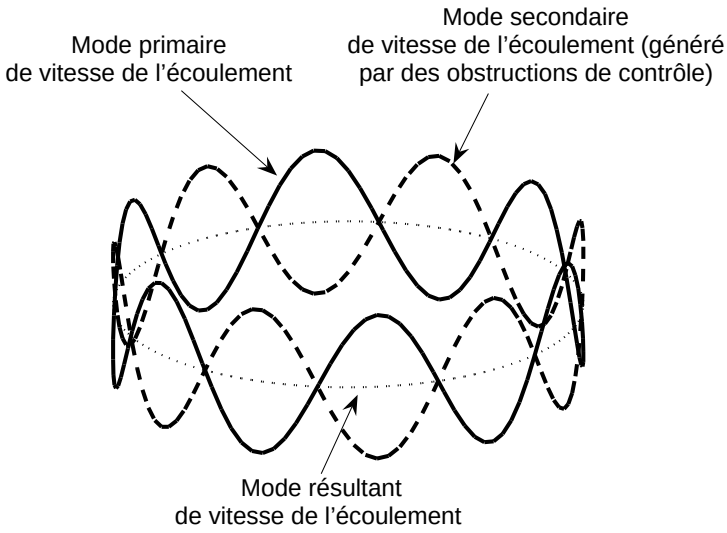

Figure 2.10 Principe du contrôle passif adaptatif de l'écoulement

Nous classons ici une technique de contrôle semi-active particulière, qui n'est ni une technique de contrôle passif conventionnelle, ni une technique de contrôle actif conventionnelle. Elle consiste à créer volontairement une non-uniformité dans l'écoulement pour créer des sources aéroacous-

tiques secondaires en opposition de phase avec les sources primaires (Fig. 2.10). La génération de cette non-uniformité secondaire est réalisée grâce à l'ajout d'obstructions dans l'écoulement. Cette méthode est passive dans le sens où le contrôle d'une raie ne nécessite pas d'injection d'énergie. Elle s'inspire aussi des méthodes de contrôle actif, dans le sens où la position des obstructions doit être adaptée, pour générer une onde acoustique en opposition de phase avec l'onde primaire à contrôler. Cette méthode peut aussi être adaptative pour suivre les éventuelles variations temporelles de l'écoulement primaire. Nous parlerons alors de **contrôle passif adapté** pour contrôler la partie stationnaire de l'écoulement et de **contrôle passif adaptatif** pour contrôler la partie instationnaire de l'écoulement. Dans toutes les études menées sur le sujet, seule la composante stationnaire de l'écoulement primaire a été contrôlée (contrôle passif adapté).

Les premiers à avoir trouvé le concept sont Fournier *et al.* [101]. L'idée de base consistait à annuler des variations circonférentielles de vitesse d'écoulement, générées par une première rangée de cylindres, grâce à une deuxième rangée circonférentielle de profils aérodynamiques (compensateurs). Dans une expérience de démonstration en conduit mais sans rotor, ils ont orienté circonférentiellement la deuxième rangée de telle sorte que la vitesse de la distorsion de l'écoulement soit largement réduite dans un plan situé entre les deux rangées (emplacement du rotor fictif).

Nelson [102] a ensuite mené une étude analytique préliminaire pour estimer le potentiel de réduction du bruit de raie de soufflante de turboréacteur à l'aide d'obstructions dans l'écoulement. À partir du modèle théorique proposé par Goldstein [15], Neslon propose de minimiser une somme pondérée d'harmoniques de la FPP à partir d'obstructions interagissant avec le rotor. Quelques simulations lui ont permis de montrer que le contrôle d'une raie pouvait entraîner l'amplification des autres raies.

Polacsek *et al.* [103] ont simulé l'interaction entre des obstructions de contrôle cylindriques et un rotor pour minimiser le bruit de raie à la FPP à l'aide d'un solveur RANS (Reynolds Averaged Navier Stokes). Des expériences sur un modèle réduit de compresseur leur ont permis d'obtenir des atténuations de pression acoustique de 8 dB lorsque les cylindres généraient un mode acoustique de conduit en opposition de phase avec le mode primaire se propageant dans le conduit. Cependant l'atténuation de la FPP s'accompagne de l'amplification des harmoniques d'ordres supérieurs. Neuhaus *et al.* [100] ont aussi placé des petits cylindres pouvant translater axialement et tourner circonférentiellement. La pression acoustique a ainsi été atténuée de 12,6 dB en aval à la FPP mais l'amplitude des harmoniques a augmenté. Un brevet basé sur le même principe a été déposé par Anderson [104]. Un autre brevet a été déposé par Farrell *et al.* [105] sur une technique semblable, permettant de varier sinusoïdalement le jeu en bout de pales (grâce à une virole creusée sinusoïdalement).

Dans les études précédentes, le positionnement des obstructions était manuel. Seul Kota [88] (2005) et Kota *et al.* [13] (2006) se sont intéressés au positionnement automatique des obstruc-

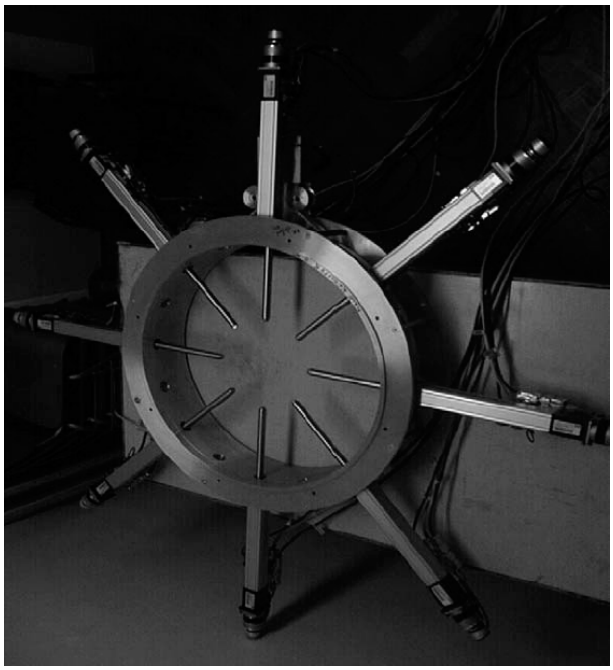

Figure 2.11 Cylindres de contrôle (d'après Kota *et al.* [13])

tions, en se basant sur les développement théoriques de Nelson [102]. Après avoir remarqué que le positionnement d'un seul cylindre pouvait générer d'autres modes que celui à contrôler, Kota a formulé un problème de minimisation de la somme des puissances acoustiques des différents modes se propageant dans le conduit. Un algorithme du gradient a été implanté pour trouver les longueurs d'insertions de plusieurs cylindres dans l'écoulement (Fig. 2.11) afin de minimiser le bruit rayonné à plusieurs fréquences. À faible vitesse de rotation (seul le mode plan pouvait se propager à la FPP), une atténuation maximale de puissance acoustique du mode plan de 25 dB a été obtenue en utilisant un cylindre pour générer le bruit primaire et deux cylindres pour le contrôler. Des atténuations de pression acoustique en champ lointain (hors conduit) de 6 dB pour la FPP, 8 dB pour son premier harmonique et une amplification de 5 dB pour son deuxième harmonique ont été mesurées. Pour des FPP plus élevées, la présence de trois modes pouvant se propager à la FPP a limité considérablement l'atténuation de puissance acoustique dans le conduit FPP à 2 dB en utilisant 18 ou 19 cylindres de contrôle. Kota note [88] que l'algorithme du gradient est inadapté dans la plupart des cas, car la convergence vers un minimum local est plus probable que vers le minimum global du bruit rayonné. En effet, la présence d'un bruit de fond important dans le conduit, l'effet non linéaire de la longueur des cylindres sur la pression acoustique et le couplage entre les différents cylindres de contrôle rendent les surfaces d'erreur bruitées et non quadratiques, ainsi, la convergence vers le minimum global est très délicate.

Il reste donc deux lacunes majeures aux techniques de contrôle passif adaptatif du bruit de raie de ventilateur :

– La conception d'obstructions permettant d'atténuer une raie sans amplification des autres raies ;
– La mise au point d'algorithmes d'adaptation de la position des obstructions qui convergent vers un minimum global de puissance acoustique.

Cette thèse propose de s'intéresser plus particulièrement à la première lacune. En effet, la conception d'obstructions pouvant contrôler le mode le plus rayonnant, sans régénération d'autres modes, devrait limiter le nombre d'actionneurs et faciliter la mise en œuvre d'un contrôleur. Il sera alors possible d'utiliser des algorithmes de contrôle découplés qui ajustent la position d'une seule obstruction pour atténuer une seule raie (plutôt que l'ajustement simultané de plusieurs positions d'obstructions pour atténuer la somme de toutes les raies). Nous proposons, dans cette thèse, d'ajuster la distance axiale entre le rotor et les obstructions de contrôle pour varier l'intensité d'interaction ; et d'ajuster la position circonférentielle des obstructions pour varier la phase de l'onde acoustique secondaire générée. Le chapitre 6 s'intéresse à la conception des obstructions de contrôle, basée sur un modèle analytique de type Sears. Le chapitre 7 proposera une validation expérimentale des performances acoustiques en champ libre des obstructions présentées au chapitre 6.

CHAPITRE 3

INVERSION DU MODÈLE DE MORSE ET INGARD

CONTRÔLE DU BRUIT TONAL DES VENTILATEURS AXIAUX SUBSONIQUES PARTIE 1 : RECONSTRUCTION DES SOURCES AEROACOUSTIQUES À PARTIR DE PRESSIONS ACOUSTIQUES EN CHAMP LOINTAIN

CONTROL OF TONAL NOISE FROM SUBSONIC AXIAL FAN PART 1 : RECONSTRUCTION OF AEROACOUSTIC SOURCES FROM FAR-FIELD SOUND PRESSURE

Anthony GÉRARD, Alain BERRY et Patrice MASSON (2005) Journal of Sound and Vibration, vol. 288, p. 1049-1075.

Avant propos

Les chapitres 3 et 4 reposent sur le modèle de Morse et Ingard [3]. Ce modèle est bien adapté au calcul du champ de pression acoustique en champ libre à partir d'une distribution de sources dipolaires correspondant aux forces exercées par les pales sur le fluide.

Suffisant pour les travaux relatés dans les deux prochains chapitres, ce modèle est cependant moins commode pour l'integration des théories classiques de portances instationnaires des profils minces. Pour cette raison, le modèle de Blake sera considéré dans les chapitres 5, 6 et 7.

Les notations utilisées dans les chapitres 3 et 4 sont conformes à celles de Morse et Ingard.

3.1 Abstract

An inverse method is investigated to evaluate the unsteady rotating forces (dipole strength distribution) acting by the fan on the fluid from far-field acoustic pressure measurements. A development based on the tonal noise generated by a propeller is used to derive a discretized form of the direct problem. The inversion of this direct problem is ill-posed and requires optimisation technique to stabilize the solution for small perturbations in the measured acoustic input data. The reconstruction reveals that the conditioning of the inverse model depends on the aeroacoustic source and far-field sensor locations as well as on the frequency under investigation. Simulations show that an adequate choice of a regularization parameter leads to a satisfactory reconstruction of imposed unsteady rotating forces in the presence of measurement noise, and a correct localization of acoustic "hot spots" on the radiation surface. Preliminary experimental results also show the ability to extrapolate the radiated sound field at blade passage frequency (BPF), and harmonics, from the reconstructed forces. These data are exploited in the second part of this paper to evaluate various active control strategies for tonal fan noise.

3.2 Introduction

Due to the increasing demand of improved passenger safety and comfort and to the increasing use of communication systems, interior acoustic comfort of future automobiles is expected to be one of the main decision making factors in an extremely competitive market. Tonal noise of axial engine cooling fans is among the several noise sources inside an automobile. For fans with equal blade pitch, dominant tones are radiated underhood by engine cooling fans at the Blade Passing Frequency (BPF, typically around 300Hz) and its multiples, and are transmitted in the car interior. Therefore, there is a need for manufacturers of engine cooling units to design improved,

low-noise axial fans. These two companion papers investigate active control of tonal noise from axial automotive fans as a solution to increase interior acoustic comfort of cars. The first part details an inverse aeroacoustic model to characterize an automotive axial fan as an extended acoustic source ; the second part exploits this aeroacoustic model in active control simulations and experiments in free field.

Fan noise has been a topic of research since the first analytical aeroacoustic models by Ffowcs Williams et al. [16], Wright [17] or Lowson [19] some 30 years ago. Direct methods have been developed for the calculation of the radiated sound field based on the dynamic forces applied by the blades on the fluid in a fixed reference frame. Rotor tonal noise resulting from vane/rotor interaction or non-uniform flow conditions has been extensively studied [16, 17, 19], and it has been demonstrated that, at a rotation Mach number below 0.8 [15], the quadrupolar source can be neglected and the unsteady pressure along the blade surface is equivalent to a dipole distribution. However, it is difficult in practice to estimate the strength of this extended acoustic source. State-of-the-art CFD or aeroacoutic codes presently attempt to predict the unsteady aerodynamics and both the tonal and broadband sound radiation of the propeller [106] ; on the other hand, the measurement of pressure fluctuations on the fan blades require sophisticated or expensive experimental techniques such as integrated piezoplastic sensors [45] or other miniature pressure transducers [41].

Alternative inverse aeroacoustic problems have been recently investigated to overcome these difficulties and to develop non contact measurement techniques. For example, Li et al. [69] developed an inverse method to reconstruct the blade surface pressure distribution from the radiated sound field. Their work is based on the inversion of the Farassat integral solution of the Ffowcs Williams and Hawkings equation, assuming that the aerodynamic loading on the surface of the propeller is steady. Luo et al. [68] also proposed an inverse aeroacoustic model of rotor wake/stator interaction based on a Fredholm integral equation of the first kind. The unsteady surface distribution on the stator surface is derived from the radiated sound field. Other studies focused on the inverse aeroacoustic model of a rectangular wing or a flat plate interacting with a gust [65] [66] [67]. The above inverse aeroacoustic models generally lead to the inversion of an ill-conditioned matrix. Numerical results demonstrate that optimisation and regularization techniques have been successfully used to solve these problems [59] but no experimental results have been reported yet for the source characterization of axial fans.

This paper investigates an inverse aeroacoustic approach to model the elementary acoustic source distribution on the surface of an axial fan from its far-field noise directivity. The derivation of an accurate and physically realistic acoustic model of an axial fan is the first step towards an effective active noise control strategy. The proposed inverse model takes into account the flow disturbance responsible for the tonal noise generation of subsonic axial fans. In the first section of the paper, the direct aeroacoustic model is detailed, whereby the far-field radiated sound is related to the non-uniform flow and the blade pressure distribution by solving the Helmholtz

integral following the approach of Morse et al. [3]. The inverse model is detailed in the following section, and a regularization technique is proposed to overcome a poor conditioning of the inverse problem. The inversion is first tested on simple examples to assess the influence of a number of parameters (such as the discretization of the fan source, frequency and sensing configuration) on the conditioning of the inverse model. Then, a numerical case related to non-uniform upstream flow condition is conducted to demonstrate the feasibility of the reconstruction approach and the ability to distinguish the acoustically radiating components obtained from flow non-uniformities. Finally, preliminary experimental results for the extrapolation of the radiated sound field at blade passage frequency (BPF) and at its harmonics are presented on an actual engine cooling system.

3.3 A direct model for tonal noise of subsonic axial flow fans

The general aeroacoustic equations derived by Ffowcs Williams and Hawkings (FW-K) [16] include the case of a moving surface in an infinite fluid medium at rest outside the flow region [15], and therefore can be used to extract the physical mechanisms of axial fan noise. In general, the expression of the acoustic pressure in the fluid involves three terms : The first term is associated with a moving quadripole source that represents the generation of sound due to turbulent volume sources and corresponds to the solution of the Lighthill theory. This quadripole source is significant only if the blade tip Mach number exceeds 0.8 [15] and is therefore irrelevant to the automotive fan noise, for which blade tip Mach numbers generally don't exceed 0.15. The second term is related to a moving dipole source due to the unsteady forces exerted by the solid surfaces on the fluid. This is the well known 'loading noise' or 'dipole noise', the principal cause of fan noise [15, 17]. The last term is equivalent to a monopole radiation due to the volume displacement effects of the moving surfaces, also called 'thickness noise'. The efficiency of thickness noise is poor at low fan rotation speed since the circumferential phase velocity of the fluid pressure fluctuations generated by the moving blades is well below sonic velocity [10]. Therefore, the main source term for subsonic axial fans is the distribution of forces applied by the blades on the fluid. Periodic forces (steady rotating forces or unsteady rotating forces due to non-uniform but stationary upstream flow) lead to discrete tones generation while random forces (such as turbulent boundary forces) lead to broadband noise.

This section focuses primarily on the discrete tone generation at the BPF and its multiples due to non-uniform, stationary upstream flow field. Indeed, when the flow entering the fan is uniform, the blade forces are steady in a coordinate system rotating with the propeller, but they have an angular frequency equal to $\omega_1 = B\Omega$ in a fixed reference frame (Ω is the angular velocity of the fan and B is the number of blades, assuming an equal blade pitch). For subsonic fans, the circumferential velocity of these forces is below the sound speed, thus this source (first derived by Gutin) does not radiate efficiently. However, even a slight flow irregularity (non-uniform flow) causes circumferentially-varying blade forces and gives rise to a considerably larger radiated sound

at the BPF and its harmonics, especially in the axial direction of the fan [3]. In many instances, axial fans operate in a non-uniform flow : this is the case of engine cooling axial fans that operate behind a radiator/condenser system or in the wake of inlet guide vanes. The interactions between the flow and the blades can be classified into potential interactions and wake interactions [15].

There are many theoretical investigations of the radiated acoustic pressure as a function of the fluctuating forces exerted by the rotating blades on the fluid [3, 15, 17, 19], assuming that these forces can be mathematically modelled or experimentally measured. We chose to use the direct fan noise model of Morse and Ingard [3] because it leads to explicit analytical solutions of the radiated sound field. In this model, Morse and Ingard directly postulate the forces into the spectral domain (circumferential Fourier series decomposition) and introduce these forces as dipolar source terms in the Helmholtz equation to derive the radiated sound field [3]. In constrast, the FW-H theory introduces the force source terms in the spatial domain using a retarded time formulation [15]. Moreover, Fowcs Williams and Hawkings derived their equation by extending the Lighthill acoustic analogy to include the effects of solid boundary surfaces. As opposed to this, Morse and Ingard directly assumed that the force distribution on a surface generates a dipolar-like sound field and can be calculated by introducing them into the Helmholtz integral. Thus, the Morse and Ingard model should be seen as capable of predicting *"the sound field produced by a source distribution which, in its essentials, could serve as a model for a propeller"* [3]. In spite of these differences, both approaches lead to qualitatively very similar expressions of the sound radiation.

The system under study and coordinate systems are depicted in Fig. 3.1. Polar coordinates (r_1, φ_1) are used to specify a point on the fan area, and spherical coordinates (r, φ, θ) or Cartesian coordinates (x,y,z) are used to specify a point in the acoustic domain. The main derivations of the Morse and Ingard model are recalled in this section. The first step of the direct model is to obtain the aerodynamic forces per unit area at (r_1, φ_1) acting on the rotor blades for a non-uniform flow passing through the fan. The second step derives the acoustic radiation of the corresponding elementary dipoles at the BPF and its harmonics at (r, φ, θ).

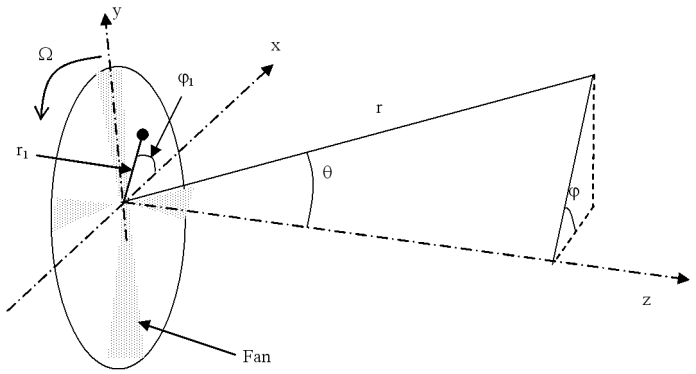

Figure 3.1 Sound radiation from an axial fan (coordinate systems).

3.3.1 Case of uniform flow

The aerodynamic pressure exerted by the fan blades on the fluid are decomposed into an axial (z) component related to the thrust and a circumferential component related to the drag. The pressure is assumed to be zero in the area between the blades. In a uniform flow, the fluid pressure in a fixed reference frame is periodic in time with an angular frequency $\omega_1 = B\Omega$, with its amplitude independent of φ_1 and its phase proportional to φ_1. Thus the time Fourier series of the axial component of the aerodynamic pressure can be written as :

$$f_z(t; r_1, \varphi_1) = \sum_{s=-\infty}^{+\infty} A_s(r_1) e^{-is\omega_1(t-\frac{\varphi_1}{\Omega})} = f_z^0(r_1) \sum_{s=-\infty}^{+\infty} \alpha_s(r_1) e^{isB\varphi_1} e^{-is\omega_1 t} \tag{3.1}$$

with $\alpha_s(r_1) = \frac{A_s(r_1)}{f_z^0(r_1)}$; $i = \sqrt{-1}$ and t is the time. In Eq. (3.1), $\alpha_s(r_1)$ is the coefficient of the Fourier series of the axial pressure in the time domain, representing the complex strength of the s^{th} harmonic of the BPF and $f_z^0(r_1)$ is the time average value of the axial force per unit area at the radial position r_1. In the following, the circumferential component of the aerodynamic pressure (related to aerodynamic drag on the blades) will be neglected in comparison to the axial aerodynamic pressure (z component) since this is usually the case for a well-designed propeller.

3.3.2 Case of non-uniform flow

In the case of a circumferentially varying (but stationary) flow, the time average axial force per unit area f_z^0 is now a function of both r_1 and φ_1. This force can itself be expanded into a spatial Fourier series over the circumferential coordinate :

$$f_z^0(r_1, \varphi_1) = \bar{f}_z^0(r_1) \sum_{q=-\infty}^{q=+\infty} \beta_q(r_1) e^{iq\varphi_1} \tag{3.2}$$

where β_q is the Fourier coefficient of the q^{th} circumferential harmonic that accounts for the non-uniformity with respect to φ_1, and $\bar{f}_z^0(r_1)$ is the circumferential average of $f_z^0(r_1, \varphi_1)$ at the radial position r_1. Even if the circumferential variation of the upstream flow is small, it generally leads to considerably larger radiated sound at low Mach number [3,48]. In the case of non-uniform flow, the expression of the fluctuating axial pressure is therefore :

$$f_z(t; r_1, \varphi_1) = \bar{f}_z^0(r_1) \sum_{s=-\infty}^{+\infty} \sum_{q=-\infty}^{+\infty} \alpha_s(r_1)\beta_q(r_1) e^{i(sB+q)\varphi_1} e^{-is\omega_1 t} \tag{3.3}$$

3.3.3 Free field acoustic radiation

The axial fluctuating blade forces appear as dipole terms in the Helmholtz radiation integral, so the acoustic pressure can be expressed by integrating the unsteady rotating forces over the fan area A,

$$p(t;r,\varphi,\vartheta) = \iint_A f_z(t;r_1,\varphi_1) g_{1z}(t;r_1,\varphi_1;r,\vartheta,\varphi) r_1 dr_1 d\varphi_1 \tag{3.4}$$

where g_{1z} is the sound field from a unit strength point force in the z direction at (r_1,φ_1). Following Morse and Ingard [3] , a far-field ($r >> r_1$) approximation of g_{1z} is given by

$$g_{1z} = -ik\cos\vartheta \frac{e^{ikr}}{4\pi r} \sum_{m=-\infty}^{+\infty} i^m J_m(kr_1\sin\vartheta) e^{im(\varphi-\varphi_1)} e^{-i\omega t} \tag{3.5}$$

where $k = \omega/c$ is the acoustic wavenumber, c is the sound speed, ω is the angular frequency of the radiated sound and J_m is the cylindrical Bessel function of order m. In order to express the resulting far-field radiation of the fan at the multiples of the BPF, one must substitute Eqs. (3.3) and (3.5) into Eq. (3.4) and set $\omega = s\omega_1$ and$k = s\omega_1/c = sk_1$. Solving for the Helmholtz integral, and using the orthogonality relations $\int_0^{2\pi} e^{i(sB+q)\varphi_1} e^{-im\varphi_1} d\varphi_1 = 2\pi$ if $sB+q = m$ and $\int_0^{2\pi} e^{i(sB+q)\varphi_1} e^{-im\varphi_1} d\varphi_1 = 0$ if $sB+q \neq m$, the acoustic radiation due to axial forces is finally given by :

$$\begin{aligned} p_(t;r,\varphi,\vartheta) &= -\frac{ik_1\cos\vartheta}{4\pi r} \sum_{s=-\infty}^{+\infty} \sum_{q=-\infty}^{+\infty} i^{sB+q} e^{isk_1 r} e^{i(sB+q)\varphi - is\omega_1 t} \\ &\quad \times \int_{a_1}^{a_2} s\bar{f}_z^0(r_1)\alpha_s(r_1)\beta_q(r_1) J_{sB+q}(sk_1 r_1\sin\vartheta) 2\pi r_1 dr_1 \end{aligned} \tag{3.6}$$

In Eq. (3.6), s and q represent the Fourier series expansions of the dipole strength over time t and over the circumferential coordinate φ_1, respectively. Moreover, a_1 and a_2 are the interior radius and exterior radius of the fan, respectively.

Morse and Ingard [3] proposed the following alternative form of Eq. (3.6),

$$
\begin{aligned}
p\,(t;r,\vartheta,\varphi) \;=\; & \frac{\cos\vartheta}{r}\sum_{n=1}^{+\infty}(nk_1) \\
& \times\Bigg\{\sum_{l=0}^{+\infty}\int_{a_1}^{a_2}\bar{f}_z^0(r_1)\alpha_n(r_1)\beta_l(r_1)J_{nB-l}(nk_1r_1\sin\vartheta) \\
& \sin[nk_1(r-ct)+(nB-l)(\varphi+\frac{\pi}{2})]r_1dr_1 \\
& +\sum_{l=0}^{+\infty}\int_{a_1}^{a_2}\bar{f}_z^0(r_1)\alpha_n(r_1)\beta_l(r_1)J_{nB+l}(nk_1r_1\sin\vartheta) \\
& \sin[nk_1(r-ct)+(nB+l)(\varphi+\frac{\pi}{2})]r_1dr_1\Bigg\} \qquad (3.7)
\end{aligned}
$$

where n and l are indices respectively accounting for time Fourier series decomposition and circumferential Fourier series decomposition.

It can be seen from Eq. (3.7) that the radiated sound field can be decomposed into two groups of progressing waves. The first group involves Bessel functions of order *nB-l*, which corresponds to a rapidly rotating source pattern ; the associated acoustic pressure field rotates with an angular velocity

$$\omega_- = \frac{n\omega_1}{nB-l} = \frac{nB}{nB-l}\Omega$$

which is larger than Ω. The second group of waves involves Bessel functions of order *nB+l*, which corresponds to a slowly rotating source pattern ; the acoustic pressure field rotates with an angular velocity

$$\omega_+ = \frac{n\omega_1}{nB+l} = \frac{nB}{nB+l}\Omega$$

which is smaller than Ω . For all values of nB, the J_{nB-l} terms are much larger than the J_{nB+l} terms, provided that the argument $nk_1r_1\sin\vartheta$ is roughly smaller than 1. In this case, the second group of waves is therefore an inefficient noise radiator and can be neglected. Thus, Eq. (3.7) can be suitably approximated by :

$$
\begin{aligned}
p(t;r,\vartheta,\varphi) &= \frac{\cos\vartheta}{r}\sum_{n=1}^{+\infty}(nk_1) \\
&\quad \times \sum_{l=0}^{+\infty}\int_{a_1}^{a_2} \bar{f}_z^0(r_1)\alpha_n(r_1)\beta_l(r_1)J_{nB-l}(nk_1r_1\sin\vartheta)\sin[nk_1(r-ct) \\
&\quad +(nB-l)(\varphi+\frac{\pi}{2})]r_1dr_1
\end{aligned} \tag{3.8}
$$

It can also be noted that the case $l{=}nB$ generally has a large contribution in the sum and results in a $J_0(nk_1r_1\sin\vartheta)$ directivity function, which has its maximum along the fan axis ($\vartheta{=}0$). In such a case, all the elementary radiating dipoles fluctuate in phase (the theoretical wave speed is infinite) and the directivity of the sound radiation is a dipole along the fan axis. In practice, the sound pressure must be computed with Eq. (3.8) by summing the circumferential Fourier coefficients l around the value nB for a particular multiple n of the BPF.

The analytical results derived in this section are consistent with those derived by Lowson [19], Goldstein [15] or by Blake [4]. The models are qualitatively equivalent except for the definition of the source terms.

3.4 Inverse model

3.4.1 Discretizing the direct model

In the following, Eq. (3.6) is written in terms of a time harmonic expansion :

$$
p(t;r,\varphi,\vartheta) = \sum_{s=-\infty}^{s=+\infty} p_s(s\omega_1;r,\varphi,\vartheta)e^{-is\omega_1 t} \tag{3.9}
$$

with :

$$
\begin{aligned}
p_s(s\omega_1;r,\varphi,\vartheta) &= -\frac{ik_1\cos\vartheta}{4\pi r}\sum_{q=-\infty}^{+\infty} i^{sB+q}e^{isk_1r}e^{i(sB+q)\varphi} \\
&\quad \times \int_{a_1}^{a_2} s\bar{f}_z^0(r_1)\alpha_s(r_1)\beta_q(r_1)J_{sB+q}(sk_1r_1\sin\vartheta)2\pi r_1dr_1
\end{aligned} \tag{3.10}
$$

Discretizing the integral over r_1 and truncating the sum over the circumferential harmonics q in Eq. (3.10) leads to

$$p_s(s\omega_1; r, \varphi, \vartheta) = -\frac{ik_1 \cos\vartheta}{4\pi r_j} \sum_{q=q_{\min}}^{q=q_{\max}} i^{sB+q} e^{isk_1 r} e^{i(sB+q)\varphi} \times \sum_{i=1}^{I} s\bar{f}_z^0(r_{1i})\alpha_s(r_{1i})\beta_q(r_{1i}) J_{sB+q}(sk_1 r_{1i}\sin\vartheta_j) 2\pi r_{1i}\Delta r_1 \quad (3.11)$$

where r_{1i} are I equally spaced points in the interval $[a_1\, a_2]$ separated by Δr_1 and $q_{\min}$, $q_{\max}$ are the minimal and maximal circumferential harmonics in the sum ; in the calculation of Eq. (3.10), $q_{\min}$, $q_{\max}$ are chosen such that $q_{\min} < -sB < q_{\max}$. Finally, we introduce the index j to discretize the radiation space into J locations $p_{sj} = p_s(s\omega_1; r_j, \varphi_j, \vartheta_j)$,

$$p_{sj} = -\frac{ik_1 \cos\vartheta_j}{4\pi r} \sum_{q=q_{\min}}^{q=q_{\max}} i^{sB+q} e^{isk_1 r_j} e^{i(sB+q)\varphi_j} \times \sum_{i=1}^{I} s\bar{f}_z^0(r_{1i})\alpha_s(r_{1i})\beta_q(r_{1i}) J_{sB+q}(sk_1 r_{1i}\sin\vartheta) 2\pi r_{1i}\Delta r_1 \quad (3.12)$$

Eq. (3.12) can be written in a compact form

$$p_{sj} = \sum_L H_{sjL} f_{sL} \quad (3.13)$$

where the i and q indices have been condensed into a single index $L = (i, q)$, $f_{sL} = \bar{f}_z^0(r_{1i})\alpha_s(r_{1i})\beta_q(r_{1i})$ is a source vector that characterizes the dipole strength distribution at radial location i , for the time harmonic s and circumferential harmonic q. Moreover,

$$H_{sjL} = -\frac{isk_1 \cos\vartheta_j}{2r_j} i^{sB+q} e^{isk_1 r_j} e^{i(sB+q)\varphi_j} \Delta r_1 J_{sB+q}(sk_1 r_{1i}\sin\vartheta_j) r_{1i}$$

is a transfer function relating the source strength f_{sL} to the radiated sound field p_{sj}. Eq. (3.13) is a linear system that can be brought in matrix form,

$$\mathbf{p_s} = \mathbf{H_s}\mathbf{f_s} \quad (3.14)$$

$\mathbf{p}_s$ is a vector of far-field acoustic pressures measured at J locations, $\mathbf{f}_s$ is a vector of coefficients for unsteady rotating axial forces per unit area exerted by the blades on the fluid and $\mathbf{H}_s$ is

the transfer function between the force coefficients and the far-field acoustic pressure. All these quantities are defined for the multiple s of the Blade Passing Frequency.

3.4.2 Formulation of the inverse model

The objective of the inverse model is to obtain the source vector $\mathbf{f}_s$ from measured far-field acoustic data $\mathbf{p}_s$. To achieve this, the problem can be transformed into the minimization of a quadratic function. We define the far-field acoustic pressure measurements $\hat{\mathbf{p}}_\mathbf{s}$ to be equal to the predicted acoustic pressure plus an error $\mathbf{e}_s$:

$$\hat{\mathbf{p}}_\mathbf{s} = \mathbf{H}_\mathbf{s}\mathbf{f}_s + \mathbf{e}_s \tag{3.15}$$

The vector $\mathbf{f}_s$ can be obtained using the approach proposed by Nelson & Yoon [59] for the estimation of acoustic source strength by inverse methods. The cost function J_s to be minimized at $\omega = s\omega_1$ is defined as :

$$J_s = \sum_{j=1}^{J} |e_{sj}|^2 = \mathbf{e}_\mathbf{s}^\mathbf{H}\mathbf{e}_\mathbf{S} \tag{3.16}$$

where H denotes the Hermitian transpose and e_{sj} is the error between the predicted and the measured acoustic pressure at the frequency $\omega = s\omega_1$ and location j. The minimization of J_s leads to the optimal estimate of the source force vector $\mathbf{f}_{s0}$:

$$\mathbf{f}_\mathbf{s0} = \mathbf{H}_\mathbf{s}^+ \hat{\mathbf{p}}_\mathbf{s} \tag{3.17}$$

where $\mathbf{H}_\mathbf{s}^+ = \left[\mathbf{H}_\mathbf{s}^\mathbf{H}\mathbf{H}_\mathbf{s}\right]^{-1}\mathbf{H}_\mathbf{s}^\mathbf{H}$ designates the pseudo-inverse of the matrix $\mathbf{H}_\mathbf{s}$. There is a single solution of this minimization provided $\left[\mathbf{H}_\mathbf{s}^\mathbf{H}\mathbf{H}_\mathbf{s}\right]$ is positive definite. In our problem $\mathbf{f}_\mathbf{s}^\mathbf{H}\left[\mathbf{H}_\mathbf{s}^\mathbf{H}\mathbf{H}_\mathbf{s}\right]\mathbf{f}_\mathbf{s} = \mathbf{p}^\mathbf{H}\mathbf{p}$ is positive, which implies that the minimum is unique. Moreover, if the number of measurement points J is equal to the number of terms $I(q_{\max} - q_{\min} + 1)$ of the source vector to be determined, the solution can be simply written $\mathbf{f}_{s\mathbf{0}} = \mathbf{H}_s^{-1}\hat{\mathbf{p}}_s$. If $J < I(q_{\max} - q_{\min} + 1)$, the solution is not unique.

3.4.3 Conditioning the inverse model

The sensitivity of the solution ($\mathbf{f}_{s0}$) to small changes ($\delta\hat{\mathbf{p}}_s$) in $\hat{\mathbf{p}}_s$is determined by the condition number κ of the matrix $\mathbf{H}_s$, which can be defined as :

$$\kappa(\mathbf{H}_s) = \|\mathbf{H}_s\| \, \|\mathbf{H}_s\|^{-1} = {}^{\sigma_{\max}}\!/_{\sigma_{\min}} \tag{3.18}$$

where $\|\mathbf{H}_s\|$ is the 2-norm of the matrix $\mathbf{H}_s$**,** and σ_{min} and σ_{max} are respectively the smallest and the largest singular value of $\mathbf{H}_s$. The sensitivity of the solution can be directly derived from this condition number [59] :

$$\frac{\|\delta\mathbf{f}_{s0}\|}{\|\mathbf{f}_{s0}\|} = \kappa(\mathbf{H}_s)\frac{\|\delta\hat{\mathbf{p}}_s\|}{\|\hat{\mathbf{p}}_s\|} \tag{3.19}$$

When κ is small, $\mathbf{H}_s$ is well conditioned and small deviations in the pressure vector do not produce significant changes $\delta\,\mathbf{f}_{s0}$ in the force vector solution. But when κ is large, the problem is said to be ill-posed because small changes in $\hat{\mathbf{p}}_s$ lead to considerably large errors in the solution. In order to avoid a large discrepancy in the singular values of $\mathbf{H}_s$ and therefore an ill-conditioned problem, a stabilisation approach[1] is used where the force term is multiplied by a penalty factor. This method leads to the following alternative cost function :

$$J_{\mathbf{s}} = \mathbf{e}_{\mathbf{s}}^{\mathbf{H}}\mathbf{e}_{\mathbf{s}} + \beta\mathbf{f}_{\mathbf{s}}^{\mathbf{H}}\mathbf{f}_{\mathbf{s}} \tag{3.20}$$

where β is a regularization factor. Finally, the solution of this new minimization problem is given by [59] :

$$\mathbf{f}_{s0} = [\mathbf{H}_s^{\mathbf{H}}\mathbf{H}_s + \beta\mathbf{I}]^{-1}\mathbf{H}_s^{\mathbf{H}}\hat{\mathbf{p}}_s \tag{3.21}$$

3.4.4 Choice of the regularization parameter

[1] Il s'agit en fait de la régularisation de Tikhonov

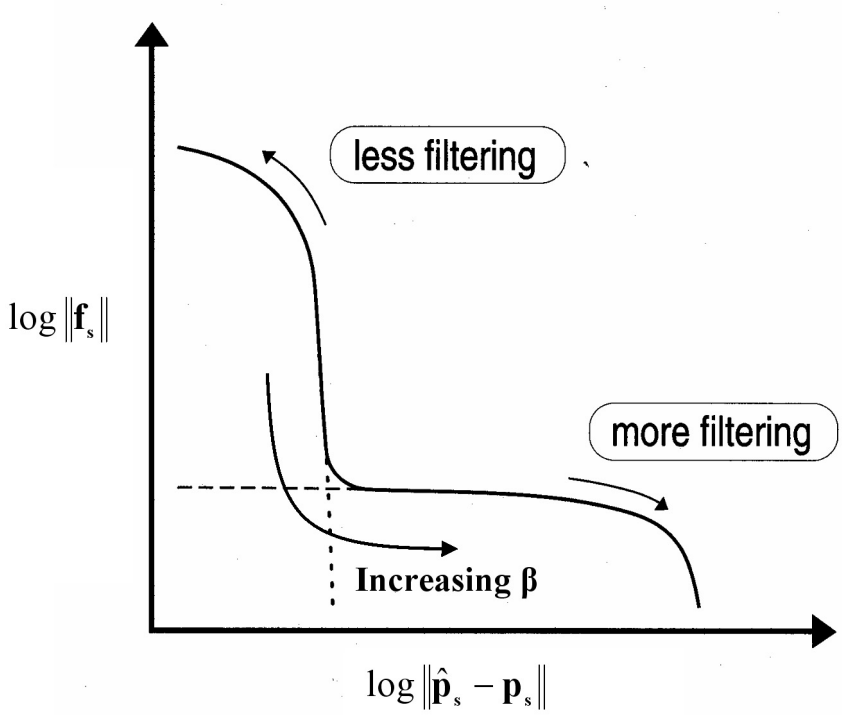

Figure 3.2 The generic form of the L-curve. Adapted from [14] with the notations of the present paper.

The key point for a good regularization is a correct choice of the regularization parameter β. The approach used in this paper is the L-curve criterion [14, 63]. The L-curve consists of plotting the 2-norm $\|\mathbf{f_s}\|$ of the regularised solution versus the residual 2-norm $\|\hat{\mathbf{p}}_\mathbf{s} - \mathbf{p_s}\|$ in log-log scale, corresponding to various values of β. The generic L-curve is shown in Fig. 3.2 [14]. This curve can be decomposed into two regions : 1) in the part of the curve on the right of the corner, the solution is over-regularized, this situation is also called over-smoothing and 2) in the part of the L-curve above the corner, the regularised solution is dominated by the effects of error in the input data (such as measurement noise in the acoustic pressures $\hat{\mathbf{p}}_\mathbf{s}$), the solution is under-regularized, this situation is called under-smoothing. In between these two regions, an optimal regularization parameter can be found, for which there is a trade-off between both under-smoothing and over-smoothing situations, such that the residual $\|\hat{\mathbf{p}}_\mathbf{s} - \mathbf{p_s}\|$ is reasonably small and the regularised solution has a reasonably small norm $\|\mathbf{f_s}\|$ [14, 63]. There are other methods to find the optimal regularization parameter but the L-curve criterion seems to be more robust [14, 63] than the generalised cross validation technique for example. In this paper, the optimal parameter corresponding to the maximum curvature of the L-curve corner is determined manually.

3.5 Numerical simulations

3.5.1 Sensitivity analysis

Setting

A typical automotive engine cooling fan is considered in the simulation, with the following parameters : exterior diameter $2a_2 = 30$cm, interior diameter $2a_1 = 12.5$cm, rotational speed $\Omega/2\pi = 50$ Hz (the Mach number at blade tip is therefore 0.14), $B = 6$ blades with uniform blade pitch (the Blade Passing Frequency is therefore 300 Hz). The fan radius is discretised into I equally spaced points r_{1i} $(1 \leqslant i \leqslant I)$ in the interval $[a_1\, a_2]$. The aeroacoustic sources over the fan area are defined according to Eq. (3.3), with $f_{sL} = \bar{f}_z^0(r_{1i})\alpha_s(r_{1i})\beta_q(r_{1i}) = 1$ when $q = -sB$ and $f_{sL} = \bar{f}_z^0(r_{1i})\alpha_s(r_{1i})\beta_q(r_{1i}) = 0$ when $q \neq -sB$. This simple situation corresponds to a sound radiation for a particular multiple of the BPF $\omega = s\omega_1$ due only to the circumferential harmonic $q = -sB$; in reality, the sound pressure at $\omega = s\omega_1$ as given by Eq. (3.8) is a combination of various circumferential harmonics q centred around $q = -sB$, but the circumferential harmonic $q = -sB$ has the largest contribution to the resulting sound pressure for subsonic fan operation. The far-field acoustic directivity was calculated according to Eq. (3.6) at J equally spaced downstream points, either on an arc of circle located in the (xz) plane ($\phi = 0$, Fig. 3.1), or on a hemispheric surface centred on the fan. The angles $\theta = -\frac{\pi}{2}$ and $\theta = +\frac{\pi}{2}$ (Fig. 3.1) were not included in the calculations of the far-field directivity since the zero acoustic pressure in these directions would render $\mathbf{H}$ singular.

The numerical scheme of the inverse model is : (i) Impose unsteady aerodynamic forces $\mathbf{f}_s$ over the surface of the blade ; (ii) Calculate the resulting acoustic pressure at the far-field points according to Eq. (3.13) (direct model) ; (iii) Reconstruct the forces $\mathbf{f}_{s0}$ using Eq. (3.21) (inverse model). The results of the direct model are plotted in Fig. 3.3 in terms of the dipole strength distribution and downstream acoustic directivity at the Blade Passing Frequency ($s = 1$). Note that the acoustic directivity of the fan has been superposed with the acoustic directivity of a monopole of identical on-axis directivity. These results show that only the circumferential harmonic $q = 6$ of the dipole strength in Eq. (3.2) contributes to the far-field sound ; moreover, the acoustic directivity of the fan in this case is perfectly dipolar.

In order to account for the presence of noise in the inverse model, a random noise is added to the "measured" far-field data as follows :

$$\mathbf{p_s}_n = \mathbf{p}_s + \mathbf{e}_n$$

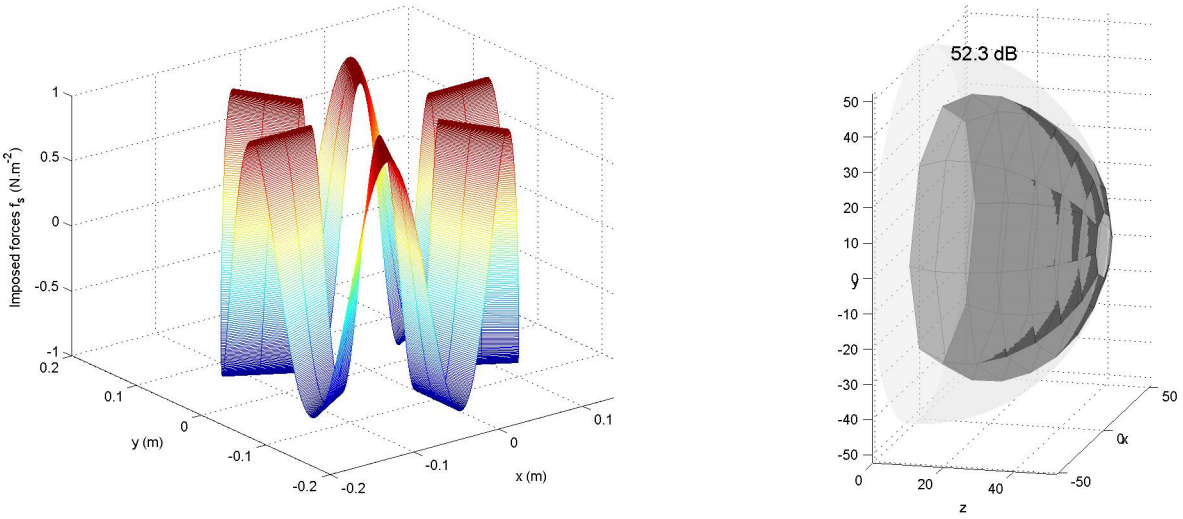

(a) (b)

Figure 3.3 Numerical results of the direct model at the Blade Passing Frequency ($s = 1$), $2a_2 = 30$cm, $2a_1 = 12.5$cm, $\Omega/2\pi = 50$Hz, $B = 6$; (a) : imposed dipole strength distribution ; (b) : far-field acoustic directivity. The acoustic directivity of the fan has been superimposed with the acoustic directivity of a monopole of identical on-axis directivity (pale grey surface).

where $\mathbf{p_s}$ is the prediction from the direct model, Eq. (3.14), $\mathbf{p}_{sn}$ is a noisy prediction and $\mathbf{e}_{sn}$ is a normally distributed random error vector which has a zero mean and a variance σ^2. The signal to noise ratio is defined as :

$$\frac{S}{N} = 20 \log_{10} \left[\frac{1}{J} \frac{|\mathbf{p}_s|^2}{\sigma^2} \right]^{1/2} \tag{3.22}$$

In the following sections, the inverse model is analyzed in terms of the regularization parameter β, the geometrical sensor arrangement, the frequency and the signal to noise ratio. Moreover, the spatial discretization of the fan used in the source reconstruction assumes $I = 3$ equally spaced points r_{1i} $(1 \leqslant i \leqslant 3)$ in the radial direction and 9 circumferential harmonics of the dipole strength distribution ($q_{\min} = -sB-4$,$q_{\max} = -sB+4$). Therefore the dimension of the unknown source vector $\mathbf{f}_s$ is $I(q_{\max} - q_{\min} + 1) = 27$.

Influence of the regularization parameter β

The inverse model is ill-posed, which means that small errors in the input data lead to large perturbations in the solution if no care is taken in the choice of β. The case of a zero noise ($S/N = \infty$), $s = 1$ (aeroacoustic sources at the Blade Passing Frequency) and $J = 64$

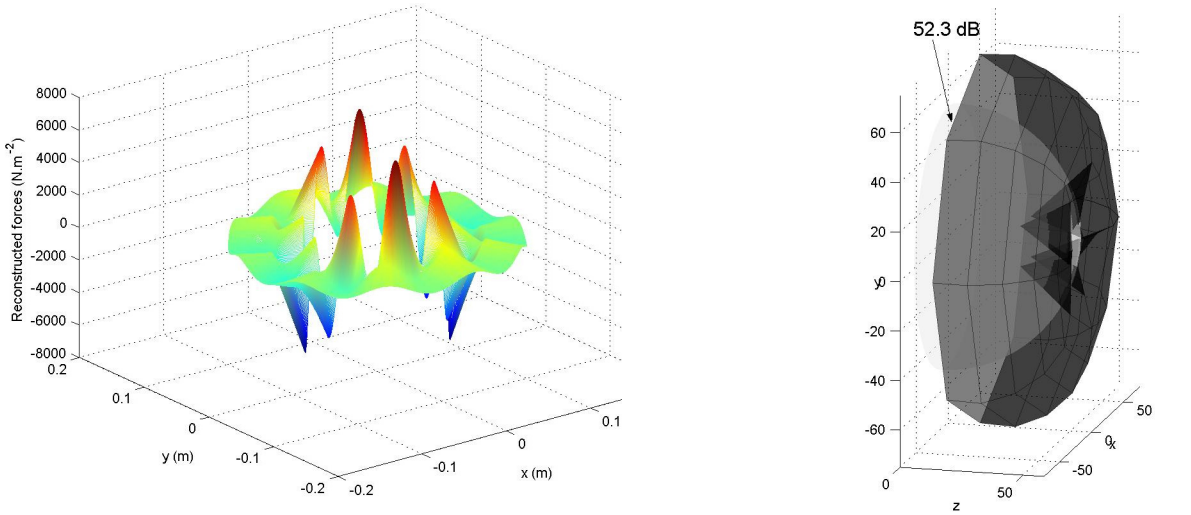

(a)

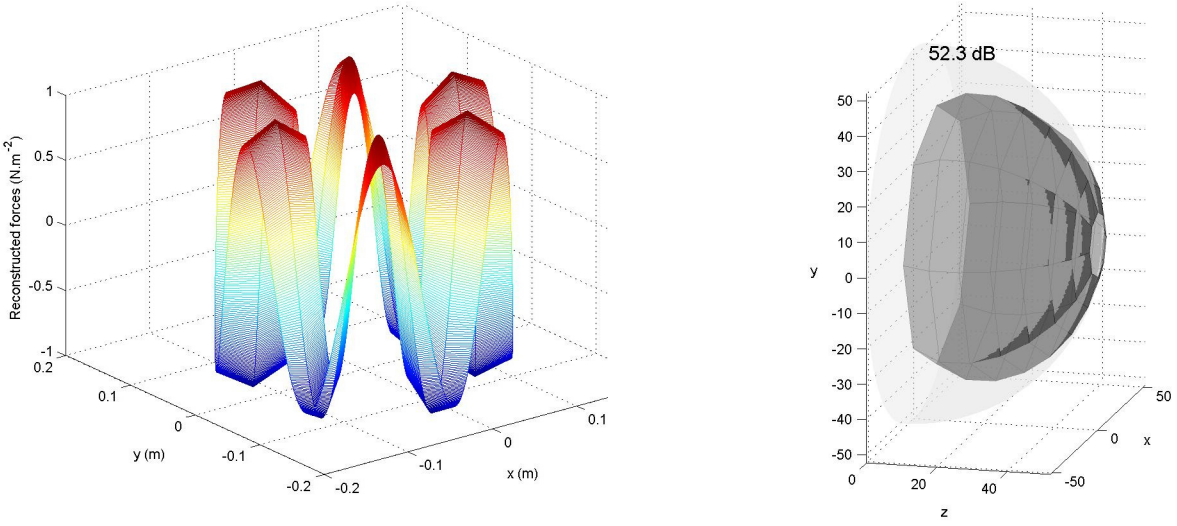

(b)

Figure 3.4 Left-hand column : reconstructed dipole strength distribution over the fan area at 1 BPF ($s = 1$) and right-hand column : reconstructed downstream far-field directivity for various values of the regularization parameter β : (a) $\beta = 0$, (b) $\beta = 10^{-10}$, (c) $\beta = 10^{-0}$. Zero noise ($S/N = \infty$), $J = 64$ far-field points on a downstream hemispheric surface. The acoustic directivity of the fan has been superimposed with the acoustic directivity of a monopole of identical on-axis directivity (pale grey surface).

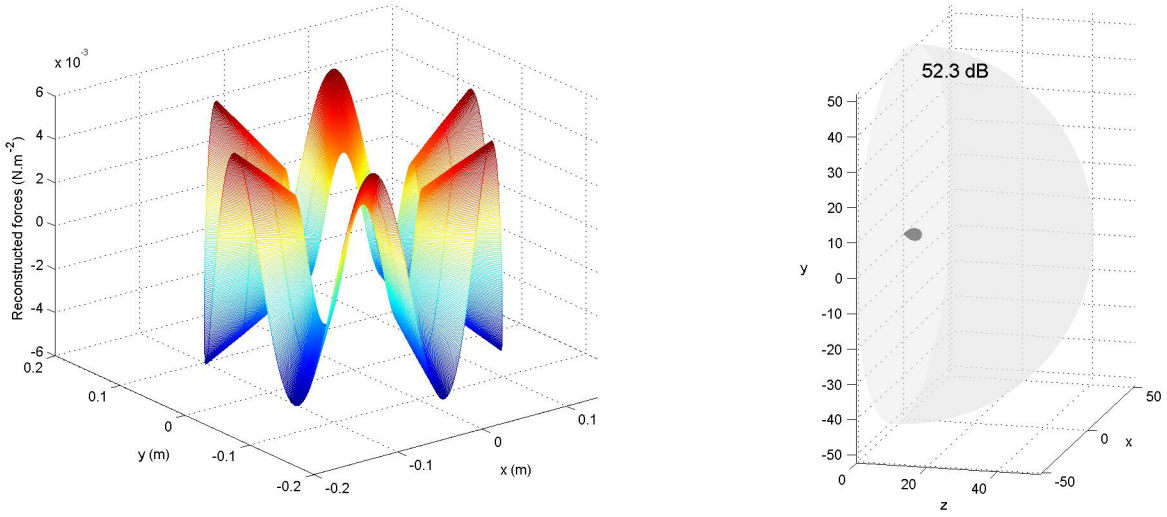

(c)

Figure 3.4 (Continued)

downstream far-field points regularly spaced on a hemispheric surface is first chosen in order to study the influence of β on the reconstructed unsteady force and the reconstructed acoustic directivity. In this case, the condition number κ of the matrix $\mathbf{H}_s$ is large (7×10^{10}), which means that the problem is ill-conditioned.

Fig. 3.4 shows the reconstructed dipole strength distribution over the fan area and the reconstructed downstream far-field directivity for various values of β. These results are to be compared to the imposed data of Fig. 3.3. When no regularization of the inverse problem is imposed (β=0), contributions of other circumferential Fourier modes than q=-sB lead to errors in the magnitude of the reconstructed force and the reconstructed and imposed acoustic radiation neither fit in magnitude nor in directivity. For large values of β (10^0), the distribution of the reconstructed force is correct but the magnitude is much smaller than the imposed one, because such large values of β significantly decrease the ratio between the smallest and the largest singular value of $\mathbf{H}_s$; moreover, the estimated acoustic radiation is erroneous in this case. The intermediate value $\beta = 10^{-10}$ yields a satisfactory reconstruction of both the aeroacoustic sources and acoustic far-field.

Fig. 3.5 shows the L-curves associated to the inversion of the system at BPF and its first three harmonics. As already noted by several authors [65] [59] [63], the regularization parameter is not an arbitrary choice. In the case depicted here, the values $10^{-12} < \beta < 5 \times 10^{-4}$ provides an optimal reconstruction range for which $\|\mathbf{f_s}\|$ is constant as a function of β and leads to a good match between the estimated acoustic pressure and the imposed acoustic field. As demonstrated in [14], for a very small β, the L-curves do not have a vertical branch in the uppermost part but

a horizontal asymptote since no noise is added to the input acoustic pressure vector.

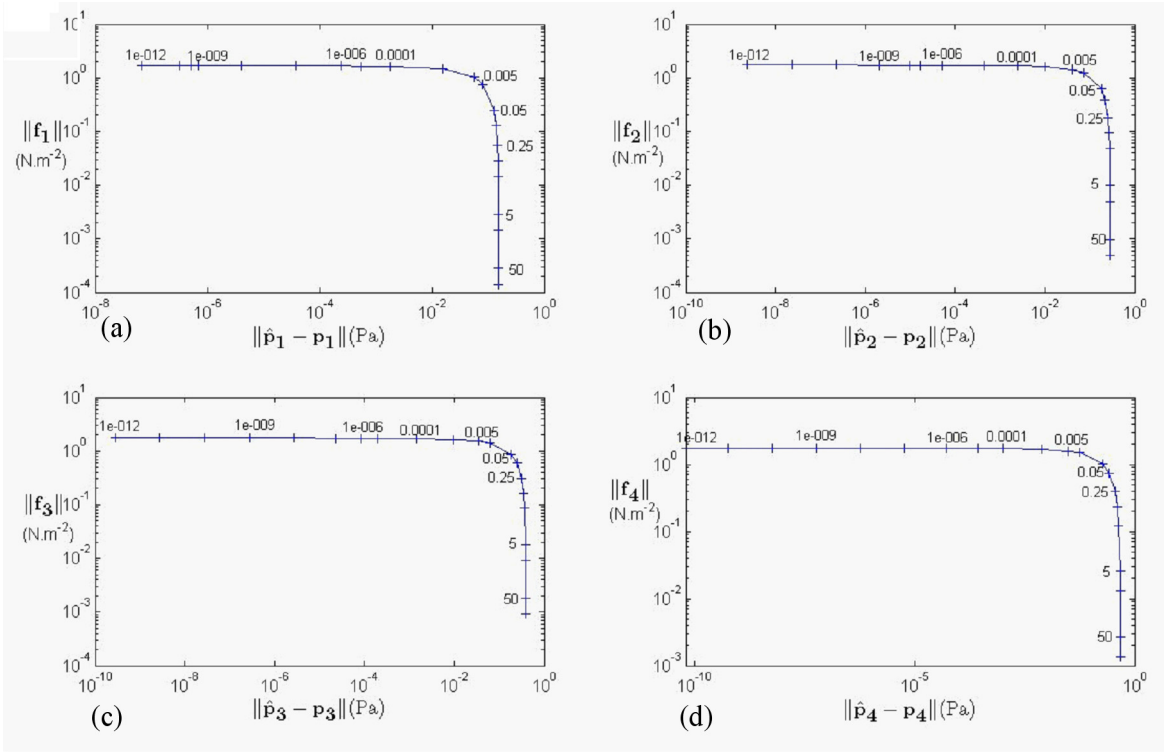

Figure 3.5 L-curves corresponding to the source reconstruction at BPF and its first three harmonics. (a) : s=1, (b) : s=2, (c) : s=3, (d) : s=4. Zero noise ($S/N = \infty$), J=64 far-field points on a downstream hemispheric surface. The values of β are indicated on the curves.

Influence of the signal to noise ratio S/N

A random noise (normal distribution with zero average) is now algebraically added to the imposed far-field data as given by Eq. (3.22). The influence of S/N on the reconstruction is analysed in terms of the inversion of the system at BPF via the L-curve behaviour in Fig. 3.6. When measurement noise is added, a vertical asymptote appears for low values of the regularization parameter. Moreover, Fig. 3.6 shows that the region of optimal reconstruction with respect to the regularization parameter narrows as S/N increases. The optimal values of β corresponding to the L-curve corners are about 10^{-6}, 10^{-5} and 10^{-3} for the signal-to-noise ratios of 20 dB, 5 dB and 1 dB respectively, which means that more filtering is required when adding noise in the input data. A satisfactory reconstruction of the far-field data not leading to excessive values of the forces $\|\mathbf{f_s}\|$ is achievable for a signal to noise ratio up to 0dB.

Influence of the geometrical arrangement of sensors

The inverse problem is now investigated with respect to the geometrical arrangement of downstream far-field acoustic sensors. Two arrangements are investigated (Fig. 3.7) : a circular

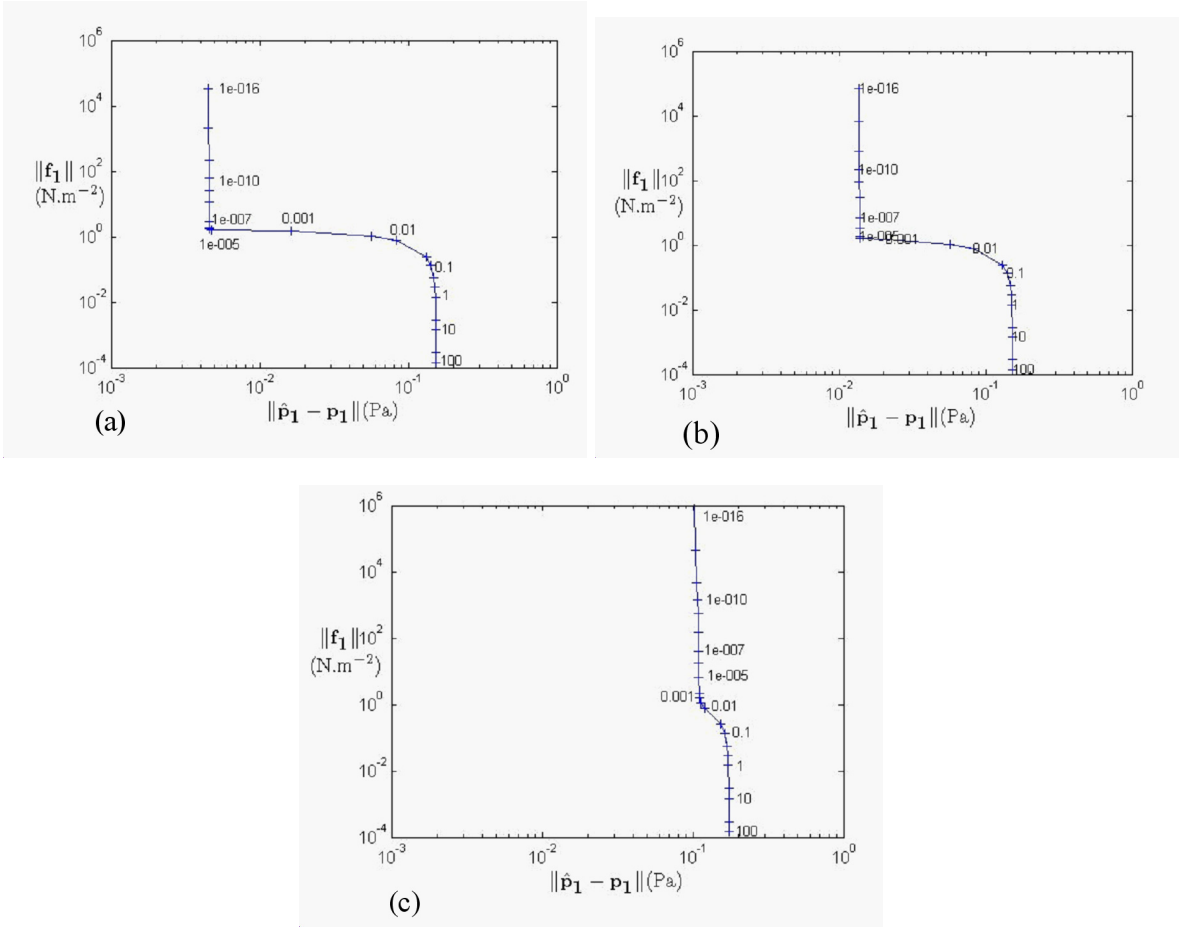

Figure 3.6 L-curves corresponding to the inversion of BPF for various values of the signal to noise ratio S/N : (a) S/N=20 dB (b) S/N=5 dB (c) S/N=1 dB. J= 64 far-field points on a downstream hemispheric surface. The values of β are indicated on the curves.

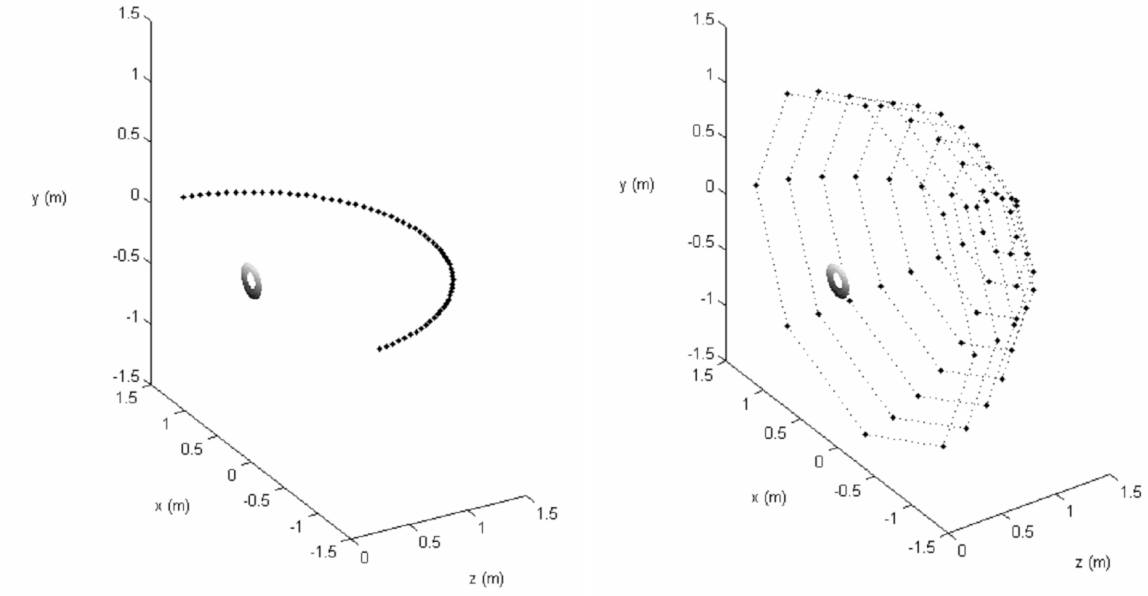

(a) (b)

Figure 3.7 Downstream radiation space meshing (the radiation surface of the fan is shown at the center). (a) 64 sensors on an arc of a circle from ϑ=-80 ° to ϑ=80 ° and φ=0 °, and (b) 64 sensors on a hemispheric surface.

arc located in the plane φ=0 ° and extending from ϑ=-80 ° to ϑ=80 °, or a regular distribution on a hemispheric surface. In both cases, 64 sensors are assumed. Fig. 3.8 shows the condition number $\kappa(\mathbf{H})$ as a function of frequency for the 2 sensor arrangements and for $s = 1$, $I = 3$. At low frequency, the condition number κ is large for both sensor arrangements; the resulting poor conditioning of the inverse problem is due to the insufficient spatial resolution of the source for frequency below 200Hz. As the frequency increases, the condition number improves for the hemispheric arrangement of sensor while κ remains large for the circular arrangement. As expected, a circular sensor arrangement is therefore less appropriate than a hemispheric arrangement to reconstruct the surface source distribution.

In order to test the ability of the circular sensor arrangement to reconstruct the forces $\mathbf{f}_s$, the source reconstruction is conducted with $\Omega/2\pi = 50$ Hz, $\beta = 10^{-5}$, $s = 1$, S/N= 20 dB. The optimal reconstruction (Fig. 3.9) shows that the inverse model is able to reconstruct the forces from 64 measurement points located on a circular arc even if the transfer matrix $\mathbf{H}$ is badly conditioned. From these estimated forces, a correct acoustic directivity is reconstructed. This can be explained by the dipole axial symmetry radiated by the imposed forces described in the setting.

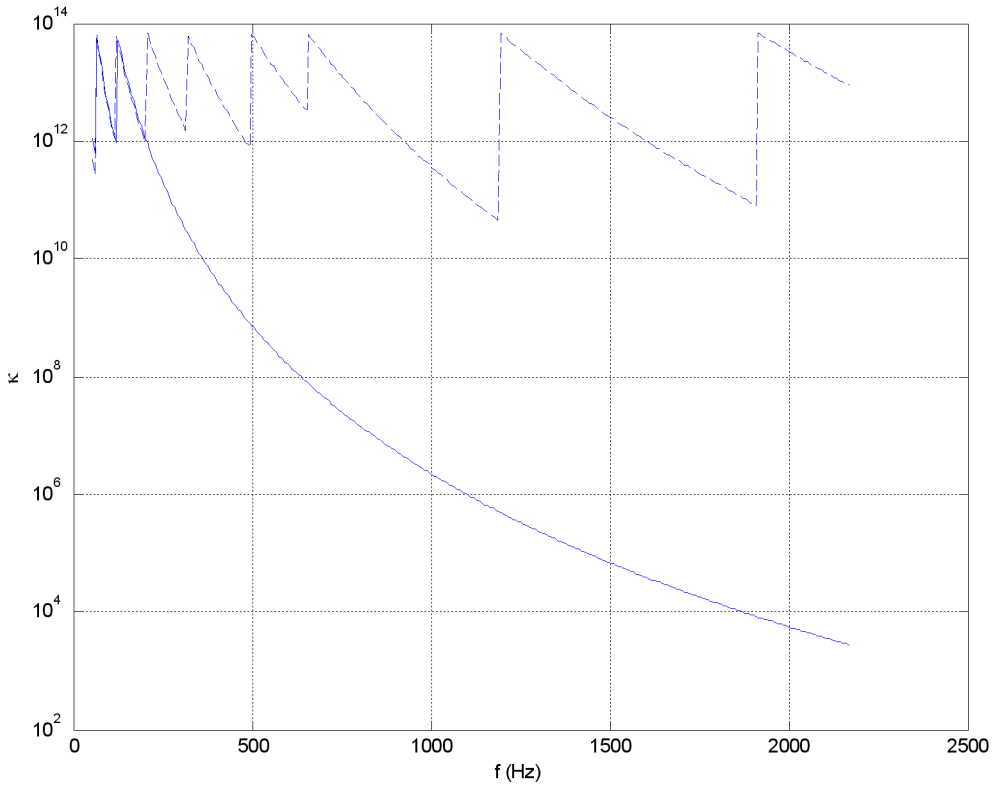

Figure 3.8 Condition number κ of the matrix $\mathbf{H}$ as a function of f for different sensor arrangements. I=3, s=1, q_{min}=sB-4, q_{max}=sB+4. J=64 measurements points (solid : on a hemispheric surface, dashed : on an arc of a circle as shown in Fig. 3.7.)

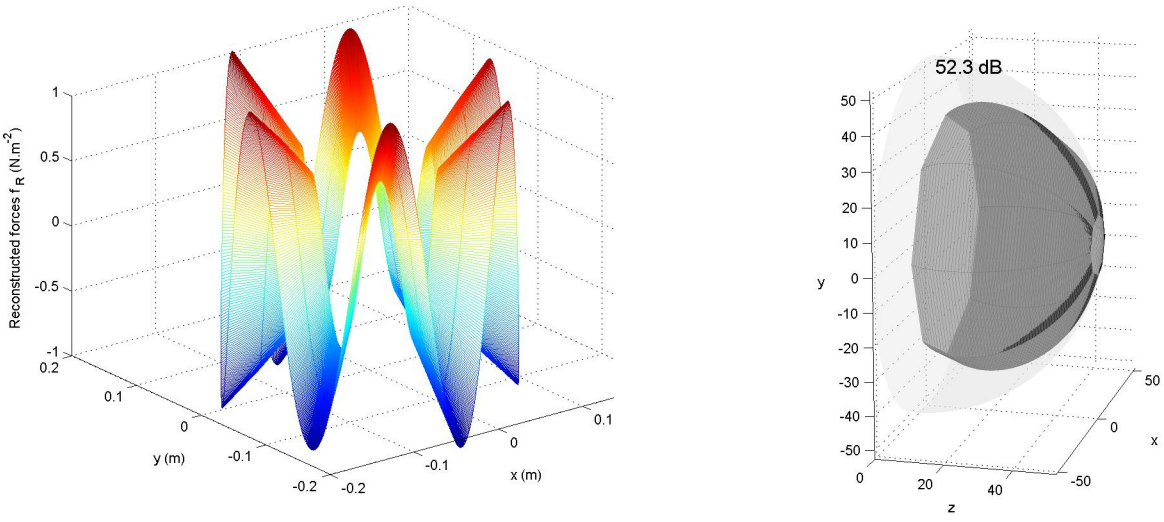

(a) (b)

Figure 3.9 (a) Reconstructed dipole strength distribution over the fan area and (b) reconstructed downstream far-field directivity for β =10^{-5}, $s = 1$, S/N= 20 dB. $J = 64$ far-field points on arc of a circle. The acoustic directivity of the fan has been superimposed with the acoustic directivity of a monopole of identical on-axis directivity (pale grey surface).

3.5.2 Simulation of fan source reconstruction for non-uniform flow

To illustrate the inverse model for non-uniform flow condition, the following case is considered : the source strength function $f_z^0(r_1, \varphi_1)$ of Eq. (3.2) is given by

$$f_z^0(r_1, \varphi_1) = \begin{cases} 1 & \text{if } -\frac{\Phi_1}{2} + 2n\pi \leqslant \varphi_1 \leqslant +\frac{\Phi_1}{2} + 2n\pi \\ 0 & \text{otherwise} \end{cases} \tag{3.23}$$

This situation describes a spatial variation of the source distribution in the circumferential direction, and may therefore represent a strongly circumferentially non-uniform flow. From Eq. (3.2), the circumferential Fourier coefficients β_q are given in this case by $\beta_q(r_1) = \frac{\Phi_1}{2\pi} \frac{\sin(\frac{q\Phi_1}{2})}{\frac{q\Phi_1}{2}}$. Moreover, the circumferential average $\bar{f}_z^0(r_1)$ and the time Fourier coefficients $\alpha_s(r_1)$ are arbitrarily set to unity and Φ_1 is set to 15 $^\circ$. Therefore, the coefficients of the imposed unsteady rotating force vector $\mathbf{f_s}$ in equation (3.14) reduce to $f_{sL} = \bar{f}_z^0(r_{1i})\alpha_s(r_{1i})\beta_q(r_{1i}) = \beta_q$. All other data are similar to the previous sections ($B = 6$, $\Omega/2\pi = 50$Hz). Fig. 3.10 shows the corresponding dipole strength distribution over the fan area and its circumferential Fourier series decomposition (truncated to order 60) along 2 radii : $r_1 = 8$cm and $r_1 = 14$cm.

In this example, the inversion is carried out for the first 4 harmonics of the BPF (s= 1,2,3,4),

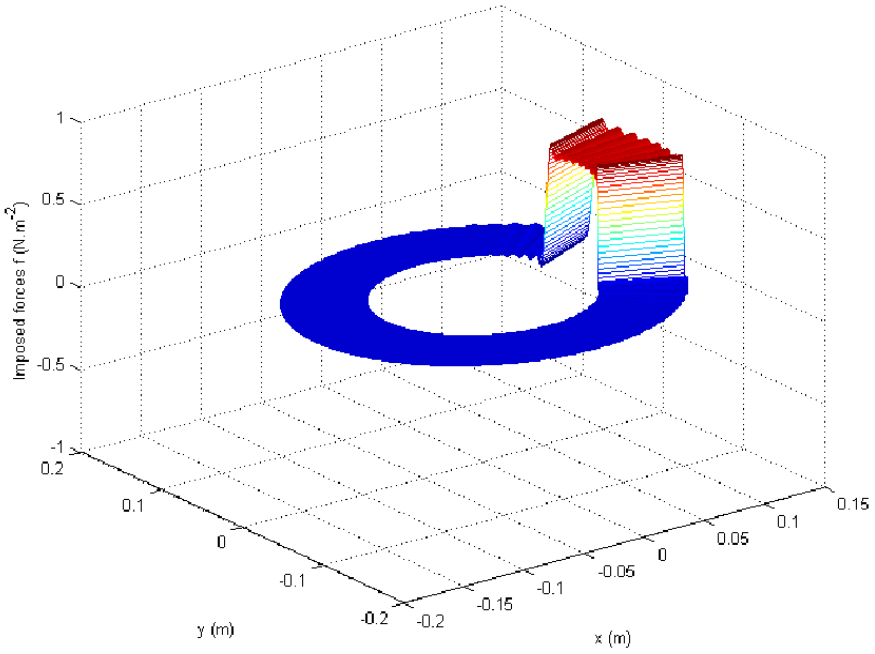

(a)

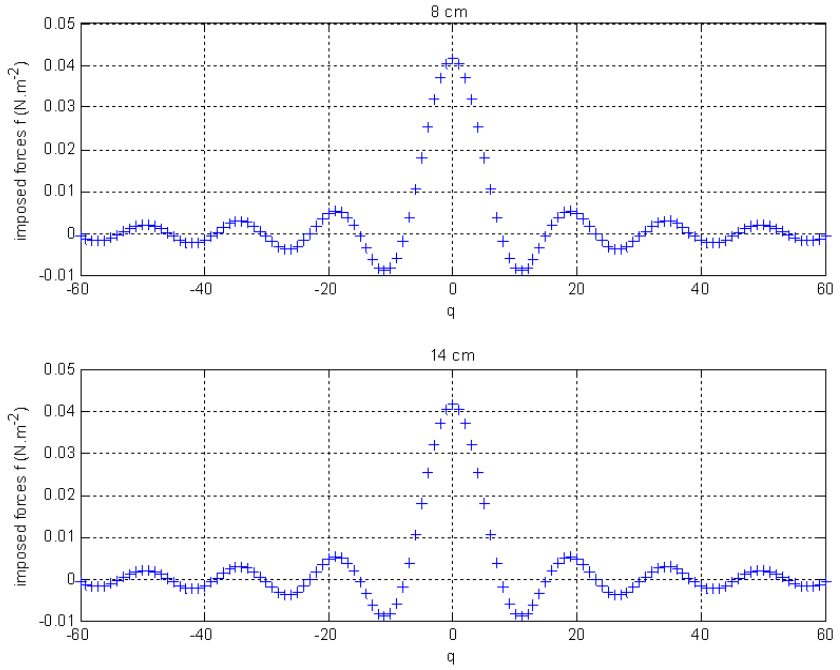

(b)

Figure 3.10 (a) Imposed dipole strength distribution over the fan area and (b) its circumferential Fourier series decomposition (truncated to order 60) along 2 radii : $r_1 = 8$cm and $r_1 = 14$cm (right).

the propeller was discretized in 2 circles ($I = 2$) located at $r_{11} = 8$ cm and r_{12}= 14 cm and the number of circumferential harmonics q is chosen such that $q_{\min} = -sB-2$, $q_{\max} = -sB+3$, thus $Q = 6$; the dimension of the unknown source vector $\mathbf{f}_s$ is therefore $I(q_{\max}-q_{\min}+1) = 12$. Finally $J = 36$ acoustic pressure sensors are simulated on a hemispheric surface 1.5 m downstream the fan, with a signal to noise ratio of $S/N = 5$dB.

The condition number of the transfer matrix $\mathbf{H}$ is given by $\kappa = 3.7 \times 10^4$ at BPF ($s = 1$), $\kappa = 2.1 \times 10^3$ at 2 BPF ($s = 2$), $\kappa = 380$ at 3 BPF ($s = 3$), and $\kappa = 108$ at 4 BPF ($s = 4$). Optimal values of the regularization parameter derived from the corresponding L-curve corners are : $\beta = 5 \times 10^{-7}$ for s=1 and $\beta = 10^{-4}$ for s=2,3,4. These values were found to be sufficient to provide both accurate reconstruction of the far-field data and acceptable values of the force per unit area vector $\|\mathbf{f}_s\|$.

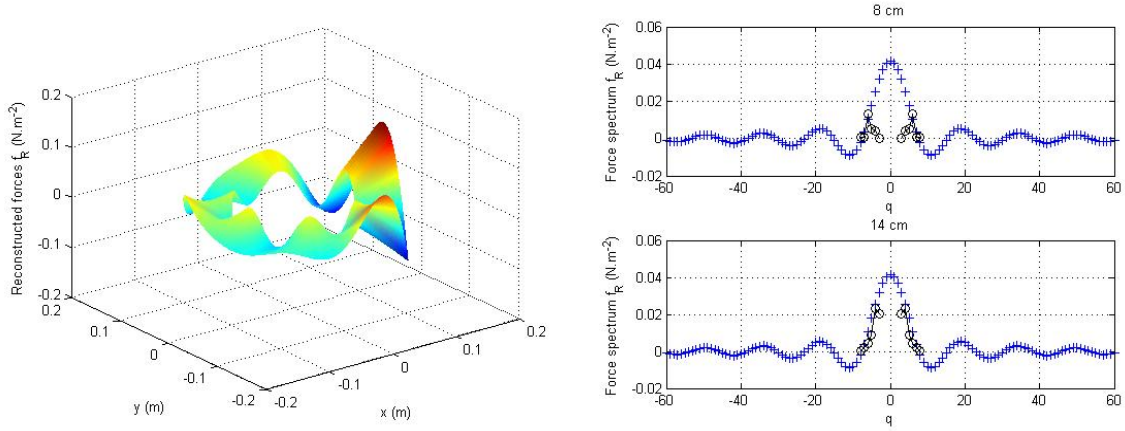

(a)

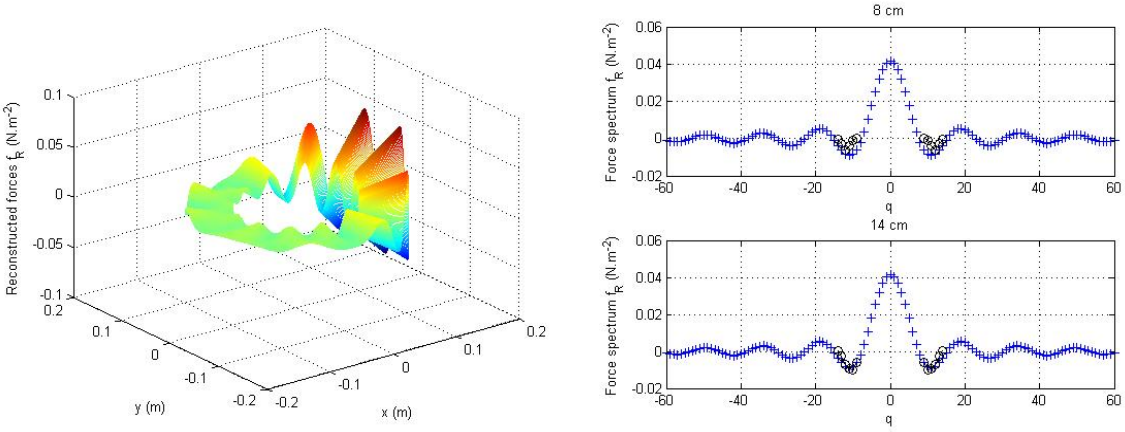

(b)

Figure 3.11 Left-hand column : reconstructed dipole strength distribution over the fan area and right-hand side column : its circumferential Fourier series decomposition (truncated to order 60) along 2 radii : $r_1 = 8$cm and $r_1 = 14$cm. (a) s=1, (b) s=2, (c) s=3, (d) s=4. $S/N = 5$ dB, J= 36 far-field points on a downstream hemispheric surface.

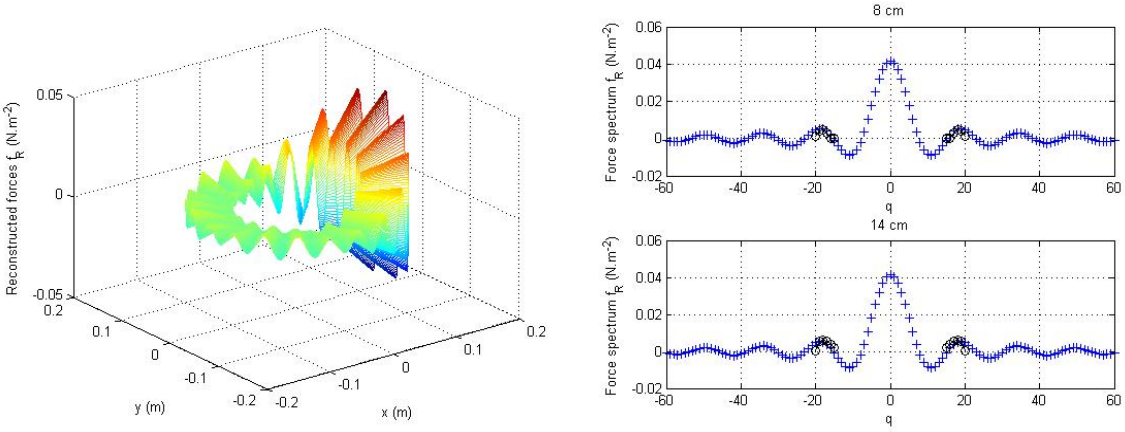

(c)

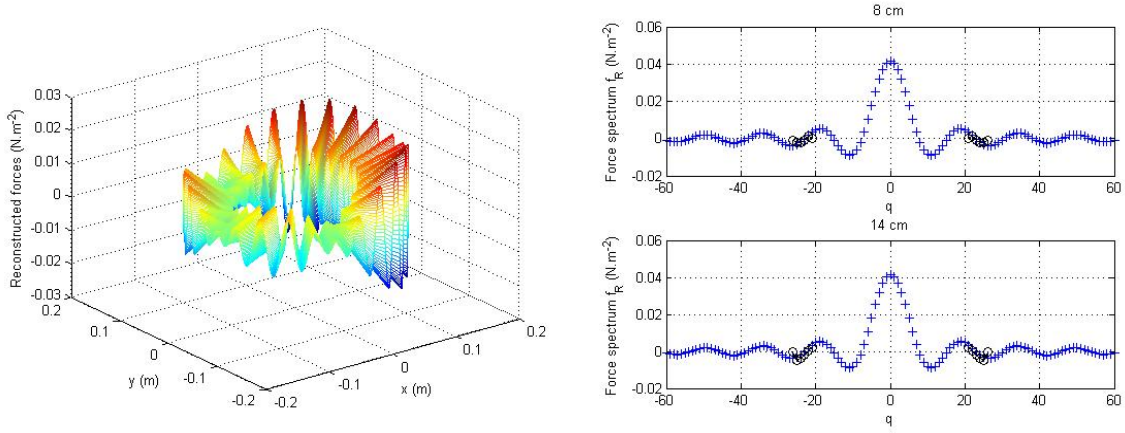

(d)

Figure 3.11 (Continued)

This section focuses on the ability of the inverse model to reconstruct the dipole strength distribution of Fig. 3.10, both in the spatial and circumferential wavenumber domains. Fig. 3.11 presents the results of the inverse model for the first four harmonics of BPF $s = 1, 2, 3, 4$. These results show that the circumferential location of the maximum force acting by the blade on the fluid can be predicted from the inversion at each of the 4 harmonics, but the imposed distribution of Fig. 3.10 cannot be accurately reconstructed from each of these plots. Moreover, the circumferential wavenumber spectrum of the reconstructed force distribution is generally in good agreement with the imposed force spectrum, especially for the outer radial element (low order circumferential harmonics are poorly reconstructed at the inner radial element for $s = 1$). Finally, the source distributions for the first four harmonics of BPF $s = 1, 2, 3, 4$ are superposed in Fig. 3.12 to represent the complete circumferential wavenumber spectrum of the unsteady forces. The superposition of the forces estimated from the first four harmonics significantly improves the quality of the reconstruction. The reconstructed force distribution is close to the imposed distribution of Fig. 3.10 ; however, the magnitude of the reconstructed forces is not as large as the amplitude of the imposed forces because low order circumferential harmonics are not properly reconstructed over the whole radiation surface.

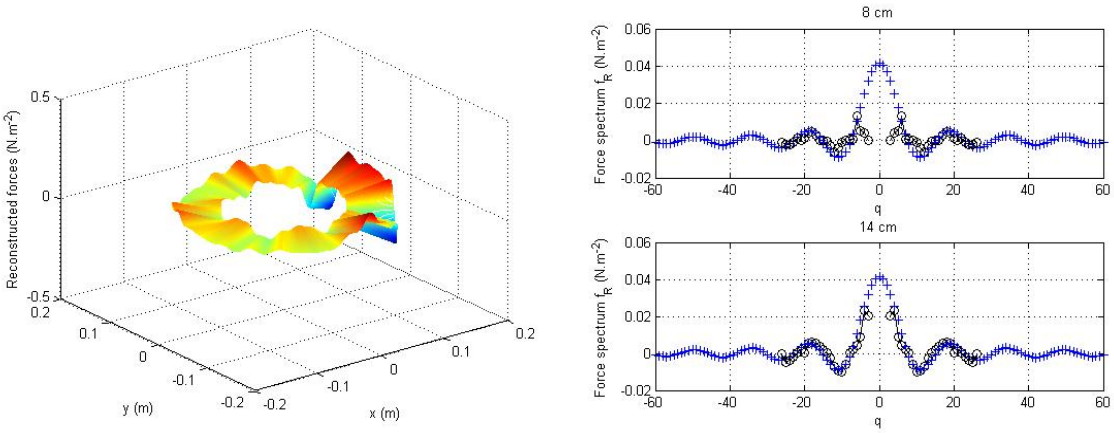

(a) (b)

Figure 3.12 Representation of the axial forces acting by the rotor on the fluid per unit surface : (a) reconstructed forces in the plane of the fan and (b) circumferential Fourier series decomposition (bilateral spectrum), up : inner radius 8 cm, down : outer radius 14 cm ; + : imposed forces, o : reconstructed forces. S/N = 5 dB, V=2, Q_1 = -sB-2, Q_2 = -sB+3, s = 1, 2, 3, 4 ; J = 36 on a hemispheric surface.

To summarize, the inverse model is able to partially reconstruct the unsteady rotating forces acting by the blades on the fluid and thus locate "hot spot" non-uniform flow entering the fan. The acoustic signature of the fan measured at a relatively low number of locations is a useful tool to derive the unsteady behaviour of the fluid near the propeller surface even in presence of measurement noise.

3.6 Preliminary experimental results

3.6.1 Experimental set up

The inversion procedure to extract aeroacoustic source distributions from far-field acoustic data was tested on an automotive axial fan. Experiments were conducted on an engine cooling unit consisting of a symmetric 6-bladed ($B = 6$) axial fan and a radiator. The fan has an exterior diameter of 30cm and a central hub of 12.5cm in diameter. A small (4×8 cm) rectangular piece of adhesive tape was bonded on the upstream side of the radiator at about 5 cm from the fan axis in order to enhance the non-uniformity of the incoming flow and therefore increase tonal noise radiation. The unit was driven by a variable DC source (0-20V/0-60A) which was adjusted to set a rotational speed of the fan of 50 Hz. The set up was placed in a semi-anechoic room with the fan axis horizontal and at 50 cm above the ground, and absorbing material was placed on the ground under the set up in order to minimise ground reflections (Fig. 3.13).

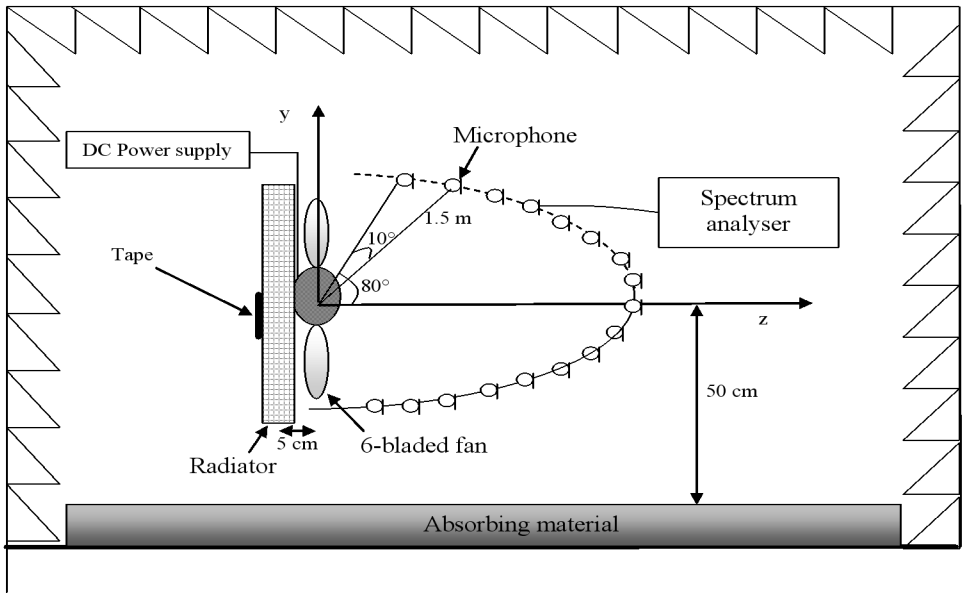

Figure 3.13 Experimental set up

For simplicity, acoustic measurements were performed at $J = 17$ equally spaced locations on a arc of a circle in the horizontal plane at 1.5m from the fan centre. The microphone directions ranged from $\theta = -80^0$ to $\theta = 80^0$ from the fan axis. A circular arrangement of sensors was found sufficient to provide a satisfactory source reconstruction in theory when the radiated sound field is axi-symmetric (Fig. 3.9). This is especially true at BPF, where the measured radiated sound field is almost dipolar and the circumferential harmonic of the force q=6 is found to be the main contributor. The circular arrangement is still expected to provide an acceptable solution for the first harmonic of the BPF, where the experimental directivity showed a dipolar radiation slightly shifted from the fan axis. A windscreen was mounted on the microphone to minimise the effect

of flow noise. Far-field conditions from the fan centre are found at distances over 1.5 m since this distance is much larger than the propeller radius and represents approximately 1.3 wavelengths for $s = 1$ (300Hz) and 2.6 wavelengths for $s = 2$ (600Hz). Note that the measured quantity was the far-field acoustic power spectrum (obtained by averaging 20 time sequences for a given location) using a single microphone which was sequentially moved over the arc of a circle, in order to further remove flow noise from the acoustic data. Therefore, the phase variations of the acoustic pressure over the circular arc were not considered in the source reconstruction scheme.

In the inversion scheme, the propeller was discretized in 2 circles ($I = 2$) located at r_{11} = 8 cm and r_{12}= 14 cm and the number of circumferential harmonics q is chosen such that $q_{\min} = -sB-3$, $q_{\max} = -sB+3 \quad Q = 7$; therefore the dimension of the unknown source vector $\mathbf{f}_s$ is $I(q_{\max} - q_{\min} + 1) = 14$. The condition number in this case is $\kappa = 8.9 \times 10^8$ at BPF (s = 1) and $\kappa = 6.5 \times 10^5$ at 2 BPF ($s = 2$). The inversion problem for such a configuration is relatively ill-conditioned because the acoustic sensors cover only an arc of a circle instead of the whole downstream half-space (see section 3.5.1).

3.6.2 Experimental results

Figs. 3.14 and 3.15 show the reconstructed dipole strength distribution over the fan area and the measured and reconstructed far-field directivity over the sensor arc at BPF and at 2 BPF, for various values of the regularization parameter. Fig. 3.16 shows the corresponding L-curves for $s = 1$ and $s = 2$.

A value of $\beta = 10^{-6}$ corresponding to the corner of the two L-curves of Fig. 3.16 was chosen for the regularization parameter for both s=1 and s=2 since it provides a reasonably small error $\|\hat{\mathbf{p}}_\mathbf{s} - \mathbf{p}_\mathbf{s}\|$ without leading to an excessive value of the source strength $\|\mathbf{f}_\mathbf{s}\|$. The measured and estimated directivity at $s = 1$ (Fig. 3.14) and $s = 2$ (Fig. 3.15) are in good agreement for $\beta = 10^{-6}$. The measured and reconstructed directivity at $s = 1$ is axi-symmetric and dipolar. As expected, the dipole strength distribution over the fan shows a dominant $q = sB = 6$ circumferential harmonic for $\beta = 10^{-6}$. However, the measured and reconstructed directivity at $s = 2$ is not symmetric with respect to the fan axis. In this case, a superposition of several circumferential harmonics is necessary to reproduce the measured acoustic directivity for $\beta = 10^{-6}$. It can be noticed however that the value of the estimated source strength is rather sensitive to the value of the regularization parameter. This large sensitivity results from the poor conditioning of the problem when simply a circular arrangement of sensor is used to reconstruct a source strength distribution over the source area. Grace et al. [66] made similar observations in the context of a slightly different inverse model.

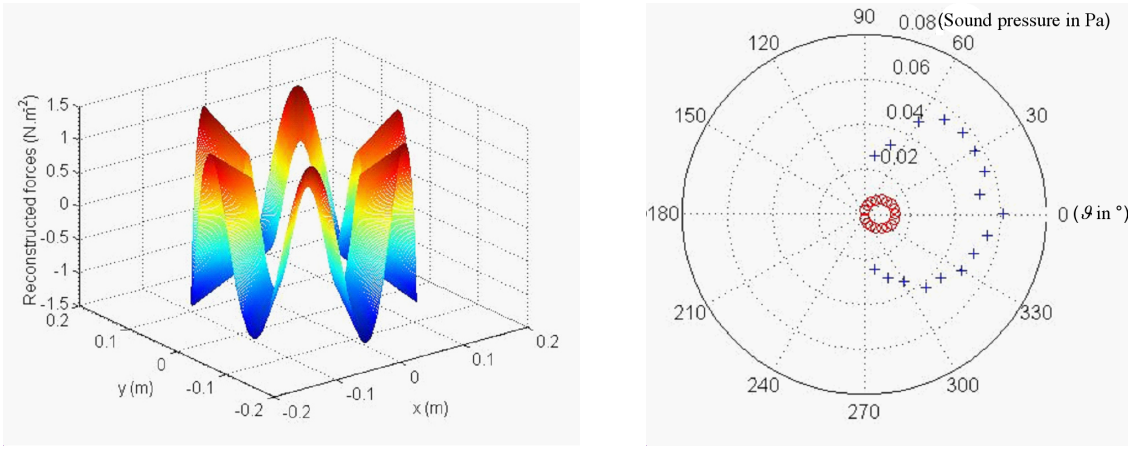

(a)

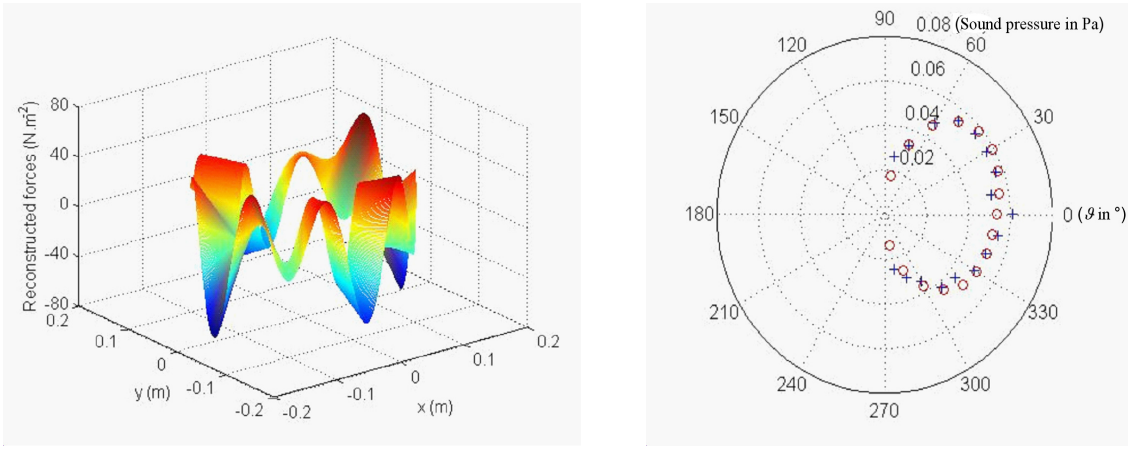

(b)

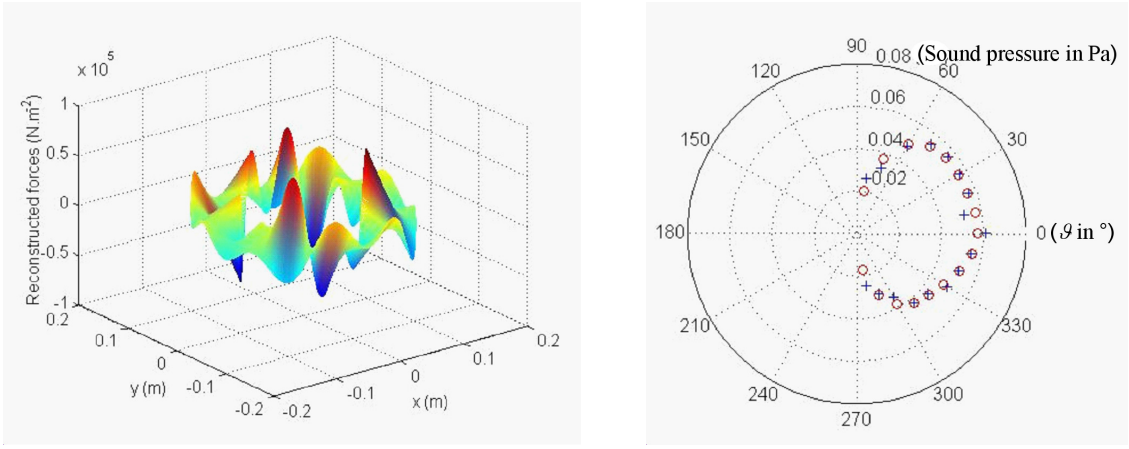

(c)

Figure 3.14 Left-hand column : reconstructed dipole strength distribution over the fan area at 1 BPF ($s = 1$) and right-hand column : reconstructed far-field directivity (+ : measured directivities, o : reconstructed directivities) for various values of the regularization parameter β : (a) $\beta = 10^{-2}$, (b) $\beta = 10^{-6}$, (c) $\beta = 10^{-14}$. J= 17 *measured* points on a downstream arc of a circle.

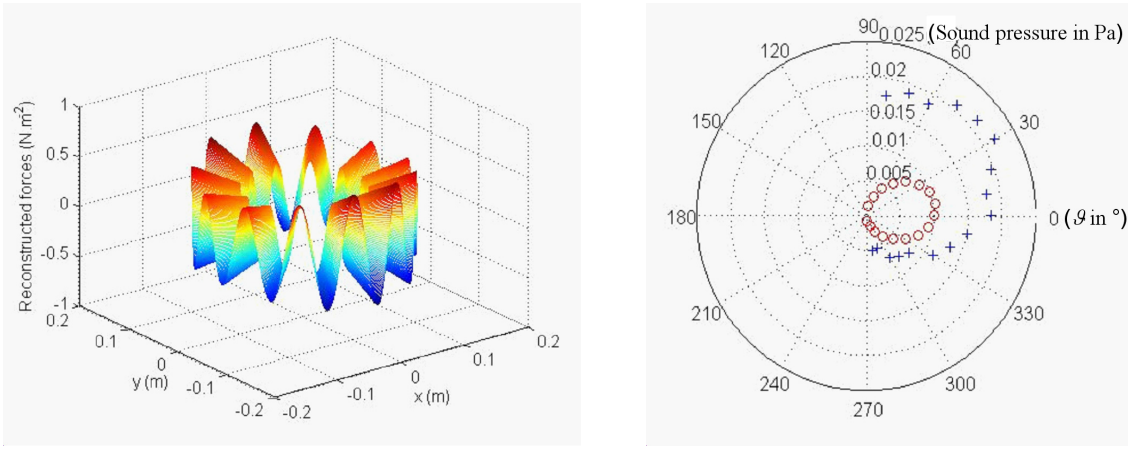

(a)

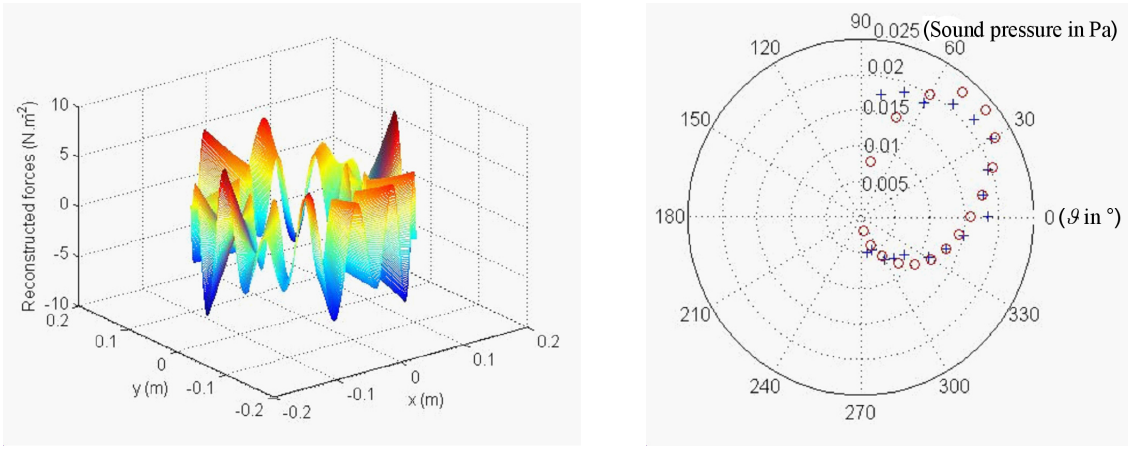

(b)

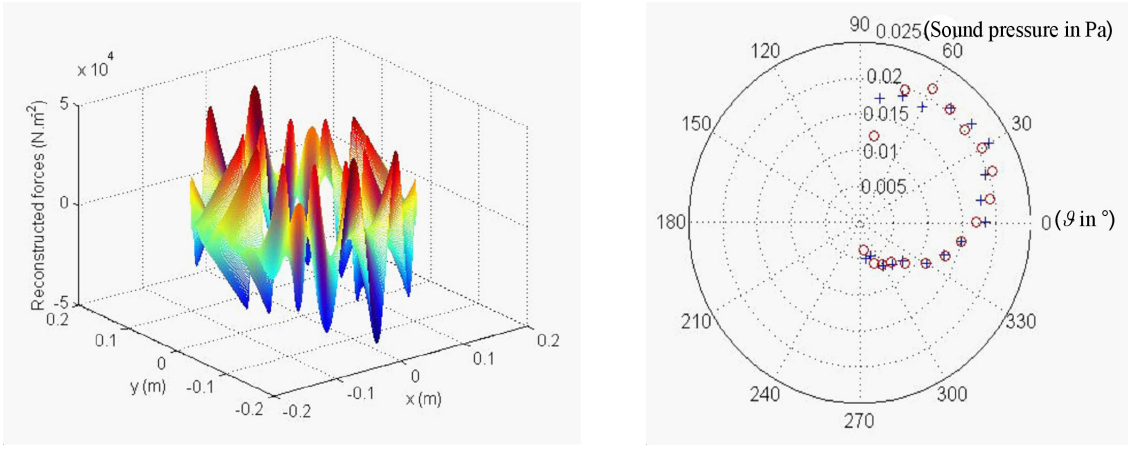

(c)

Figure 3.15 Left-hand column : reconstructed dipole strength distribution over the fan area at 2 BPF ($s = 2$) and right-hand column : reconstructed far-field directivity (+ : measured directivities, o : reconstructed directivities) for various values of the regularization parameter β : (a) $\beta = 10^{-2}$, (b) $\beta = 10^{-6}$, (c) $\beta = 10^{-14}$. J= 17 *measured* points on a downstream arc of a circle.

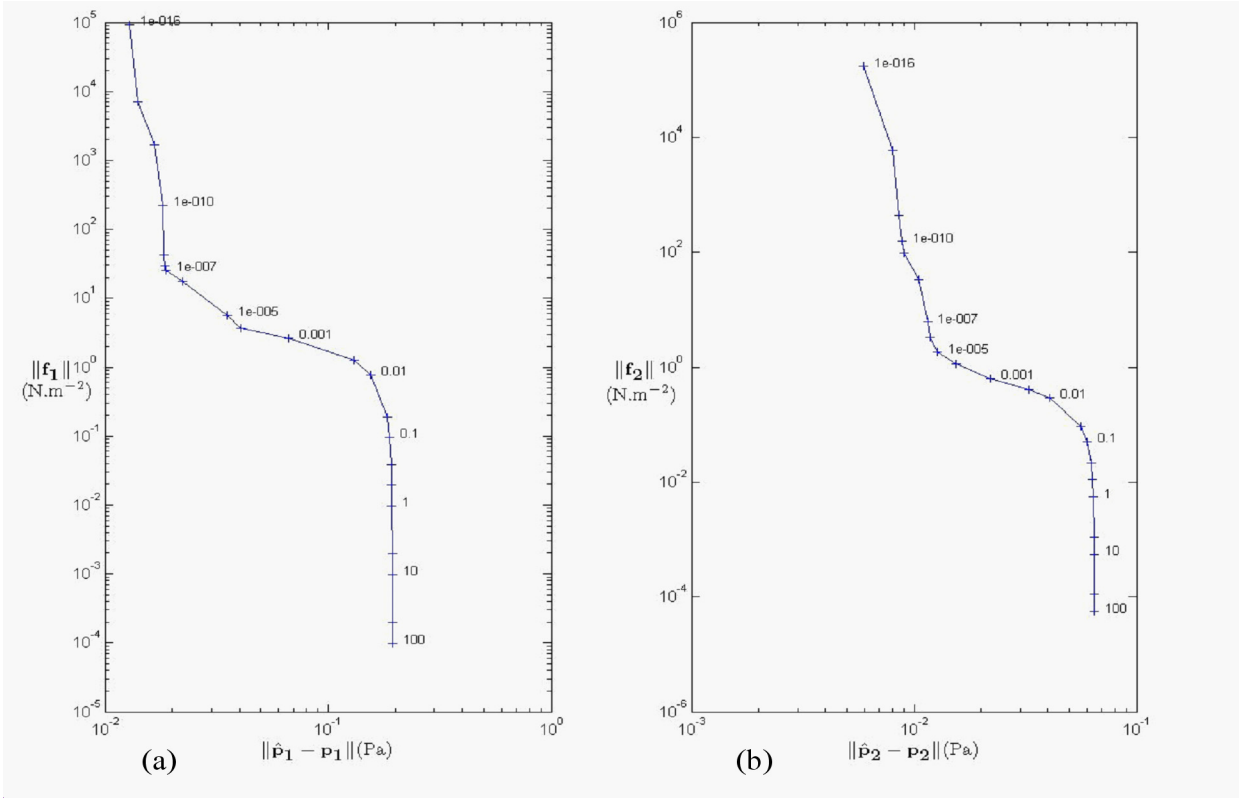

Figure 3.16 L-curves corresponding to the source reconstruction at : (a) BPF ($s = 1$), and : (b) 2BPF ($s = 2$). J= 17 measured points on a downstream arc of circle. The values of β are indicated on the curves.

3.7 Conclusion

An inverse aeroacoustic model aiming at reconstructing the aerodynamic forces (dipole strength distribution) acting by the fan blades at multiples of the Blade Passing Frequency on the fluid has been developed. It is based on a discrete form of Morse & Ingard's analytical direct model that relates the unsteady forces to the radiated sound field. To overcome the ill-conditioning of the inverse problem, a penalisation of the source strength is used to stabilise the solution. Numerical simulations and experimental results for an engine cooling fan demonstrate the ability of the inverse model to reconstruct the dipole strength distribution over the fan surface, and possibly locate acoustic "hot spots" of the fan resulting from circumferentially non-uniform upstream flow, under realistic conditions of signal to noise ratio and acoustic far-field sensing arrangement. This method can thus serve as a non-intrusive technique to estimate the unsteady forces acting on the rotating blades and a tool for studying the interaction between a non-uniform flow and a rotor. In the second part of this paper, the inverse model is exploited in order to derive optimal control source and error sensor arrangements for active control of tonal noise from engine cooling axial fans.

3.8 Acknowledgments

This work has been supported by the AUTO21 Network of Centres of Excellence and Siemens VDO Automotive Inc. The authors wish to thank Sylvain Nadeau from Siemens VDO Automotive Inc. for his collaboration in this research.

3.9 Nomenclature

a_1	Inner rotor radius
a_2	Outer rotor radius
B	Number of blades
c	Speed of sound
$\mathbf{e}$	Error vector
f_z	Axial pressure component acting on the rotor
f_z^0	Time average value of the axial pressure
$\bar{f}_z^0$	Circumferential average value of f_z^0
g_{1z}	Green function (dipolar radiation along the z axis)
$\mathbf{H}_s$	Transfer function matrix at $\omega = s\omega_1$
i	Imaginary number ($\sqrt{-1}$)
I	Number of radial elements
J	Number of point in the discretized radiation space

J_s	Cost function at $\omega = s\omega_1$
J_{sb+q}	Bessel function of the $(sB+q)^{th}$ order
k	Wave number (k=sk_1=$s\omega_1/c$ with ω_1=$B\Omega$)
p	Acoustic pressure
p_s	Acoustic pressure at $s\omega_1$
$\hat{\mathbf{p}}_\mathbf{s}$	Far-field acoustic pressure measurement vector at $s\omega_1$
q_{min}, q_{max}	Minimum and maximum circumferential order q to be reconstructed
Q	Number of circumferential harmonics to be reconstructed
S/N	Signal to noise ratio
$r, \varphi, \vartheta; x, y, z$	Spherical and Cartesian coordinates in the radiation space
r_1, φ_1	Polar coordinates in the rotor plane
t	Time
α_s	Time Fourier coefficient
β	Regularisation parameter
β_q	Azimuthal Fourier coefficient
Δr_1	Distance between two radial elements
κ	Condition number
σ^2	Variance of the random error vector added to the simulated sound pressures
σ_i	Singular values
ω	Angular frequency
ω_1	Blade Passage Angular frequency (ω_1=$B\Omega$)
Ω	Angular velocity of the rotor

Subscripts and indices

q, l	Circumferential index
s, n	Frequency index
i	Radial element
j	Radiation space discretization index
L	Condensed Source discretization index (i,q)
z	Axial component
φ	Tangential component

Superscripts

H	Hermitian
$*$	Complex conjugate
$+$	Pseudo-inverse

3.10 Bilan

Dans cette première partie, un modèle inverse basé sur le modèle analytique discrétisé de Morse et Ingard, a été développé. Des simulations ont permis de montrer le potentiel d'un modèle inverse pour estimer les forces instationnaires périodiques agissant sur les pales du rotor à partir de mesures de pressions acoustiques rayonnées en champ lointain, en utilisant la méthode de régularisation de Tikhonov. Une analyse de sensibilité du modèle inverse par rapport au choix du paramètre de régularisation, du rapport signal sur bruit des données d'entrée (pressions acoustiques) ainsi que de l'arrangement géométrique des capteurs de mesure a été menée. Dans ce chapitre, la courbe en L a été utilisée pour choisir le paramètre de régularisation. Ce paramètre, associé au coin de la courbe en L, est un bon choix pour obtenir un compromis entre une solution régularisée de norme faible (physiquement acceptable) et une erreur résiduelle faible entre le champ acoustique mesuré et extrapolé. Cette méthode pour choisir le paramètre de régularisation est suffisante dans le cas des simulations, où le coin de la courbe en L est bien marqué. Des résultats expérimentaux préliminaires à partir de mesures de pression acoustique sur un arc de cercle ont ensuite permis d'utiliser le modèle inverse comme outil d'extrapolation du champ acoustique rayonné par le rotor à la FPP et de son premier harmonique. Des simulations de contrôle actif basées sur ces extrapolations sont présentées dans le prochain chapitre.

Le modèle inverse a été approfondi et remanié à l'aide du modèle de Blake dans le chapitre 5. En effet, le modèle de Blake est très bien adapté au modèle de Sears, reliant les portances instationnaires au profil de vitesse d'écoulement. Ce modèle est donc utile pour la validation expérimentale du modèle inverse, à l'aide de mesures anémometriques de l'écoulement entrant dans le ventilateur. Un cas expérimental, proche du cas numérique présenté au paragraphe 3.5.2, sera aussi exposé dans le chapitre 5. De plus, quand les mesures de pression acoustique deviennent trop bruitées, le coin de la courbe en L n'est pas bien marqué. Des critères graphiques basés sur la courbure de la courbe en L ainsi que la condition de Picard seront utilisés pour choisir le paramètre de régularisation. Dans le chapitre 5 les notations changeront pour se conformer à celles de Blake, procurant ainsi plus de cohésion entre le modèle de Sears et le modèle de Blake.

CHAPITRE 4

CONTRÔLE ACTIF ACOUSTIQUE

CONTRÔLE DU BRUIT TONAL DES VENTILATEURS AXIAUX SUBSONIQUES PARTIE 2 : SIMULATIONS ET EXPÉRIENCES DE CONTRÔLE ACTIF EN CHAMP LIBRE

CONTROL OF TONAL NOISE FROM SUBSONIC AXIAL FAN PART 2 : ACTIVE CONTROL SIMULATIONS AND EXPERIMENTS IN FREE FIELDS

Anthony GÉRARD, Alain BERRY et Patrice MASSON (2005) Journal of Sound and Vibration, vol. 288, p. 1077-1104.

4.1 Abstract

This paper deals with the global control of engine cooling fan noise in free field at the Blade Passing Frequency (BPF) and its first harmonic. The aim of this paper is to investigate the feasibility of using a single loudspeaker in front of the fan to cancel the tonal noise. A simplified model of fan noise, which only takes into account the most radiating circumferential mode of the forces acting by the fan on the fluid, is first combined with an unbaffled loudspeaker model to predict the residual sound field for various sensor configurations. Metrics for global control such as sound directivity or sound power attenuation reveal that the control is effective with this simplified model in the whole space at low frequency, depending on the number and location of the error sensors. However, for non-homogeneous flow, other circumferential modes may contribute to the sound radiation and then, the inverse model described in the companion paper is used to provide a more accurate extrapolated sound field from the reconstructed unsteady aerodynamic forces acting by the fan on the fluid. Simulation results demonstrate the global control in the downstream half space of the blade passing frequency and its first harmonic using a single error microphone and a single control source. A Single-Input Single-Output (SISO) adaptive feedforward controller is implemented experimentally to drive the control loudspeaker. The tones at the BPF and at its first harmonic are attenuated by up to 28 dB and 18 dB respectively at the far field error microphone.

4.2 Introduction

Fan noise and aerodynamic noise are, in general, accounting for an increasing part of the total noise inside the cabin as motors are becoming quieter. A particular annoying source comes from the tonal noise of automotive axial engine cooling fans residing within a range from 100 to 700 Hz. For those frequencies, passive techniques are bulky, inefficient and cannot be applied to the automotive industry but active control techniques are better adapted to those frequencies and have a great potential for an "at the source" control.

Many investigators have focussed on the active control of low frequency ducted fan noise (see for example Nelson and Elliot [74], Eriksson et al. [76], Yeung *et al.* [77]). These approaches are based on a modal description of sound propagation in ducts (waveguides), which consider plane waves for frequencies with wavelengths at least twice the greatest dimension of the cross-section of the duct and which require a single loudspeaker to be actively cancel. For higher frequencies, a non-uniform acoustic pressure distribution associated with higher order propagating modes appears. Efforts have been made to control both the low frequency tonal noise and broadband noise. The active control techniques use either 1) an acoustic reference signal, where the system instability which may occur due to the feedback of the control signal to the reference microphone

is prevented by modelling this feedback loop and subtracting it from the measured reference (internal model controller [76]) or 2) an optical sensor for periodic sources that eliminates this feedback constraint, which is appropriate for active tonal fan noise control. Erikson [76] for example reported attenuations of about 10 dB over the range 20 Hz- 300 Hz. Passive/active hybrid noise control systems have also been studied to reduce both discrete and broadband noise. Kostek [78] developed a system combining fully active noise control with adaptive passive tunable Helmholtz resonators for ducted fan noise.

Recently, Wong [44] proposed a hybrid solution to control the exhaust fan noise of a computer room into a corridor. He used a short square duct with thick wool blanket that provides a passive system to attenuate broadband noise above 800 Hz, a decrease in the A-weighted overall sound pressure of 2 dB was obtained. Then, he combined it with an active control system for tonal noise attenuation using a loudspeaker mounted in the short duct to cancel the tonal noise up to 25 dB for the first Blade Passing Frequency (BPF). This cannot be applied to the automotive engine cooling fan because of space constraints.

Recent works have also been conducted on the computer simulations on the active control of fan tones radiated from the intake of turbofans using an annular secondary source ring and in-duct error sensors or external error sensors (Joseph *et al.* [85]). Thomas *et al.* [82] applied a feedforward filtered-X LMS to an operational engine turbofan and obtained attenuations up to 12 dBA for the fundamental frequency and 5 dBA along the engine axis with reference transducers mounted on the engine case, providing BPFs information, far field error microphones and annular secondary source ring (24 loudspeakers) mounted in the inlet.

A speaker dipole arrangement (up to 3) around each vane of a three-vane stator was investigated by Myers and Fleeter [98] to attenuate the propagating acoustic wave due to rotor-stator interaction by up to 15 dB in the upstream and 15.7 dB in the downstream for the circumferential mode -2. All the previously cited researches are based on an acoustical duct modal approach, principally aiming at reducing the blade passing frequencies tones but cannot directly apply to the automotive engine cooling fan case.

Other papers on turbofan noise consist in actively reducing the unsteady rotor/stator interaction. Rao *et al.* [99] demonstrated the control of the unsteady interactions between a stator and a rotor of a 1/14-scale turbofan by injecting wakes from the trailing edge of stator vanes using microvalves and consequently reduced the BPF tone in the whole measured space by up to 8.2 dB depending on the speed of the fan and the measurement direction, and the sound power level was reduced by up to 4.4 dB. The main advantage of this approach is the reduction of the circumferential variation velocity of the flow ; it can therefore control the sound at the source but the spectrum presented in this paper does not show a complete cancellation of the discrete noise and is too expensive for an automotive application. Kousen and Verdon [97] have shown that it is possible to control the noise generated by wake/blade row interactions through the

use of anti-sound actuators on the blade surfaces from an analytical/numerical approach but no experimental results are available. Yu and Li [107] have also theoretically investigated the feasibility of reducing the gust/cascade interaction noise using dipolar secondary sources distributed on cascade surfaces. The amplitudes of the secondary sources are obtained from an aeroacoustic inverse model.

One can also note few studies discussing the active control of the free field radiation of small axial flow fans, like Lauchle et al. [95] who used a small baffled axial flow fan itself as a "crude loudspeaker". A near field microphone and a tachometer served as an error sensor and as a reference signal respectively. The acoustic pressure at the error microphone was reduced by 20 dB for the BPF, 15 dB for the 1^{st} harmonic of the BPF and 8 dB for the 2^{nd} harmonic of the BPF. A directivity pattern shows that the fundamental tone radiation is attenuated in the whole half space. Moreover, the sound power at the BPF and 1^{st} harmonic was reduced by 13 dB and 8 dB respectively. The main disadvantage of this technique for an automotive application is the use of a (bulky) shaker used to produce the anti noise source and the potential coupling of vibrations with the environment of the fan such as the radiator. Quinlan [92], who modified the radiation impedance of the fan by placing a single secondary source close to the fan to reduce the acoustic energy propagating in the far field, globally attenuated the noise radiated by small axial flow fans. The A-weighted sound power level measured attenuations were 12 dB for the fundamental blade tone and 10 dB for the 1^{st} BPF. The main constraint of this approach is the use of small fans since the distance between the two sources greatly affects the efficiency of the control system (the distance must be negligible compared to the acoustic wavelength to be controlled).

This paper addresses the issue of global control of engine cooling fan noise on the BPF and its first harmonic in free field. The approach use analytical and experimental investigations to demonstrate the feasibility of using a single loudspeaker in front of the fan to cancel the tonal noise. The engine cooling fans under investigation are 6-bladed symmetric and 7-bladed non symmetric fans with an external diameter given by $2a_2 = 30$ cm and a hub diameter given by $2a_1 = 12.5$ cm. Rotating speed of the fans is 50 Hz, so the blade passing frequency is 300 Hz and its first harmonic (2 BPF) is 600 Hz etc... for the six-bladed fan.

In this paper, a simplified analytical model is first used to describe the interference arising between the fan noise and the secondary source noise, and global control criteria in free field are defined. This model is however only valid when only the most radiating circumferential mode is considered. An important aspect of this research is the use of a direct-inverse aeroacoustic model presented in the companion paper [5] to calculate equivalent sources of a propeller for a non-homogeneous stationary flow field, which is the main phenomenon of tonal noise generation for subsonic fans. Using this model, active control simulations are conducted based upon the primary source extrapolated from the reconstructed unsteady forces given by the inverse aeroacoustic calculations to compare the radiated directivities with and without control (see also [108]). Finally, experimental results are presented to corroborate the simulations.

4.3 A simple active control model of free field fan noise

This section aims at simulating the acoustic interference resulting from a simplified, yet realistic description of the axial fan and a secondary (or control) source. Our starting point is a simplified, axisymmetric free field acoustic radiation pattern of the fan derived from the first part of this investigation [5], combined with a model of an unbaffled, co-axial oscillating piston as shown in Fig. 4.1. In what follows, the piston amplitude is calculated such that the sum of the resulting squared sound pressures $p(r, \vartheta_l)$ is minimized at L locations (r, ϑ_l) $(0 \leqslant l \leqslant L)$ in the far field, where r and ϑ_l denote the distance from the fan centre and angle with respect to the fan axis, for the l^{th} control point.

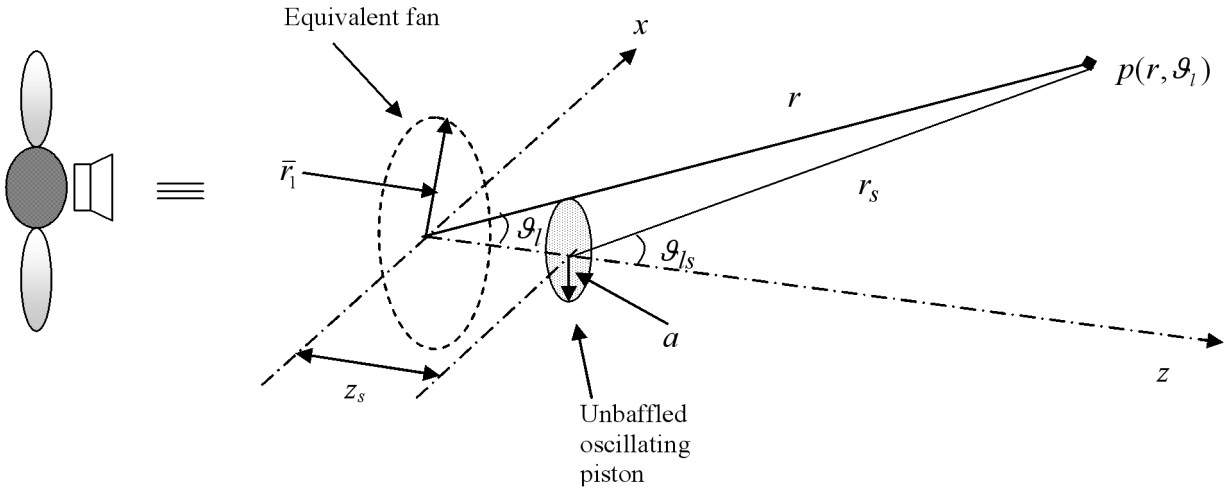

Figure 4.1 Active control arrangement for free field fan noise control.

4.3.1 Simplified fan noise model

The far field sound pressure at multiples of the fan blade passing frequency due to axial loading forces on the blades can be expressed from Eq. (3.6) of the companion paper [5]. However, several simplifications can lead to a more convenient form for preliminary analytical active control simulations. First, the fan effective area is reduced to an equivalent distribution of dipoles distributed along a mean radius of the fan $r_1 = \bar{r}_1$. This approximation is expected to be accurate if the spatial extent of the fluctuating pressures is less than a wavelength of the sound generated and is probably also adequate for the spanwise distribution, unless there is a substantial change in phase across the fan span [19]. Also, only the 0 order Bessel function (q=-nB) is considered since it corresponds to the most radiating component in Eq. (3.6) of [5] for a subsonic fan. In this case, all the elementary radiating dipoles are in phase and the directivity of the radiation is a dipole normal to the plane of the propeller. Thus, the far field acoustic pressure is symmetric with respect to the fan axis. Note that the index s of the companion paper has been replaced by n in this paper since s will serve as the secondary source subscript. It will be useful to consider

the spectral components of the sound pressure at multiples n of the BPF. Considering the above simplifications, the primary sound field can be written $p_p(t;r,\vartheta) = \sum_n p_p(n\omega_1;r,\vartheta)e^{-in\omega_1 t}$, with :

$$p_p(n\omega_1;r,\vartheta) = -ink_1 q_p \frac{e^{ink_1 r}}{4\pi r} J_0(nk_1\bar{r}_1 \sin\vartheta)\cos\vartheta \tag{4.1}$$

where $q_p = F_t\alpha_n(\bar{r}_1)\beta_{nB}(\bar{r}_1)$ is the primary complex source strength of the simplified primary source model and $F_t = \int_{a_1}^{a_2} f_z^0(r_1)2\pi r_1 dr_1$ is the total thrust of the propeller ; $\omega_1 = B\Omega$ is the blade passing frequency (BPF), B is the number of blades, Ω is the fan rotational speed, $k_1 = \frac{\omega_1}{c}$, c is the sound speed. The n and q indices represent time and circumferential Fourier decompositions of the fluctuating forces in a fixed reference frame. The quantities α_n and β_q are the corresponding Fourier coefficients of the blade forces at a radial distance r_1 from the fan axis and f_z^0 is the time-averaged value of the blade force at a radial distance r_1. Moreover, a_1 and a_2 are the interior radius and exterior radius of the fan, respectively.

In the active control simulations, q_p is arbitrarily fixed to unity. Eq. (4.1) provides a simple analytical primary source model for tonal fan noise, which can be used to evaluate the performance of an active control system.

To anticipate the following development of a more realistic fan noise model (section 4.6), Fig. 4.2 shows a comparison between the radiation field extrapolation derived from an inverse model of fan noise at BPF and at its first harmonic (1 BPF and 2 BPF) [5] and the approximated radiation obtained by Eq. (4.1) (in-phase dipoles along a mean radial line). The directivities are compared to downstream measurement experimental data for the BPF and its first harmonic and show that under this particular loading condition (fan + radiator + rectangular obstruction behind the radiator), the simplified model is quite accurate for 1 BPF but is less precise for 2 BPF[1]. However, under other fan loading conditions, the simplified model could be more accurate for 2 BPF. The rough approximation of Eq. (4.1) can serve as a first analysis of the active noise control without knowledge of experimental data, considering a dipolar sound radiation field for the first few harmonics of the BPF.

4.3.2 Secondary source model

If a single control source is assumed, it should be located close to the primary source and exhibit a similar spatial directivity. Since an axial fan operating at subsonic speeds roughly behaves like an equivalent dipole at first multiples of the BPF [5], another dipole radiating at the same set of frequencies but in opposite phase, close to the primary source is a good choice

[1]Le choix d'un paramètre de régularisation volontairement très petit aurait mené à de meilleures extrapolation du champ acoustique rayonné. En contrepartie, les termes sources auraient été largement surestimés

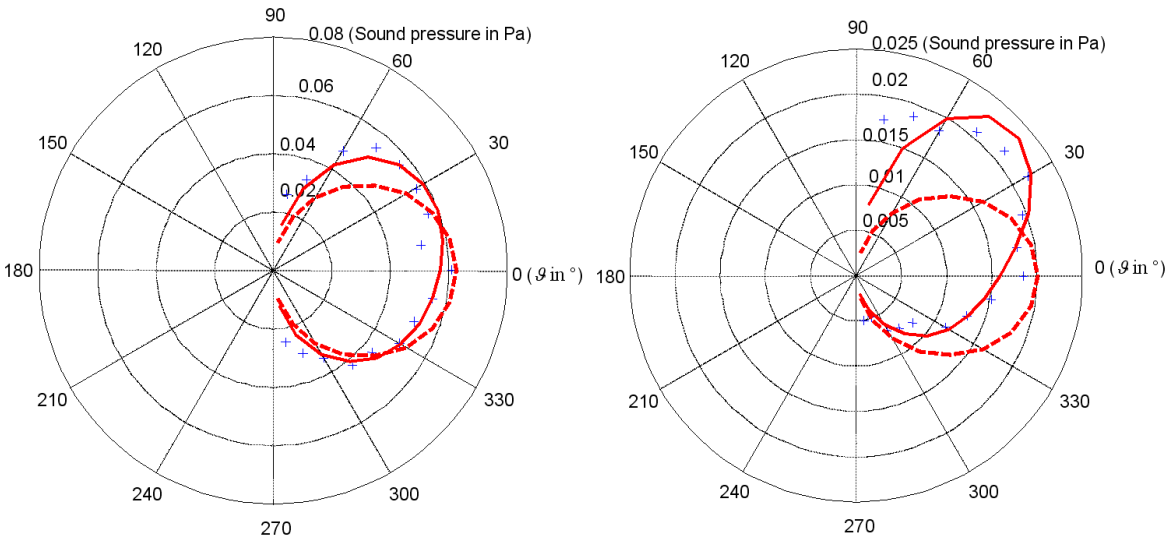

(a) (b)

Figure 4.2 Comparison between the simplified fan noise model of Eq. (4.1) (dashed line), the radiation field extrapolation from an inverse model of the fan (solid line) and experimental data (crosses). (a) BPF (n = 1), (b) 2 BPF (n = 2)

for globally controlling the sound field radiated by the fan. This can be achieved by using an unbaffled loudspeaker located at a distance z_s from the fan. A classical idealised model of an unbaffled loudspeaker is a circular piston of radius a radiating in free field as illustrated in Fig. 4.1. The far field acoustic pressure of such a secondary source at a distance r_s from the piston centre and angle ϑ_s with respect to the piston axis is [3] :

$$p_s(t; r_s, \vartheta_s) = \sum_n p_s(n\omega_1; r_s, \vartheta_s) e^{-in\omega_1 t}$$

$$p_s(n\omega_1; r_s, \vartheta_s) = -ink_1 q_s \frac{e^{ink_1 r_s}}{4\pi r_s} \left[\frac{2J_1(nk_1 a \sin\vartheta_s)}{nk_1 a \sin\vartheta_s} \right] \cos\vartheta_s \tag{4.2}$$

where q_s is the amplitude of the force driving the piston, J_1 is the cylindrical Bessel function of order 1. For long wavelengths (relative to piston radius) the factor in brackets is approximately one. Thus the loudspeaker radiates like a point dipole oriented along the z axis at low frequencies. Moreover, when $\vartheta_s = 0$, $ka \sin\vartheta_s = 0$ and the factor in brackets is also equal to 1.

4.3.3 Minimisation of the sum squared pressure at far field error microphone locations

In this section, the control source strength q_s is adjusted in order to minimise the total sound pressure at a number of far field locations $(r, \vartheta_l) \quad (0 \leqslant l \leqslant L)$. Following Nelson [74], let us consider L error sensors in the far field and define the acoustic pressure vector

$$\mathbf{p} = [p(n\omega_1; r, \vartheta_1) \quad \dots \quad p(n\omega_1; r, \vartheta_l) \quad \dots \quad p(n\omega_1; r, \vartheta_L)]^T \tag{4.3}$$

where ϑ_l is the angular position of the l^{th} sensor. The linear superposition principle is used to sum the contribution of the primary and the secondary fields in order to calculate the total sound pressure in the far field :

$$\mathbf{p} = \mathbf{z_p} q_p + \mathbf{z_s} q_s \tag{4.4}$$

with $\mathbf{z}_p$ and $\mathbf{z}_s$ are the vectors of complex acoustic transfer function of the primary and the secondary sources respectively, defined by Eqs. (4.5) and (4.6) :

$$\mathbf{z_p} = \left[-ink_1 \frac{e^{ink_1 r}}{4\pi r} J_0(nk_1 \bar{r}_1 \sin\vartheta_1) \cos\vartheta_1 \quad \dots \quad -ink_1 \frac{e^{ink_1 r}}{4\pi r} J_0(nk_1 \bar{r}_1 \sin\vartheta_L) \cos\vartheta_L \right]^T \tag{4.5}$$

$$\begin{aligned} \mathbf{z_s} \quad = \quad & \left[-ink_1 \frac{e^{ink_1 r_s}}{4\pi r_s} \left[\frac{2J_1(nk_1 a \sin\vartheta_{s1})}{nk_1 a \sin\vartheta_{s1}} \right] \cos\vartheta_{s1} \right. \\ & \left. \dots \quad -ink_1 \frac{e^{ink_1 r_s}}{4\pi r_s} \left[\frac{2J_1(nk_1 a \sin\vartheta_{sL})}{nk_1 a \sin\vartheta_{sL}} \right] \cos\vartheta_{sL} \right]^T \end{aligned} \tag{4.6}$$

where r and r_s denote the distance of the l^{th} sensor from the primary source and the secondary source, respectively. Moreover, ϑ_l and ϑ_{sl} denote the angle of the l^{th} sensor with respect to the z-axis from the primary and secondary source respectively. We introduce a cost function equal to the sum of the squared acoustic pressures at the L sensors, for each integer multiple n of the BPF ω_1 :

$$J_p = \sum_{l=1}^{L} |p(n\omega_1; r, \vartheta_l)|^2 = \mathbf{p^H p} \tag{4.7}$$

in which the superscript H is the Hermitian operator.

Substituting Eq. (4.4) into Eq. (4.7) leads to a quadratic Hermitian function of the complex secondary source strength [74] :

$$J_p = |q_p|^2 \, \mathbf{z_p^H z_p} + q_p^* \mathbf{z_p^H z_s} q_s + q_s^* \mathbf{z_s^H z_p} q_p + |q_s|^2 \, \mathbf{z_s^H z_s} \tag{4.8}$$

where * is the complex conjugate symbol. Since $\mathbf{z_s^H z_s}$ is a positive quantity, J_p has a unique global minimum which is obtained for an optimal control force driving the piston equal to :

$$q_{s0} = -\frac{\mathbf{z_s^H z_p}}{\mathbf{z_s^H z_s}} q_p \tag{4.9}$$

The optimal control source strength can be somewhat simplified by using the following far field approximations in Eqs. (4.5) and (4.6) : $\vartheta_{sl} \approx \vartheta_l$, $r_s \approx r$ in the denominator of Eqs. (4.5) and (4.6), and $r_s \approx r - z_s \cos\vartheta_l$ in the exponential term of Eqs. (4.5) and (4.6). After some algebra, the Eq. (4.9) leads to :

$$q_{s0} = -q_p \frac{\sum_{l=1}^{L} e^{ink_1 z_s \cos\vartheta_l} J_0(nk_1 \bar{r}_1 \sin\vartheta_l) \left(\frac{2J_1(nk_1 a \sin\vartheta_l)}{nk_1 a \sin\vartheta_l} \right) \cos^2\vartheta_l}{\sum_{l=1}^{L} \left(\frac{2J_1(nk_1 a \sin\vartheta_l)}{nk_1 a \sin\vartheta_l} \right)^2 \cos^2\vartheta_l} \tag{4.10}$$

Case $L = 1$

If L=1 (one error microphone located at (r, ϑ_0)), Eq. (4.10) reduces to

$$q_{s0} = -q_p \left[\frac{nk_1 a \sin\vartheta_0}{2J_1(nk_1 a \sin\vartheta_0)} \right] J_0(nk_1 \bar{r}_1 \sin\vartheta_0) e^{ink_1 z_s \cos\vartheta_0} \tag{4.11}$$

If $\vartheta_0 = 0$, the term in bracket is unity. Thus, the resulting sound pressure field when Eq. (4.11) is satisfied is given by :

$$
p(n\omega_1; r, \vartheta) =
\begin{cases}
p_p(n\omega_1; r, \vartheta)\left(1 - \frac{J_0(nk_1\bar{r}_1 \sin\vartheta_0)}{J_1(nk_1 a \sin\vartheta_0)} \frac{J_1(nk_1 a \sin\vartheta)}{J_0(nk_1\bar{r}_1 \sin\vartheta)} \frac{\sin\vartheta_0}{\sin\vartheta} e^{ink_1 z_s(\cos\vartheta_0 - \cos\vartheta)}\right) & \vartheta_0 \neq 0, \vartheta \neq 0 \\
p_p(n\omega_1; r, \vartheta)\left(1 - \frac{1}{J_0(nk_1\bar{r}_1 \sin\vartheta)} \frac{2J_1(nk_1 a \sin\vartheta)}{nk_1 a \sin\vartheta} e^{ink_1 z_s(1 - \cos\vartheta)}\right) & \vartheta_0 = 0, \vartheta \neq 0 \\
p_p(n\omega_1; r, \vartheta)\left(1 - J_0(nk_1\bar{r}_1 \sin\vartheta_0) \frac{nk_1 a \sin\vartheta_0}{2J_1(nk_1 a \sin\vartheta_0)} e^{ink_1 z_s(\cos\vartheta_0 - 1)}\right) & \vartheta_0 \neq 0, \vartheta = 0 \\
0, \quad \vartheta_0 = 0, \vartheta = 0
\end{cases}
\tag{4.12}
$$

where p_p denotes the primary sound field given by Eq. (4.1). Eq. (4.12) gives a general expression of the resulting field as a function of the primary and secondary source arrangement. It provides a useful analytical formulation for preliminary investigations of active control of fan noise using an unbaffled loudspeaker.

For long wavelength approximation ($\lambda >> a, \bar{r}_1$) Eq. (4.12) can be reduced to a simpler form :

$$
p(n\omega_1; r, \vartheta) \approx p_p(n\omega_1; r, \vartheta)\left(1 - e^{ink_1 z_s(\cos\vartheta_0 - \cos\vartheta)}\right) \tag{4.13}
$$

with $p_p(n\omega_1; r, \vartheta) \approx -ink_1 q_p \frac{e^{ink_1 r}}{4\pi r} \cos\vartheta$. At low frequency, both the fan and the control loudspeaker radiate like point dipoles. From Eq. (4.13), the condition for global attenuation of the resulting sound field in the entire far field is the same as for two monopole sources : $k_1 z_s < \pi/6$ or $12 < \lambda/z_s$ [74].

4.4 Far field sound directivity after control

Numerical results of active control simulation are presented in this section. The configuration investigated corresponds to the sound radiation of a typical automotive engine cooling axial fan ($\bar{r}_1 = 12$cm) in the frequency range 0-700Hz that includes 1 BPF and 2 BPF. A control piston of radius $a = 4$cm is located at a distance $z_s = 5$cm from the fan. This arrangement corresponds to the experimental set-up presented in section 4.7 of this paper. For this configuration, $10 < \lambda/z_s$, $12 < \lambda/a$ and $4 < \lambda/\bar{r}_1$, therefore the above theoretical conditions for global control are reasonably well satisfied. In the simulations, the primary source strength is fixed to $q_p = 1$, and the secondary source strength is calculated from Eq. (4.10) or (4.11). The results are plotted in terms of the far field sound directivity with and without control.

Case $L = 1$

Fig. 4.3 shows the directivity plots in the case of $L = 1$ single far field error microphone at various angular positions $\vartheta_0 = 0, \pi/6, \pi/3$ in the downstream half-space. The left column is obtained for a frequency $f = 300$Hz and the right column for $f = 600$Hz ; these values correspond respectively to $n = 1$ and $n = 2$ in the case of a 6-bladed axial fan operating at a rotating speed of 50Hz. In the case of the left column, $\lambda/z_s \approx 23$, $\lambda/a \approx 28$ and $\lambda/\bar{r}_1 \approx 9.4$, and both the primary and control sources almost behave as point dipoles in this case. The spatial directivity of the control source in Fig. 4.3 reasonably matches the directivity of the fan, resulting in a significant sound attenuation in the error microphone half-space. The best global attenuation in the downstream half-space is obtained for $\vartheta_0 = \pi/6$ in this case. The downstream directivity in the case $\vartheta_0 = 0$ is typical of a weakly radiating equivalent quadrupole source. Note however that the control performance is generally much less in the upstream half-space.

In the case of right column of Fig. 4.3 ($f = 600$Hz), $\lambda/z_s \approx 11$, $\lambda/a \approx 14$ and $\lambda/\bar{r}_1 \approx 4.7$. The spatial extent of the primary source and secondary source become important and their radiation is not perfectly dipolar. The control performance is significantly less than for $f = 300$Hz but appreciable global reduction of the downstream sound field can still be achieved, especially for $\vartheta_0 = 0$ and $\vartheta_0 = \pi/6$. Moderate or negligible reduction is observed in the upstream half-space.

In summary, a single secondary unbaffled oscillating piston is able to match the radiation pattern of a simple model of a typical engine cooling fan in the frequency range 0-600Hz. Therefore, it is expected that a single control source and a single far field error microphone are effective in controlling the downstream sound field of such a fan.

Case $L > 1$

In order to more effectively control both the upstream and downstream sound fields, it may be appropriate to introduce a number of far field error microphones distributed in several directions $\vartheta_l \quad (0 \leqslant l \leqslant L)$. Fig. 4.4 shows the directivity plots for the same primary and secondary source arrangement as previously, but with several error microphones distributed in the upstream or downstream half-space. The secondary source in this case is adjusted to minimise the sum of the squared pressures at the error sensors. The disturbance frequency in Fig. 4.4 is $f = 300$Hz, therefore $\lambda/z_s \approx 23$, $\lambda/a \approx 28$ and $\lambda/\bar{r}_1 \approx 9.4$ as in left column of Fig. 4.3. These results indicate that several error sensors distributed in the whole space are effective in controlling both the upstream and downstream sound radiation (the primary and secondary directivities are nearly coincident). However, when comparing the results of Figs. 4.3 and 4.4, one notes that if the objective is to reduce the radiation in the downstream half-space only, then adding more error sensors in this half-space does not significantly improve the control performance. This observation is however closely related to the axial symmetry of the simplified aeroacoustic model of the fan.

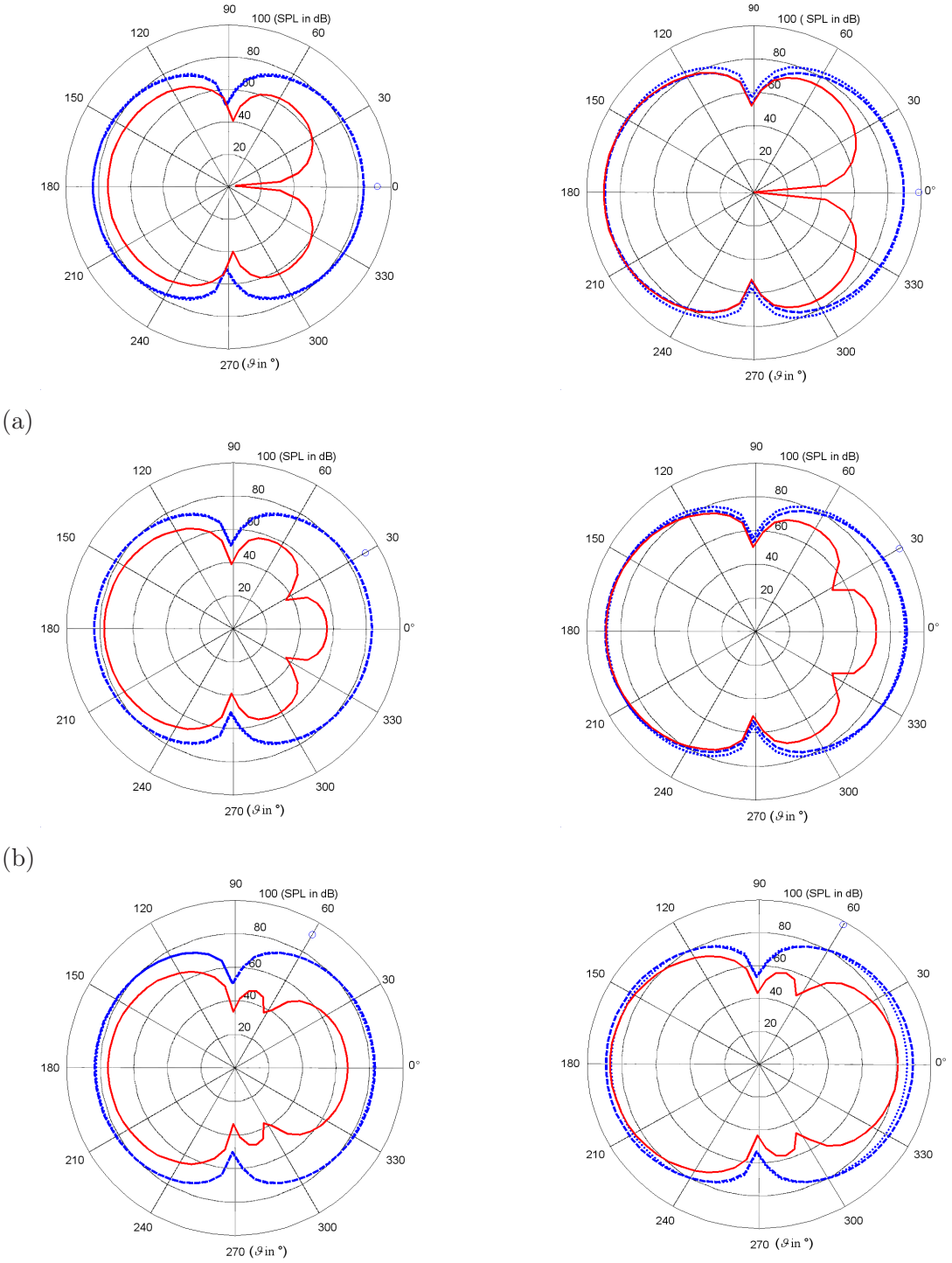

Figure 4.3 Far field sound directivity in the case $L = 1$ for various error sensor positions. Primary source (dashed line), secondary source (dotted line) and global (solid line). Left-hand column : f=300 Hz $\lambda/z_s \approx 23$, $\lambda/a \approx 28$ and $\lambda/\bar{r}_1 \approx 9.4$. Right-hand column : f=600 Hz ; $\lambda/z_s \approx 11$, $\lambda/a \approx 14$ and $\lambda/\bar{r}_1 \approx 4.7$. (a) $\theta_0 = 0$; (b) $\theta_0 = \frac{\pi}{6}$; (c) $\theta_0 = \frac{\pi}{3}$.

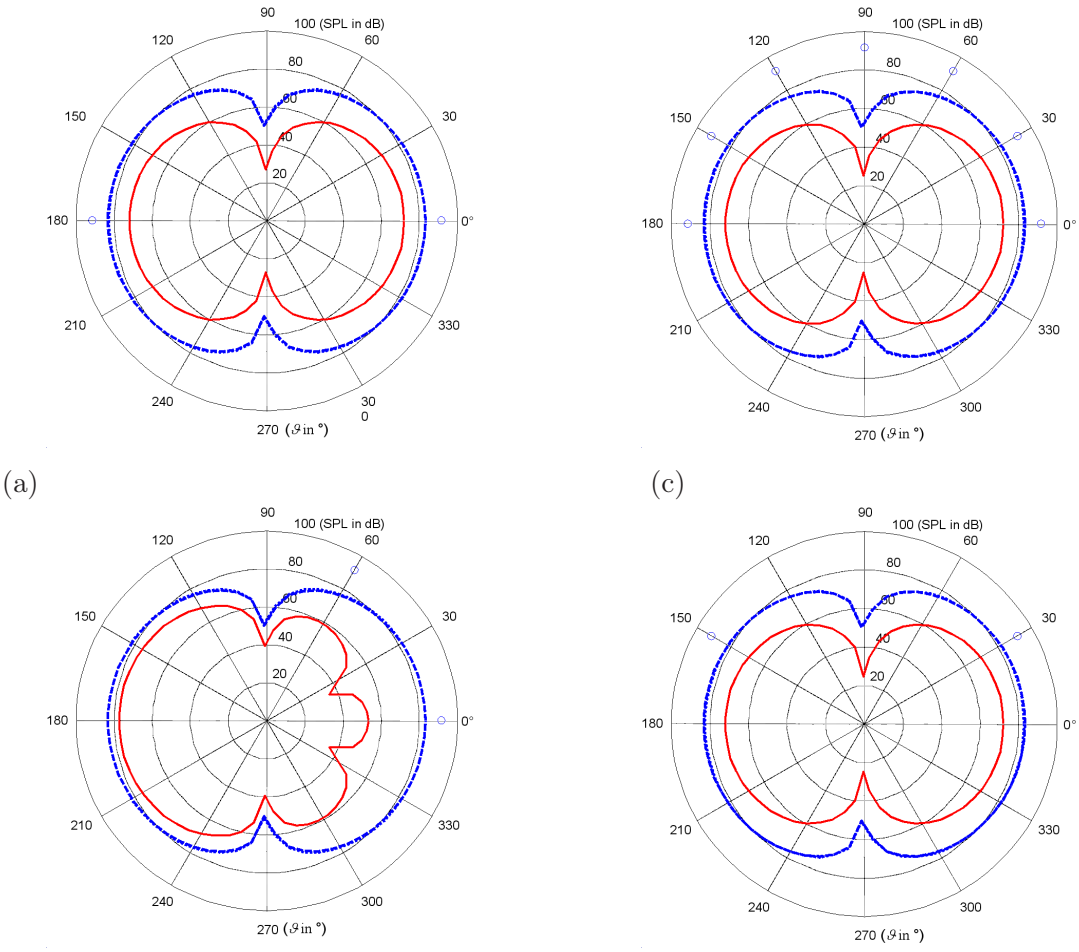

Figure 4.4 Far field sound directivity at f=300 Hz in the case $L > 1$ for various error sensor positions : (a) ϑ_1=0 and $\vartheta_2 = \pi$, (b) $\vartheta_l = l\pi/6$, l=[0,1,2,3,4,5,6], (c) ϑ_1=0 and $\vartheta_2 = \pi/3$, (d) $\vartheta_1 = \pi/3$ and ϑ_2=$5\pi/6$. Primary source (dashed line), secondary source (dotted line) and global (solid line) ; $\lambda/z_s \approx 11$, $\lambda/a \approx 14$ and $\lambda/\bar{r}_1 \approx 4.7$.

In reality, a non-uniform upstream flow entering the fan translates into a non-axially symmetric directivity of the primary sound field [5]. Therefore, the control effectiveness when using an axially symmetric control source may be decreased in this case. However, this simple model provides a useful tool for a preliminary design and understanding of the tonal fan noise active control when a loudspeaker is located in front of the fan.

4.5 Metrics for global control

4.5.1 Far field sound pressure

Following Nelson [74] for the case of two coupled monopoles, it is possible to compare the squared far field sound pressure produced by the interference of the two sources $|p(r,\vartheta)|^2$ to that produced by the fan alone $|p_p(r,\vartheta)|^2$ for any direction ϑ, from Eq. (4.12) for $L = 1$ or from Eq. (4.4) for $L > 1$. The condition for a global attenuation of the sound field in all directions is given by :

$$\eta = \frac{|p(r,\vartheta)|^2}{|p_p(r,\vartheta)|^2} < 1 \quad \forall \quad \vartheta \tag{4.14}$$

In order to illustrate the effectiveness of the active control in the far field, the parameter $\log \eta$ is plotted in Fig. 4.5 as a function of the direction $-\pi \leqslant \vartheta \leqslant \pi$ and the non-dimensional wavelength λ/z_s in the case of $L = 1$ error sensor for two different locations of the error sensor : $\vartheta_0 = 0$ and $\vartheta_0 = \pi/4$. The configuration investigated is similar to the previous section, and representative of an actual engine cooling fan (mean radius of the fan $\bar{r}_1 = 12$cm, control piston of radius $a = 4$cm at $z_s = 5$cm from the fan centre). The horizontal plane $\log \eta = 0$ is also plotted in Fig. 4.5 in order to illustrate the limit for global control : configurations for which $\log \eta < 0$ correspond to a sound pressure attenuation and $\log \eta > 0$ are associated to a sound pressure increase in the corresponding direction. In the case $\vartheta_0 = 0$, a sound pressure attenuation is obtained in all directions as long as $\lambda/z_s > 13$; when $\lambda/z_s \leqslant 13$, an increased sound pressure is observed in the directions near $\vartheta = \pm\pi/2$, i.e. near the plane of the fan. In the case $\vartheta_0 = \pi/4$, the condition for global sound pressure attenuation is slightly less stringent, $\lambda/z_s > 11$; for smaller wavelength, a sound pressure reinforcement is also observed near $\vartheta = \pm\pi/2$. For a source separation $z_s = 5$cm, the condition $\lambda/z_s > 13$ ($\vartheta_0 = 0$) implies an upper frequency limit of about 520Hz for global sound pressure attenuation, whereas $\lambda/z_s > 11$ ($\vartheta_0 = \pi/4$) implies an upper limit of about 620Hz. These values suggest that such a Single-Input Single-Output (SISO) active control arrangement is able to globally reduce the first 2 tones of a 6-bladed automotive fan operating at a rotational speed of 50Hz in free field.

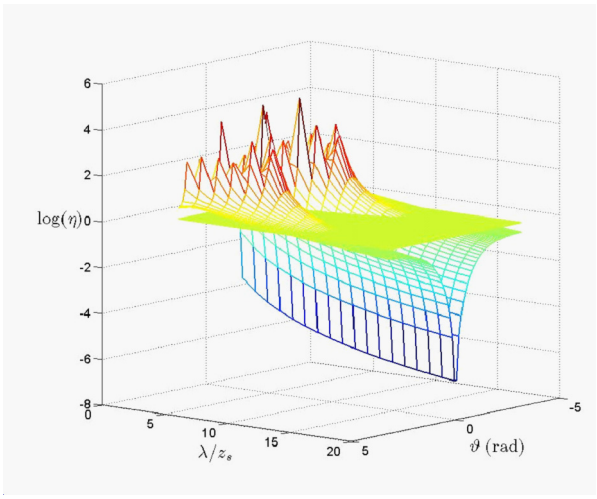

(a)

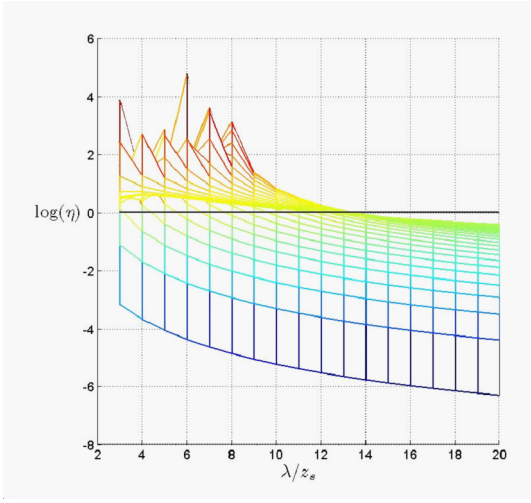

(b)

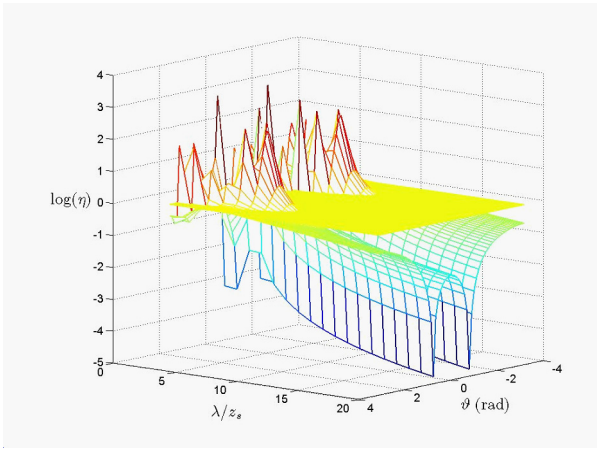

(c)

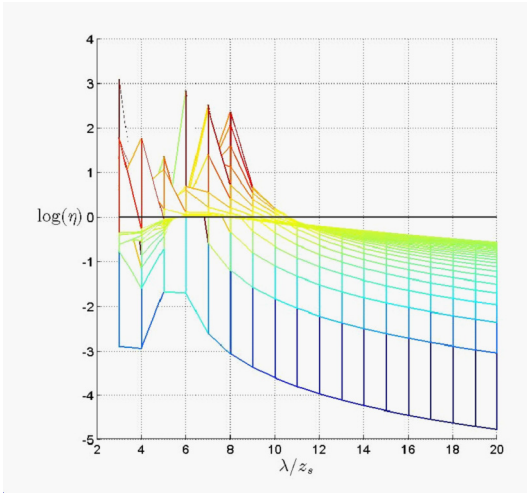

(d)

Figure 4.5 Control parameter $\log(\eta)$ as a function of far field direction ϑ and non-dimensional wavelength λ/z_s for $L = 1$, $\bar{r}_1 = 12$cm, $a = 4$cm, $z_s = 5$cm. (a) 3-D view point, $\vartheta_0 = 0$, (b) projection in the plane $(\log(\eta),\lambda/z_s)$, $\vartheta_0 = 0$, (c) 3-D view point, $\vartheta_0 = \pi/4$, (d) projection in the plane $(\log(\eta),\lambda/z_s)$, $\vartheta_0 = \pi/4$.

4.5.2 Sound power

Another quantity of interest to evaluate the global control performance is the sound power attenuation. A reduction by the active control system of the total sound power is a less constraining condition than a reduction of the far field sound pressure in all directions. The total sound power of the primary and secondary source combination is related to the far field sound pressure $p(r,\vartheta)$ by :

$$W = \frac{1}{2}\int_0^{\pi}\int_0^{2\pi} \frac{|p(r,\vartheta)|^2}{\rho c} r^2 \sin\vartheta d\vartheta d\varphi \tag{4.15}$$

where ρ is the mass density of air and φ is a spherical coordinate defined in Fig. 4.1 of [5],. The r dependence disappears in W because the far field sound pressure $p(r,\vartheta)$ is inversely proportional to r. Moreover the simplified primary and control source models imply that the radiated sound field is axially-symmetric, thus :

$$W = \frac{\pi r^2}{\rho c}\int_0^{\pi} |p(r,\vartheta)|^2 \sin\vartheta d\vartheta \tag{4.16}$$

The integral in Eq. (4.16) needs to be evaluated numerically from the far field sound pressure obtained from Eq. (4.12) for $L = 1$ or from Eq. (4.4) for $L > 1$, using I discrete values of ϑ_i spaced by $\Delta\vartheta$, $W = \frac{\pi r^2}{\rho c}\Delta\vartheta \sum_{i=1}^{I} |p(r,\vartheta_i)|^2 \sin\vartheta_i$. We then define a new control parameter η_W as the ratio of the sound power with and without control,

$$\eta_W = \frac{W}{W_p} \tag{4.17}$$

Fig. 4.6 shows the value of $10\log\eta_W$ as a function of the non-dimensional wavelength λ/z_s (top graph) or frequency (bottom graph) for the same problem as before (mean radius of the fan $\bar{r}_1 = 12$cm, control piston of radius $a = 4$cm at $z_s = 5$cm from the fan centre), and for $L = 1$ far field error microphone located at various directions $\vartheta_0 = 0,\ \pi/6,\ \pi/3$. It is seen that more oblique directions of the error sensor with respect to the fan axis yield better sound power attenuation after control. Also, a reduction of the sound power is obtained when $\lambda/z_s > 9$ for $\vartheta_0 = 0$, when $\lambda/z_s > 8$ for $\vartheta_0 = \pi/6$ and when $\lambda/z_s > 5.5$ for $\vartheta_0 = \pi/3$ (corresponding to $f = 750$Hz, $f = 970$Hz and $f = 1270$Hz, respectively in the particular arrangement of the present study). These conditions are slightly less restrictive than imposing a reduction of the far field sound pressure in *all* directions of space, as discussed in section 4.5.1. For such a 6-bladed automotive fan operating at a rotational speed of 50Hz, a one control loudspeaker – one error

microphone system would optimally provide a sound power difference ($10\log\eta_W$) between -9dB and -13dB at 1 BPF (300Hz), and between -2dB and -6dB at 2 BPF (600Hz).

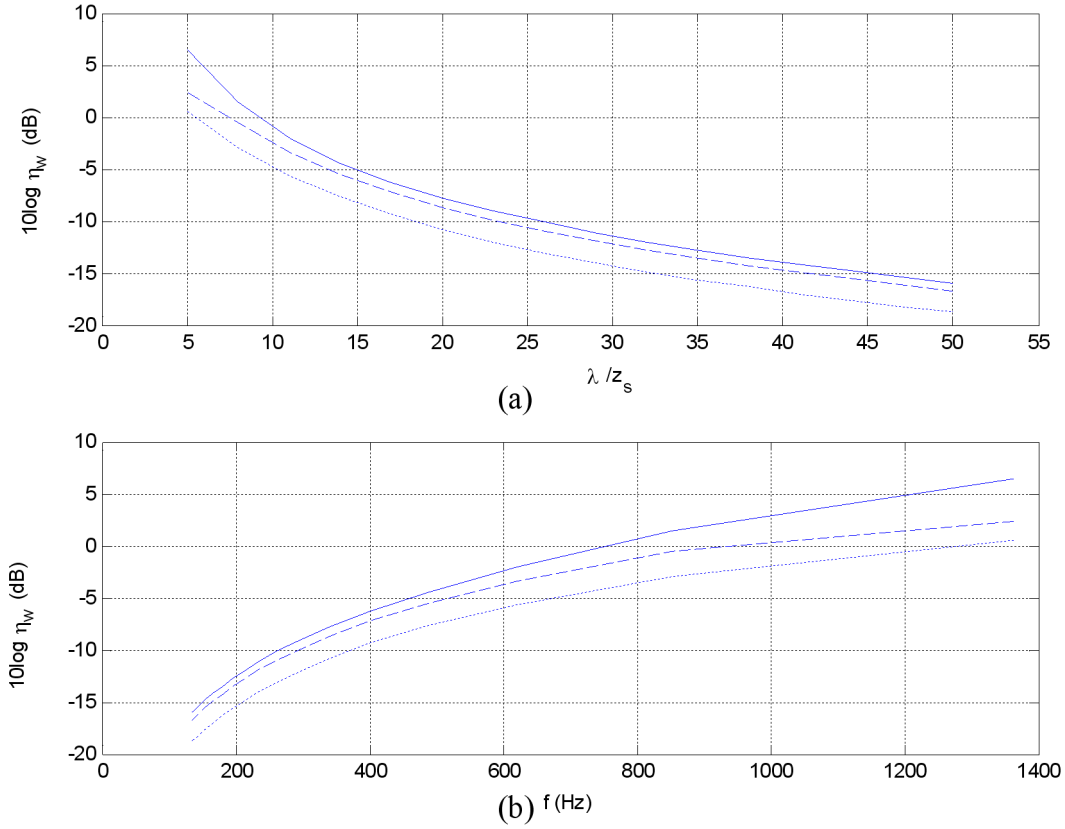

Figure 4.6 (a) Sound power parameter $10\log\eta_W$ as a function of non-dimensional wavelength λ/z_s and (b) $10\log\eta_W$ as a function of frequency for $L=1$, $\bar{r}_1=12$cm, $a=4$cm, $z_s=5$cm and for various error microphone directions $\vartheta_0=0$ (solid line), $\vartheta_0=\pi/6$ (dashed line), $\vartheta_0=\pi/3$ (dotted line).

Fig. 4.7 shows similar results when more error sensors are added ($L=2$). These results show that two cancellation points symmetrically located upstream and downstream on the fan axis ($\vartheta_1=0$ and $\vartheta_2=\pi$) give the best attenuation of the total sound power. In this configuration, the active control would provide a sound power difference ($10\log\eta_W$) of -13dB at 300Hz, and -7dB at 600Hz. The additional gain with respect to a single downstream error microphone is thus marginal.

Certain practical situations require that the sound field be controlled in just a half-space (e.g. downstream). In this case, it is more appropriate to introduce a modified half-space sound power parameter $\eta_W^{half}=\frac{W^{half}}{W_p^{half}}$ in which W^{half} and W_p^{half} are the sound power radiated in a half-space with and without control and are obtained by carrying the integration over $0\leqslant\vartheta\leqslant\pi/2$ in Eq. (4.16). Fig. 4.8 shows the corresponding half space control performance $10\log\eta_W^{half}$ when only $L=1$ downstream error sensor is used in various directions $\vartheta_0=0,\ \pi/6,\ \pi/3$. It is clear

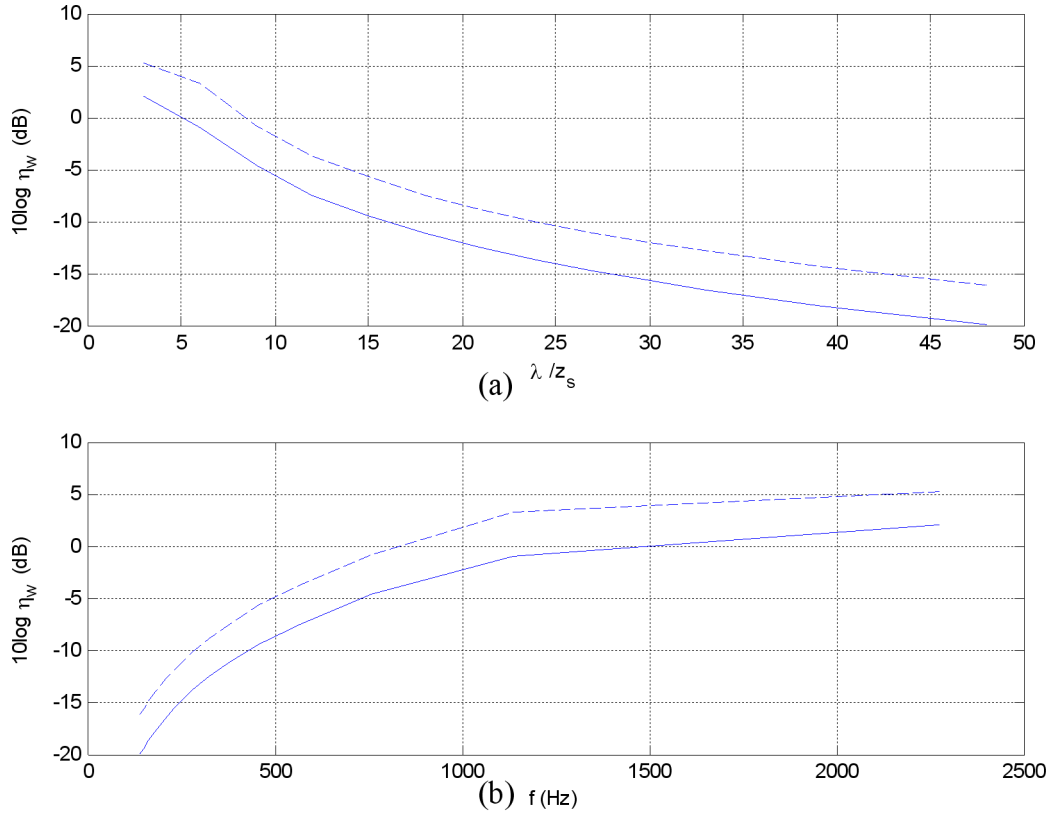

Figure 4.7 (a) Sound power parameter $10\log\eta_W$ as a function of non-dimensional wavelength λ/z_s and (b) $10\log\eta_W$ as a function of frequency for $\bar{r}_1 = 12$cm, $a = 4$cm, $z_s = 5$cm and for various error microphone arrangements : L=2, $\vartheta_1 = 0$ and $\vartheta_2 = \pi$ (solid line) ; L=2, $\vartheta_1 = 0$ and $\vartheta_2 = \pi/3$ (dashed line).

that an increased control performance can be obtained by relaxing the constraint of upstream sound field reduction. In this case, a single downstream error microphone is able to provide a downstream sound power reduction when $\lambda/z_s > 6$ for $\vartheta_0 = 0$, $\lambda/z_s > 3$ for $\vartheta_0 = \pi/6$, $\lambda/z_s > 4.5$ for $\vartheta_0 = \pi/3$. The optimal downstream sound power reduction is between -20dB and -23dB at 300Hz and between -11dB and -16dB at 600Hz.

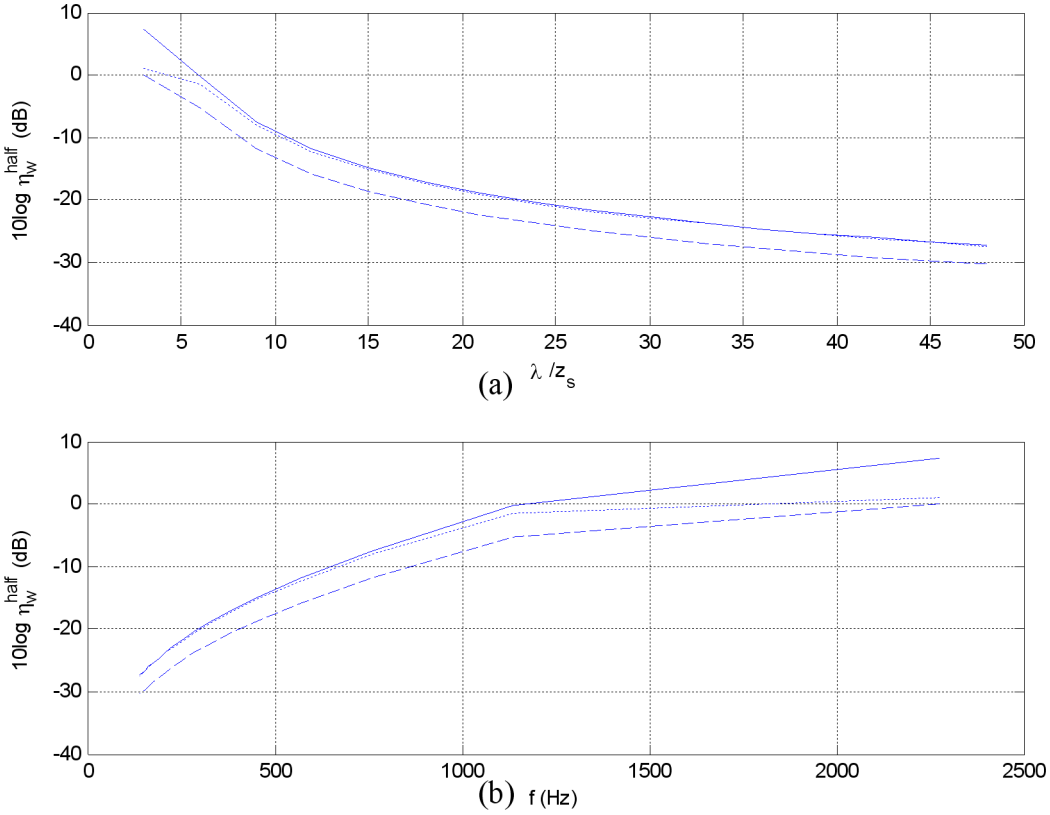

Figure 4.8 (a) Half-space sound power parameter $10\log\eta_W^{half}$ as a function of non-dimensional wavelength λ/z_s and (b) $10\log\eta_W^{half}$ as a function frequency for $L = 1$, $\bar{r}_1 = 12$cm, $a = 4$cm, $z_s = 5$cm and for various error microphone directions $\vartheta_0 = 0$ (solid line) ; $\vartheta_0 = \pi/6$ (dashed line) ; $\vartheta_0 = \pi/3$ (dotted line).

4.6 Active control simulations using the inverse aeroacoustic model

The previous simulations are based on a simple fan noise model which only takes into account the circumferential mode $q = -nB$ in the calculation of the radiated sound field, Eq. (4.1). This assumption implies that the acoustic directivity is axially symmetric and has a maximum on the fan axis. Therefore it is expected that a secondary dipole source located in front of the fan is able to match this primary directivity pattern and sufficient to provide an effective sound attenuation. In reality, other circumferential modes ($q \neq -nB$) may contribute significantly to sound radiation for non-homogeneous flow. This results in a non-axially symmetric radiation

directivity that can be more accurately predicted making use of the inverse model [5]. In this section, the inverse model is used to obtain a continuous extrapolated sound field from a discrete set of measurement points through the reconstruction of the forces acting by the blades on the fluid [5]. The continuous primary sound field is then combined with the secondary sound field to derive the resulting field and to simulate optimal active control of fan tones.

We start with the general expression of the primary multi-tonal fan noise in spherical coordinates (r, φ, ϑ), $p_p(t; r, \varphi, \vartheta) = \sum_n p_p(n\omega_1; r, \varphi, \vartheta) e^{-in\omega_1 t}$ where $\omega_1 = B\Omega$ is the blade passing frequency and according to Eq. (3.6) of the companion paper [5],

$$\begin{aligned} p_p(n\omega_1; r, \varphi, \vartheta) &= -\frac{ik_1 \cos\vartheta}{4\pi r} \sum_{q=-\infty}^{+\infty} i^{nB+q} e^{ink_1 r} e^{i(nB+q)\varphi} \\ &\quad \times \int_{a_1}^{a_2} n f_z^0(r_1) \alpha_n(r_1) \beta_q(r_1) J_{nB+q}(nk_1 r_1 \sin\vartheta) 2\pi r_1 dr_1 \end{aligned} \tag{4.18}$$

Following [5], it is possible to write

$$p_p(n\omega_1; r, \varphi, \vartheta) = -ink_1 q_p \frac{e^{ink_1 r}}{4\pi r} \cos\vartheta \tag{4.19}$$

where

$q_p = -\sum_{q=-\infty}^{+\infty} \sum_i \mathrm{i}^{nB+q} e^{\mathrm{i}(nB+q)\varphi} f_z^0(r_{1i}) \alpha_n(r_{1i}) \beta_q(r_{1i}) J_{nB+q}(nk_1 r_{1i} \sin\vartheta) 2\pi r_{1i} \Delta r_1$ is the complex primary source at the n^{th} multiple of the BPF, i denotes discretization of the radial coordinate over the fan area and r_{1i} are I equally spaced points in the interval $[a_1\, a_2]$ with a step of Δr_1. The value of the source terms $f_z^0(r_{1i}) \alpha_n(r_{1i}) \beta_q(r_{1i})$ in q_p is adjusted to fit measured far field sound pressure data as discussed in [5].

The same secondary source model as before is assumed (unbaffled oscillating piston), therefore, $p_s(n\omega_1; r, \vartheta_) = -ink_1 q_s \frac{e^{ink_1 r_s}}{4\pi r_s} \left[\frac{2J_1(k_1 a \sin\vartheta_)}{k_1 a \sin\vartheta}\right] \cos\vartheta$ where q_s is the strength of the control source. Combining the primary and secondary sound field,

$$\begin{aligned} p(n\omega_1; r, \varphi, \vartheta) &= p_p(n\omega_1; r, \varphi, \vartheta) + p_s(n\omega_1; r, \vartheta) \\ &= -ink_1 \frac{e^{ink_1 r}}{4\pi r} \cos\vartheta \left(q_p + q_s e^{-z_s \cos\vartheta} \left[\frac{2J_1(k_1 a \sin\vartheta)}{k_1 a \sin\vartheta}\right] \right) \end{aligned} \tag{4.20}$$

The secondary source strength is adjusted to minimise the far field squared sound pressure

at a number of far field locations (r, ϑ_l) $(0 \leqslant l \leqslant L)$, as discussed in section 4.3.3. The expression of $\mathbf{z}_p$ becomes :

$$\mathbf{z_p} = \left[-ink_1 \frac{e^{ink_1 r}}{4\pi r} \cos\vartheta_1 \quad \dots \quad -ink_1 \frac{e^{ink_1 r}}{4\pi r} \cos\vartheta_L \right]^T \tag{4.21}$$

4.6.1 Six-bladed fan with equal blade pitches

The simulation presented here involves primary source data which have been derived from directivity measurements of a 6-bladed fan ($B = 6$) with equal blade pitches. The actual fan has a radius R = 15cm and a 12.5 cm diameter central hub. The rotational speed has been fixed to Ω = 50 Hz so that the first 2 disturbing tones are at 1 BPF = 300Hz and 2 BPF = 600Hz. In order to identify the inverse aeroacoustic model of the fan, the acoustic directivity of the fan was measured in an anechoic room at 17 regularly spaced points on a circular arc at 1.5 m from the fan centre, with $\varphi = 0$ and $-80^\circ < \vartheta < 80^\circ$ in the downstream half-space. Fig. 4.9 shows directivity plots for the fan alone (as derived from the inverse aeroacoustic model), the adjusted secondary source and the two optimally combined sources. The control loudspeaker arrangement is similar to the previous sections (a = 4cmand z_s = 5cm) and $L = 1$ error microphone was considered at $\vartheta_0 = 0,\ \pi/4$ in the downstream half-space. The directivity plots show that the primary sound field is not axially symmetric, whereas the secondary source directivity remains symmetric. Consequently, the control performance is degraded as compared to the simplified primary source model of Figs. 4.2 and 4.3. However, trends are similar and the control is still global in the downstream half-space with only one cancellation point and one secondary source. For the BPF, the simulated sound power reductions are about -10.8 dB and -13.8 dB when the error microphone are located at $\vartheta = 0$ and $\vartheta = \pi/4$ respectively. As far as 2 BPF is concerned, the reductions are -4.8 dB and -5.8 dB for $\vartheta = 0$ and $\vartheta = \pi/4$ respectively. The choice of the error sensor location can therefore be optimised for a frequency while deteriorating the control of other the frequency to be controlled. The simulated attenuations from the inverse model are less than the modified half-space sound power parameter $10 \log \eta_W^{half}$ calculated from the simplified fan noise model in that case.

4.6.2 Seven-bladed fan with unequal blade pitched

The results presented in this section involve a 7-bladed fan ($B = 7$) with unequal blade pitches. Unequal blade pitches ensure a lower tonal sound radiation at integer multiples of the blade passing frequency but on the other hand generate additional tones at multiples of the rotational speed. The fan has a radius R = 15cm and a 12.5 cm diameter central hub. The rotational speed has been fixed to Ω = 48.5Hz so that 2 most important disturbing tones are at

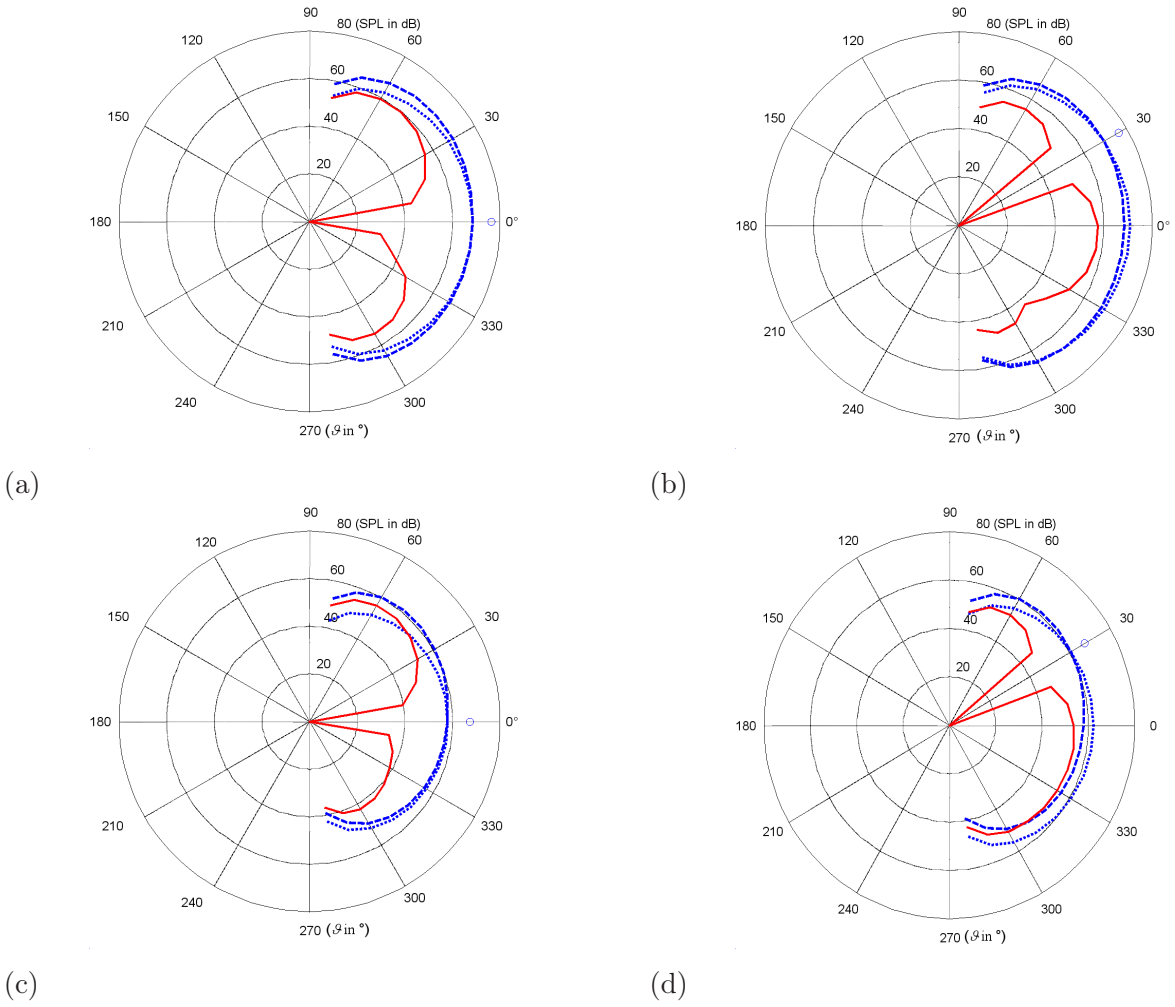

Figure 4.9 Primary source (dashed), secondary source (dotted) and resulting field (solid) downstream directivity from the inverse aeroacoustic primary source model, 6-bladed fan with equal blade pitches; $a = 4$cm and $z_s = 5$cm) (a) ϑ_0=0, f=300 Hz, (b) $\vartheta_0 = \pi/4$, f=300 Hz, (c) ϑ_0=0, f=600 Hz (d) $\vartheta_0 = \pi/4$, f=600 Hz.

1 BPF = 340Hz and 2 BPF = 680Hz. The same experimental procedure as for the 6-bladed fan was used to identify the inverse aeroacoustic model. Fig. 4.10 shows directivity plots for the fan alone (as derived from the inverse aeroacoustic model), the adjusted secondary source and the two optimally combined sources. The control loudspeaker arrangement is similar to previously (a = 4cm and z_s = 5cm) and $L = 1$ error microphone was considered at $\vartheta_0 = 0,\ \pi/6$ in the downstream half-space. Again, the directivity plots show that the primary sound field is not axially symmetric, and the control performance is degraded as compared to the simplified primary source model of Figs. 4.2 and 4.3. However, trends are similar and the control is still global in the downstream half-space with only one cancellation point and one secondary source. For the BPF, the simulated sound power reductions are -11.1 dB and -12.0 dB when the error microphone are located at $\vartheta = 0$ and $\vartheta = \pi/6$ respectively. As far as 2 BPF is concerned, the reductions are -13.9 dB and -14.1 dB for $\vartheta = 0$ and $\vartheta = \pi/6$ respectively. However, one have to remark that those simulated sound power attenuations cannot be achieved experimentally since the reduction of tonal noise is limited by the broadband noise. The accuracy of the attenuation is also limited by the quality of the extrapolated primary sound field directivity. The more dispersed the measured acoustic pressures are, the more complicated the reconstruction is, it can therefore deteriorate the simulated active noise control attenuations.

4.7 Active control experiments

In the previous sections, it has been shown that a single dipole located in front of the fan is theoretically capable of globally reducing the long wavelength tonal noise of the fan in free field. In this section, active noise control experiments in free field are presented. The measured directivities and metrics in the downstream half-space with and without control are compared to the previous predictions.

4.7.1 Experimental set up

Experiments were conducted on two engine cooling units consisting of a symmetric 6-bladed fan or a non-symmetric 7-bladed fan, a radiator and a condenser. In the experiments with the 6-bladed fan, the condenser was removed and a small (4×8 cm) rectangular piece of adhesive tape was bonded on the upstream side of the radiator at about 5 cm from the fan axis in order to enhance the non-uniformity of the incoming flow and therefore increase tonal noise radiation. The unit was driven by a variable DC source (0-20V/0-60A) ; the rotational speed of the fan could be continuously adjusted by modifying the input voltage. The fan has an exterior diameter of 30cm and a central hub diameter of 12.5cm.

A small midrange unbaffled control loudspeaker of 8cm in diameter was bonded at the center of

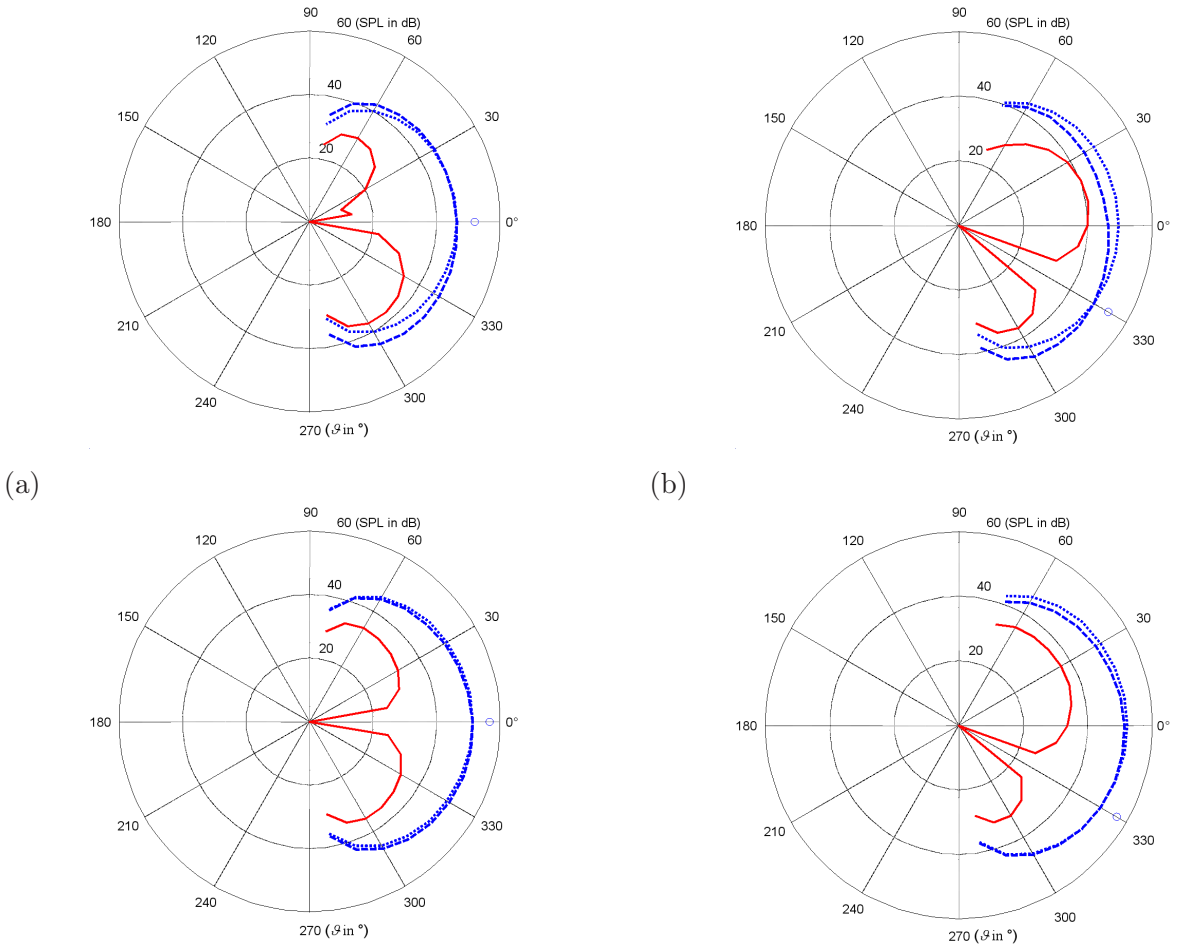

(a) (b)

(c) (d)

Figure 4.10 Primary source (dashed), secondary source (dotted) and resulting field (solid) downstream directivity from the inverse aeroacoustic primary source model, 7-bladed fan with unequal blade pitches; $a = 4$cm and $z_s = 5$cm) (a) ϑ_0=0, f=340 Hz, (b) $\vartheta_0 = \pi/6$, f=340 Hz, (c) ϑ_0=0, f=680 Hz (d) $\vartheta_0 = \pi/6$, f=680 Hz.

the stator, corresponding to the center of rotation of the fan hub (fixed in the laboratory reference frame). The average distance between the plane of the blades and the loudspeaker membrane was $z_s = 5$cm. It was verified that the loudspeaker has negligible effect on the downstream flow of the fan ; in the reported results, all noise data of the fan alone were measured with the control loudspeaker in place. A SISO adaptive feedforward controller was implemented to drive the control loudspeaker. An infrared optical tachometer was mounted on the fan in order to extract a reference signal containing the relevant frequencies : a small rectangular piece of reflective tape was bonded to the outer rotating rim of the blade in order to provide a rectangular pulse train from the detector circuit placed on a fixed location of the frame. In the case of the 6-bladed symmetric fan, 6 pieces of reflective tape were equally distributed on the outer rim, so that the reference signal is a train of rectangular pulses with a period equal to the blade passing frequency. In the case of the 7-bladed fan with unequal blade pitches, the reference signal must be designed to contain multiples of the rotational speed of the fan, with important components at multiples of the BPF : this was achieved by unequally distributing 7 reflective strips on the outer rim.

An error microphone (TMS 1/4" made by PCB) was placed at 1.5m from the fan centre in the downstream half-space ; the microphone could be moved at various directions ϑ_0 from the fan axis. A windscreen was mounted on the microphone to minimise the effect of flow noise. The physical elements of the feedforward active control set-up are shown in Fig. 4.11. The set-up was placed in a semi-anechoic room with the fan axis horizontal and at 50 cm above the ground. 12 cm of absorbing material (conasorb F) were placed on the ground under the set-up in order to minimise ground reflections.

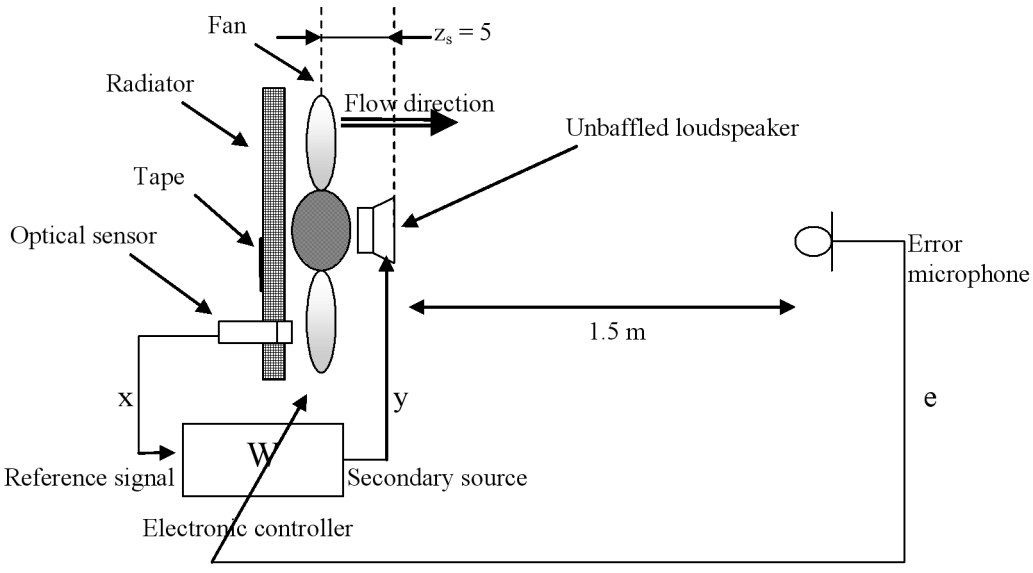

Figure 4.11 Physical elements of the single channel feedforward active control of free field fan noise.

Active control simulations for this configuration have shown that global control of the downstream sound field can be obtained up to approximately 700Hz using a single control source. Given

that the rotational speed was fixed to approximately 50Hz, the experimental objective was therefore a global attenuation of downstream noise at 1 BPF and 2 BPF. A time-domain adaptive filtered-X LMS feedforward controller [75] was implemented under a dSPACE/Simulink real-time control environment. The sampling frequency was set to 3000 Hz, and anti-aliasing and reconstruction low-pass filters were placed at input and output stages of the digital signal processing board. The cut-off frequency of the low-pass filters was set to 800Hz in the case of the 6-bladed fan and 1200Hz in the case of the 7-bladed fan. The secondary path (transfer function between loudspeaker input and error microphone output) was identified off-line by feeding a broadband noise to the secondary source and using an adaptive LMS identification with a 64-tap FIR filter. The control filter was implemented as an FIR filter with 4 coefficients (6-bladed symmetric fan) or 32 coefficients (7-bladed non-symmetric fan). The measured coherence between the reference sensor and the error microphone at 1 BPF and 2 BPF was larger than 0.98 in all experiments conducted.

At last, a HP 35665A spectrum analyser was used to measure the power spectrums (20 averages for each measurement) at 17 regularly spaced points on a circular arc at 1.5 m from the fan centre, with $\varphi = 0$ and $-80^\circ < \vartheta < 80^\circ$ in the downstream half-space to evaluate the directivity of the primary (without control) and the resulting radiated (with control) sound field.

4.7.2 Experimental results on 6-bladed fan with equal blade pitches

The rotational speed of the fan was adjusted to $\Omega = 50$ Hz so that the first 2 disturbing tones are at 1 BPF = 300Hz and 2 BPF = 600Hz. Fig. 4.12 shows the power spectrum of the sound pressure measured at the error microphone location ($\vartheta_0 = 0$) with and without active control. The tones at 1 BPF (300Hz) and 2 BPF (600 Hz) are decreased by 28 dB and 18 dB respectively at the error microphone location, and the residual sound field at these frequencies is essentially the broadband, uncorrelated noise. The size of the control filter (4 coefficients) and the low-pass filtering under 800Hz leave the tone at 3 BPF unchanged by the control.

The measured directivity without and with active control is shown in Fig. 4.13. When the error microphone is located on the fan axis ($\vartheta_0 = 0$), the directivity pattern after control is typical of a quadrupole radiation and the tonal noise is globally reduced. Very good agreement between predicted and measured residual sound field is obtained at 1 BPF. Note that the predicted residual sound field has been limited in the following figures to the frequency band of the broadband noise. The agreement is not as good at 2 BPF because of the less precise reconstruction of the primary sound field of the fan by the inverse method at this frequency [5].

We can have an idea of the sound power reduction from the measured radiation directivity by using the modified half-space sound power parameter $10 \log \eta_W^{half}$ described in section 4.5.2. The

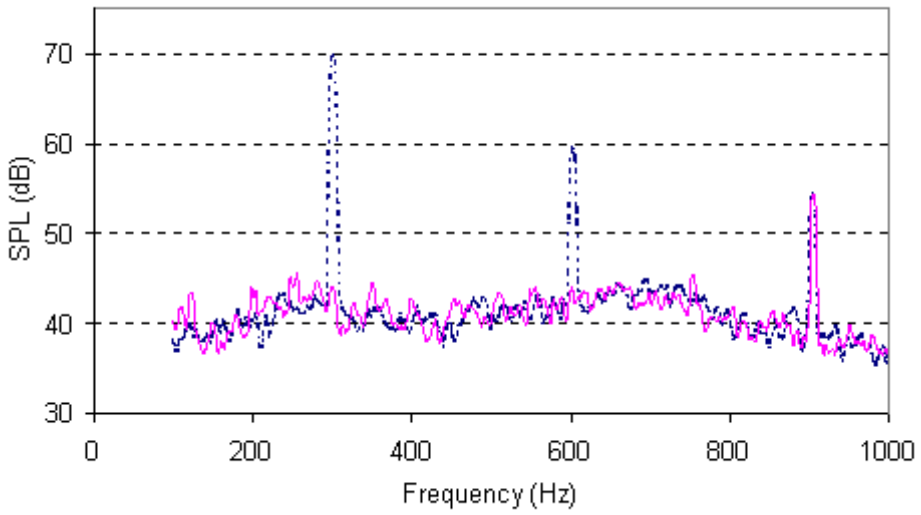

Figure 4.12 Power spectrum of the sound pressure at the error sensor position (ϑ_0=0) for a 6-bladed (with equal pitches) automotive fan noise, with (solid line) and without (dashed line) active control.

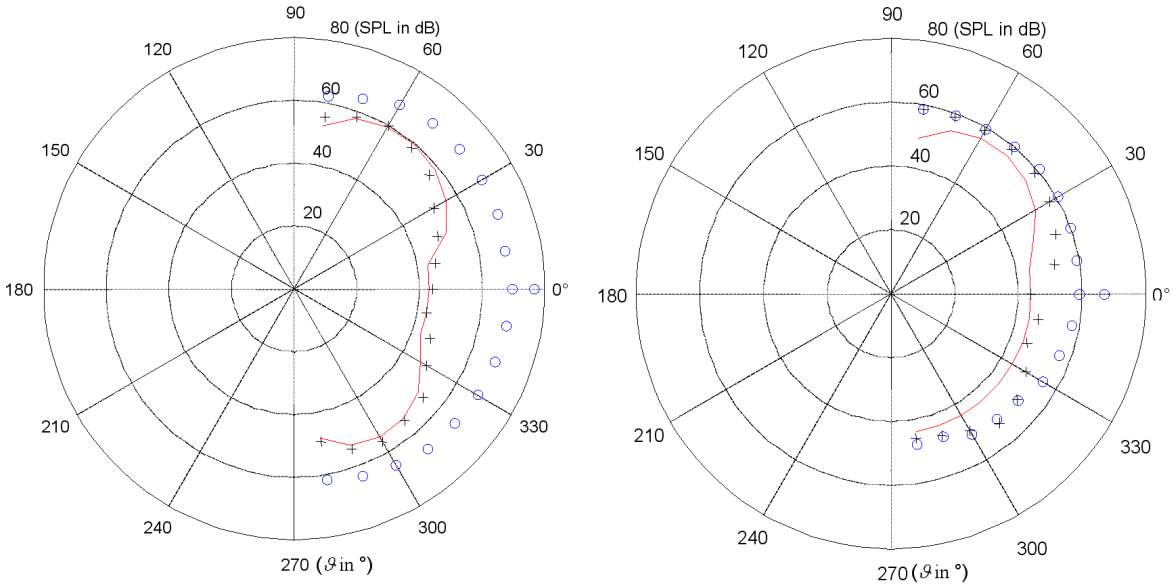

(a) (b)

Figure 4.13 Measured downstream directivity of a 6-bladed (with equal pitches) automotive fan noise at (a) 1 BPF and (b) 2 BPF. Without control (o), with control (+), predicted resulting sound field (solid line). Error microphone at ϑ_0=0.

reductions calculated from the simplified fan noise model, from the inverse aeroacoustic model of the fan and the measurements are compared in Table 4.1.

Frequency	Simplified fan noise model (dB)	Inverse aeroacoustic model (dB)	Experimental measurements (dB)
1 BPF (300 Hz)	-19.8	-10.8	-10.8
2 BPF (600 Hz)	-11.1	-4.8	-1.5

Tableau 4.1 Comparison between the predicted sound power attenuation ($10 \log \eta_W^{half}$) and the experimental directivity measurements for the BPF and its first harmonic (6-bladed fan).

As already shown in Fig. 4.13, the agreement between measured attenuation in the downstream half space attenuations and from the inverse aeroacoustic model is very good for 1 BPF, whereas there is a difference of 3.3 dB for 2 BPF. But, it can be seen that the sound power reduction estimated from the inverse model is more accurate than the reduction estimated from the simplified fan noise model for that case.

4.7.3 Experimental results on 7-bladed fan with unequal blade pitches

In the case of the non-symmetric fan, the rotational speed of the fan was adjusted to $\Omega = 48.5$Hz so that the first two disturbing tones are approximately at 1 BPF = 340Hz and 2 BPF = 680Hz. Fig. 4.14 shows the power spectrum of the sound pressure level at the error microphone location ($\vartheta_0 = 0$) with and without active control. The irregular blade spacing has the effect of spreading the acoustic energy over all integer multiples of the rotational speed. The tones at 1 BPF and 2 BPF are still dominant, however their level is lower than for the fan with equal blade pitches. The reference signal in this case is a pulse train with a fundamental period equal to the rotation period of the fan and therefore contains multiple harmonics of the rotation speed. The active control mainly reduces the most energetic peaks at 1 BPF (340 Hz) and 2 BPF (680 Hz) and has a moderate effect on other multiples of the rotational speed of the fan.

Fig. 4.15 shows the acoustic directivity with and without active control when the error microphone is at $\vartheta_0 = 0$. The 2 tones at 1BPF and 2 BPF are globally reduced after control and the radiation pattern is once again representative of a quadrupole. The agreement between the measured and predicted sound field after control is reasonably good.

Figs. 4.16 and 4.17 show additional results for an error microphone located at $\vartheta_0 = \frac{\pi}{6}$. Again, an effective global control of the tones at 1 BPF and 2 BPF are obtained in this configuration, with a satisfactory directivity agreement between experimental and theoretical control results.

As done for the 6-bladed fan with equal blade pitches, the reductions calculated from the

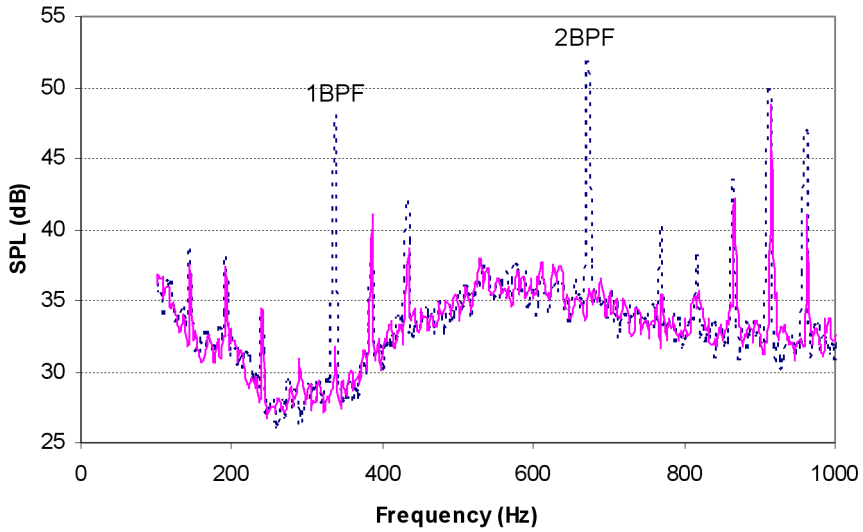

Figure 4.14 Power spectrum of the sound pressure at the error sensor position (ϑ_0=0) for a 7-bladed (with unequal pitches) automotive fan noise, with (solid line) and without (dashed line) active control.

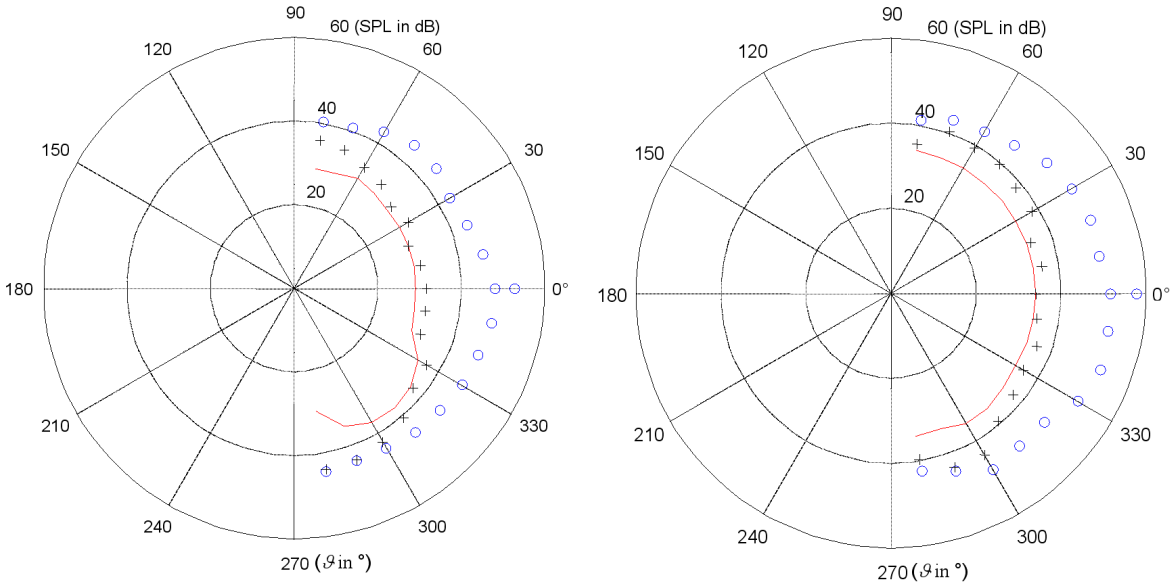

(a) (b)

Figure 4.15 Measured downstream directivity of a 7-bladed (with unequal pitches) automotive fan noise at (a) 1 BPF and (b) 2 BPF. Without control (o), with control (+), predicted resulting sound field (solid line). Error microphone at ϑ_0=0.

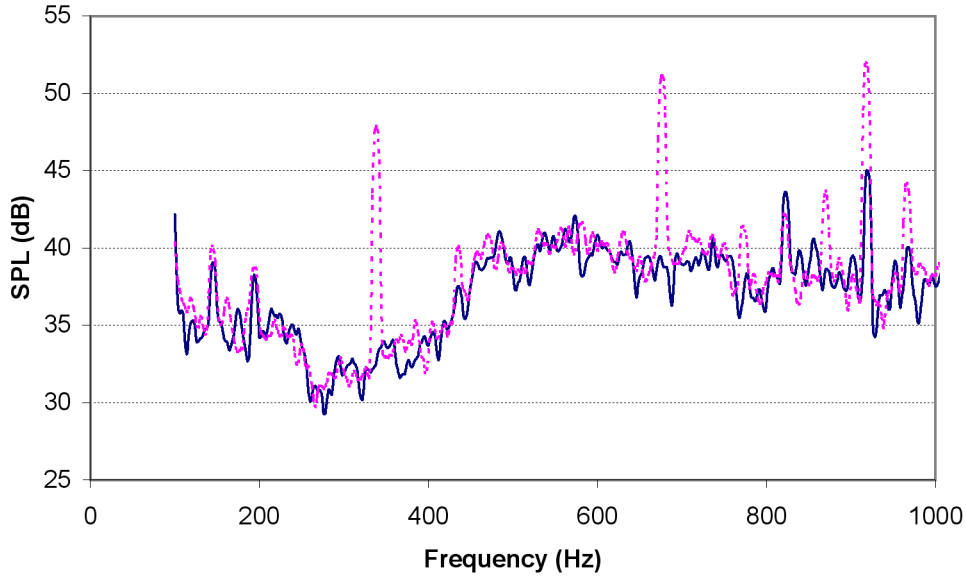

Figure 4.16 Power spectrum of the sound pressure at the error sensor position ($\vartheta_0 = \frac{\pi}{6}$) for a 7-bladed (with unequal pitches) automotive fan noise, with (solid line) and without (dashed line) active control.

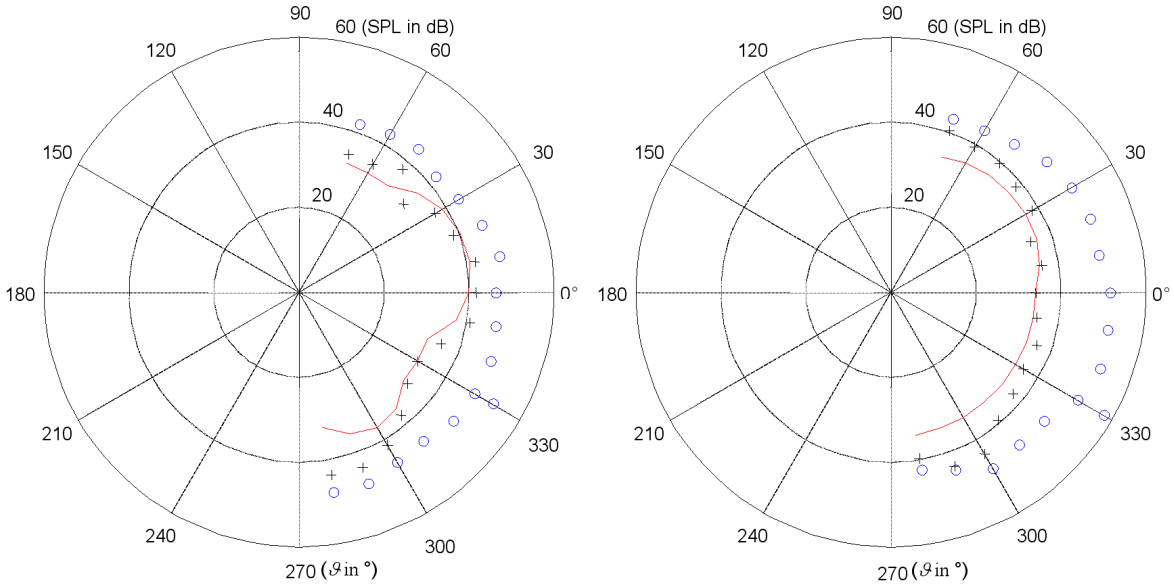

(a) (b)

Figure 4.17 Measured downstream directivity of a 7-bladed (with unequal pitches) automotive fan noise at (a) 1 BPF and (b) 2 BPF. Without control (o), with control (+), predicted resulting sound field (solid line). Error microphone at $\vartheta_0 = \frac{\pi}{6}$.

simplified fan noise model, from the inverse aeroacoustic model of the fan and the measurements are compared in Table 4.2.

Frequency	Simplified fan noise model (dB)	Inverse aeroacoustic model (dB)	Experimental measurements (dB)
1 BPF (300 Hz)			
$\vartheta = 0$	-18.5	-11.1	-5
$\vartheta = \pi/6$	-21.8	-12.1	-5
2 BPF (600 Hz)			
$\vartheta = 0$	-9.1	-11.9	-7
$\vartheta = \pi/6$	-13.4	-13.8	-7.1

Tableau 4.2 Comparison between the predicted sound power attenuation ($10 \log \eta_W^{half}$) and the experimental directivity measurements for the BPF and its first harmonic (7-bladed fan).

The predicted sound power reductions using the inverse model are overestimated and are not as good as for the 6-bladed fan. This can be explained by the different loading conditions between the two experiments and also by the fact that the first BPF directivity is sparse and not well defined, hence the primary sound field is difficult to extrapolate. But the predicted attenuations are still better when using the primary sound field from the inverse model, at least for 1 BPF. Since the directivity of 2 BPF is quasi dipolar, the modelled resulting radiation using the simplified model give similar results as those obtained using the inverse model.

However, the control is still global in the downstream half space and no differences are to be noted in the sound power reduction for $\vartheta_0 = 0$ and $\vartheta_0 = \pi/6$.

4.8 Conclusion

A model for the fan noise valid when only the most radiating modal component of the flow is taken into account was first derived and combined with a model for loudspeaker radiation to demonstrate the ability of a single loudspeaker located at the front of the fan to attenuate the free field radiation in the whole space or in a single half-space as a function of the geometrical features of the primary and secondary source as well as the distance between them. The performance of the approach was evaluated using three metrics for global control. A more detailed model for fan radiation was then presented and used to perform control simulations under non-homogeneous flow conditions. This direct-inverse aeroacoustic model was used to calculate the equivalent sources of a propeller for a non-homogeneous stationary flow field. Simulation results making use of the equivalent sources given by the inverse aeroacoustic model were relevant to predict the resulting sound field for long wavelengths. Tonal sound was significantly reduced to the level of the broadband noise at the error microphone location and a global control in the

downstream half space was achieved.

The experimental results clearly demonstrated the ability of the active control system to significantly attenuate the blade passing frequency and its first harmonic (up to 28 dB) in free field. The amount of reduction achieved at the second and higher harmonics of the BPF greatly depends on the location of the error sensor because of the multi-lobed directivities. But, as the noise levels are lower at these higher frequencies, this is not really detrimental ; moreover, the attenuation of these frequencies can be achieved passively. The use of a SISO feedforward controller with a filtered-X LMS algorithm also leads to robust adaptive control, and the location of the error microphone is almost a free choice if the loudspeaker is located at the front of the fan. The best arrangement from an active fan noise control point of view is the use of a symmetrical propeller because of the fewer number of harmonics to be controlled and easier measurement of the reference signal. Moreover, the better the primary and secondary source directivities are in agreement, the better the control is. As the secondary source is dipolar, the best control should be achieved at low frequencies and when the fan presents almost axially symmetric patterns.

Future work involves implementing this active noise control system in a vehicle and to investigate an alternative technique to sense the error signal in rugged automotive conditions. The boundary conditions will not be the same but preliminary results shows the feasibility of an "at the source" active control of tonal noise. Future experimental work on the control of the BPF and its harmonics in the whole free space using more than one error microphone will also be conducted to completely assess the simulations in free field.

4.9 Acknowledgments

This work has been supported by the AUTO21 Network of Centres of Excellence and Siemens VDO Automotive Inc. The authors wish to thank Sylvain Nadeau from Siemens VDO Automotive Inc. for his collaboration to this research. The authors also thank Dr. Yann Pasco for his contribution to the experimental active noise control.

4.10 Nomenclature

a	Piston radius
a_1	Inner rotor radius
a_2	Outer rotor radius
B	Number of blades
c	Speed of sound
f	Frequency

f_z	Axial pressure component acting on the rotor
f_z^0	Time average value of the axial pressure
F_t	Total thrust of the propeller
g_{1z}	Green function (dipolar radiation along the z axis)
i	Imaginary number ($\sqrt{-1}$)
I	Number of radial elements
J_p	Cost function
J_{nb+q}	Bessel function of the $(nB+q)^{th}$ order
k	Wave number ($k=sk_1=s\omega_1/c$ with $\omega_1=B\Omega$)
L	Number of control point
p	Acoustic pressure
q_p, q_s	Complex source strength of the primary and secondary sources
q_{min}, q_{max}	Minimum and maximum circumferential order q to be reconstructed
$r, \varphi, \vartheta; x, y, z$	Spherical and Cartesian coordinates in the radiation space
$r_1,\ \varphi_1$	Polar coordinates in the rotor plane
$\bar{r}_1$	Mean radius of the fan
t	Time
W	Total sound power
z_s	Source separation
$\mathbf{z}$	Complex acoustic transfer function
α_n	Time Fourier coefficient
β_q	Azimuthal Fourier coefficient
Δr_1	Distance between two radial elements
η	Sound pressure control parameter
η_W	Sound power control parameter
η_W^{half}	Half-space sound power parameter
λ	Wavelength
ρ	Mass density of air
ω	Angular frequency
ω_1	Blade Passage Angular frequency ($\omega_1=B\Omega$)
Ω	Angular velocity of the rotor

Subscripts and indices

l	Control point index
p	Primary source subscript
q	Circumferential index
n	Harmonic order of the BPF
s	Secondary source subscript
i	Radial element index
L	Condensed Source discretization index (i,q)

z	Axial component subscript
φ	Tangential component subscript

Superscripts

H	Hermitian
T	Vector transpose
$*$	Complex conjugate

4.11 Bilan

Dans ce chapitre, une stratégie de contrôle actif par anticipation a été développée en champ libre. Des simulations, basées sur un modèle simplifié du ventilateur ou sur les sources équivalentes calculées à partir du modèle inverse (décrit dans le chapitre précédent), ont montré qu'un contrôle global des deux premières raies était possible pour un ventilateur de radiateur d'automobile avec un petit haut-parleur non-bafflé situé devant le moyeu du ventilateur. Des expériences de contrôle actif ont été menées sur des ventilateurs à pales symétriques ou asymétriques, grâce à l'implémentation d'un contrôleur par anticipation Fx-LMS monocanal. Des atténuations de niveau de pression acoustique de 28 dB et 18 dB ont respectivement été obtenues à la FPP et son premier harmonique au microphone d'erreur. Des atténuations de puissance acoustique de 11.5 dB et 1.5 dB ont été mesurées sur un arc de cercle en aval du ventilateur pour la FPP et son premier harmonique. Un rotor possédant des pales non-identiques et non-régulièrement espacées selon la circonférence, nécessite le contrôle d'autres raies, distribuées à des multiples de la fréquence de rotation (sous-harmoniques de la FPP). Pour contrôler ces raies supplémentaire, plus de coefficients de contrôle sont alors nécessaires. De plus, les atténuations obtenues expérimentalement sont moins grandes pour les fréquences sous harmoniques que pour la FPP et son premier harmonique. L'utilisation d'un ventilateur à pales identiques et régulièrement espacées est donc conseillée pour le contrôle actif acoustique. Un seul haut parleur non-bafflé, situé devant le moyeu, devrait aussi pouvoir contrôler globalement une onde plane se propageant dans un conduit.

Bien que les techniques de contrôle actif soient viables dans beaucoup de cas, nous avons décidé, à ce stade du projet, de nous orienter vers un contrôle passif adapté des sources de bruit de raie. Plutôt que de contrôler la conséquence acoustique de la non-uniformité de l'écoulement, nous nous sommes intéressés au contrôle des composantes spectrales circonférentielles de l'écoulement les plus rayonnantes à la FPP et ses harmoniques. Nous pensons ainsi obtenir une méthode de contrôle plus résistante à des conditions d'utilisation inhospitalières, tel un compartiment moteur d'une automobile. Les atténuations ainsi obtenues devraient aussi être moins sensibles aux conditions aux limites du domaine acoustique. De plus, beaucoup de pistes restent à explorer

dans ce sujet récent.

CHAPITRE 5

INVERSION DU MODÈLE DE BLAKE

EVALUATION DES SOURCES AÉROACOUSTIQUES DE BRUIT BRUIT DE RAIE DES VENTILATEURS SUBSONIQUES PAR MODÈLES INVERSES

EVALUATION OF TONAL AEROACOUSTIC SOURCES IN SUBSONIC FANS USING INVERSE AEROACOUSTIC MODELS

Anthony GÉRARD, Alain BERRY, Patrice MASSON et Yves GERVAIS, accepté pour publication le 20 juin 2006 au Journal de l'American Institute of Aeronautics and Astronautics.

Avant propos

Alors que les chapitres précédents étaient basés sur le modèle de Morse et Ingard [3], les suivants s'appuieront sur celui de Blake [4]. Ce choix est justifié par une "meilleure" description des termes sources dans le modèle de Blake. En particulier, ce modèle est bien adapté à la théorie de Sears, reliant le profil de vitesse entrant dans le ventilateur aux portances instationnaires des pales du rotor. Ces portances instationnaires permettent ensuite de calculer le rayonnement acoustique à la FPP et ses harmoniques en champ libre.

Les notations des trois prochains chapitres changeront pour se conformer à celles de Blake.

5.1 Abstract

This paper aims at quantifying the most acoustically radiating modes of the blade unsteady lift and inflow velocity in the circumferential spectral domain and at localizing "hot spot" interaction areas over the fan. The proposed method is based on the inversion of the Blake model for tonal noise from subsonic fans. The unsteady lift formulation is first used to reconstruct the circumferential blade loading variations from the tonal noise radiation in free field. Then the unsteady lift is related to the inflow velocity distortions by a compressible blade response function. Discretizing the lift and velocity in the direct model leads to ill-conditionned aeroacoustic transfer matrices. The Tikhonov regularization technique is used to stabilize the inversion. The curvature of the L-curve is used to choose the regularization parameter such that the sources strength vectors are optimally reconstructed. The singular value decomposition and the discrete Picard condition are also used to analyse the stability of the sources reconstructions. One experimental case is considered to demonstrate the capability of the inverse model to qualitatively reconstruct the blade loading and inflow velocity variations from acoustic pressure measurements in the case of an automotive engine cooling fan.

5.2 Introduction

Acoustic radiation of fans is highly dependent on the non-uniform flow ingested by the rotor, e.g. potential and wake rotor-stator interaction. If the flow is non-uniform but stationary, it leads to periodic unsteady blade lift, which radiates tonal noise at the blade passage frequency and its harmonics. Both the magnitude and the directivity of radiated tones depend on the circumferential modal content of the unsteady lift [4]. Therefore, the acoustic radiation intrinsically contains information about the unsteady lift and non-uniform inflow velocity. A simple and convincing experimental illustration of this effect consists of placing an obstruction next to the upstream or

downstream flow field of a subsonic fan in free field. Moving the obstruction results in changes in tonal noise level and directivity.

The goal of inverse aeroacoustic models is to reconstruct the source strength distribution from a set of acoustic pressure measurements. However, the inversion of aeroacoustic direct models sometimes leads to mathematically discrete ill-posed problems, as already noted by Li *et al.* [69] and Luo *et al.* [68]. The ill-posed problems are often overcome by the Tikhonov regularization technique [69] [68] [59] that penalizes the source strength to be reconstructed.

In a previous paper [5], the inverse aeroacoustic approach was investigated to model the elementary source distribution on the surface of an axial fan based on the Morse and Ingard direct model and preliminary experimental results were provided. The present paper is a further investigation on the reconstruction of the sources in terms of unsteady lift and inflow velocity, based on the models derived by Blake. Further experimental investigation is also carried out for a 3-D hemispheric acoustic measurement meshing. Moreover, an original method is proposed for choosing the regularization parameter of the Tikhonov regularization technique, based on a combination of the curvature of the L-curve and the Picard condition, which gives useful information about the convergence of the reconstructed solution.

In the first section of the paper, we present the Blake models, which relate the unsteady lift or the inflow velocity to the tonal noise radiation, and their discretization. Then, the Tikhonov regularization technique and the crucial point of choosing the regularization parameter are addressed. In the final section, experimental results are presented to show the feasibility of the proposed method for an automotive engine cooling fan. Particular attention is paid to the choice of the regularization parameter for this application.

5.3 Direct Models

Many aeroacoustic models have been developed to calculate the tonal noise radiation of fans in free field. Among the most common are the model of Lowson [19], the model of Morse and Ingard [3], based on the Helmholtz integral and the model of Blake [4] based on the Curle's equation for example. The approach used in this paper is based on the model proposed by Blake, which relates the radiated noise to the unsteady lift experienced by the blades. Moreover, this model provides a relationship between the deterministic inflow velocity and the unsteady lift using Sears-like functions. The advantage of the velocity formulation when inverting the direct model is that the non-uniform velocity profile reconstruction can be compared to hot-wire anemometer measurements. On the other hand, the unsteady lift formulation permits comparison with experimental data provided by blade-integrated pressure sensors.

5.3.1 Unsteady lift formulation

In order to examine the acoustic radiation of axial fans, it is convenient to use the polar coordinate system $\mathbf{y} = (R, \theta, y_3)$ to describe the sources on the blades and the spherical coordinate system $\mathbf{x} = (r, \varphi, \alpha)$ to describe the acoustic free field, as shown in Fig. 5.1. Both coordinate system origins are located at the center of the rotor.

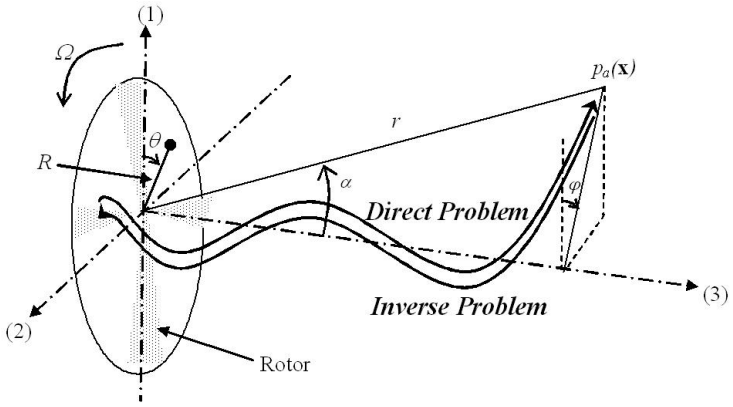

Figure 5.1 Sound radiation from a fan (Coordinate systems)

The rotor is considered as an array of rotating surfaces. As formulated by Curle [4], the acoustic pressure due to a source at location $\mathbf{y}$ and emitting at time τ can be expressed at position $\mathbf{x}$ and time t by an integral equation of the form :

$$p_a(\mathbf{x}, t) = \frac{1}{4\pi} \int \int \int_{\mathcal{V}(\tau)} \left[\frac{1}{r} \left(\dot{q} - \frac{\partial F_i'''}{\partial y_i} + \frac{\partial^2 T_{ij}}{\partial y_i \partial y_j} \right) \right] dV(\mathbf{y}, \tau) \tag{5.1}$$

where the first term $\dot{q}$ is a monopolar source related to the rate of mass injection per unit volume, the second term $\frac{\partial F_i'''}{\partial y_i}$ is a dipolar term that represents the distribution of force per unit volume and the third term $\frac{\partial^2 T_{ij}}{\partial y_i \partial y_j}$ is a quadripolar term related to the Lighthill tensor T_{ij}. The integral in Eq. (5.1) has to be evaluated at a retarded time $\tau = t - |\mathbf{r}| / c_0$, where $\mathbf{r}$ is the distance between the source and the field point where the acoustic pressure has to be evaluated and c_0 is the speed of sound. When the fan tip Mach number is subsonic, as is the case for automotive engine cooling fans investigated in this paper, the monopolar and the quadripolar terms can be neglected in Eq. (5.1) [4].

The force per unit volume $F'''(R, \theta_b, y_3, t)$ exerted by the blades on the fluid at location (R, θ_b, y_3) is decomposed into an axial component $F_3'''(R, \theta_b, y_3, t) = F'''(R, \theta_b, y_3, t) \cos\gamma$ and a tangential component $F_\theta'''(R, \theta_b, y_3, t) = F'''(R, \theta_b, y_3, t) \sin\gamma$, where γ is the pitch angle and θ_b is the circumferential angle rotating with the blades. Moreover, the forces are assumed to be

concentrated in the plane $y_3 = 0$. This assumption is acceptable as long as the axial dimension of the rotor ($\approx$ pitch angle $\times$ chord $= \gamma \times C$) is much smaller than the acoustic wavelength. Thus, the force per unit volume can be changed to the instantaneous pressure difference across the rotor disk $F^{'''}(R, \theta_b, y_3, t) = F^{''}(R, \theta_b, t)\delta(y_3)$.

Following Blake [4], the blade lift per unit span $F'(R,t)$ is then calculated by integrating the instantaneous pressure differential across the rotor $F^{''}(R, \theta_b, t)$ along the chord ($-C/2R < \theta_b < C/2R$). For a circumferentially periodic inflow perturbation composed of wavelengths $2\pi R/\mathtt{w}$, where $\mathtt{w} =]-\infty; +\infty[$ is the Fourier circumferential order of the perturbation, the circumferential and radial distribution of the fluctuating lift on the rotor blades in a frame rotating with the rotor can be expressed as follows :

$$F'(R,\theta,t) = \frac{dL(R,\theta,t)}{dR} = \sum_{s=0}^{B-1} \sum_{\mathtt{w}=-\infty}^{\mathtt{w}=+\infty} F'(\mathtt{w},R) e^{-i\mathtt{w}\Omega t} e^{i\mathtt{w}(\theta+\theta_{\mathtt{w}}(R))} \delta(\theta - s\frac{2\pi}{B}) \tag{5.2}$$

where the index s refers to the blades and the index $\mathtt{w}$ refers to the circumferential harmonic order of the lift, B is the number of blades and Ω is the rotation speed of the rotor in rad.s^{-1}. Eq. (5.2) represents a series of B line forces[1] spaced at regular intervals $2\pi/B$ around the circumferential direction. The phase of the lift along the span (due to the sweep of the blade or the incident gust) is taken into account by $\theta_{\mathtt{w}}(R)$.

Blake obtained the sound pressure $p_a(\mathbf{x}, t)$ radiated by B blades by integrating (over the span) the product of the lift per unit span $F'(\mathtt{w}, R)$ projected over circumferential mode $\mathtt{w}$ and the appropriate Green function for rotating dipolar sources in free field. The far-field approximation ($r \gg R$) is given by :

$$p_a(\mathbf{x},t) = \sum_{m=-\infty}^{\infty} \sum_{\mathtt{w}=-\infty}^{\infty} \left[P_a(\mathbf{x},\omega)\right]_{\mathtt{w},m} e^{-imB\Omega t} \tag{5.3}$$

with :

[1] Dans le cas d'un rotor de corde C=5 cm, la compacité acoustique selon la corde, définie par l'inégalité $\frac{\omega C}{2c_0} < \pi$, est respectée jusqu'à des fréquences de 6000 Hz environ. Par la suite, nous nous limiterons à l'analyse de fréquences inférieures à 1200 Hz. L'approximation de lignes de forces représentant les pales est donc justifiée.

$$[P_a(\mathbf{x},\omega)]_{\mathtt{w},m} = \underbrace{\frac{-ik_0Be^{ik_0r}}{4\pi r}e^{-i(mB-\mathtt{w})(\pi/2-\varphi)}\delta(\omega-mB\Omega)}_{\texttt{Acoustic wave propagation}} \times \int_{R_H}^{R_T} \underbrace{J_{mB-\mathtt{w}}(k_0R\sin\alpha)}_{\texttt{Bessel function term}} \times \underbrace{F^{'}(\mathtt{w},R)\,e^{i\mathtt{w}\theta_{\mathtt{w}}(R)}}_{\texttt{Unsteady lift}} \times [\underbrace{\cos\gamma\cos\alpha}_{\substack{\texttt{Axial forces}\\ \texttt{contribution}}} + \underbrace{\frac{mB-\mathtt{w}}{k_0R}\sin\gamma}_{\substack{\texttt{Tangential forces}\\ \texttt{contribution}}}]dR \tag{5.4}$$

These equations are consistent with the results derived by Lowson [19] or Morse and Ingard [3]. The first summation of Eq. (5.3) represents the combination of multiple tones at pulsations $\omega = mB\Omega$ where B is the number of blades and Ω is the rotation of the rotor in rad.s^{-1}. The second summation represents the decomposition of the lift over circumferential harmonics $\mathtt{w}$. In equation (5.4), the first term describes the propagation of the acoustic waves, which have a wave number $k_0 = \omega/c_0$ and rotate at a circumferential phase velocity equal to $\frac{mB}{mB-\mathtt{w}}\Omega$. In the integration over the radius (from the hub radius R_H to tip radius R_T), the Bessel function term refers to the ability of a circumferential mode $\mathtt{w}$ to radiate sound at the harmonic of rank m of the blade passage frequency $B\Omega$. The term $F^{'}(\mathtt{w},R)\,e^{i\mathtt{w}\theta_{\mathtt{w}}(R)}$ is the contribution of the circumferential mode $\mathtt{w}$ to the lift per unit span acting at a radius R, where the phase along the span is taken into account by $\theta_{\mathtt{w}}(R)$. The terms in brackets weight the relative importance of axial and tangential forces.

The model proposed by Blake is similar to the Morse and Ingard model [5] except for the way the sources are considered. In the Blake model, the sources are the unsteady lift per unit span ($N.m^{-1}$) whereas the sources are the forces per unit area ($N.m^{-2}$) acting by the blade on the fluid in the Morse and Ingard model. As a consequence, a multiplicative factor $2\pi R$ appears in the equation relating the acoustic pressure to the force per unit area in the Morse and Ingard model. Moreover, tangential forces were neglected in the inversion of the Morse and Ingard model [5] whereas in the present paper, both axial and tangential forces are contained in the unsteady lift source. Finally, the Morse and Ingard model is not well adapted to relate the force source terms to the non-uniform inflow velocity as opposed to the model proposed by Blake (as presented in section 5.3.2).

The unsteady lift formulations (5.3) and (5.4) will be discretized in section 5.3.3 in order to be inverted.

5.3.2 Velocity formulation

The Sears theory is used to relate the unsteady lift per unit span $F^{'}(\mathtt{w}, R)$ to the non-uniform inflow velocity $V(\mathtt{w}, R)$. To relate the unsteady lift $F^{'}(\mathtt{w}, R)$ to the non-uniform but stationnary inflow velocity, Blake [4] proposed to use a 2D Sears function, leading to an inextricable discretization problem. In this paper, instead of considering an oblique gust (with a radial and a circumferential wave number) impinging the blades, the fan rotor is decomposed into infinitesimal radial strips along the span, which individually respond to a transversal gust. In other words, at a given radius, the gust and the blade are considered of infinite span so that the gust interaction problem can be treated as a one-dimensional problem. The lift response per unit span to a transverse gust is given by the expression [4] :

$$F^{'}(\mathtt{w}, R) = \pi \rho_0 C \left| V(\mathtt{w}, R) \right| U(R) S(\sigma_\theta) \tag{5.5}$$

where ρ_0 is the density of air, C is the blade chord, $U(R) = R\Omega$ is the tangential speed of the rotor at radius R and $\sigma_\theta = \frac{k_\theta C}{2} = \frac{\mathtt{w} C}{2R}$ is the reduced frequency. Also, $V(\mathtt{w}, R)$ is the circumferential harmonic decomposition of the inflow velocity normal to the movement of the blades, such that :

$$V(\mathtt{w}, R) = \frac{1}{2\pi} \int_0^{2\pi} v(\theta, R) e^{-i\mathtt{w}\theta} d\theta, \qquad v(\theta, R) = \sum_{\mathtt{w}=-\infty}^{\infty} V(\mathtt{w}, R) e^{i\mathtt{w}\theta} \tag{5.6}$$

Moreover, in Eq. (5.5), $S(\sigma_\theta)$ is the incompressible Sears function defined as follows [19] :

$$S(\sigma_\theta) = \frac{1}{i\sigma_\theta [K_0(i\sigma_\theta) + K_1(i\sigma_\theta)]} \tag{5.7}$$

where K_0 and K_1 are respectively the zeroth-order and first-order modified Bessel functions. However, if the reduced frequency is large enough, such that the time for an acoustic wave to travel the chord is not negligible in comparison to the time for a blade to travel an inflow velocity disturbance, a compressible Sears function is recommended. The model of Amiet [27] is used to include the low-frequency approximation of the compressible Sears function :

$$S_c(\sigma_\theta, M_r) = \frac{S(\sigma_\theta/\beta_r^2)}{\beta_r} \left[J_0(M_r^2 \sigma_\theta/\beta_r^2) + i J_1(M_r^2 \sigma_\theta/\beta_r^2) \right] e^{-i\sigma_\theta f(M_r)/\beta_r^2} \tag{5.8}$$

with :

$$\beta_r \equiv \sqrt{1 - M_r^2}$$

and

$$f(M_r) \equiv (1 - \beta_r)\mathtt{ln}M_r + \beta_r \mathtt{ln}(1 + \beta_r) - \mathtt{ln}2$$

where $M_r = \Omega R/c_0$ is the rotation Mach number, J_0 et J_1 are respectively the zeroth-order and first-order ordinary Bessel functions. A criterion for the applicability of Eq. (5.8) is given by Amiet [27] : $\sigma_\theta M_r/\beta_r^2 < 1$ or $\mathtt{w} < \frac{2R(1-M_r^2)}{CM_r}$. This condition is satisfied up to $\mathtt{w} = 43$ for a $C = 5$ cm chord blade rotating at $\Omega = 2\pi \times 50$ rad.s^{-1} at a 10 cm radius. This condition therefore provides an upper bound of the circumferential harmonic $\mathtt{w}$ in Eq. (5.3) when the velocity formulation is used.

5.3.3 Discretization of the direct problems

Unsteady lift formulation

To determine the unsteady lift of the blades from a set of acoustic pressure measurement points, the equation (5.3) must first be discretized to allow inversion. The procedure described in Ref. [5] is adopted. In Eq. (5.3), the summation over $\mathtt{w}$ is truncated from $\mathtt{w}_{min}$ to $\mathtt{w}_{max}$. The discretization of the integral over R (index i) and the acoustic radiation space discretization (index j) lead to the following expression of the radiated sound pressure at the frequency $mB\Omega$ and at point j :

$$\begin{aligned} p_{mj} &= -\frac{ik_0 B e^{ik_0 r_j}}{4\pi r_j} \sum_{\mathtt{w}=\mathtt{w}_{min}}^{\mathtt{w}_{max}} e^{-i(mB-\mathtt{w})(\pi/2-\varphi_j)} \\ &\quad \times \sum_{i=1}^{I} F'(\mathtt{w}, R_i)\, e^{i\mathtt{w}\theta_{\mathtt{w}}(R_i)} [\cos\gamma \cos\alpha_j + \frac{mB - \mathtt{w}}{k_0 R_i} \sin\gamma] J_{mB-\mathtt{w}}(k_0 R_i \sin\alpha_j) \Delta R \end{aligned} \tag{5.9}$$

A linear system can therefore be written :

$$p_{mj} = \sum_i \sum_{\mathtt{w}} H_{mji\mathtt{w}} f_{i\mathtt{w}} \tag{5.10}$$

with :

$$
\begin{aligned}
H_{mji\mathtt{w}} &= -\frac{ik_0 B e^{ik_0 r_j}}{4\pi r_j} e^{-i(mB-\mathtt{w})(\pi/2-\varphi_j)} \\
&\quad \times [\cos\gamma \cos\alpha_j + \frac{mB-\mathtt{w}}{k_0 R_i} \sin\gamma] J_{mB-\mathtt{w}}(k_0 R_i \sin\alpha_j) \Delta R \qquad (5.11) \\
f_{i\mathtt{w}} &= F'(\mathtt{w}, R_i)\, e^{i\mathtt{w}\theta_{\mathtt{w}}(R_i)} \qquad (5.12)
\end{aligned}
$$

where ΔR is the distance between two discretized radii and $H_{mji\mathtt{w}}$ is the aeroacoustic matrix transfer that relates the unsteady lift vector $f_{i\mathtt{w}}$ to the tonal noise in far-field p_{mj}. In Eq. (5.12), the term $e^{i\mathtt{w}\theta_{\mathtt{w}}(R_i)}$ takes into account the phase of the lift along the span. The corresponding matrix formulation is written as follows :

$$
\mathbf{p} = \mathbf{H}\mathbf{f} \qquad (5.13)
$$

Velocity formulation

Inserting Eq. (5.5) in Eq. (5.4) and making use of the discretization previously described leads to :

$$
p_{mj} = \sum_i \sum_{\mathtt{w}} Z_{mji\mathtt{w}} v_{i\mathtt{w}} \qquad (5.14)
$$

with :

$$
\begin{aligned}
Z_{mji\mathtt{w}} &= -\pi\rho_0 C U(R_i) S(\sigma_\theta) \frac{ik_0 B e^{ik_0 r_j}}{4\pi r_j} e^{-i(mB-\mathtt{w})(\pi/2-\varphi_j)} \\
&\quad \times [\cos\gamma \cos\alpha_j + \frac{mB-\mathtt{w}}{k_0 R_i} \sin\gamma] J_{mB-\mathtt{w}}(k_0 R_i \sin\alpha_j) \Delta R \qquad (5.15) \\
v_{i\mathtt{w}} &= |V(\mathtt{w}, R_i)|\, e^{i\mathtt{w}\theta_{\mathtt{w}}(R_i)} \qquad (5.16)
\end{aligned}
$$

where $Z_{mji\mathtt{w}}$ is the aeroacoustic transfer matrix that relates the non-uniform inflow velocity $v_{i\mathtt{w}}$ to the tonal noise in far-field p_{mj}. In Eq. (5.16), the term $e^{i\mathtt{w}\theta_{\mathtt{w}}(R_i)}$ is the complex phase of the transversal gust along the blade span. The corresponding matrix formulation is written as follows :

$$\mathbf{p} = \mathbf{Z}\mathbf{v} \tag{5.17}$$

The Sears function $S(\sigma_\theta)$ in Eq. (14) can be replaced by the function $S_c(\sigma_\theta, M_r)$ defined in Eq. (5.8) to take compressibility effects into account.

5.4 Inverse model

The inverse problem consists of solving Eqs. (5.13) or (5.17) for the unsteady lift $\mathbf{f}$ or the non-uniform inflow velocity $\mathbf{v}$ respectively. In order to overcome the poor conditioning inherent to these inverse problems, the Tikhonov regularization technique is used in this section [14]. The singular value decomposition (SVD) of a generic matrix and the discrete Picard condition are then presented to analyse the stability of the regularized solution. The curvature of the L-curve is also introduced as tool to choose the regularization parameter.

5.4.1 Solution

The dimensions of the aeroacoustic transfer matrices are $\dim(\mathbf{H}) = \dim(\mathbf{Z}) = (M \times J, I \times W)$, where M is the number of acoustic tones, J is the number of sound pressure measurement points, I is the number of discretized radii on the rotor and W is the number of circumferential lift modes to be reconstructed. The matrices $\mathbf{H}$ and $\mathbf{Z}$ to be inverted are intrinsically poorly conditioned because of the large dynamics of the matrix coefficients, introduced by the Bessel function in Eqs. (5.10) and (5.14). Indeed, the value of the Bessel function $J_{mB-\mathtt{w}}$ shows a sharp peak when $\mathtt{w} = mB$. A physical interpretation is that the circumferential mode mB has a strong contribution to the acoustic tone at the frequency $mB\Omega$, since all the elementary dipoles on the rotor radiate in phase.

The Tikhonov regularization is used to stabilize the inversion of the direct discrete problems [14]. In the case of unsteady lift reconstruction, it consists of minimizing the sum of the energy of the error ($\mathbf{e} = \hat{\mathbf{p}} - \mathbf{H}\mathbf{f}$), between the measured sound field $\hat{\mathbf{p}}$ and the predicted sound field $\mathbf{H}\mathbf{f}$, and the energy of the source term $\mathbf{f}$ multiplied by a regularization parameter β. This leads to the following cost function :

$$J = \mathbf{e}^H\mathbf{e} + \beta\mathbf{f}^H\mathbf{f} \tag{5.18}$$

where the superscript H denotes the Hermitian of a matrix.

The solution of this minimization problem is given by [14] :

$$\mathbf{f_{reg}} = \left[\mathbf{H}^H\mathbf{H} + \beta\mathbf{I}\right]^{-1}\mathbf{H}^H\hat{\mathbf{p}} \tag{5.19}$$

In Ref. [5], the transfer matrix $\mathbf{H}$ was decomposed in M sub-matrices $\mathbf{H_m}$, each associated with the acoustic radiation $\mathbf{p_m}$ at frequency $mB\Omega$:

$$\mathbf{p_m} = \mathbf{H_m}\mathbf{f_m} \tag{5.20}$$

or :

$$\begin{pmatrix} p_{m1} \\ \vdots \\ p_{mj} \\ \vdots \\ p_{mJ} \end{pmatrix} = \begin{pmatrix} H_{m1\mathtt{w}_{min}^{(m)}} & \cdots & H_{m1\mathtt{w}_{max}^{(m)}} & \cdots & \cdots & H_{m1i\mathtt{w}^{(m)}} & \cdots & \cdots & H_{m1I\mathtt{w}_{max}^{(m)}} \\ \vdots & & \vdots & & & \vdots & & & \vdots \\ H_{mj1\mathtt{w}_{min}^{(m)}} & \cdots & H_{mj1\mathtt{w}_{max}^{(m)}} & \cdots & \cdots & H_{mji\mathtt{w}^{(m)}} & \cdots & \cdots & H_{mjI\mathtt{w}_{max}^{(m)}} \\ \vdots & & \vdots & & & \vdots & & & \vdots \\ H_{mJ1\mathtt{w}_{min}^{(m)}} & \cdots & H_{mJ1\mathtt{w}_{max}^{(m)}} & \cdots & \cdots & H_{mJi\mathtt{w}^{(m)}} & \cdots & \cdots & H_{mJI\mathtt{w}_{max}^{(m)}} \end{pmatrix} \begin{pmatrix} f_{1\mathtt{w}_{min}^{(m)}} \\ \vdots \\ f_{1\mathtt{w}_{max}^{(m)}} \\ \vdots \\ \vdots \\ f_{i\mathtt{w}^{(m)}} \\ \vdots \\ \vdots \\ f_{I\mathtt{w}_{max}^{(m)}} \end{pmatrix} \tag{5.21}$$

The inversion of Eq. (5.21) leads to the lift distribution that generates the acoustic tone at $mB\Omega$. The advantage of this "mono-harmonic" formulation is that one can only select the most contributing circumferential modes $\mathtt{w}^{(m)}$ of the lift around mB ($\mathtt{w}_{min}^{(m)} = mB-2$ to $\mathtt{w}_{max}^{(m)} = mB+2$ for example) to the radiation to the discrete frequency $mB\Omega$. This formulation leads to the inversion of a series of smaller and better conditioned matrices $\mathbf{H_m}$ than $\mathbf{H}$ since only low-order Bessel functions are involved. Each solution vector $\mathbf{f_{reg,m}}$ is given by :

$$\mathbf{f_{reg,m}} = \left[\mathbf{H_m}^H\mathbf{H_m} + \beta_m\mathbf{I}\right]^{-1}\mathbf{H_m}^H\hat{\mathbf{p}}_\mathbf{m} \tag{5.22}$$

Subsequently, these solution vectors $\mathbf{f_{reg,m}}$, each containing a few circumferential modes around mB, are assembled to form the vector containing all the reconstructed circumferential modes. The disadvantage is that M linear systems have to be inverted, thus M regularization parameters have to be chosen.

In the present paper, a "multi-harmonic" formulation is proposed. The matrix $\mathbf{H}$ includes the contribution of all circumferential modes (from $\mathtt{w}_{min} = 1$ to $\mathtt{w}_{max} = 4B + 4$ for example) to the radiation of all discrete acoustic tones $mB\Omega$ (from $m = 1$ to $m = 4$ for example) :

$$\begin{pmatrix} p_{11} \\ \vdots \\ p_{1J} \\ \vdots \\ \vdots \\ p_{mj} \\ \vdots \\ \vdots \\ p_{MJ} \end{pmatrix} = \begin{pmatrix} H_{111\mathtt{w}_{min}} \cdots & H_{111\mathtt{w}_{max}} & \cdots & \cdots & H_{11i\mathtt{w}} & \cdots & \cdots & H_{11I\mathtt{w}_{max}} \\ \vdots & \vdots & & & \vdots & & & \vdots \\ H_{1J1\mathtt{w}_{min}} \cdots & H_{1J1\mathtt{w}_{max}} & \cdots & \cdots & H_{1Ji\mathtt{w}} & \cdots & \cdots & H_{1JI\mathtt{w}_{max}} \\ \vdots & \vdots & & & \vdots & & & \vdots \\ \vdots & \vdots & & & \vdots & & & \vdots \\ H_{mj1\mathtt{w}_{min}} \cdots & H_{mj1\mathtt{w}_{max}} & \cdots & \cdots & H_{mji\mathtt{w}} & \cdots & \cdots & H_{mjI\mathtt{w}_{max}} \\ \vdots & \vdots & & & \vdots & & & \vdots \\ \vdots & \vdots & & & \vdots & & & \vdots \\ H_{MJ1\mathtt{w}_{min}} \cdots & H_{MJ1\mathtt{w}_{max}} & \cdots & \cdots & H_{MJi\mathtt{w}} & \cdots & \cdots & H_{MJI\mathtt{w}_{max}} \end{pmatrix} \begin{pmatrix} f_{1\mathtt{w}_{min}} \\ \vdots \\ f_{1\mathtt{w}_{max}} \\ \vdots \\ \vdots \\ f_{i\mathtt{w}} \\ \vdots \\ \vdots \\ f_{I\mathtt{w}_{max}} \end{pmatrix} \tag{5.23}$$

It leads to a larger and more badly conditioned matrix $\mathbf{H}$ as compared to $\mathbf{H_m}$, since the transfer matrix has a very large coefficient dynamics introduced by the Bessel function, due to non-radiating and efficiently-radiating modes respectively. The advantage of the "multi-harmonic" formulation is that only one linear system has to be inverted (The solution is given by Eq. (5.19)), thus one has to chose a single regularization parameter to reconstruct all modes (from $\mathtt{w}_{min}$ to $\mathtt{w}_{max}$).

Replacing $\mathbf{H}$ by $\mathbf{Z}$ and $\mathbf{f_{reg}}$ by $\mathbf{v_{reg}}$ in Eq. (5.19) leads to the regularized solution of the inverse problem in terms of the inflow velocity :

$$\mathbf{v_{reg}} = \left[\mathbf{Z}^H\mathbf{Z} + \beta\mathbf{I}\right]^{-1}\mathbf{Z}^H\hat{\mathbf{p}} \tag{5.24}$$

5.4.2 Stability of the regularized solution

In order to evaluate the stability of the solution, the discrete Picard condition [14] is considered. To introduce this condition, the singular value decomposition (SVD) of a generic matrix $\mathbf{A} \in \mathbb{Z}^{M \times N}$ is performed for an overdetermined system ($M \geq N$) so that the solution of the inverse problem is unique :

$$\mathbf{A} = \mathbf{U}\boldsymbol{\Sigma}\mathbf{V}^T = \sum_{n}^{N} \mathbf{u_n} \sigma_n \mathbf{v_n^T} \tag{5.25}$$

where $\mathbf{U} = (\mathbf{u_1}, ..., \mathbf{u_N}) \in \mathbb{Z}^{M \times N}$ is the matrix of the left singular vectors of $\mathbf{A}$ and $\mathbf{V} = (\mathbf{v_1}, ..., \mathbf{v_N}) \in \mathbb{Z}^{N \times N}$ is the matrix of the right singular vectors of $\mathbf{A}$. The columns of matrices $\mathbf{U}$ and $\mathbf{V}$ are orthonormal, $\mathbf{U^T U} = \mathbf{V^T V} = \mathbf{I_N}$, where $\mathbf{I_N}$ is the $N \times N$ identity matrix, and the diagonal matrix $\boldsymbol{\Sigma} = \text{diag}(\sigma_1, ..., \sigma_N)$ contains the non-negative singular values in decreasing order.

The regularized Tikhonov solution of the generic linear system $\mathbf{A}\boldsymbol{\phi} = \boldsymbol{\psi}$ can be expressed in terms of the SVD of the matrix $\mathbf{A}$ [14] :

$$\boldsymbol{\phi}_{reg} = \sum_{n=1}^{N} \sigma_n \frac{\mathbf{u_n^T}\boldsymbol{\psi}}{\sigma_n^2 + \beta} \mathbf{v_n} \tag{5.26}$$

From Eq. (5.26), it can be seen that the regularization parameter β has a stabilizing effect by avoiding the division by particularly small singular values σ_n. Moreover, the discrete Picard condition states that the coefficients $|\mathbf{u_n}^T \boldsymbol{\psi}|$ must decay faster to zero than the singular values σ_n to obtain a stable regularized solution [14]. If the Picard condition is not satisfied, the reconstructed solution will significantly deviate from the exact solution, even if a regularization technique has been used. This is of fundamental importance for choosing the optimal regularization parameter. Replacing $\mathbf{A}$ by $\mathbf{H}$ or $\mathbf{Z}$ in Eq. (5.25) leads respectively to the SVD of the lift and velocity aeroacoustic transfer matrix. Moreover, replacing $\boldsymbol{\psi}$ by $\hat{\mathbf{p}}$ and $\boldsymbol{\phi}_{reg}$ by $\mathbf{f_{reg}}$ or $\mathbf{v_{reg}}$ in Eq. (5.26) leads to the regularized solution in terms of the SVD of the lift and the inflow velocity, respectively.

5.4.3 Choosing the regularization parameter

The crucial point of the regularization is the choice of the regularization parameter β. The L-curve corner criterion is one of the most classically used techniques [5] [14]. The L-curve consists of plotting the 2-norm $\eta(\beta) = \log \|\mathbf{f_{reg}}\|$ of the regularized solution versus the residual 2-norm $\zeta(\beta) = \log \|\hat{\mathbf{p}} - \mathbf{H}\mathbf{f_{reg}}\|$, corresponding to various values of β. An ideal L-curve is plotted in Fig. 5.2-a from a simulated acoustic pressure vector $\hat{\mathbf{p}}$ with a very large signal to noise ratio (60 dB). The L-curve (Fig. 5.2-a) can be decomposed into two regions : (1) for small β (part of the L-curve above the corner), the regularized solution is dominated by the effects of errors in the input data (such as measurement noise in the acoustic pressures $\hat{\mathbf{p}}$), the solution is under-regularized and (2) for large β (part of the curve on the right side of the corner), the solution is over-regularized, leading to excessive residual error. In between these two regions, an optimal regularization parameter can be found at the corner, for which there is a trade-off between under- and over-regularization. The corner is selected as the point of maximum curvature of the L-curve (Fig. 5.2-b). The curvature is defined as [14] :

$$\kappa(\beta) = \frac{\zeta'\eta'' - \zeta''\eta'}{\{(\zeta')^2 + (\eta')^2\}^{3/2}} \tag{5.27}$$

where differentiation (') is with respect to β.

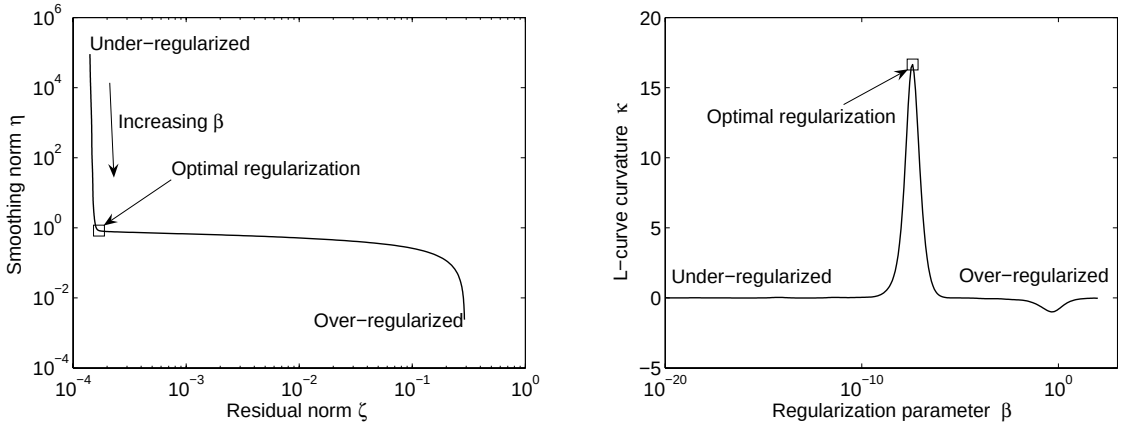

(a) L-curve

(b) L-curve curvature

Figure 5.2 L-curve and its curvature for a large S/N ratio (60 dB)

When realistic measurement noise is present in the acoustic pressure vector $\hat{\mathbf{p}}$, it is difficult to clearly identify the corner of the L-curve and the curvature plot can exhibit more than one maximum. In such a case, a local maximum is chosen from the curvature plot, with the help of

the discrete Picard condition, to eliminate under or over-regularized solutions, as discussed in the following section.

5.5 Experimental results

The aim of this section consists of identifying the lift source term $\mathbf{f}$ and the velocity source term $\mathbf{v}$ from a set of sound pressure measurement points $\hat{\mathbf{p}}$. The Tikhonov regularization technique is used to stabilize the inversion of the linear systems given by Eqs. (5.13) and (5.17). The regularization parameters are chosen by using the analysis tools presented in Section 5.4.

5.5.1 Experimental set-up

The experiments were conducted on a 6-bladed automotive engine cooling fan with equal blade pitches. The case considered in this section demonstrates the capability of the inverse model to experimentally qualitatively reconstruct the circumferential variation of blade loading during the rotation of the propeller : a triangular obstruction was added between two vanes of the stator (see Fig. 5.9-a). This obstruction covers a 34° angular section and strongly interacts with the rotor. As shown below, such an obstruction significantly modifies the tonal radiation of the fan. The objective of the inverse model is to pinpoint the lift fluctuation and the inflow velocity variation associated to such an obstruction.

The fan has an exterior diameter of 30 cm and a central hub of 12.5 cm in diameter. The rotational speed of the fan is set to 48.5 Hz (2910 RPM). Measurements were carried out in an anechoic room to respect the free field radiation condition. Since the radiated acoustic tones are stationary, the measurements were recorded using only four microphones : a reference microphone located at 1.8 m in the upstream axial direction of the fan and three scanning microphones spaced on a 1.8 m radius downstream half circle in directions $\alpha = 0°, 20°, 40°, 55°, 70°$. The three scanning microphones are then moved by increments of $\Delta\varphi = 45°$ in the circumferential direction to generate $J = 33$ acoustic measurement locations. The averaged auto-spectra of the scanning microphone signals provide the magnitude of the sound pressure and the averaged cross-spectra between the reference and the scanning microphones signals provide the phase of the sound pressure relative to the reference microphone. The measurements were restricted to the blade passage frequency (BPF = 291 Hz) and its first three harmonics ($M = 4$). The far-field condition is respected for a 1.8 m radius hemispheric surface since this radius is larger than the largest wavelength of interest (1.17 m) and larger than the diameter of the fan (30 cm). A sampling frequency of 4000Hz is large enough to sense acoustic pressures up to the highest frequency of interest and the spectral resolution is 2.5 Hz. Moreover, 50 linear averages per measurement point were carried out.

As the discretization of the fan is concerned, $I = 3$ circles located at radii $R_1 = 7$ cm, $R_2 = 10.5$ cm and $R_3 = 14$ cm were chosen. The minimum circumferential harmonic is $\mathtt{w}_{min} = 1$ and the maximum circumferential harmonic is $\mathtt{w}_{max} = 32$. Thus, the number of unknowns in Eqs. (5.13) and (5.17) is $(\mathtt{w}_{max} - \mathtt{w}_{min} + 1) \times I = 96$ and the number of equation is $J \times M = 132$. The linear systems are thus over-determined. The condition numbers of the matrices $\mathbf{H}$ and $\mathbf{Z}$ are $\text{cond}(\mathbf{H}) = \sigma_1/\sigma_{96} = 1.7 \times 10^{13}$ and $\text{cond}(\mathbf{Z}) = \sigma_1/\sigma_{96} = 1.66 \times 10^{12}$, which indicate that the transfer matrices $\mathbf{H}$ and $\mathbf{Z}$, relating respectively the unsteady lift and the non-uniform inflow velocity to the radiated sound field, are poorly conditioned.

5.5.2 Choosing the regularization parameter

In order to choose the regularization parameter, the L-curve and its curvature are first plotted. Two regularization parameters corresponding to different local maxima of the curvature are chosen. The selected values of β are then inserted into Eq. (5.26) and the Picard condition relating $|\mathbf{u_n^T \hat{p}}|$ and σ_n is analyzed. In the following, the left superscripts (lift) and (vel) refer to the lift reconstruction and to the non-uniform inflow velocity reconstruction respectively.

Unsteady lift reconstruction

In the case of the lift reconstruction, the L-curve and its curvature are plotted in Figs. 5.3-a and 5.3-b. The corner of the L-curve is difficult to precisely locate and its curvature exhibits a number of local maxima. The regularization parameter corresponding to the maximum of curvature of the L-curve is ${}^{\text{lift}}\beta_1 = 3 \times 10^{-6}$ and the regularization parameter corresponding to the last local maximum curvature is ${}^{\text{lift}}\beta_2 = 3.6 \times 10^{-3}$. In Figs. 5.4 and 5.5, the singular values (dots) located to the left of the vertical line correspond to the squared singular values larger than the regularization parameter ${}^{\text{lift}}\beta_1$ and ${}^{\text{lift}}\beta_2$ respectively. The regularization has a negligible impact on the contribution of these singular values. The singular values located to the right of the vertical line correspond to the squared singular values smaller than the regularization parameter. These singular values are dampened by the regularization. To illustrate the dampening of the singular values, the term $\frac{|{}^{\mathbf{lift}}\mathbf{u_n^T \hat{p}}|}{{}^{\text{lift}}\sigma_n}$ (open circles), corresponding to a non-regularized problem is compared to the term ${}^{\text{lift}}\sigma_n \frac{|{}^{\mathbf{lift}}\mathbf{u_n^T \hat{p}}|}{{}^{\text{lift}}\sigma_n^2+\beta}$ (stars), corresponding to the regularized problem. For the low-order singular values, the open circles and the stars are superimposed, which means that these first singular values are unaffected by the regularization. When the squared singular values are close to the regularization parameter β, the stars start to deviate from the open circles, which means that these singular values are slightly dampened by the regularization parameter. Finally, for the high order singular values, the terms $\frac{|{}^{\mathbf{lift}}\mathbf{u_n^T \hat{p}}|}{{}^{\text{lift}}\sigma_n}$ increase and the terms ${}^{\text{lift}}\sigma_n \frac{|{}^{\mathbf{lift}}\mathbf{u_n^T \hat{p}}|}{{}^{\text{lift}}\sigma_n^2+\beta}$ decrease, which means that the sum in Eq. (5.26) will diverge if no regularization is applied. For the discrete Picard condition to be satisfied, the coefficients $|{}^{\mathbf{lift}}\mathbf{u_n^T \hat{p}}|$ (crosses) must decrease faster than the singular values ${}^{\text{lift}}\sigma_n$ (dots) i.e. the term $\frac{|{}^{\mathbf{lift}}\mathbf{u_n^T \hat{p}}|}{{}^{\text{lift}}\sigma_n}$ (open circles) should decrease. Therefore, the

regularization parameter has to be chosen such that the singular values that do not satisfy the discrete Picard condition are sufficiently dampened. Replacing β by ${}^{\text{lift}}\beta_1 = 3 \times 10^{-6}$ in the term ${}^{\text{lift}}\sigma_n \frac{|{}^{\text{lift}}\mathbf{u_n^T}\hat{\mathbf{p}}|}{{}^{\text{lift}}\sigma_n^2+\beta}$ of Eq. (5.26) leads to less singular values affected by the regularization parameter (${}^{\text{lift}}\beta_1 < {}^{\text{lift}}\sigma_n^2$ for $n < 59$, Fig. 5.4) than replacing β by ${}^{\text{lift}}\beta_2 = 3.6 \times 10^{-3}$ (${}^{\text{lift}}\beta_2 < {}^{\text{lift}}\sigma_n^2$ for $n < 22$, Fig. 5.5). Choosing ${}^{\text{lift}}\beta_2$ leads to dampen all the singular values for which the discrete Picard condition is not satisfied, whereas many singular values that do not satisfy the discrete Picard condition are unaffected by the regularization parameter ${}^{\text{lift}}\beta_1$. Thus, the best regularization parameter is ${}^{\text{lift}}\beta_2$ *a priori*.

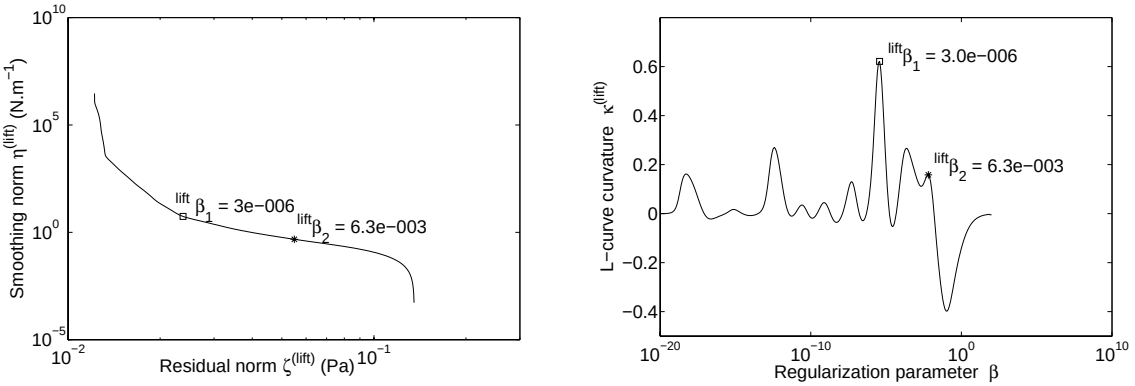

(a) L-curve

(b) L-curve curvature

Figure 5.3 L-curve and its curvature - Unsteady lift reconstruction

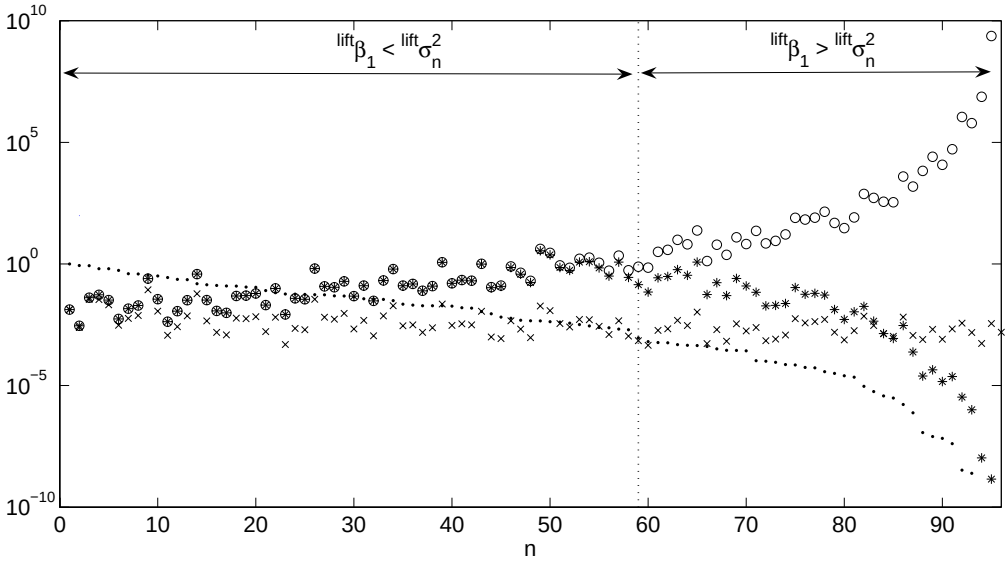

Figure 5.4 The singular values ${}^{\text{lift}}\sigma_n$ (dots), coefficients $|{}^{\text{lift}}\mathbf{u_n^T}\hat{\mathbf{p}}|$ (crosses), coefficients $|{}^{\text{lift}}\mathbf{u_n^T}\hat{\mathbf{p}}|/{}^{\text{lift}}\sigma_n$ (open circles) and ${}^{\text{lift}}\sigma_n \frac{|{}^{\text{lift}}\mathbf{u_n^T}\hat{\mathbf{p}}|}{{}^{\text{lift}}\sigma_n^2+{}^{\text{lift}}\beta_1}$ (stars) - Lift reconstruction, ${}^{\text{lift}}\beta_1 = 3 \times 10^{-6}$.

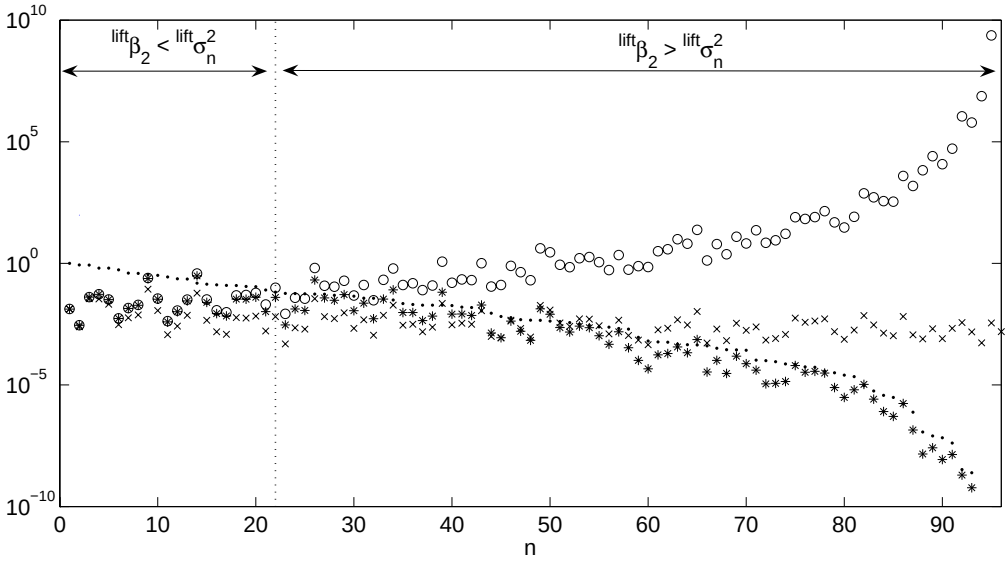

Figure 5.5 The singular values ${}^{\text{lift}}\sigma_n$ (dots), coefficients $|{}^{\text{lift}}\mathbf{u_n^T}\hat{\mathbf{p}}|$ (crosses), coefficients $|{}^{\text{lift}}\mathbf{u_n^T}\hat{\mathbf{p}}|/{}^{\text{lift}}\sigma_n$ (open circles) and ${}^{\text{lift}}\sigma_n \frac{|{}^{\text{lift}}\mathbf{u_n^T}\hat{\mathbf{p}}|}{{}^{\text{lift}}\sigma_n^2 + {}^{\text{lift}}\beta_2}$ (stars) - Lift reconstruction, ${}^{\text{lift}}\beta_2 = 6.3 \times 10^{-3}$.

Non-uniform inflow velocity reconstruction

In the case of the velocity reconstruction, the L-curve and its curvature are plotted in Figs. 5.6-a and 5.6-b. The corner of the L-curve is difficult to precisely locate and its curvature exhibits a number of local maxima. However, contrary to the L-curve curvature associated to the lift reconstruction (Fig. 5.3-b), the maximum of curvature of the L-curve corresponds to the last local maximum, corresponding to ${}^{\text{vel}}\beta_2 = 4.9 \times 10^{-2}$. Another regularization parameter, ${}^{\text{vel}}\beta_1 = 1.7 \times 10^{-5}$, corresponding to the previous local maximum is chosen to illustrate the effect of the choice of the regularization parameter on the velocity reconstruction. In Figs. 5.7 and 5.8, the singular values (dots) located to the left of the vertical line correspond to the squared singular values larger than the regularization parameter ${}^{\text{vel}}\beta_1$ and ${}^{\text{vel}}\beta_2$ respectively. The regularization has a negligible impact on the contribution of these singular values. The singular values located to the right of the vertical line correspond to the squared singular values smaller than the regularization parameter. These singular values are dampened by the regularization. Replacing β by ${}^{\text{vel}}\beta_1 = 1.7 \times 10^{-5}$ in the term ${}^{\text{vel}}\sigma_n \frac{|{}^{\text{vel}}\mathbf{u_n^T}\hat{\mathbf{p}}|}{{}^{\text{vel}}\sigma_n^2 + \beta}$ of Eq. (5.26) (stars in Figs. 5.7 and 5.8) leads to less singular values affected by the regularization parameter (${}^{\text{vel}}\beta_1 < {}^{\text{vel}}\sigma_n^2$ for $n < 54$, Fig. 5.7) than replacing β by ${}^{\text{vel}}\beta_2 = 4.9 \times 10^{-2}$ (${}^{\text{vel}}\beta_2 < {}^{\text{vel}}\sigma_n^2$ for $n < 17$, Fig. 5.8). Choosing ${}^{\text{vel}}\beta_2$ leads to dampen all the singular values for which the discrete Picard condition is not satisfied ($\frac{|{}^{\text{vel}}\mathbf{u_n^T}\hat{\mathbf{p}}|}{{}^{\text{vel}}\sigma_n}$ not decreasing, open circles in Figs. 5.7 and 5.8), whereas many singular values that do not satisfy the discrete Picard condition are unaffected by the regularization parameter ${}^{\text{lift}}\beta_1$. Thus, the best regularization parameter is ${}^{\text{vel}}\beta_2$ *a priori*.

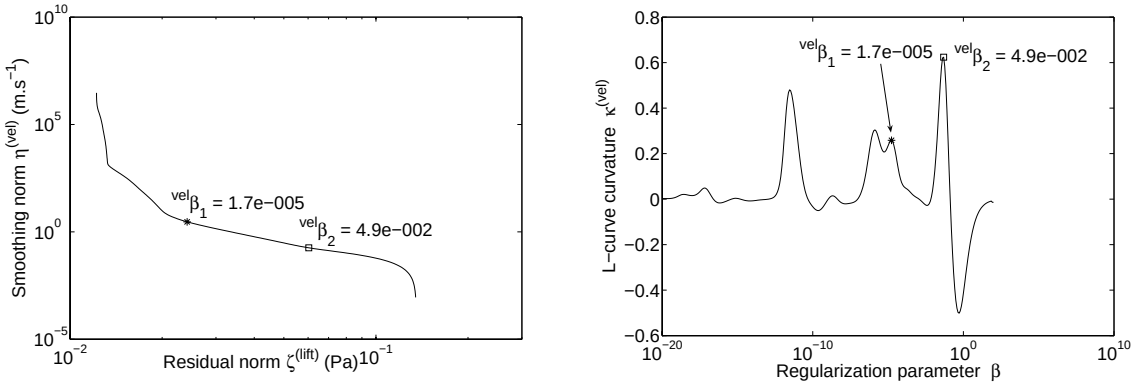

(a) L-curve

(b) L-curve curvature

Figure 5.6 L-curve and its curvature - Non-uniform inflow velocity reconstruction

In both cases (lift and velocity reconstructions), the "*a priori*" optimal regularization parameter corresponds to the last local maximum of the L-curve curvature.

5.5.3 Unsteady lift and non-uniform inflow velocity reconstructions

The reconstruction of unsteady lift and non-uniform inflow velocity is presented in this section. In order to study the influence of the regularization parameter on the reconstruction, the reconstructed lift using ${}^{\text{lift}}\beta_1$ is compared to the reconstructed lift using ${}^{\text{lift}}\beta_2$ and the reconstructed velocity using ${}^{\text{vel}}\beta_1$ is compared to the reconstructed velocity using ${}^{\text{vel}}\beta_2$.

Unsteady lift reconstruction

The spatial reconstruction of the unsteady lift is superimposed to a photograph of the fan under investigation in Figs. 5.9-a and 5.9-b. When ${}^{lift}\beta_1 = 3 \times 10^{-6}$ is used in the regularization, the obstruction cannot be located by the inverse problem (Fig. 5.9-a) but when ${}^{lift}\beta_2 = 3.6 \times 10^{-3}$ is chosen, it is possible to locate a lift fluctuation near the obstruction (Fig. 5.9-b). Moreover, when ${}^{lift}\beta_1$ is chosen, the magnitude of the solution is ten times larger than the magnitude of the solution when ${}^{lift}\beta_2 = 3.6 \times 10^{-3}$ is chosen. Therefore, ${}^{lift}\beta_1 = 3 \times 10^{-6}$ leads to an under-regularized solution. When ${}^{lift}\beta_2 = 3.6 \times 10^{-3}$, the regularized solution shows that a blade experiences a negative lift when passing through the obstruction zone while positive lifts are observed when a blade enters or quits the obstruction zone. The lift fluctuations outside the obstruction can be partly attributed to the interaction between the rotor and the stator vanes. These fluctuations can also partly originate from the truncation of the sum over the circumferential order `w` in Eq. (5.10) and errors in the reconstruction of certain circumferential lift modes. As already noted [5], very-low order circumferential modes are not properly reconstructed since

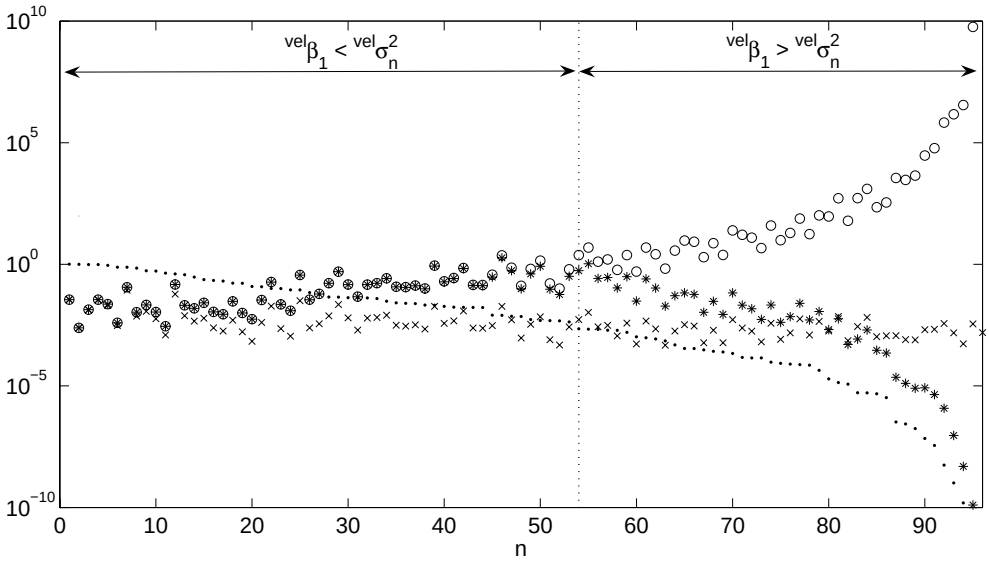

Figure 5.7 The singular values $^{\text{vel}}\sigma_n$ (dots), coefficients $|^{\text{vel}}\mathbf{u_n^T}\hat{\mathbf{p}}|$ (crosses), coefficients $|^{\text{vel}}\mathbf{u_n^T}\hat{\mathbf{p}}|/^{\text{vel}}\sigma_n$ (open circles) and $^{\text{vel}}\sigma_n \frac{|^{\text{vel}}\mathbf{u_n^T}\hat{\mathbf{p}}|}{^{\text{vel}}\sigma_n^2 + {}^{\text{vel}}\beta_1}$ (stars) - Non-uniform inflow reconstruction, $^{\text{vel}}\beta_1 = 1.7 \times 10^{-5}$.

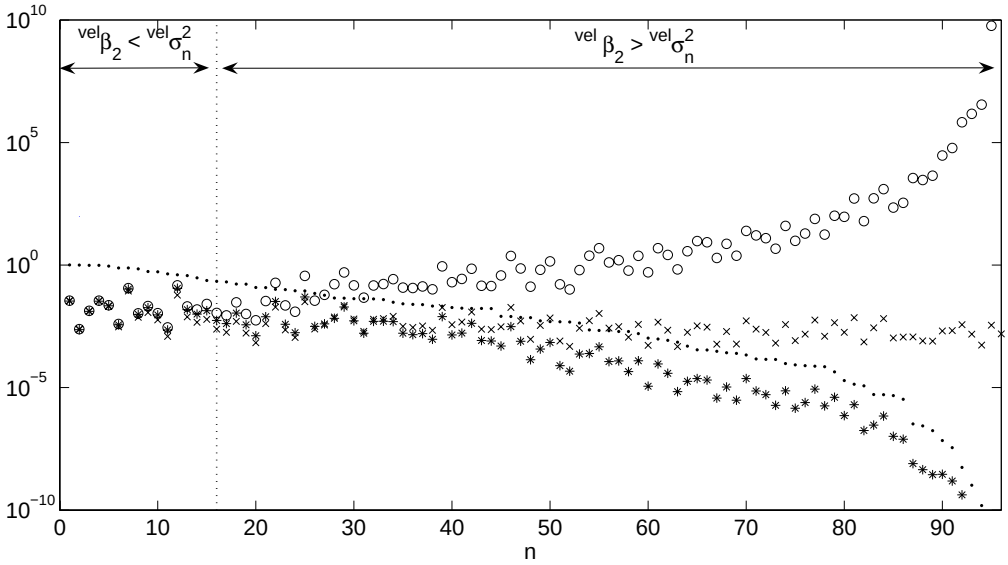

Figure 5.8 The singular values $^{\text{vel}}\sigma_n$ (dots), coefficients $|^{\text{vel}}\mathbf{u_n^T}\hat{\mathbf{p}}|$ (crosses), coefficients $|^{\text{vel}}\mathbf{u_n^T}\hat{\mathbf{p}}|/^{\text{vel}}\sigma_n$ (open circles) and $^{\text{vel}}\sigma_n \frac{|^{\text{vel}}\mathbf{u_n^T}\hat{\mathbf{p}}|}{^{\text{vel}}\sigma_n^2 + {}^{\text{vel}}\beta_2}$ (stars) - Non-uniform inflow reconstruction, $^{\text{vel}}\beta_2 = 4.9 \times 10^{-2}$.

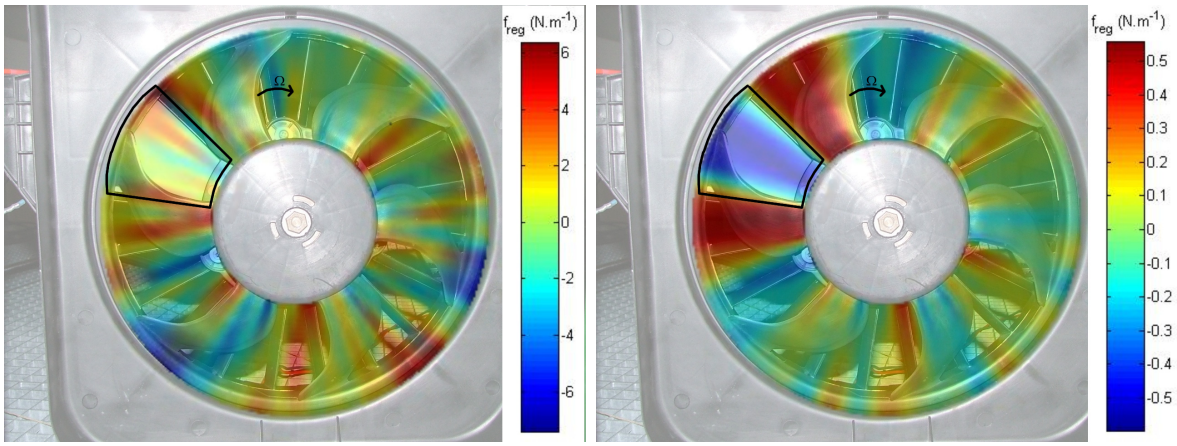

(a) Spatial unsteady lift, ${}^{lift}\beta_1 = 3 \times 10^{-6}$

(b) Spatial unsteady lift, ${}^{lift}\beta_2 = 3.6 \times 10^{-3}$

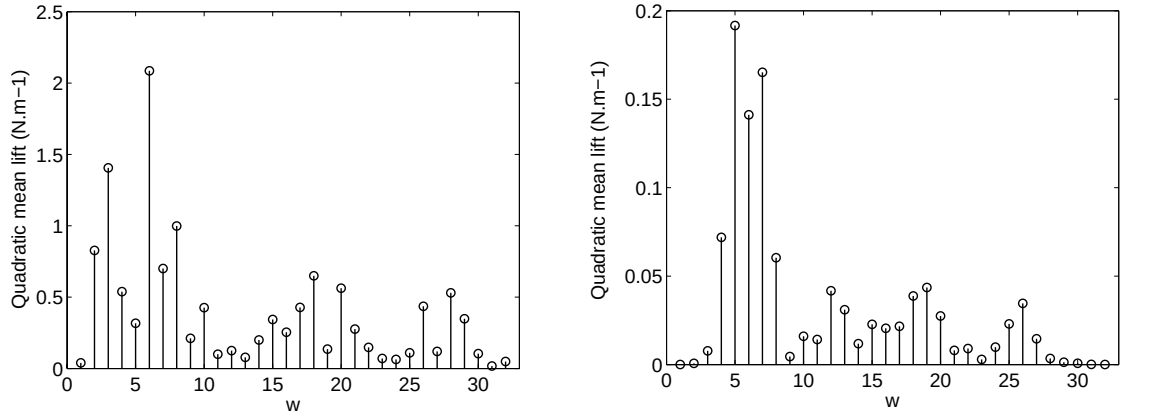

(c) Spectral unsteady lift, ${}^{lift}\beta_1 = 3 \times 10^{-6}$

(d) Spectral unsteady lift, ${}^{lift}\beta_2 = 3.6 \times 10^{-3}$

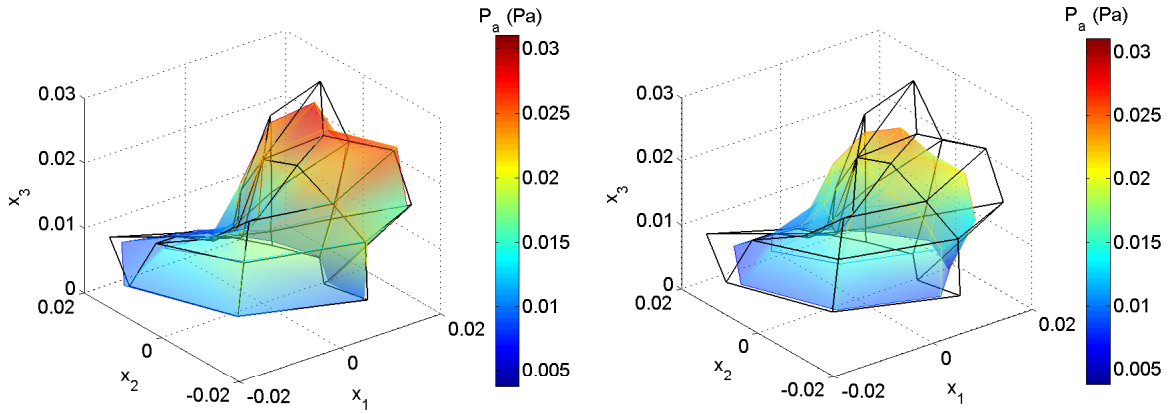

(e) BPF directivity, ${}^{lift}\beta_1 = 3 \times 10^{-6}$

(f) BPF directivity, ${}^{lift}\beta_2 = 3.6 \times 10^{-3}$

Figure 5.9 Left-hand column : regularization parameter ${}^{lift}\beta_1 = 3 \times 10^{-6}$. Right-hand column : regularization parameter ${}^{lift}\beta_2 = 3.6 \times 10^{-3}$. a and b : spatial unsteady lift, c and d : spectral unsteady lift, e and f : BPF acoustic directivity

Tableau 5.1 Comparison of the root mean square of the regularized lift modes $\bar{f}_{reg}(mB)|_{\text{lift}}\beta_1$ and $\bar{f}_{reg}(mB)|_{\text{lift}}\beta_2$ to the magnitude of the estimated lift modes $\|f_{est}(mB)\|$, calculated from Eq.(5.28)

mB	6	12	18	24
$\bar{f}_{reg}(mB)\|_{\text{lift}}\beta_1$, $N.m^{-1}$	2.089	0.137	0.653	0.064
$\bar{f}_{reg}(mB)\|_{\text{lift}}\beta_2$, $N.m^{-1}$	0.138	0.035	0.036	$9.6.10^{-3}$
$\|f_{est}(mB)\|$, $N.m^{-1}$	0.218	0.033	0.032	$9.0.10^{-3}$

their contribution to the tonal noise is negligible for a 6-bladed rotor. The lift fluctuation near the obstruction is qualitatively different from the unsteady blade forces reconstructions presented in Ref. [109], which can be explained by the differences in the formulation of the direct problems, as discussed in section 5.3.3. In Ref. [109], M "mono-harmonic" sub-matrices were inverted and the tangential forces related to the drag were neglected. In this paper, a single "multi-harmonic" matrix is inverted and both axial and tangential forces are taken into account in the model.

The spectral content of the unsteady lift is shown in Figs. 5.9-c and 5.9-d, where the root mean square of the spectral unsteady lift averaged over the radius, defined as $\bar{f}_{reg}(\mathtt{w}) = \sqrt{\frac{\sum_i^I f_{i\mathtt{w}} f_{i\mathtt{w}}^*}{I}}$ is plotted versus the Fourier circumferential order $\mathtt{w}$. The choice of ${}^{lift}\beta_1 = 3 \times 10^{-6}$ also leads to larger reconstructed magnitudes (Fig. 5.9-c) than choosing the regularization parameter ${}^{\text{lift}}\beta_2 = 3.6 \times 10^{-3}$ (Fig. 5.9-d). The choice of ${}^{\text{lift}}\beta_2 = 3.6 \times 10^{-3}$ has the effect of filtering out certain unsteady lift modes at the ends of the spectrum (Fig. 5.9-d). The regularization filters out the modes associated to the smallest singular values, which correspond to the least radiating modes. A larger regularization will dampen more singular values thus filtering out more components in the lift spectrum.

The circumferential mode $\mathtt{w} = mB$ is the most radiating mode at pulsation $mB\Omega$. Furthermore, it is the only mode that radiates sound in the axial direction ($\alpha = 0$) due to the 0^{th} order Bessel function in Eq. (5.4) when $\mathtt{w} = mB$. Thus, if one is interested to reconstruct only these most radiating modes, a single microphone can be located in the axial direction. Replacing the acoustic field point coordinate $\mathbf{x} = (r, \phi, \alpha) = (r, 0, 0)$, using the relation $\mathtt{w} = mB$ in Eq.(5.4) and assuming that the lift per unit span $F'(\mathtt{w}, R)$ is constant along the span, leads to an estimate of the mB^{th} order mean lift per unit span :

$$f_{est}(mB) = i\frac{4\pi r \left[P_a(r, 0, 0; mB\Omega)\right]_{mB,m}}{k_0 B e^{ik_0 r} \cos\gamma (R_T - R_H)} \tag{5.28}$$

Table A.1 shows the magnitude of the estimated mean lift modes $\|f_{est}(mB)\|$ of order mB

$(1 \leq m \leq 4)$ from Eq.(5.28), compared to the root mean square of the regularized lift modes $\bar{f}_{reg}(mB)|_{^{\text{lift}}\beta_1}$ and $\bar{f}_{reg}(mB)|_{^{\text{lift}}\beta_2}$. The lift magnitude of the modes mB given by the Eq.(5.28) is comparable to the magnitude given by the regularized inverse problem when $^{\text{lift}}\beta_2$ is chosen. When $^{\text{lift}}\beta_1$ is used, the regularized solutions are more than four times larger than the estimated $\bar{f}_{mB}$.

Thus, the choice of an *a priori* optimal regularization parameter $^{\text{lift}}\beta_2$ from the curvature of the L-curve and the discrete Picard condition, has then been validated by a qualitative localization of the lift fluctuations associated to the obstruction and a quantitative estimation of the lift associated to the most radiating modes mB $(1 \leq m \leq 4)$.

Finally, Figs. 5.9-e and 5.9-f show the extrapolated acoustic radiation directivity from the regularized solution $\mathbf{p} = \mathbf{H}\mathbf{f}_{\mathbf{reg}}$ (solid surface) and the measured acoustic radiation directivity $\hat{\mathbf{p}}$ (mesh surface) at the blade passage frequency (291 Hz). The largest regularization parameter $^{lift}\beta_2$ results in a less accurate acoustic field extrapolation at the blade passage frequency (Fig. 5.9-e). This can also be seen in the L-curve (Fig. 5.3-a), where the residual norm $\zeta^{(lift)}$ is smaller when choosing $^{lift}\beta_1$ rather than $^{lift}\beta_2$. This illustrates the trade-off between a small smoothing norm and a small residual norm.

Non-uniform inflow velocity reconstructions

In order to study the influence of the regularization parameter on the reconstruction, the reconstructed velocities and the reconstructed acoustic directivity are shown in Fig. 5.10. The left and right graphs correspond respectively to $^{\text{vel}}\beta_1 = 1.7 \times 10^{-5}$ and $^{\text{vel}}\beta_2 = 4.9 \times 10^{-2}$.

The spatial reconstruction of the non-uniform inflow velocity is superimposed to a photograph of the fan under investigation in Figs. 5.10-a and 5.10-b. For $^{\text{vel}}\beta_1 = 1.7 \times 10^{-5}$, the obstruction cannot be located by the inverse problem (Fig. 5.10-a) but for $^{\text{vel}}\beta_2 = 4.9 \times 10^{-2}$ it is possible to locate a velocity variation near the obstruction (Fig. 5.10-b). The magnitude of the reconstructed solutions is twelve times larger for $^{\text{vel}}\beta_1$ than for $^{vel}\beta_2$. Moreover, the fluctuations of the inflow velocity (Fig. 5.10-b) are phase-shifted from the fluctuations of the lift (Fig. 5.9-b) near the obstruction. This can be attributed to the complex Sears function in the transfer matrix $\mathbf{Z}$ that shifts the phase between the lift and the gust. The velocity variations outside the influence zone of the obstruction can be partly attributed to the interaction between the rotor and the stator vanes and to errors in the reconstruction of certain modes or truncation of the sum over the circumferential `w` in Eq. (5.14).

(a) Spatial non-uniform inflow velocity, ${}^{vel}\beta_1 = 1.7 \times 10^{-5}$

(b) Spatial non-uniform inflow velocity, ${}^{vel}\beta_2 = 4.9 \times 10^{-2}$

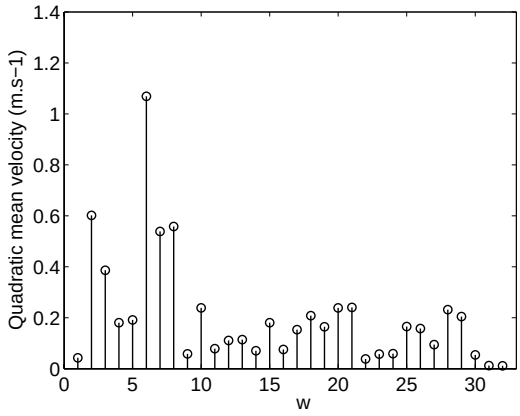

(c) Spectral non-uniform inflow velocity, ${}^{vel}\beta_1 = 1.7 \times 10^{-5}$

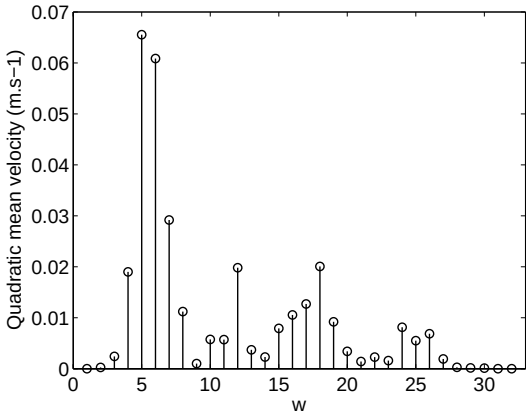

(d) Spectral non-uniform inflow velocity, ${}^{vel}\beta_2 = 4.9 \times 10^{-2}$

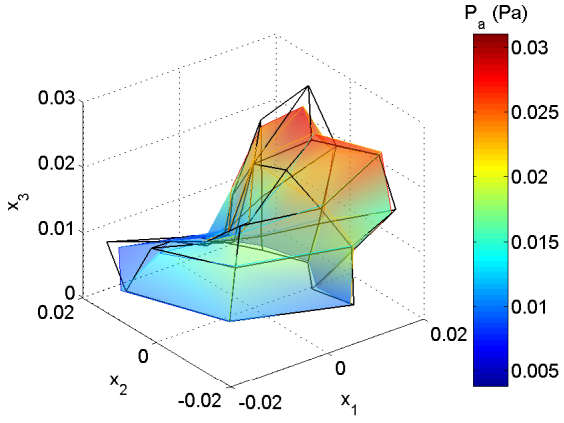

(e) BPF directivity, ${}^{vel}\beta_1 = 1.7 \times 10^{-5}$

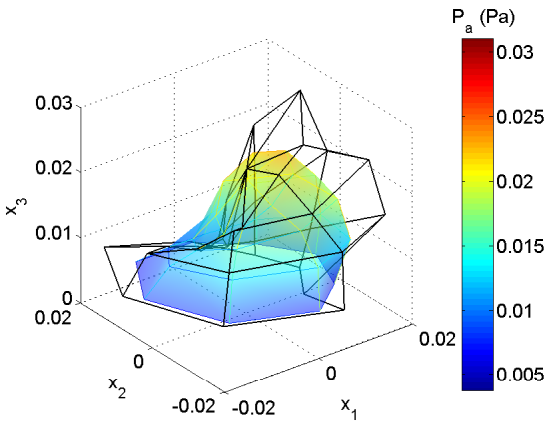

(f) BPF directivity, ${}^{vel}\beta_2 = 4.9 \times 10^{-2}$

Figure 5.10 Left-hand column : regularization parameter ${}^{\text{vel}}\beta_1 = 1.7 \times 10^{-5}$. Right-hand column : regularization parameter ${}^{\text{vel}}\beta_2 = 4.9 \times 10^{-2}$. a and b : spatial inflow velocity, c and d : spectral inflow velocity, e and f : BPF acoustic directivity

Tableau 5.2 Comparison of the root mean square of the regularized velocity modes $\bar{v}_{reg}(mB)|_{^{\text{vel}}\beta_1}$ and $\bar{v}_{reg}(mB)|_{^{\text{vel}}\beta_2}$ to the magnitude of the estimated velocity modes $\|v_{est}(mB)\|$, calculated from Eq.(5.29)

mB	6	12	18	24
$\bar{v}_{reg}(mB)\|_{^{\text{vel}}\beta_1}$, $m.s^{-1}$	1.069	0.100	0.209	0.059
$\bar{v}_{reg}(mB)\|_{^{\text{vel}}\beta_2}$, $m.s^{-1}$	0.0611	0.020	0.020	$8.2.10^{-3}$
$\|v_{est}(mB)\|$, $m.s^{-1}$	0.111	0.024	0.028	$9.1.10^{-3}$

The spectral content of the inflow velocity is shown in Figs. 5.10-c and 5.10-d, where the root mean square of the non-uniform inflow velocity averaged over the radius, defined as $\bar{v}_{reg}(\mathtt{w}) = \sqrt{\frac{\sum_i^I v_{i\mathtt{w}} v_{i\mathtt{w}}^*}{I}}$ is plotted versus the Fourier circumferential order $\mathtt{w}$. As already noted for the lift reconstruction, the largest regularization parameter leads to more inflow velocity modes filtered out (more singular values are dampened).

The mode $\mathtt{w} = mB$ is also the most radiating velocity mode at pulsation $mB\Omega$. Similarly to Section 5.5.3, replacing the acoustic field point coordinate $\mathbf{x} = (r, \phi, \alpha) = (r, 0, 0)$, inserting Eq. (5.5) into Eq.(5.4), using the compressible Sears function defined in Eq. (5.8), using the relation $\mathtt{w} = mB$ in Eq.(5.4) and assuming that the inflow velocity $v(\mathtt{w}, R)$ is constant along the blade span, leads to an estimate of the mB^{th} order mean velocity :

$$v_{est}(mB) = i\frac{4r\left[P_a(r,0,0;mB\Omega)\right]_{mB,m}}{\rho_0 CU(\frac{R_H+R_T}{2})S_c(\sigma_\theta)k_0 B e^{ik_0 r}\cos\gamma(R_T - R_H)} \tag{5.29}$$

Table 5.2 shows the magnitudes of the estimated velocity modes $\|v_{est}(mB)\|$ of order mB ($1 \leq m \leq 4$) from Eq. (5.29), compared to root mean square of the regularized lift modes $\bar{v}_{reg}(mB)|_{^{\text{vel}}\beta_1}$ and $\bar{v}_{reg}(mB)|_{^{\text{vel}}\beta_2}$. The velocity magnitude of the modes mB given by the Eq.(5.29) is nearly the same as the magnitude given by the regularized inverse problem when $^{\text{vel}}\beta_2$ is used but important deviations are observed when $^{\text{vel}}\beta_1$ is chosen.

Therefore, as already noted for the unsteady lift reconstruction, the last local maximum of the L-curve curvature (Fig. 5.6-b) corresponds to the optimal regularization parameter in the experimental cases shown in this paper. First, the choice of $^{\text{vel}}\beta_2$ leads to dampen the singular values that do not satisfy the discrete Picard condition. Subsequently, the velocity variations associated to the obstruction are clearly visible when choosing $^{\text{vel}}\beta_2$. Finally, quantitative estimations of the mB^{th} order mean velocity from a "well-posed problem" (Eq. (5.29)) confirm *a posteriori* that the choice of the regularization parameter $^{\text{vel}}\beta_2$ is optimal.

Finally, Figs. 5.10-e and 5.10-f show the extrapolated acoustic radiation directivities from the regularized solution $\mathbf{p} = \mathbf{Z}\mathbf{v}_{\mathbf{reg}}$ (solid surface) and the measured acoustic radiation directivity $\hat{\mathbf{p}}$ (mesh surface) at the blade passage frequency (291 Hz). The largest regularization parameter ${}^{\text{vel}}\beta_2$ gives a less precise acoustic field extrapolation at the blade passage frequency (Fig. 5.10-e). This can also be observed in the L-curve (Fig. 5.6-a), where the residual norm $\zeta^{(lift)}$ is larger for ${}^{\text{vel}}\beta_2$ than for ${}^{\text{vel}}\beta_1$.

Link between the unsteady lift and the non-uniform inflow velocity reconstructions

Although the unsteady lift and the inflow velocity are analytically related through the Sears model (or Amiet model for compressible flow), the link between the *regularized* unsteady lift and the *regularized* inflow velocity is not straightforward. The order of the singular values of the transfer matrices $\mathbf{H}$ and $\mathbf{Z}$ and the regularization effects must be analyzed with care to compare the unsteady lift and the velocity reconstructions.

First, the diagonal matrix $\mathbf{\Sigma} = \text{diag}(\sigma_1, ..., \sigma_N)$, containing the non-negative singular values of $\mathbf{H}$ or $\mathbf{Z}$ in decreasing order is different for $\mathbf{H}$ and $\mathbf{Z}$. On the one hand, the largest singular values of the aeroacoustic transfer matrix $\mathbf{H}$ relating the unsteady lift to the acoustic pressure field are associated to the lowest discretized radii of the rotor. On the other hand, the largest singular values of the aeroacoustic transfer matrix $\mathbf{Z}$ relating the non-uniform inflow velocity to the acoustic pressure field are associated to the largest discretized radii. This can be observed by relating the transfer matrices $\mathbf{Z}$ and $\mathbf{H}$ as follows :

$$Z_{mji\mathtt{w}} = g_{i\mathtt{w}} R_i^2 H_{mji\mathtt{w}} \tag{5.30}$$

with

$$g_{i\mathtt{w}} = -i\pi\rho_0 C \frac{2\beta_r^2 \left[J_0(M_r^2\sigma_\theta/\beta_r^2) + iJ_1(M_r^2\sigma_\theta/\beta_r^2)\right]}{\mathtt{w}C[K_0(i\sigma_\theta/\beta_r^2) + K_1(i\sigma_\theta/\beta_r^2)]} e^{-i\sigma_\theta f(M_r)/\beta_r^2} \tag{5.31}$$

where the different terms in Eq. (5.31) are defined in section 5.3.2.. The reduced frequency σ_θ depends on R_i and $\mathtt{w}$ and M_r depends on R_i. In Eq. (5.30), $\|g_{i\mathtt{w}}\|$ decreases as a function of R_i but the term $\|g_{i\mathtt{w}} R_i^2\|$ increases as a function of R_i, which means that the term R_i^2 in Eq. (5.30) increases the coefficients of the matrix $\mathbf{Z}$ associated to the largest discretized radii.

Subsequently, since the regularization filters out the lowest singular values, the velocity is better reconstructed at outer radii using the velocity formulation (inversion of Eq. (5.14)) than by calculating the inflow velocity from the unsteady lift (using Eq. (5.5) coupled with inversion

of Eq. (5.10)).

Therefore, to compare the inversion of the velocity formulation to the inflow velocity calculated from the reconstructed unsteady lift, the following linear system has to be solved :

$$p_{mj} = \sum_i \sum_{\mathtt{w}} \frac{Z_{mji\mathtt{w}}}{R_i^2}(v_{i\mathtt{w}} R_i^2) \tag{5.32}$$

rather than the linear system of Eq. (5.14). This formulation is used to rearrange the singular value order of the velocity formulation so that the the singular values associated to the lowest radii are larger (as in the case of the lift formulation). In index notation, the regularized solution is then given by :

$$v_l^{reg} = \frac{\{v_{i\mathtt{w}} R_i^2\}_{reg}}{R_i^2} \tag{5.33}$$

with the contracted index $l = i\mathtt{w}$.

Thus, the filtering effect of the regularization on the reconstructed lift as a function of the radius is similar to the one obtained by the regularization of the inversion of Eq. (5.32). In Fig. 5.11, the velocity reconstruction calculated from the reconstructed lift (through a compressible Sears function) is compared to the reconstructed velocity obtained by Eq. (5.33). Preliminary experimental results are also shown in Fig. 5.11.

The mean wake velocity profile generated by the downstream obstruction (Figs. 5.10-a,b) has been measured with a single hot wire anemometer. The hot wire was located at various radial positions ($R = 8$ cm, $R = 11$ cm and $R = 14$ cm) in the upstream flow, at 0.5 cm from the blade leading edge. The hot wire anemometer was moved circumferentially from $-\pi/4$ to $\pi/4$ around the obstruction by increments of $\pi/20$. The hot wire signal was acquired for 3.4 s, corresponding to 159 revolutions of the fan rotating at 2800 r.p.m.. The sampling frequency was set to 4800 Hz to give 102 samples per revolution. The hot wire was installed to provide maximum voltage, perpendicular to the blade leading edge, thus giving an estimation of the transversal gust velocity (relative to the blade) generated by the obstruction. The measured mean velocity at different radii and circumferential locations is shown in Fig. 5.11. The continuous part of the reconstructed velocities are imposed to the mean value of the measured velocity over the circumferential direction.

The reconstructed inflow velocity obtained from the inversion of Eq. (5.32) is smoother than the inflow velocity calculated from the reconstructed unsteady lift. The latter is expected to be

more accurate since the number of dampened singular values is lower in this case. As already discussed above, the velocity reconstruction using both methods decreases as the radius increases. Using the velocity inversion model of Eq. (5.14) would lead to a larger inflow velocity for the largest radius but would decrease the magnitude of the inflow velocity for the lowest radial location.

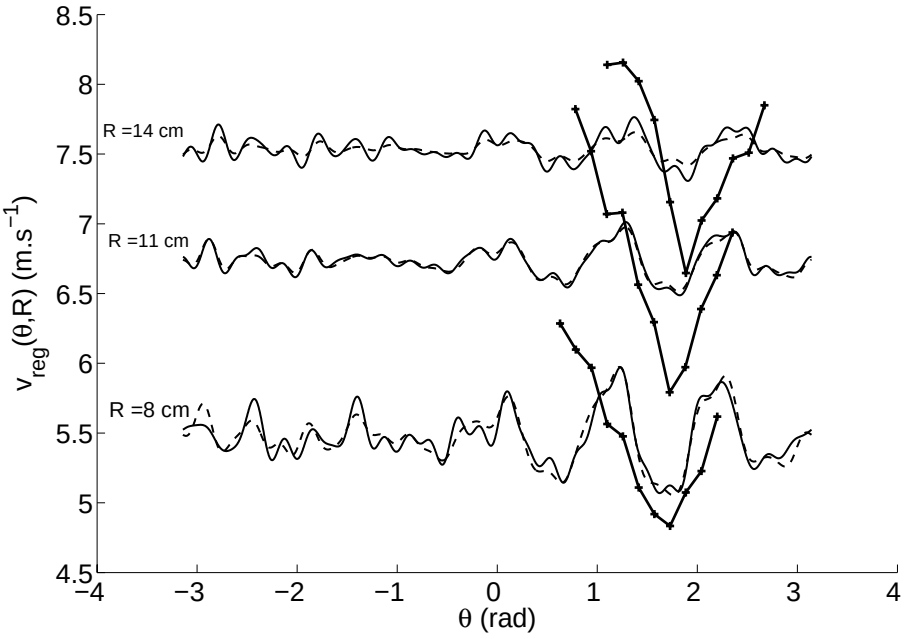

Figure 5.11 Comparison of the reconstructed velocities at different radii. Line : velocity calculated from the reconstructed unsteady lift, dashed line : reconstructed velocity from Eq. (5.33) and thick line : experimental data from hot wire anemometer measurements.

The reconstructed wake velocity irregularity is well located by the inverse models when compared to the anemometer measurements. However the magnitude of the reconstructed velocity is under-estimated since the lowest circumferential orders of the inflow velocity, which are energetic, are filtered out by the regularization. However, the highest acoustically radiating orders of the non-uniform inflow velocity are expected to be accurately reconstructed. Further experimental anemometer data covering the whole rotor circumference would be required to measure the circumferential spectrum of the inflow. Then, this spectrum could be compared to the estimated circumferential spectrum of the inflow velocity reconstructed by the proposed inverse models.

5.6 Conclusion

Two dependent inverse aeroacoustic models for tonal noise radiation from subsonic axial fans, based on the Blake formulations have been proposed. In order to accurately reconstruct the

unsteady lift and the inflow velocity, the Tikhonov regularization of the inverse problem has to be introduced and the regularization parameter must be chosen with care. The amount of regularization introduced by this parameter can be analyzed in terms of the number of dampened singular values of the aeroacoustic transfer matrices, to select the most appropriate local maximum of the L-curve curvature. For the experimental cases shown in this paper, the last local maximum of the L-curve curvature has been found to be optimal. Many simulations and experimental reconstructions support this observation.

This method can serve as a quantitative non-intrusive estimation of the most radiating deterministic unsteady lift modes and the deterministic non-uniform inflow velocity modes. The non-radiating modes are filtered out by the regularization. When the reconstructed modes are transformed into the spatial domain, it is possible to localize "hot spots" of interaction between the rotor and its environment. However, the method is qualitative in that the filtered modes in the spectral domain lead to an under-estimation of the spatial lift fluctuation or inflow velocity variation, as revealed by the preliminary hot wire anemometer measurements. Further experimental investigation could be carried out by completing the preliminary hot wire anemometer measurements and by comparing the reconstructed unsteady lift to experimental data provided by sensors embedded in the blades.

Another application of the proposed inverse models is sound field extrapolation. It can be applied for active or passive (inflow velocity or lift modifications in order to decrease tonal noise radiation) control purposes, to simulate the fan primary sound field in the whole radiation space from a set of acoustic pressure measurements. In this situation, a small regularization parameter can be chosen to minimize the residual norm, even if the solution is under-regularized.

5.7 Acknowledgments

This work has been supported by the AUTO21 Network of Centres of Excellence and Siemens VDO Automotive Inc. The authors wish to thank Sylvain Nadeau from Siemens VDO Automotive Inc. for his collaboration and Philippe-Aubert Gauthier from Université de Sherbrooke for helpful discussions.

5.8 Nomenclature

$\mathbf{A}$	Generic matrix
B	Number of blades
c_0	Speed of sound, m.s^{-1}
C	Blade chord, m

$\mathbf{e}$	Quadratic error vector $\mathbf{e} = \hat{\mathbf{p}} - \mathbf{p}$, Pa
$\mathbf{f}$	Unsteady lift vector, N.m^{-1}
$F^{'}$	Lift per unit span N.m^{-1}
$F^{'''}, F^{''}$	Force per unit volume, N.m^{-3} and per unit area, N.m^{-2}
$\mathbf{H}$	Lift transfer matrix, m^{-1}
i	Imaginary number $\sqrt{-1}$
I	Number of radial elements
J	Number of points in the discretized radiation space
J_n, K_n	Ordinary and modified Bessel functions, nth order
k_0	Acoustic wave number $k_0 = \omega/c_0$, rad.m^{-1}
k_θ	Circumferential wave number $k_\theta = \mathtt{w}/R$, rad.m^{-1}
L	Lift, N
M, N	Row and column dimension of matrix $\mathbf{A}$
M	Number of acoustic tones
M_r	Rotational Mach number $M_r = \Omega R/c_0$
p_a	Acoustic pressure, Pa
$\mathbf{p}$	Acoustic pressure vector $\mathbf{p} = \mathbf{Hf}$ or $\mathbf{p} = \mathbf{Zv}$, Pa
$\hat{\mathbf{p}}$	Vector of measured far-field acoustic pressures, Pa
q	Rate of mass injection per unit volume, Kg.m^{-3}.s^{-1} ($\dot{q} = \partial q/\partial t$)
R_H, R_T	Fan hub and tip radii, m
S	Incompressible Sears function
Sc	Compressible Sears function
t	Time, s
U	Tangential speed of the rotor $U = \Omega R$, m.s^{-1}
$\mathbf{U}$	Left singular matrix
$\mathcal{V}$	Source volume, m^3
v, V	Spatial and spectral inflow velocity, m.s^{-1}
$\mathbf{v}$	Inflow velocity vector, m.s^{-1}
$\mathbf{V}$	Right singular matrix
$\mathtt{w}_{min}, \mathtt{w}_{max}$	Minimum and maximum circumferential order to be reconstructed
W	Number of circumferential harmonics to be reconstructed
$\mathbf{x}; r, \varphi, \alpha$	Acoustic field point coordinate ; spherical coordinates
$\mathbf{y}; R, \theta, y_3$	Acoustic source point coordinate ; cylindrical coordinates
T_{ij}	Lighthill's stress tensor
$\mathbf{Z}$	Velocity transfer matrix, N.s.m^{-3}
β	Regularization parameter
γ	Rotor blade pitch angle, rad
δ	Delta-Dirac function
ΔR	Distance between two radial elements, m
ζ	Residual 2-norm $\|\mathbf{e}\|$
η	2-norm of the regularized solution

θ_b	Circumferential angle rotating with the blades, rad
$\theta_{\mathtt{w}}$	Phase of the lift (or velocity) source, rad
κ	Curvature of L-curve
ρ_0	Air density, Kg.m^{-3}
σ_θ	Reduced frequency $\sigma_\theta = k_\theta C/2$
$\mathbf{\Sigma}$	Diagonal matrix of singular values σ_n
τ	Time delay, s
$\boldsymbol{\phi}$	Generic solution vetor
$\boldsymbol{\psi}$	Generic right-hand side vetor
ω	Angular frequency $\omega = mB\Omega$, rad.s^{-1}
Ω	Angular velocity of the rotor, rad.s^{-1}

Subscripts and indices

3	Axial component
est	Estimate
i	Radial element index
j	Radiation space discretization index
m	Acoustic frequency index
reg	Regularized
$\mathtt{w}$	Circumferential index
θ	Tangential component

Superscripts

H	Hermitian
T	Transposed
lift	Lift
vel	Velocity

5.9 Bilan

Dans ce chapitre, un modèle inverse, basé sur le modèle analytique de Blake, a été développé. Sa formulation est très similaire à celle utilisée pour l'inversion du modèle de Morse et Ingard, au chapitre 3. Cependant, alors que l'inversion du modèle de Morse et Ingard permet la reconstruction de forces par unité de surface, le modèle de Blake permet la reconstruction de portances instationnaires par unité d'envergure ainsi que de vitesses d'écoulement traversant le ventilateur. La formulation en vitesse du problème inverse se prête mieux à la validation expérimentale par des mesures anémométriques à fil chaud. De plus, des mesures effectuées sur un

hémisphère ont considérablement amélioré les reconstructions des sources de bruit de raie par rapport au demi-cercle de mesure utilisé dans le chapitre 3. Pour assurer un choix correct du coefficient de régularisation, et ainsi une bonne reconstruction des portances et vitesses d'écoulement, la courbure de la courbe en L et la condition de Picard ont été associées de manière originale. Plus précisément, le dernier maximum local de la courbure de la courbe en L est choisi si la condition de Picard est respectée (ce qui est souvent le cas). Sinon, il faut choisir un autre maximum local de la courbure de la courbe en L qui respecte la condition de Picard. Comme les modes associés aux plus faibles valeurs singulières sont filtrées par la régularisation, les portances et profils de vitesse reconstruits sont sous-estimés, ce qui a été montré par des mesures de profils de vitesse par fil chaud. Les reconstructions respectent néanmoins les ordres de grandeurs des vitesses mesurées et concordent qualitativement avec les zones perturbées de l'écoulement pour une interaction entre le rotor et une large obstruction introduite entre deux aubes de stator. Les modèles inverses fournissent donc des méthodes sans contact d'estimation des sources de bruit de raie, utiles pour l'analyse de l'écoulement, et donc son contrôle. Ces modèles offrent aussi un outil d'extrapolation du champ acoustique rayonné par un rotor à la FPP et ses harmoniques.

Le modèle de Blake (comme celui de Goldstein [15]) est très bien adapté aux travaux présentés dans les deux prochaines sections, sur le contrôle passif adapté de l'écoulement car il permet de calculer la portance instationnaire et le champ de pression acoustique à partir de profils de vitesse mesurés ou imposés dans le sillage des obstructions de contrôle.

CHAPITRE 6

CONTRÔLE PASSIF ADAPTÉ, PARTIE I : INTERACTION ROTOR/OBSTRUCTIONS DE CONTRÔLE

CONTRÔLE DU BRUIT DE RAIE DES VENTILATEURS AXIAUX SUBSONIQUES EN UTILISANT DES OBSTRUCTIONS DE CONTRÔLE DANS L'ÉCOULEMENT PARTIE 1 : INTERACTION ENTRE LE ROTOR ET LES OBSTRUCTIONS DE CONTRÔLE

CONTROL OF TONAL NOISE FROM SUBSONIC AXIAL FANS USING FLOW CONTROL OBSTRUCTIONS PART 1 : INTERACTION BETWEEN THE FLOW CONTROL OBSTRUCTIONS AND THE ROTOR

6.1 Abstract

This paper investigates the analytical calculation of blade unsteady lift spectrum when interacting with a neighboring obstruction, designed to control tonal noise. The approach used in these companion papers is to add a secondary unsteady lift mode, of equal intensity but opposite in phase with the primary unsteady lift mode so that the resultant of both primary and secondary modes is null. To control one unsteady lift mode (consequently an acoustic tone) without affecting the harmonics of the controlled mode (consequently the harmonics of the acoustic tone to be controlled), it is important for the secondary unsteady lift to be harmonically selective. We have therefore evaluated the harmonic content of the blade unsteady lift generated by the proposed control obstructions. To this purpose, an original equation is derived using the infinitesimal radial strips theory coupled with the one-dimensional Sears gust analysis. The spectrum of the blade unsteady lift is then analyzed for three types of obstructions : a series of trapezoidal obstructions, a sinusoidal obstruction and a series of cylindrical obstructions. The use of salient obstructions leads to a large unsteady lift harmonic content. An optimized wake width of the trapezoidal obstruction leads to a low harmonic content rate of 5.5%. A Gaussian approximation of the measured inflow velocity profile generated by a sinusoidal obstruction leads to a relatively low harmonic content rate of 18.8%, which indicates that most of the energy is contained in the fundamental mode of the blade unsteady lift. Finally, a rotor/rods interaction experiment is adapted from the literature to show that the use of small-diameter cylinders leads to a higher harmonic content rate of 45.7%. In the companion paper [9], the obstructions described here are experimentally tested as a tool for controlling the tonal noise of an automotive engine cooling fan by interfering the most radiating primary mode of the blade unsteady lift.

6.2 Introduction

In this paper and in the companion paper, a passive method is proposed for reducing the forces responsible for the tonal noise from subsonic axial-flow fans using flow obstructions. Tonal noise is mainly generated by the non-uniform flow entering the fan, leading to fluctuating unsteady forces acting by the blades on the fluid. When decomposing these forces using circumferential Fourier transform, it can be seen that few circumferential modes are responsible for the tonal noise, especially for acoustically compact fans. Therefore, it is herein proposed to adequately position a flow control obstruction in order to destructively interfere with the most radiating primary circumferential mode of the fluctuating force. The concept of controlling tonal noise by adding flow control obstructions has been investigated by a few authors [102], [103], [104] and [105]. The first preliminary theoretical study about the potential of using flow control obstructions to control fan tonal noise was conducted by Nelson [102]. He considered the use of $2N$ independent flow obstructions to control N modes in order to attenuate the fan tonal noise generated by inlet

flow distorsions. The amplitude of the wake deficit behind each obstruction is calculated so that it minimizes a weighted sum of the sound power at the Blade Passage Frequency (BPF) and its harmonics. The risk of amplification of the harmonics of the BPF while attempting to control the sound power at BPF was pointed out. The only modelling of the rotor/flow control obstruction was proposed by Polacsek *et al* [103]. They used a computational aeroacoustic model based on a Reynolds averaged Navier-Stokes 2-D solver to estimate the unsteady force components on blades due to the control cylindrical obstructions. The magnitude of several circumferential unsteady force modes is found to be non-negligible so that the control of the Blade Passage Frequency (BPF) tone can increase the harmonics of the BPF. In previous literature about the passive approach described above, there is no investigation on designing obstructions that do not affect the upper harmonics while controlling an acoustic tone. Waitz and al. [12] proposed several strategies for reduction of turbomachinery fan noise such as the removal of the blade boundary layer and the addition of fluid through the rotor blade trailing edge to minimize the wakes shed by the rotor blades, thus making the flow in the stator more uniform, reducing unsteady loading and radiated noise. An unsteady, thin shear layer Navier-Stokes calculation on the stator was used to provide a numerical parametrization of the effects of Gaussian wake widths generated by the rotor, and impinging in the stator vanes, on the amplitude of the acoustic mode propagating in the duct. They concluded that a wake width approximatively equal to the rotor pitch leads to maximize the amplitude of the BPF with respect to its higher harmonics.

In this paper, by contrast to ref. [12], the wake is generated by the control obstruction and impinges in the rotor. A simple integral equation is derived in this paper to predict analytically the spectrum of the rotor blade unsteady lift generated by the flow control obstructions, and the companion paper [9] presents the acoustic performance of the control approach for an automotive engine cooling fan. The literature review related to the concept of flow obstruction to control tonal noise is more detailed in the companion paper. In this paper, we provide the key references, useful for designing flow control obstructions analytically.

The modelling of airfoil or blade unsteady lift is a topic of research since the beginning of the 20^{th} century with the analysis of a flat plate in a sinusoidally oscillatory motion [110]. Sears obtained a fundamental result on the fluctuating lift experienced by an airfoil passing trough a transversal sinusoidal gust [20], based on the "airfoil theory for non-uniform motion" [111]. Afterwards, models have been further investigated to take two-dimensional gusts [112], [113], [114] and compressibility effect [27] into account. More recently, the Sears problem has been revisited to include the effect of mean flow angle of attack and the airfoil camber on the gust response [115] and more sophisticated methods to assess the importance of non-linearity have been presented. An analysis on the three-dimensional effects of blade force on the sound generated by an annular cascade in distorted flows has also been investigated [116], which is particularly adapted for subsonic ducted-fans. Finally, in the last decade, several numerical studies attempted to calculate the unsteady blade forces with the objective to predict tonal noise [103], [31], [33], [30].

The numerical approach has been discarded in this study, and instead a simpler and faster analytical method based on the compressible approximation of the Sears function derived by Amiet [27] is used. A periodic inflow distorsion due to the interaction of rotating blades with a neighboring obstruction is either imposed or fitted from experimental measurements. This inflow velocity serves as an input for the calculation of the unsteady lift per unit span at a given radius. The unsteady lift is then calculated by integrating the unsteady lift per unit span along the span using an infinitesimal strip theory, which can be done by assuming that the problem can be locally treated as a one-dimensional problem. The sweep of the blades and the phase of the gust along the span are taken into account. The calculation is performed into the spectral domain since the periodic unsteady lift responsible for tonal noise is of interest. The final objective is to evaluate the unsteady lift spectra generated by the interaction between the rotor and the control obstructions and to choose the obstruction leading to the lowest harmonic content of the blade unsteady lift. From a control point of view, the ideal case would be a pure sinusoidal flow field pattern, leading to a single circumferential unsteady lift mode. In such a case, it is possible to control each unsteady lift mode independently, and thus control an acoustic tone without affecting the other tones.

In this paper, the control approach is first conceptually described. Then, the Sears theory associated to the infinitesimal strip theory is reviewed to calculate the unsteady lift generated by the interaction between a rotor and an obstruction. Finally, numerical examples are given for various obstruction types (trapezoidal, sinusoidal and cylindrical obstructions). An optimization of the wake width generated by the trapezoidal obstruction is also investigated. Circumferential wavenumber spectra of the blade unsteady lift produced by the interaction between the rotor and the control obstructions are presented and a harmonic content analysis is carried out to evaluate the ability of the control obstructions to selectively control a blade unsteady lift mode.

In the companion paper [9], the principle of tonal noise control using flow obstruction is first detailed and the expected sound power attenuation is given. Then the rotor/flow obstruction is experimentally assessed and indirect estimation of the unsteady lift spectra generated by the flow control obstruction are compared to the predicted unsteady lift spectra reported in this paper. Free field control of the BPF tone is then presented for the sinusoidal obstruction. In-duct control performance of the flow control approach for the BPF and its first harmonic is also presented using two optimized series of trapezoidal obstructions. The final part of the companion paper presents measurements of fan aerodynamic efficiency with and without flow control obstruction.

6.3 Control approach

In the Ffowcs-Williams and Hawkings analogy, an aeroacoustic source of noise can be decomposed in three terms. The first term is associated with a moving quadripole source that represents the generation of sound due to turbulent volume sources and corresponds to the solution of the Lighthill theory [15]. For fan noise, this quadripole source is significant only if the blade tip Mach number exceeds 0.8 [15] and is therefore irrelevant for low subsonic fans such as automotive engine cooling fans, for which blade tip Mach numbers generally do not exceed 0.15. The second term is related to a moving dipole source due to the unsteady forces exerted by the solid surfaces on the fluid. This is the well-known "loading noise" or "dipole noise", the principal cause of subsonic fan noise [15]. The last term is equivalent to a monopole radiation due to the volume displacement effects of the moving surfaces, also called "thickness noise". The efficiency of thickness noise is poor at low fan rotation speed since the circumferential phase velocity of the fluid pressure fluctuations generated by the moving blades is well below sonic velocity [15]. Therefore, the main source term for subsonic axial fans is the distribution of forces applied by the blades on the fluid. Periodic forces (steady rotating forces or unsteady rotating forces due to non-uniform but stationary upstream flow) lead to discrete tone generation while random forces (such as turbulent boundary forces) lead to broadband noise.

As formulated by Blake [4], the tonal fan noise in free field due to periodic forces can be expressed as follows :

$$p(\mathbf{x},t) = \sum_{m=-\infty}^{\infty} \sum_{\mathrm{w}=-\infty}^{\infty} \left[P(\mathbf{x},\omega)\right]_{\mathrm{w},m} e^{-imB\Omega t} \tag{6.1}$$

with :

$$\begin{aligned} \left[P(\mathbf{x},\omega)\right]_{\mathrm{w},m} \approx\ & \frac{-ik_0 B e^{ik_0 r}}{4\pi r} e^{-i(mB-\mathrm{w})(\pi/2-\varphi)} \delta(\omega - mB\Omega) \times J_{mB-\mathrm{w}}(k_0 R_m \sin\alpha) \\ & \times \tilde{L}(\mathrm{w}) \times \left[\cos\gamma\cos\alpha + \frac{mB-\mathrm{w}}{k_0 R_m}\sin\gamma\right] \end{aligned} \tag{6.2}$$

In Eqs. (6.1) and (6.2), the fan effective area is reduced to an equivalent distribution of dipoles distributed along a mean radius of the fan $R_m = 0.7 \times R_T$, where R_T is the blade tip radius [4]. This approximation is expected to be accurate if the spatial extent of the fluctuating pressures is less than a wavelength of the sound generated. The first summation in Eq. (6.1) represents the combination of multiple tones at angular frequencies $\omega = mB\Omega$ where B is the number of blades and Ω is the rotation of the rotor in rad.s^{-1}. The second summation represents the decomposition

of the lift over circumferential harmonics w. In Eq. (6.2), the first term describes the propagation of the acoustic waves, which have a wave number $k_0 = \omega/c_0$ (where c_0 is the speed of sound) and rotate at a circumferential phase velocity equal to $\frac{mB}{mB-\mathrm{w}}\Omega$. The Bessel function term refers to the ability of a circumferential lift mode w to radiate sound at the harmonic of rank m of the blade passage frequency $B\Omega$. The term $\tilde{L}(\mathrm{w})$ is the contribution of the circumferential mode w to the lift acting at the radial position R_m. The terms in brackets weight the relative importance of axial (thrust) and tangential (drag) forces, which are function of the pitch angle γ of the blades.

In the ideal case of a fan operating in a uniform flow (Fig. 6.1-a), the blades experience no lift fluctuation during the rotation ($\tilde{L}(\mathrm{w}) = 0$ for $\mathrm{w} \neq 0$). Thus, the force distribution on the blades is steady in a frame rotating with the rotor and the only source of sound is the periodic relative distance variation between the emitter (blades) and the receiver. The related radiated noise is called the Gutin noise, which is tonal at the Blade Passage Frequency (BPF) and its harmonics. The circumferential phase velocity of the sound wave generated by steady rotating forces is equal to the rotational speed of the rotor, leading to inefficient radiation at low subsonic speed.

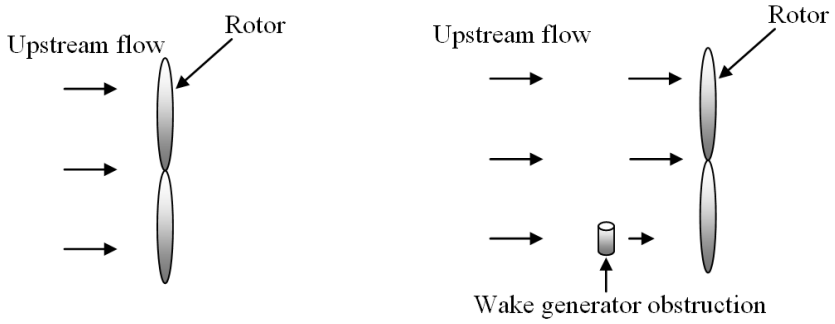

(a) Uniform flow (b) Non-uniform flow

Figure 6.1 Fan in uniform and non-uniform flow

However, even a slight upstream flow irregularity (Fig. 6.1-b) causes circumferentially varying blade forces and gives rise to a considerably larger radiated sound at the BPF and its harmonics, especially in the axial direction of the fan [5]. In many instances, axial fans operate in a non-uniform flow : this is the case of engine cooling axial fans that operate behind a radiator/condenser system or in the wake of inlet guide vanes. The interactions between the flow and the blades can be classified into potential interactions and wake interactions [15]. When the flow entering the rotor is periodic but non-uniform, the blades experience changes in angle of incidence during rotation, leading to a periodic lift fluctuation. These spatial lift fluctuations can be expanded over Fourier circumferential harmonics to analyse the acoustic radiation. At low subsonic blade speed, the acoustic radiation at the harmonic m of the BPF comes mainly from the highly radiating circumferential mode of the unsteady lift $\tilde{L}(\mathrm{w} = mB)$, because of the large magnitude of the Bessel function $J_0(k_0 R \sin\alpha)$ associated to this mode in Eq. (6.2). In such a case, all the

elementary radiating dipoles fluctuate in phase (the theoretical rotational wave velocity in Eq. (6.2) is infinite) and the directivity of the sound radiation is a dipole along the fan axis. When the rotation speed of the fan increases, the unsteady lift modes $\tilde{L}(\mathrm{w} = mB \pm 1)$ and $\tilde{L}(\mathrm{w} = mB \pm 2)$ may have a significant contribution to the acoustic radiation at frequency $m\times$BPF. However, for a typical automotive fan, the unsteady lift mode $\tilde{L}(\mathrm{w} = mB)$ is, by far, the most radiating mode at frequency $m\times$BPF. Thus, the control of this particular mode is expected to lead to large sound attenuation. The acoustic analysis of axial fans is further detailed in the companion paper [9].

To control the noise radiation at the BPF (or its harmonics $m\times$BPF), the unsteady lift mode $\tilde{L}_p(\mathrm{w} = B)$ (or $\tilde{L}_p(\mathrm{w} = mB)$) must be attenuated.

The proposed technique developed in the companion papers [9] consists of interfering with the primary unsteady lift mode $\tilde{L}_p(\mathrm{w} = B)$ by adding a secondary unsteady lift mode $\tilde{L}_s(\mathrm{w} = B)$ (or $\tilde{L}_s(\mathrm{w} = mB)$) of equal intensity but opposite in phase with the primary unsteady lift mode $\tilde{L}_p(\mathrm{w} = B)$ (or $\tilde{L}_p(\mathrm{w} = mB)$), as shown schematically in Fig. 6.2. This can be done using adequately positioned flow control obstruction(s) (also called wake generators by Polacsek *et al.* [103]). The magnitude of the secondary unsteady lift mode is controlled by the axial distance between the rotor and the flow control obstruction, and the phase of the secondary unsteady lift mode is controlled by the circumferential position of the flow control obstruction. Assuming that the superposition principle can be applied (as shown experimentally in the companion paper [9]), the resulting unsteady lift mode is theoretically zero when the primary and secondary unsteady lift modes are equal and opposite in phase.

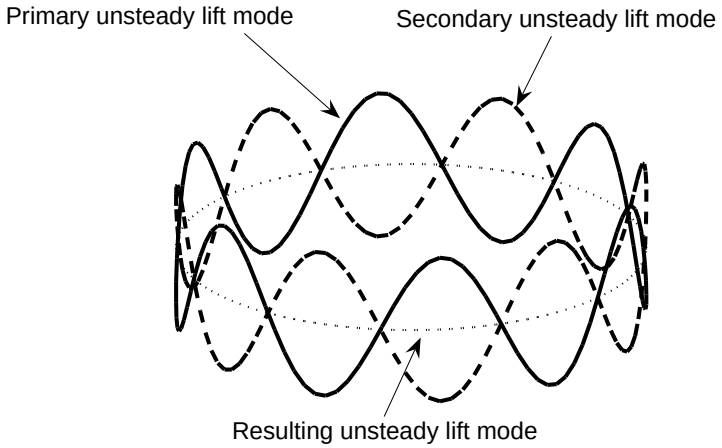

Figure 6.2 Principle of the wake generator to control the primary unsteady lift modes

The flow control obstruction must be designed with care to generate the desired secondary

unsteady lift mode. Especially, it is important that the obstruction be selective to mainly generate one unsteady lift mode, because other induced lift modes can give rise to sound radiation at higher frequencies. For example, the use of sharp control obstruction(s), such as small diameter cylinders, as proposed by Polacsek [103], Kota [13], Anderson [104] or Neuhaus [100], leads to sharp wakes and thus to a large spectral energetic content of the unsteady lift. The following sections of this paper analyse the circumferential lift spectrum of various proposed control obstructions. The design of a control obstruction geometry which is as spectrally selective as possible is the ultimate goal of the analysis.

6.4 Unsteady lift generated by control obstructions

This section aims at calculating the unsteady lift $\tilde{L}(\mathrm{w})$ of Eq. (6.2) generated by various control obstruction geometries. The results will be used to optimize the shape of the obstruction so that its circumferential spectrum of the unsteady lift is selective.

Before further investigating the modelling of the flow control obstructions/rotor interaction, the unsteady airfoil theory is summarized. When an airfoil (or a blade) moves into a non-uniform flow, the angle of incidence of the airfoil relative to the airflow is time varying, leading to dynamic pressure distribution fluctuations.

Sears [20] has developed a linear theory for a flat-plate of infinitesimal thickness encountering a gust in incompressible flow. The formulation proposed by Sears relates the unsteady lift per unit span to the incident downwash amplitude of the gust. Amiet [27] later on proposed a model for compressible flows. The compressibility effects must be taken into account when the time for an acoustic wave to travel across the blade chord is not negligible compared to the time for a fluid disturbance to cross the blade, which is the case at high frequency.

Once the blade unsteady lift per unit span is known along the span, the unsteady lift can be calculated using the strip theory by integrating the unsteady lift per unit span along the span. The sweep of the blades and the sweep of the gust along the blade span must be taken into account.

Based on the classical unsteady airfoil theory and the strip theory, a new simple integral equation is obtained to calculate the rotor unsteady lift generated by the interaction between the rotor and the obstructions, assuming that a Gaussian non-uniform inflow velocity is induced by the obstructions. The variables of this formulation are related to the geometrical characteristics of the rotor and the obstructions, and the characteristic of the non-uniform inflow velocity.

6.4.1 The Sears function for a transversal gust

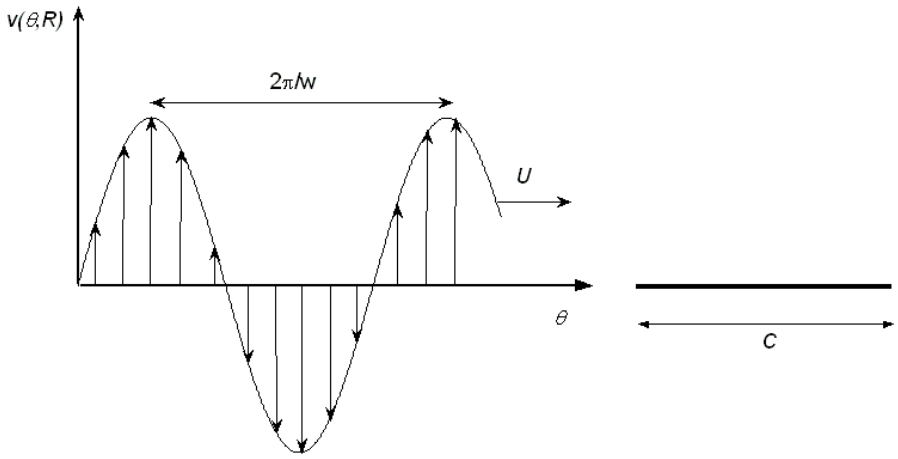

Figure 6.3 The Sears problem, blade section submitted to a transversal gust.

Let's consider a one-dimensional periodic gust with transversal velocity $v(\theta, t)$ moving in the circumferential θ-direction at speed U, as illustrated in Fig. 6.3. The lift response per unit span acting at the quarter-chord point to a transverse gust is given by the expression [4] :

$$\frac{d\tilde{L}\,(\mathrm{w}, R)}{dR} = \pi\rho_0 C\tilde{V}(\mathrm{w}, R)U(R)S(\sigma_\theta) \tag{6.3}$$

where ρ_0 is the density of air, C is the blade chord, $U(R) = R\Omega$ is the tangential speed of the rotor at radius R, $\sigma_\theta = \frac{k_\theta C}{2} = \frac{\mathrm{w}C}{2R}$ is the reduced frequency and w is the circumferential order of the gust (number of gust periods per circumference). Also, $\tilde{V}(\mathrm{w}, R)$ is the circumferential harmonic decomposition of the inflow velocity normal to the blade chord, such that :

$$\tilde{V}(\mathrm{w}, R) = \frac{1}{2\pi}\int_0^{2\pi} v(\theta, R)e^{-i\mathrm{w}\theta}d\theta \tag{6.4a}$$

and :

$$v(\theta, R) = \sum_{\mathrm{w}=-\infty}^{\infty} \tilde{V}(\mathrm{w}, R)e^{i\mathrm{w}\theta} \tag{6.4b}$$

Moreover, in Eq. (6.3), $S(\sigma_\theta)$ is the incompressible Sears function defined as follows [19] :

$$S(\sigma_\theta) = \frac{1}{i\sigma_\theta[K_0(i\sigma_\theta) + K_1(i\sigma_\theta)]} \tag{6.5}$$

where K_0 and K_1 are respectively the zeroth-order and first-order modified Bessel functions.

To account for the effect of blade camber, thickness and angle of attack of the blade, a second order analysis must be carried out [15]. However, in order to get explicit mathematical expression of the unsteady lift and simplify the calculation of the unsteady lift spectra generated by the ingestion of control obstruction wakes by the rotor, the linear analysis was considered sufficient. On the other hand, the inclusion of compressibility effects doesn't much complicate the mathematical expression of the Sears function. If the reduced frequency is large enough, such that the time for an acoustic wave to travel the chord is not negligible in comparison to the time for a blade to travel an inflow velocity disturbance, a compressible Sears function is recommended [15]. The low-frequency approximation of the compressible Sears function derived by Amiet [27] is used :

$$S_c(\sigma_\theta, M_r) = \frac{S(\sigma_\theta/\beta_r^2)}{\beta_r} \left[J_0(M_r^2\sigma_\theta/\beta_r^2) + iJ_1(M_r^2\sigma_\theta/\beta_r^2)\right] e^{-i\sigma_\theta f(M_r)/\beta_r^2} \tag{6.6}$$

with :

$$\beta_r \equiv \sqrt{1 - M_r^2}$$

and

$$f(M_r) \equiv (1 - \beta_r)\ln M_r + \beta_r \ln(1 + \beta_r) - \ln 2$$

where $M_r = \Omega R/c_0$ is the rotation Mach number, J_0 et J_1 are respectively the zeroth-order and first-order ordinary Bessel functions. A criterion for the applicability of Eq. (6.6) is given by Amiet [27] : $\sigma_\theta M_r/\beta_r^2 < 1$ or w $< \frac{2R(1-M_r^2)}{CM_r}$. This condition is satisfied up to the circumferential order $\mathrm{w}_{max} = 43$ for a $C = 5$ cm blade chord, rotating at $\Omega = 2\pi \times 50$ rad.s^{-1} at a 10 cm radius. This condition therefore provides an upper bound of the circumferential harmonic w in Eq. (6.3).

6.4.2 The infinitesimal strip theory

In this paper, instead of considering an oblique gust impinging the blades (with a radial and a circumferential wave number, which is referred to as the two-dimensional gust problem), the fan rotor is decomposed into infinitesimal radial strips along the span, which individually respond to a transversal gust. In other words, at a given radius, the gust and the blade are considered of infinite span so that the gust interaction problem can be treated as a one-dimensional gust

problem, as in the previous section. The unsteady lift per unit span (Eq. (6.3)) is then integrated along the span to yield the unsteady lift on the blade :

$$\begin{aligned}\tilde{L}(\mathrm{w}) &= \int_{R_H}^{R_T} \frac{d\tilde{L}(\mathrm{w},R)}{dR} dR \\ &= \pi\rho_0\Omega \int_{R_H}^{R_T} C(R)R\tilde{V}(\mathrm{w},R)e^{i\mathrm{w}(\theta_c(R)-\theta_g(R))}S_c(\sigma_\theta,M_r)dR \end{aligned} \tag{6.7}$$

where R_H and R_T are respectively the hub and tip radii of the rotor. In the problem of upstream obstructions generating circumferential inflow fluctuations, the transversal velocity of the gust $\tilde{V}(\mathrm{w},R)$ is the unknown in Eq. (6.7). By approximating $v(\theta,R)$ by a Gaussian function of θ behind the obstructions, it is possible to calculate its Fourier transform $\tilde{V}(\mathrm{w},R)$. Since the transversal velocity is decomposed into infinitesimal strips, the phase variation of the gust along the span $\theta_g(R)$ relatively to the phase of the chord along the span $\theta_c(R)$ (due to the sweep of the blade) must be taken into account. In Fig. 6.4, four blades and four regularly spaced obstructions are chosen to show the coordinate system used to described the sweep of the blades and the gust along the span. A square shape of the obstruction is chosen for illustration purpose.

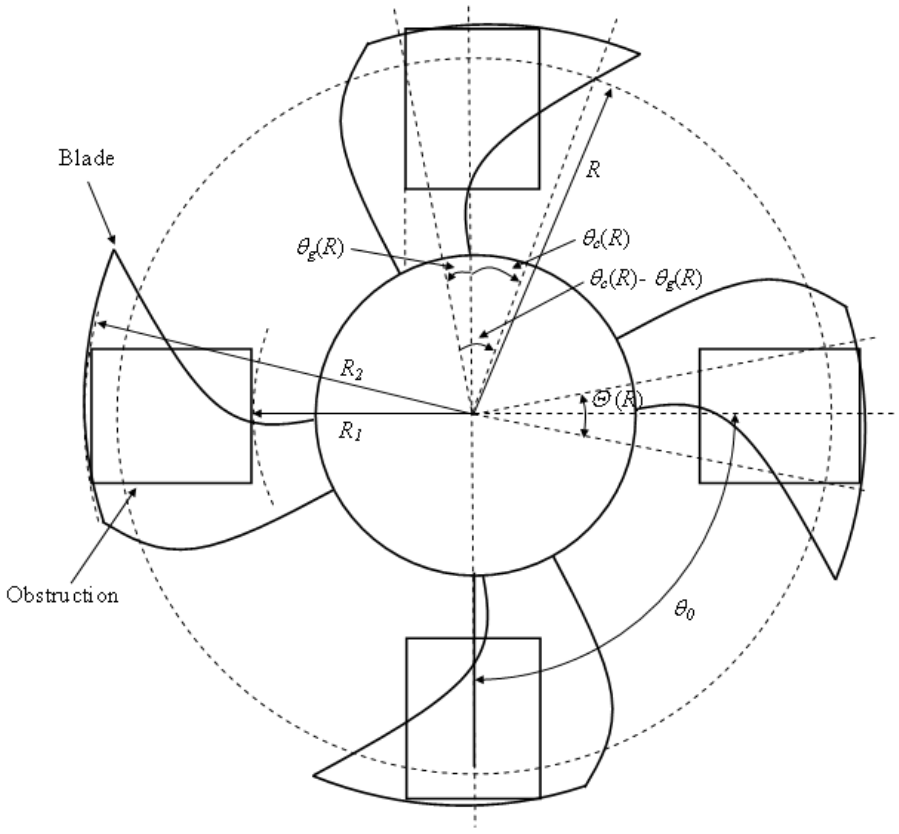

Figure 6.4 Problem geometry

Spatial transversal velocity

Since the flow responsible for tonal noise is non-uniform but stationary, a deterministic periodic spatial transversal velocity $v(\theta, R)$ is imposed over the circumferential direction θ. The flow is considered uniform in the region without obstruction $[R_H, R_1[$ and $]R_2, R_T]$, where R_1 and R_2 are respectively the inner and outer radii of the obstructions (cf Fig. 6.4). Thus the calculation of Eq. (6.7) and the spatial Fourier transform $\tilde{V}(\mathrm{w}, R)$ of $v(\theta, R)$ is only required in the interval $[R_1, R_2]$. A Gaussian velocity profile is assumed behind the portion occupied by the obstruction. The angular width of the Gaussian profile is related to the angle $\Theta(R)$ of the obstruction at radius R, so that the transversal velocity can be written as follows :

$$v(\theta, R) = v_0(R) + v_m(R) \sum_{n=-\infty}^{+\infty} e^{-\left(\frac{\theta - n\theta_0}{a(R)\Theta(R)}\right)^2}, \quad R_1 \geq R \geq R_2 \tag{6.8}$$

where $a(R)$ is the Gaussian width parameter, $v_m(R)$ is the magnitude of the inflow velocity defect and θ_0 is the angular period of the obstruction(s) as defined in Figs. 6.4 and 6.5. The uniform velocity term $v_0(R)$ can be ignored in Eq. (6.8) since it does not contribute to the unsteady lift and sound radiation at low subsonic blade speed.

The Gaussian inflow velocity distorsion assumption is versatile since the magnitude and the angular width of the Gaussian function can be adjusted as a function of the radius R to account for the distance of the obstruction/rotor axial distance, the rotation speed of the fan, the aerodynamic shape of the obstruction. Published inflow velocity measurements show Gaussian shape of the mean velocity profiles in the downstream flow field of various obstructions in various operating conditions [117] [47] [41] [39]. Experimental results reported later in this paper (section 6.5.2) also show the ability of a Gaussian function to approximate the measurement of the wake velocity profile generated by a sinusoidal obstruction. However, for a large angular obstruction located very close to the rotor, a flat top velocity profile would be more appropriate.

In order to simplify the calculation of the Fourier transform of the spatial transversal velocity, it is useful to introduce the following variable :

$$A^2(R) = \frac{\theta_0^2}{a^2\Theta(R)^2} = \frac{4\pi^2}{a^2 N^2 \Theta(R)^2} \tag{6.9}$$

where N is the number of obstructions regularly spaced over the circumferential direction and where the Gaussian width parameter $a(R)$ is considered independent of the radius R. Making use of the Poisson summation formula : $\sum_{n=-\infty}^{+\infty} f(n) = \sum_{m=-\infty}^{+\infty} \int_{-\infty}^{+\infty} f(z) e^{-2\pi i m z} dz$ with $f(n) =$

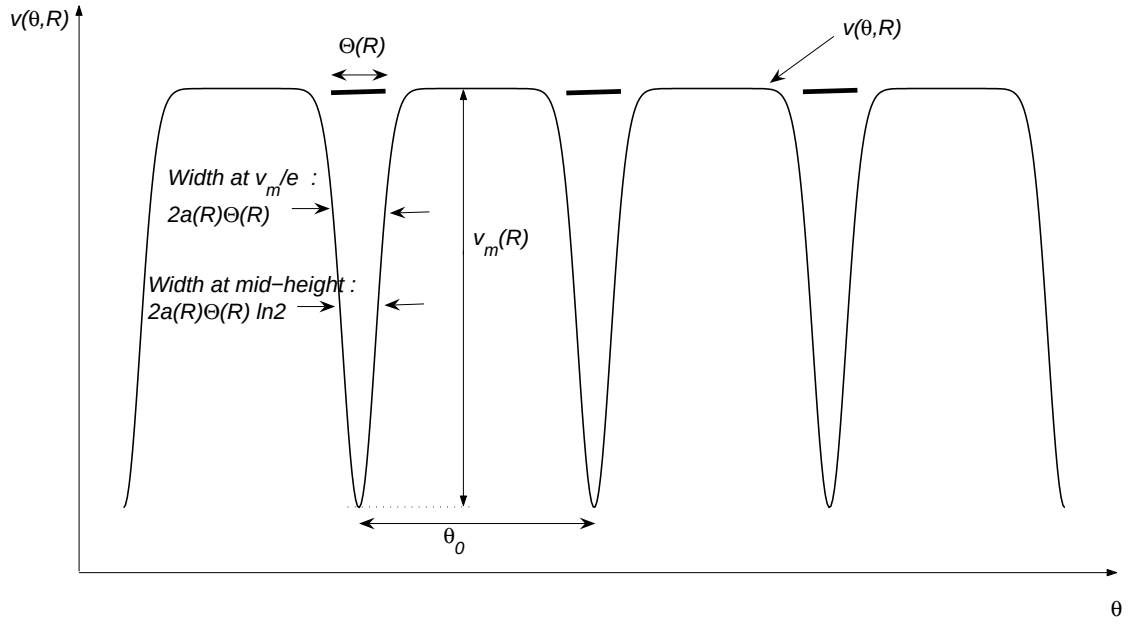

Figure 6.5 Gaussian wake velocity defect generated by upstream angular segments of width $\Theta(R)$

$e^{-\left(\frac{\theta-n\theta_0}{a\Theta(R)}\right)^2}$, the transversal velocity can be rearranged after introducing the variable $\xi = A(\frac{\theta}{\theta_0} - z)$:

$$\int_{-\infty}^{+\infty} f(z)e^{-2\pi imz}dz = -\frac{1}{A(R)}e^{-2i\pi m\frac{\theta}{\theta_0}-\frac{m^2\pi^2}{A^2(R)}}\int_{-\infty}^{+\infty} e^{-(\xi-\frac{im\pi}{A(R)})^2}d\xi \tag{6.10}$$

Since $\int_{-\infty}^{+\infty} e^{-(\xi-\frac{im\pi}{A})^2}d\xi = \sqrt{\pi}$ [118], the expansion of the spatial transversal velocity over the circumferential direction is :

$$v(\theta, R) = -v_m(R)\frac{\sqrt{\pi}}{A(R)}\sum_{m=-\infty}^{+\infty} e^{-2i\pi m\frac{\theta}{\theta_0}-\frac{m^2\pi^2}{A^2(R)}} \tag{6.11}$$

The spatial velocity profile behind the obstructions given by Eq. (6.11) is then Fourier transformed into the circumferential spectral domain and Eq. (6.7) is used to obtain the unsteady lift of the rotor blades as a function of the circumferential spectral components of the velocity.

Spectral transversal velocity

The Fourier transform $\tilde{V}(\mathrm{w}, R)$ of the the transversal velocity $v(\theta, R)$ is given by Eq. (6.4a), where the fundamental circumferential order is equal to the number of obstructions $\frac{2\pi}{\theta_0} = N$. All circumferential orders appearing in Eq. (6.4b) will be multiples of N. Calculating the Fourier transform of Eq. (6.4a) over only one angular period θ_0 leads to the following expression of the spatial Fourier transform of the transversal velocity :

$$\tilde{V}(nN, R) = -\frac{v_m(R)\sqrt{\pi}}{A(R)}\sum_{m=-\infty}^{+\infty}\mathrm{sinc}(\pi(m+n))e^{\frac{-m^2\pi^2}{A^2(R)}} \tag{6.12}$$

6.4.3 Unsteady lift integrated along the span

Eq. (6.12) is introduced into Eq. (6.7) with $R_H = R_1$ and $R_T = R_2$ to give the general expression of the unsteady lift for the circumferential order $\mathrm{w} = nN$ caused by N regularly spaced obstructions generating Gaussian wakes :

$$\tilde{L}(\mathrm{nN}) = \pi^{3/2}\rho_0\Omega\sum_{m=-\infty}^{+\infty}\mathrm{sinc}(\pi(m+n))\int_{R_1}^{R_2}\frac{v_m(R)}{A(R)}C(R)Re^{\frac{-m^2\pi^2}{A^2(R)}}e^{i\mathrm{w}(\theta_c(R)-\theta_g(R))}S_c(\sigma_\theta, M_r)dR \tag{6.13}$$

where the phase of the gust relative to the blade over the span is taken into account in the term $e^{inN(\theta_c(R)-\theta_g(R))}$. From Fig. 6.4, it can be seen that $\theta_c(R)$ depends on the sweep of the blade and that the origin of the angular position is chosen so that $\theta_g(R) = \Theta(R)/2$. Introducing Eq. (6.13) into Eq. (6.2) leads to the sound pressure field generated by the interaction between the rotor and the flow control obstruction. At the best of the author knowledge, the integral equation (6.13) is new.

The calculation steps from the spatial velocity profile to the unsteady lift generated by the control obstructions are illustrated in Fig. 6.6. Fig. 6.6-a shows a Gaussian inflow velocity profile entering the fan for the example of 6 regularly-spaced obstructions. The spatial velocity profile is then decomposed into strips and Fourier transformed. Fig. 6.6-b shows the circumferential Fourier transform of the spatial velocity as a function of R and w, which serves as input data in Eq. (6.7). In Fig. 6.6-b, the circumferential Fourier components of the velocity $\tilde{V}(\mathrm{w}, R) \neq 0$ if w$= 6n$. This second step is already taken into account in Eq. (6.13). Finally, the unsteady lift spectrum (Fig. 6.6-c) is obtained by solving the integral of Eq. (6.13) using the trapezoidal rule (128 radial elements are considered). The infinite sum over m is truncated from $m = -50$ to $m = 50$, which has been verified to ensure convergence.

6.5 Numerical examples

Since the experimental investigation has been carried out in this paper for a 6-bladed automotive engine cooling fan with equal blade pitches, regularly spaced obstructions along the circumference are proposed. The inner and outer radii of the rotor are respectively $R_H = 6.25$ cm and $R_T = 15$ cm. In the following examples, the control obstruction is designed to control the BPF tone. Three types of obstructions are considered here : a series of $N = 6$ trapezoidal obstructions (Fig. 6.7-a), a continuous $N = 6$-periods sinusoidal obstruction (Fig. 6.7-b) and a series of $N = 6$ cylindrical obstructions (Fig. 6.7-c). The three dimensional shape of the cylinders is not included in the model, i.e. the imposed Gaussian velocity behind cylindrical obstructions of diameter l would be the same as the gaussian velocity imposed behind rectangular obstructions of width d. The angles $\Theta(R)$ (Fig. 6.4) of the obstructions at radius R are defined as follows :

$$\Theta(R) = \Theta = \text{Const.} \qquad R_1 \leq R \leq R_2 \quad \text{Trapezoidal obstructions} \tag{6.14}$$

$$\Theta(R) = 2\sin^{-1}\frac{d}{2R} \qquad R_1 \leq R \leq R_2 \quad \text{Cylindrical or rectangular obstructions} \tag{6.15}$$

$$\Theta(R) = \frac{2}{N}\cos^{-1}\left(\frac{2R - R_1 - R_2}{R_2 - R_1}\right) \qquad R_1 \leq R \leq R_2 \quad \text{Sinusoidal obstruction} \tag{6.16}$$

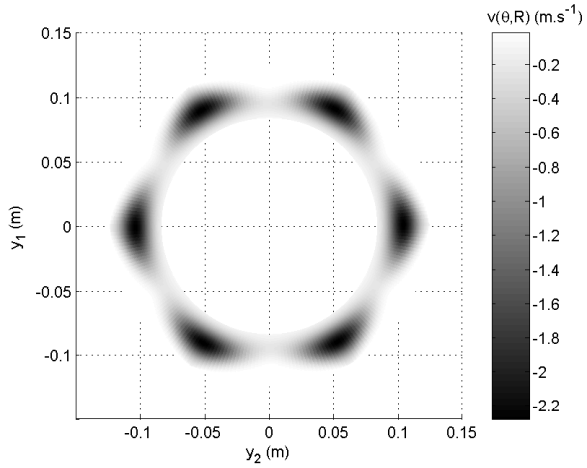

(a) Spatial velocity profile

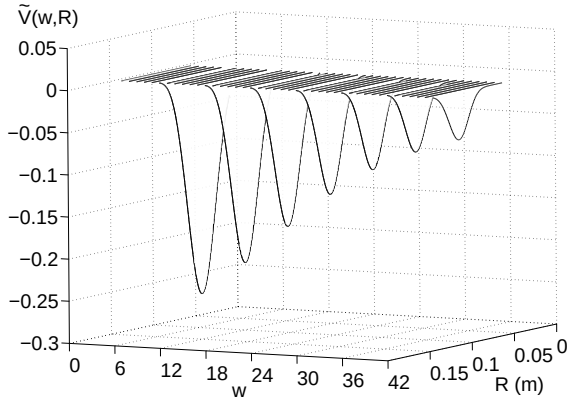

(b) Spectral velocity profile

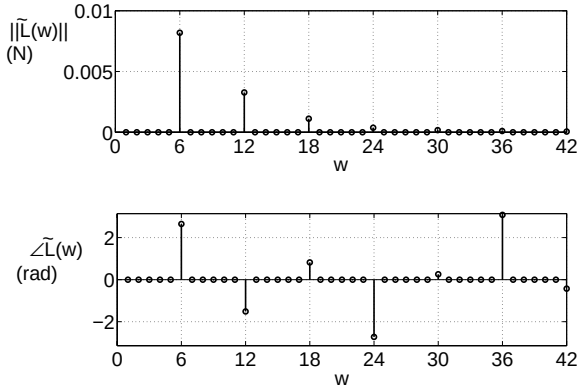

(c) Unsteady lift spectrum

Figure 6.6 Illustration of the calculation steps from the spatial velocity profile to the unsteady lift spectrum

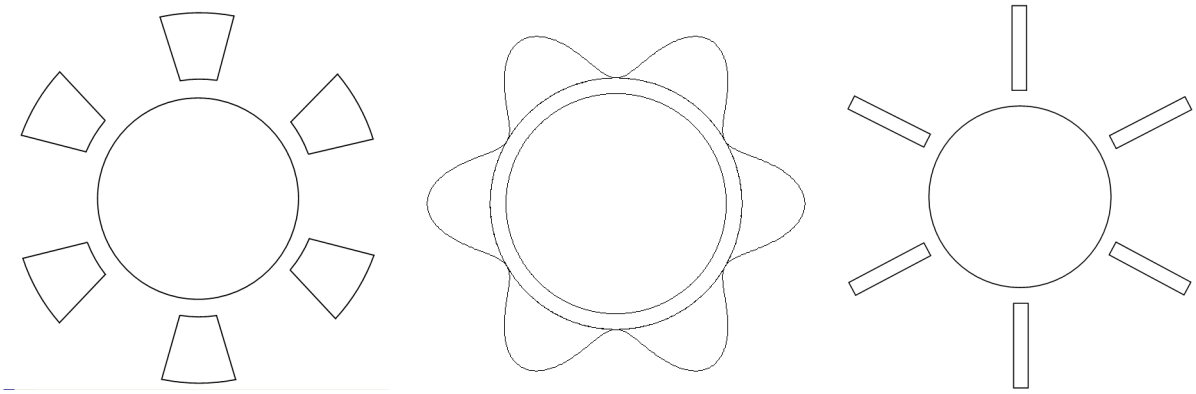

(a) 6 trapezoidal obstructions

(b) 6-periods sinusoidal obstruction

(c) 6 rectangular obstructions

Figure 6.7 The obstructions described in this paper

In the simulations presented here, the inner and outer radii of the obstructions are respectively $R_1 = 8$ cm and $R_2 = 12$ cm. The values of $\Theta(R)$ in Eqs. (6.14), (6.15) and (6.16) have to be introduced into Eq. (6.9) for the different obstructions under investigation.

The circumferential component w $= B$ of the primary unsteady lift is the most radiating at the BPF, as discussed in Section 6.3. By adding the obstructions described in this section, a secondary flow is added. Attenuation of the BPF tone is obtained when the circumferential component of the secondary lift w$= N$ is equal and opposite in phase to the circumferential component of the primary lift w$= N$. However, the higher-order circumferential components of the secondary lift w$= nN$ ($n \geq 2$) should be as small as possible in order to leave higher harmonics of the BPF unaffected by the control obstruction. Thus, the spectral content of the unsteady lift generated by the control obstructions is of interest. In this respect, the harmonic content rate $D(\%)$ is proposed and defined by :

$$D(\%) = \sqrt{\frac{\sum_{n=2}^{n_{max}} \left|\tilde{L}(nN)\right|^2}{\sum_{n=1}^{n_{max}} \left|\tilde{L}(nN)\right|^2}} \times 100 \tag{6.17}$$

where n_{max} is related to the maximum circumferential order w_{max} in Eq. (6.13) through $n_{max} = \mathrm{w}_{max}/N$. The limit $n_{max} \leq 7$ ($\mathrm{w}_{max} = n_{max} \times 6 = 42$) is imposed by the low frequency approximation of the compressible Sears function when a series of $N = 6$ obstructions is considered, as discussed in Section 6.4.1.

Note that an obstruction generating a purely sinusoidal circumferential inflow velocity distribution, thus a purely sinusoidal unsteady lift, would provide the best selection of a given single

frequency in the acoustic spectrum of the rotor. In such a case, the harmonic content rate is $D = 0\%$.

To control the $m \times BPF$ tone, the number of regularly spaced obstructions must be adjusted such that the fundamental circumferential order of the unsteady lift is $\mathrm{w} = N = mB$.

Simulations are first reported for the rotor/trapezoidal obstruction interaction, to show the influence of the product $a\Theta$ and the geometry of the blade on the unsteady lift. Then, the unsteady lift generated by the rotor/sinusoidal obstruction interaction is calculated from experimental inflow velocity measurements. Finally, the unsteady lift generated by the rotor/rectangular obstruction case is considered to compare the trapezoidal and sinusoidal flow control obstruction to a re-scaled experiment of Polacsek *et al.* [103].

6.5.1 6 trapezoidal obstructions

The case of the 6-trapezoidal obstructions/rotor interaction is useful to study the influence of the Gaussian width parameter a and the angle $\Theta(R) = \Theta = C^{te}$ of the trapezoids. Eq. (6.9) shows that the parameter of interest is the product $a\Theta$, that is representative of the wake width (Fig. 6.5). By varying $a\Theta$, it is possible to find out an optimal value of $a\Theta$ so that the harmonic content rate D is minimal, as shown in Fig. 6.8.

Two blade geometries are considered : 35° trapezoidal blades and the swept blades of an actual automotive fan under investigation in the companion paper [9]. For the trapezoidal blades, the minimum of $D = 6.7\%$ and the maximum of the ratio $\|\tilde{L}(6)\|/\|\tilde{L}(12)\| = 16$ correspond to the same value $a\Theta = 0.35$ rad, which means that most of the higher order mode energy of the lift is contained in the first harmonic $n = 2$. For the swept blades, the minimum of $D = 5.5\%$ and the maximum of the ratio $\|\tilde{L}(6)\|/\|\tilde{L}(12)\| = 18.8$ also correspond to the same value $a\Theta = 0.35$ rad. Thus, it is possible to adjust the angle Θ of the trapezoidal obstructions or the Gaussian width parameter a so that $a\Theta = 0.35$ rad.

A value of $a\Theta = 0.1$ rad is chosen to illustrate the influence of the trapezoidal obstructions on the circumferential unsteady lift spectrum. The corresponding spatial velocity defect and the spatial unsteady lift $L(\theta)$ are shown in Fig. 6.9-a and 6.9-b. The Gaussian wake assumption is particularly well adapted to this small values of $a\Theta$ (similar to the wake measured by Staiger [41]). In Fig. 6.9-b, the continuous line corresponds to the 35° trapezoidal blades and the dashed lines correspond to the automotive swept blades.

The imposed wake velocity profile generated when choosing the optimal product $a\Theta = 0.35$ rad is plotted in Fig. 6.9-c, where the dotted lines correspond to individual Gaussian velocity

profiles $e^{-\left(\frac{\theta}{a(R)\Theta(R)}\right)^2}$ (generated by individual obstructions) and the continuous line corresponds to the sum of the individual velocity profiles $\sum_{n=-\infty}^{+\infty} e^{-\left(\frac{\theta-n\theta_0}{a(R)\Theta(R)}\right)^2}$ defined in Eq. (6.8). Low overlapping of the Gaussian wakes is observed for the optimal value $a\Theta = 0.35$ rad. The spatial unsteady lift due to this imposed wake velocity profile is plotted in Fig. 6.9-d. It is clear that the lift fluctuation is almost sinusoidal.

The Gaussian overlapping at the large value $a\Theta = 0.5$ rad causes a strong velocity defect all around the circumference, as shown in Fig. 6.9-e, and the Gaussian wake approximation may not longer be valid. The corresponding spatial unsteady lift shown in Fig. 6.9-f.

In all cases, the magnitude of the unsteady lift is slightly larger for the trapezoidal blades and angular shift is also observed between the trapezoidal and the swept blades. Indeed, in practice, the blades are swept to reduce the unsteady lift by changing the phase along the leading edge when the encountered gust is radial (as it is the case for many stators and the trapezoidal obstructions).

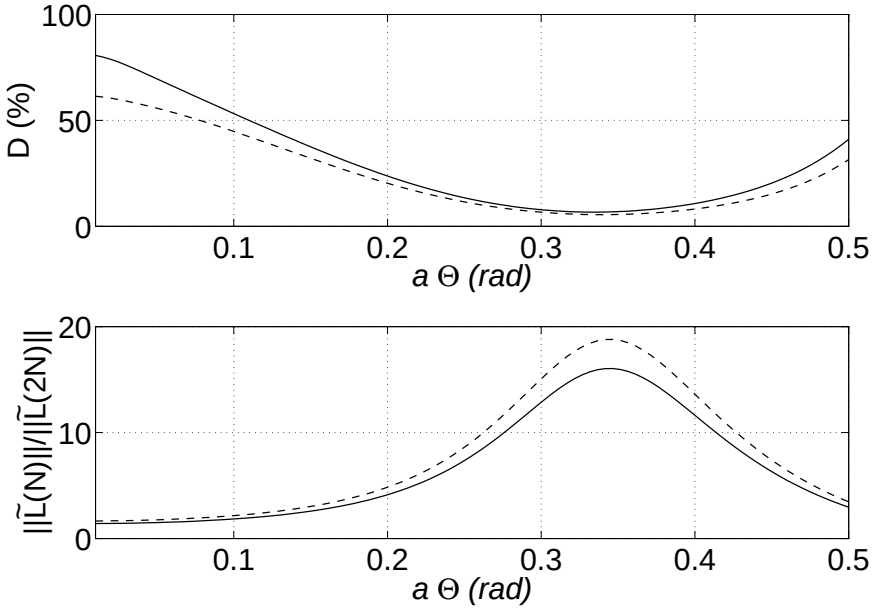

Figure 6.8 Harmonic content indicators as a function of the product $a\Theta$, $R_1 = 8\text{cm}, R_2 = 12\text{cm}$. Top : harmonic content rate $D(\%)$, bottom : ratio between the fundamental unsteady lift order and its first harmonic $\parallel \tilde{L}(N) \parallel / \parallel \tilde{L}(2N) \parallel$. Line : trapezoidal blades, dashed line : swept blades of an actual automotive fan.

Fig. 6.10 shows the normalized unsteady lift spectrum ($\frac{\tilde{L}(\text{w}=6n)}{\tilde{L}(6)}$, $1 \leq n \leq 7$) associated to the optimal wake width $a\Theta = 0.35$ rad and to the values $a\Theta = 0.1$ rad and $a\Theta = 0.5$ rad.

As observed in Figs. 6.8 and 6.9, the harmonics of the fundamental circumferential order

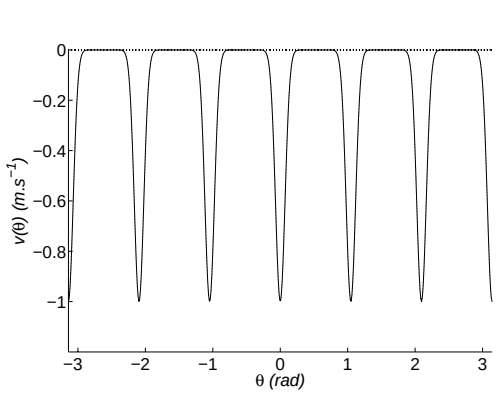

(a) Velocity profile, $a\Theta = 0.1$ rad

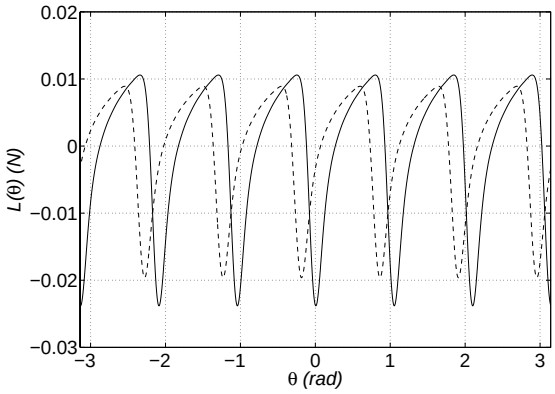

(b) Spatial unsteady lift, $a\Theta = 0.1$ rad

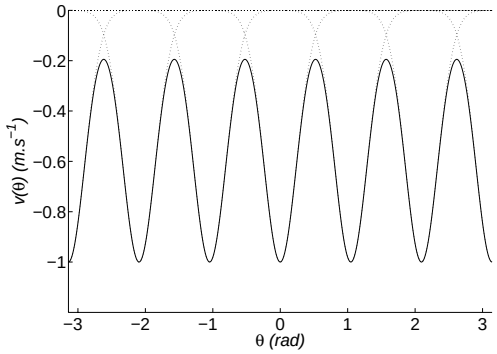

(c) Velocity profile, $a\Theta = 0.35$ rad

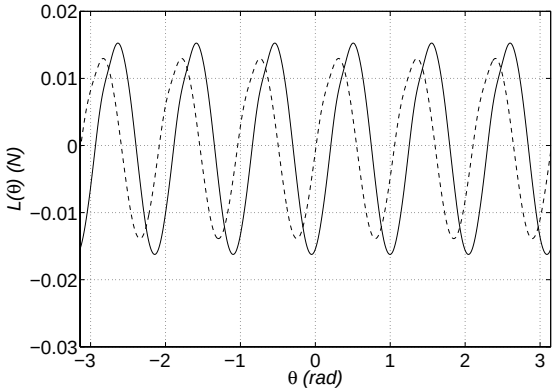

(d) Spatial unsteady lift, $a\Theta = 0.35$ rad

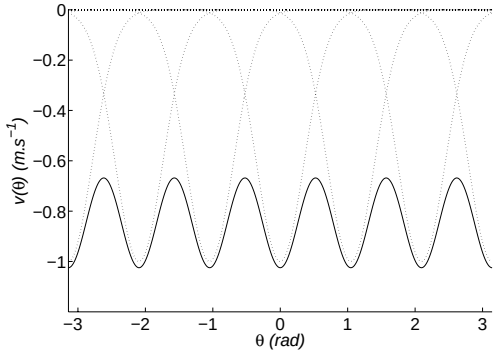

(e) Velocity profile, $a\Theta = 0.5$ rad

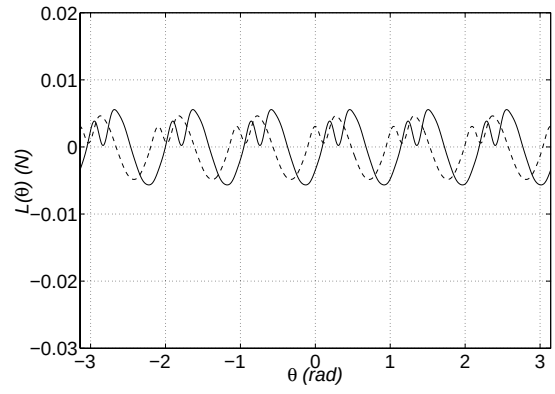

(f) Spatial unsteady lift, $a\Theta = 0.5$ rad

Figure 6.9 Gaussian overlapping for different wake widths $a\Theta$. In (a), (c) and (e), dotted lines : individual Gaussian velocity profiles and continuous lines : sum of the individual velocity profiles. In (b), (d) and (f), continuous line : trapezoidal blades, dashed line : swept blades

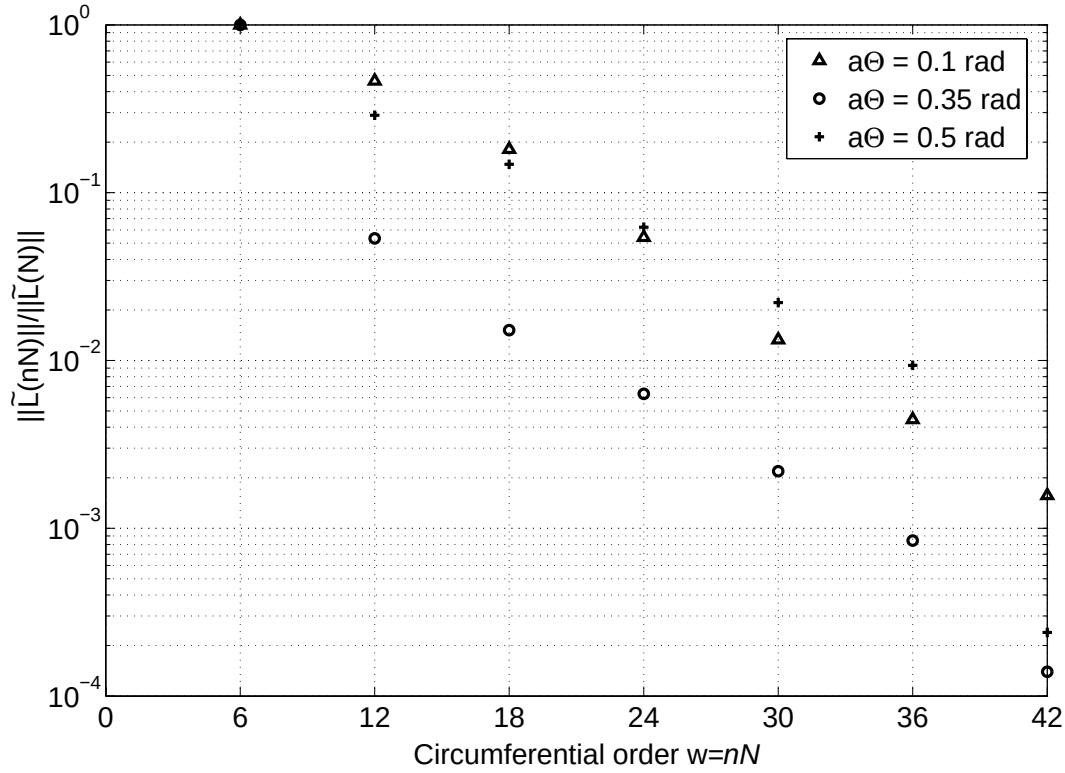

Figure 6.10 Unsteady lift spectrum - rotor/6 trapezoidal obstructions interaction for different wake widths $a\Theta$

(w = N = 6) are more energetic in the case of $a\Theta$ = 0.1 rad or $a\Theta$ = 0.5 rad than in the case of $a\Theta$ = 0.35 rad for w $\leq$ 42, or $n \leq 7$. The harmonic content rates are $D_{a\Theta=0.5} = 21.7\%$, $D_{a\Theta=0.35} = 6.0\%$ and $D_{a\Theta=0.1} = 29.1\%$. Consequently, localized and deep velocity fluctuations correspond to the generation of many circumferential components in the lift spectrum. Therefore, sharp obstructions ($a\Theta$ = 0.1 rad) or sharp circumferential zones between obstructions ($a\Theta$ = 0.5 rad) are not appropriate to selectively control a circumferential mode of the lift. The ideal analytical case $a\Theta$ = 0.35 rad ($D = 5.5\%$) will be considered as the low limit of the harmonic content rate in this paper.

Numerical parametrization of effects of the wake width generated by the rotor on the unsteady stator loading has been investigated by Waitz *et al.* [12] in turbomachines. They concluded that the Gaussian wake width at the inlet plane of the stator must be approximatively equal to the rotor pitch to maximize the amplitude of the BPF with respect to its harmonics (a 16/40 rotor-stator pitch ratio was under investigation in [12]). In the present paper, the results of the optimization of the wake width $a\Theta$ generated by the trapezoidal obstruction leads to a wake width at mid-height of the velocity defect ($2a\Theta\ln 2 = 28°$, as indicated in Fig. 6.5), which is a little smaller than the angle of the trapezoidal blades (35°). At the height v_m/e of the velocity defect, the wake width is $2a\Theta = 40°$ (Fig. 6.5), which is a little larger than the angle of the trapezoidal blades (35°). Thus, the conclusion of Waitz *et al.* can also be applied to the case of stator (control obstruction) wakes impinging in rotor blades.

6.5.2 6-periods sinusoidal obstruction

The mean wake velocity defect generated by the sinusoidal obstruction of Fig. 6.7-b has been measured with a single hot wire anemometer. The velocity measurements have then been used to approximate the coefficients of the Gaussian function describing the velocity profile behind the obstruction. The hot wire was located at various radial positions between the sinusoidal obstruction (in the upstream flow) and the rotor, near the blade leading edges (0.5 cm). The hot wire anemometer was fixed and the sinusoidal obstruction was rotated from $-\pi/6$ to $\pi/6$ (an angular period) by increments of 2°. The hot wire signal was acquired for 3.4 s, corresponding to 159 revolutions of the fan rotating at 2800 RPM. The sampling frequency was set to 4800 Hz to give 102 samples per revolution. The hot wire was aligned so that the voltage was maximum, which corresponds to a wire perpendicular to the blade leading edge, thus, giving an estimation of the transversal gust velocity (relative to the blade) generated by the sinusoidal obstruction. Fig. 6.11 shows the measured mean velocity and the adjusted Gaussian approximation of the mean velocity at different radii, defined by Eq. (6.8). Moreover, the following Gaussian function is also assumed for the radial dependence of the inflow velocity magnitude :

$$v_m(R) = v_m e^{-\left(\frac{2R-R_1-R_2}{a_R(R_2-R_1)}\right)^2} \tag{6.18}$$

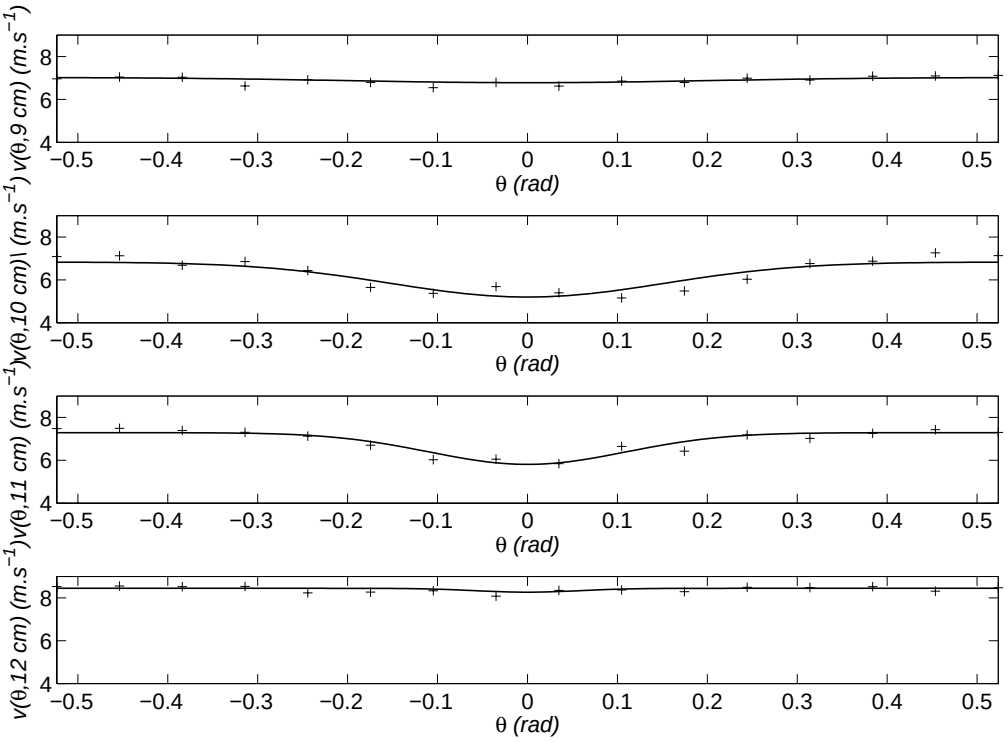

Figure 6.11 Gaussian distribution approximation (line) of the measured mean velocity defect (crosses) in the case of the sinusoidal obstruction.

The best agreement between measured experimental data and the Gaussian approximation has been obtained for $a = 0.36$, $a_R = 0.5$ and $v_m = 2$ m.s^{-1}. For simplicity, the circumferential width parameter a has been assumed independent of the radial position R. The coefficient $v_m(R)$ of the approximated Gaussian velocity function can then be introduced into Eq. (6.13). The angular sector $\Theta(R)$ of the sinusoidal obstruction as a function of the radius R defined in Eq. (6.16), and the parameter $a = 0.36$ are introduced in Eq. (6.9). The Table 6.1 shows the ratio $\parallel \tilde{L}(N) \parallel / \parallel \tilde{L}(nN) \parallel$ ($N = 6$, $1 < n < 7$) of the rotor unsteady lift spectrum generated by the interaction between the sinusoidal obstruction and the rotor. The harmonics of the fundamental circumferential unsteady lift order w = 6 are significantly below the fundamental in the lift spectrum, leading to a relatively small harmonic content rate $D = 18.1\%$. In the companion paper [9],these ratios are indirectly estimated through acoustical measurements up to the order $n = 4$ (w = 24). The sinusoidal obstruction therefore allows to control a circumferential order of the rotor unsteady lift without too much affecting the higher harmonics. In the next section, it is shown that the choice of narrow rectangular or cylindrical obstruction generates salient wakes, leading to a broader lift spectrum.

nN	6	12	18	24	30	36	42
$\parallel \tilde{L}(N) \parallel / \parallel \tilde{L}(nN) \parallel$	1	5.3	39.6	342	$7.1\times^3$	10.5×10^3	15.5×10^3

Tableau 6.1 $\parallel \tilde{L}(N) \parallel / \parallel \tilde{L}(nN) \parallel$ *ratio as a function of* nN *for the sinusoidal obstruction*

6.5.3 6 rectangular obstructions

Polacsek *et al.* have proposed to control a rotor/stator interaction mode by using a wake generator composed of cylinders of 3 mm in diameter. In their investigation, the rotor had 29 blades and the downstream stator had 33 vanes. According to the acoustic propagation conditions in a duct, the rotor/stator interaction modes are calculated from the formula $m = iB \pm jV$ [103], where i is the BPF harmonic and j is the lift harmonic order, B is the number of rotor blades and V is the number of stator vanes. Choosing 11 rods instead of 33 leads to generation of the mode $m = 1 \times 29 - 3 \times 11 = -4$, which is the only azimuthal order associated to the first radial mode that can propagate at 3500 RPM in their experimental configuration. The main disadvantage of choosing cylindrical obstructions of small diameter is that the wakes generated by the rods are very salient, leading to a high harmonic content rate of the unsteady lift. This can lead to amplification of higher acoustic tones when controlling only the BPF as noted by Polacsek *et al.* : for a sound pressure level attenuation of 8 dB at the BPF, amplifications of 6 dB, 15 dB and 11 dB were observed at the first, second and third harmonics of the BPF. Unlike Polacsek, who balances the acoustic spinning mode $m = -4$, the method proposed in the present paper consists in controlling the unsteady lift mode $N = B = 29$. However, the obstructions could also be adapted to control the spinning mode described by Polacsek [103]. The three dimensional shape of cylinder is not included in the proposed model, i.e. the imposed Gaussian velocity behind cylindrical obstructions of diameter d would be the same as the Gaussian velocity imposed behind rectangular obstructions of width d.

To simulate the unsteady lift spectrum generated by the rotor/rectangular obstructions interaction and to compare to the results already presented in this paper, an approximated equivalent re-scaled configuration is considered. Thus, a rectangular obstructions/rotor configuration using the 6-bladed rotor presented in this study and 6 rectangular obstructions of $3\text{mm} \times \frac{33}{6} = 16.5\text{mm}$ in diameter are used to simulate the most radiating rotor unsteady lift mode in free field, so that the circumferential unsteady lift spectrum can be compared to the spectra already shown in this paper.

The circumferential Gaussian width parameter a is set to 0.5, a deliberately large value that would result in a small harmonic content rate for the rectangular rotor/obstructions interaction. Moreover, no variation of the velocity profile is imposed along the radial direction ($a_R \to \infty$), similarly to the simulations carried out in Sections 6.5.1 for the trapezoidal obstruction. In Fig. 6.12, the predicted unsteady lift spectrum generated by the rectangular obstructions/rotor configura-

tion is compared to the unsteady lift spectrum generated by the 6-trapezoidal obstructions/rotor configurations ($a\Theta = 0.35$ rad, $a\Theta = 0.1$ rad) and to the 6-sinusoidal obstruction/rotor interaction.

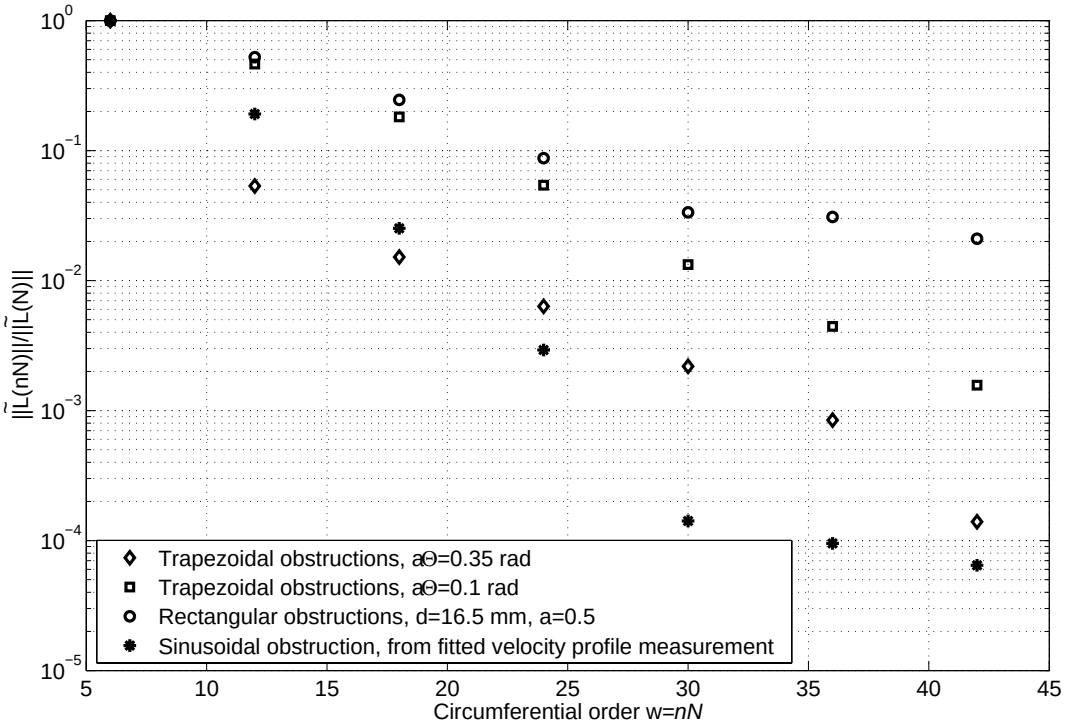

Figure 6.12 Comparison of the predicted unsteady lift spectra generated by the rectangular, sinusoidal and trapezoidal obstructions ($N = 6$).

The unsteady lift spectra due to the small rotor/rectangular obstructions interaction leads to a large harmonic content rate ($D = 45.7\%$). The salient wakes generated by the small rectangular obstructions lead to a broad lift spectrum. Thus, this solution is not selective and can not be used to control only one mode without affecting the other modes. To be selective, larger obstructions (in the circumferential direction) must be chosen.

6.6 Conclusion

A simple analytical formulation has been derived to predict the unsteady lift generated by the interaction between a rotor and an obstruction, designed to control an acoustic tone generated by the rotor. For acoustically compact fans, an acoustic tone corresponding to a multiple of the BPF is associated with essentially a given circumferential mode of the blade unsteady lift ; thererfore, it is sufficient to control only this most radiating unsteady lift mode to control each

acoustic tone. The principle of the control is thus to add a secondary unsteady lift mode, of equal intensity but opposite in phase with the primary unsteady lift mode so that the resultant of both primary and secondary lift modes is null. To control one unsteady lift mode (consequently an acoustic tone) without increasing the harmonics of the controlled mode (consequently the harmonics of the acoustic tone to be controlled), it is important for the secondary unsteady lift to be harmonically selective. The analytical formulation derived in this paper therefore provides a tool to simply evaluate the ability of the control obstruction to control one tone without affecting the other tones. The harmonic content rate of the unsteady lift generated by the proposed control obstructions can also be optimized with the proposed model.

The numerical examples show that physically compact obstructions generate salient wakes and therefore broad circumferential lift spectra. In such a case, controlling one lift mode can generate other undesirable modes. However, better designed control obstructions, such as optimized trapezoidal obstructions or sinusoidal obstructions, have a relatively low harmonic content rate. In the companion paper [9], the unsteady lift spectrum and the harmonic content rate generated by the control obstructions are indirectly estimated from experimental acoustic pressure measurements.

To optimize the geometry of a control obstruction, the rotor blade geometry must be known. Then, assuming that the wake generated by the obstruction is Gaussian, the geometrical characteristics of the obstruction can be optimized. Conversely, geometry of rotor blades (mainly the chord and the sweep as a function of the radius) can be optimized by imposing a control obstruction geometry.

Further optimization of the obstruction/blade geometries could include some of the effects neglected in this paper. A second order analysis could be investigated to take the blade camber and the mean flow angle of incidence into account [115]. Moreover, the developments of Filotas [113] or Mugridge [114] could be used to take into account non-transversal velocity profiles (e.g. derived from experimental or numerical prediction). Computational fluid dynamics (CFD) approaches could be used to refine the estimation of the pressure distribution on complex geometry blades, as proposed by Maaloum [31]. Computational fluid dynamics can also be useful to evaluate the non-stationary part of the flow.

The companion paper [9] investigates the acoustic performance of the control approach. Further insight on the control of tonal noise is first given. An experimental assessment of the rotor/obstructions interaction is carried out. Then, free-field and in-duct control performances show the ability of the approach to efficiently control the tonal noise. Finally, the impact of the obstructions on the aerodynamic performance of the fan is measured.

6.7 Acknowledgments

This work has been supported by the AUTO21 Network of Centres of Excellence (Canada) and Siemens VDO Automotive Inc. The authors wish to thank Sylvain Nadeau from Siemens Automotive Inc. and Jacky Tartarin from the Université de Poitiers (France) for their collaboration to this research.

6.8 Nomenclature

a	circumferential Gaussian width parameter
a_R	radial Gaussian width parameter
B	number of blades
c_0	speed of sound, (m.s^{-1})
C	chord of the blade (m)
D	harmonic content rate (%)
F', F''	lift per unit span (N.m^{-1}) and per unit area (N.m^{-2})
i	imaginary number $\sqrt{-1}$
J_n, K_n	ordinary and modified Bessel functions, nth order
k_0	acoustic wavenumber, $k_0 = \omega/c_0$ (rad.m^{-1})
k_θ	circumferential wavenumber $k_\theta = \mathrm{w}/R$ (rad.m^{-1})
l	cylinder diameter (m)
$\tilde{L}$	unsteady lift (N)
L_B	span of the blade (m)
M_r	rotational Mach number $M_r = \Omega R/c_0$
n	circumferential harmonic order of N, $\mathrm{w} = nN$
n_{max}	maximum circumferential harmonic order of N
N	number of cylindrical or trapezoidal obstructions, or number of lobes of the sinusoidal obstruction $N = 2\pi/\theta_0$
p	acoustic pressure (Pa)
R	radius (m)
R_1, R_2	inner and outer radius of obstructions (m)
R_m	mean radius $R_m = 0.7 \times R_T$ (m)
R_H, R_T	fan hub and tip radii (m)
S	incompressible Sears function
S_c	compressible Sears function
t	time (s)
U	tangential velocity of the rotor $U(R) = R\Omega$ (m.s^{-1})
$v, \tilde{V}$	spatial and spectral transversal inflow velocity (m.s^{-1})
v_0	circumferential uniform velocity term (m.s^{-1})

v_m	magnitude of the inflow velocity defect ($\mathrm{m.s^{-1}}$)
w	circumferential order
w_{max}	maximum circumferential order
$\mathbf{x}; r, \varphi, \alpha$	acoustic field point coordinate, spherical coordinates
γ	rotor blade pitch angle (rad)
θ	circumferential angle (rad)
θ_0	angular period (rad)
θ_c	phase variation of the chord along the span (rad)
θ_g	phase variation of the gust along the span (rad)
Θ	angle of the obstruction (rad)
ρ_0	density of air ($\mathrm{Kg.m^{-3}}$)
σ_θ	reduced frequency $\sigma_\theta = k_\theta C/2$
ω	angular frequency ($\mathrm{rad.s^{-1}}$)
Ω	angular velocity of the rotor ($\mathrm{rad.s^{-1}}$)

Subscripts and indices

m	acoustic frequency index
p	primary
s	secondary

6.9 Bilan

Dans ce chapitre, un modèle analytique reposant sur les modèles de Sears et la théorie par bande ("strip theory") a été proposé pour concevoir des obstructions permettant le contrôle d'une raie indépendamment des autres raies. Dans la littérature, les obstructions proposées sont des cylindres de faibles diamètres. Quand ces obstructions interagissent avec le rotor, elles génèrent un sillage spatial saillant, et donc beaucoup de modes circonférentiels de portance. Les cylindres présentés dans cette partie ont un taux de contenance harmonique de 45%, ce qui ne permet pas un contrôle d'un seul mode de portance indépendamment des autres. L'atténuation de la FPP risque alors de générer des harmoniques d'ordres supérieurs [103] [100] [102]. Des formes sinusoïdales et des formes trapézoïdales optimisées ont été proposées pour concevoir des obstructions de contrôle "harmoniquement pures". Pour le rotor du ventilateur de radiateur d'automobile, des taux de contenance harmonique de 5.5% et 18.8% ont respectivement été calculés pour la série de six obstructions trapézoïdales optimisée et l'obstruction sinusoïdale à 6 lobes. Les performances acoustiques de ces obstructions seront analysées dans le prochain chapitre. Les spectres de portance et les taux de contenance harmonique associés à ces obstructions y seront estimés indirectement à partir de mesures de pression acoustique.

Une règle empirique consiste à choisir des obstructions trapézoïdales possédant une portion angulaire approximativement égale à celle des pales.

CHAPITRE 7

CONTRÔLE PASSIF ADAPTÉ, PARTIE II : PERFORMANCE ACOUSTIQUE DE L'APPROCHE DE CONTRÔLE

CONTRÔLE DU BRUIT DE RAIE DES VENTILATEURS AXIAUX SUBSONIQUES EN UTILISANT DES OBSTRUCTIONS DE CONTRÔLE DANS L'ÉCOULEMENT PARTIE 1 : PERFORMANCE ACOUSTIQUE DE L'APPROCHE DE CONTRÔLE

CONTROL OF TONAL NOISE FROM SUBSONIC AXIAL FANS USING FLOW CONTROL OBSTRUCTIONS PART 1 : ACOUSTIC PERFORMANCE OF THE CONTROL APPROACH

7.1 Abstract

This paper presents the acoustic performance of a novel approach for the passive adaptive control of tonal noise radiated from subsonic fans. Tonal noise originates from non-uniform flow

that causes circumferentially varying blade forces and gives rise to a considerably larger radiated dipolar sound at the blade passage frequency (BPF) and its harmonics. The approach presented in this paper uses obstructions in the flow to destructively interfere with the primary non-uniform flow arising from stator/rotor interaction. The acoustic radiation of the obstructions is first demonstrated theoretically and then experimentally. Indirect acoustic measurements are used to validate the analytical prediction of the circumferential spectrum of the blade unsteady lift generated by the trapezoidal, sinusoidal and cylindrical obstructions presented in the companion paper [8]. The obstructions are then used to control the noise radiated both in free field and in-duct conditions. Global control was demonstrated in free field, an attenuation of 8.4 dB of the acoustic power has been measured. For the in-duct configuration, attenuation of sound pressure level up to 21 dB and 15 dB was obtained in the axial direction respectively at the BPF and at its first harmonic. Finally, the aerodynamic performances of the automotive fan used in this study are almost not affected by the presence of the control obstruction.

7.2 Introduction

Tonal noise originates from flow irregularity (non-uniform flow) that causes circumferentially varying blade forces and gives rise to a considerably large radiated dipolar sound at the blade passage frequency (BPF) and its harmonics. In many instances, axial fans operate in a non-uniform flow : this is the case of engine cooling fans that operate behind a radiator/condenser system or in the wake of inlet guide vanes.

Techniques to control fan noise can be classified into two main families : active control or passive control. The latter has been extensively studied and has allowed tonal noise to be considerably reduced (see [10] for a synthetic state of the art). These methods are principally based on the geometrical characteristics of the propeller and its environment to reduce the generation mechanisms (reduce fluctuating forces or minimize their acoustic effects). Passive techniques can be classified as *preventive techniques*. However, when passive techniques have failed, active techniques have been proposed : [6] for automotive fans, [94] for PC cooling fans or [84] for ducted fans. The active techniques are also interesting since they are effective at low frequency, where passive techniques are inefficient (such as absorbing materials). They use the destructive interference between two waves : a secondary noise generated by a secondary source (loudspeaker for example) that interferes with the fan primary noise. These techniques can be classified as *corrective techniques*.

Another approach can however be pointed out : the passive adaptive control of the forces responsible for the emitted tonal noise by homogenizing the flow entering the fan, using a particular circumferential obstruction pattern. Theoretically, the circumferential pattern having the same number of lobes as the number of rotor blades (B) will emit intensive sound at the BPF

(a mB lobed patter for the harmonic order m of the BPF). The concept is therefore to produce destructive interference between the primary source and a mB lobed-obstruction (to control the harmonic m of the BPF). The control obstruction, must be located so that the secondary radiated sound is of equal magnitude but opposite in phase compared to the primary noise. If the primary non-uniform flow is stationary, the control obstructions location must be adapted only once. However, the control obstruction locations must be adaptive to control non-stationarity non-uniform flow. This research focuss on the control of the stationary part of the non-uniform flow.

Based on the technique suggested by Nelson [102] (more detailed in the companion paper [8]), Kota et al. [13] have proposed to radially insert independent upstream rods to experimentally introduce secondary non-uniformities into the flow. The steepest-descent algorithm has been implemented to automatically adjust the protrusion of one or more cylinders into the flow in order to minimise in-duct sound power. Experimental results show that, at low fan speed (only one duct mode was present), a 6 dB reduction is obtained at the BPF in far field, whereas a reduction of 8 dB and an increase of 5 dB are to be noted for the fist harmonic and the second harmonic of the BPF. At higher fan speed (three duct modes were present), a negligible reduction of 2 dB is obtained at the BPF.

Some other recent works have been conducted on this subject and reported in the literature. Recently, a control grid (wake generator) aimed at reducing rotor/stator interaction modes in fan engines when mounted upstream of the rotor has been studied [103]. Cylindrical rods were able to generate a spinning mode of the same order and similar level as the primary interaction mode. Mounting the rods on a rotating ring allowed for adjusting the phase of the control mode so that a 8 dB sound pressure level (SPL) reduction at the BPF was achieved when the two modes were out of phase. Since the wakes generated by the rods in [103] are salient, thus have a broad spectral content, the control of a tone affect the other tones. As an illustration, the results presented in the cited paper showed amplification of 6 dB and 15 dB for the first and second harmonics of the BPF respectively. Neuhaus et al. have also used cylindrical rods to control the BPF [100].

A patent [105] was filed recently which presents a technique and an apparatus based on sinusoidal circumferential variation of the tip clearance to create a unsteady pressure field opposite in phase with respect to the primary unsteady pressure field, thus reducing tonal noise. The proposed technique is based on sinusoidal variations of the inner surface of the shroud. Other patents related to the present work can be found in the literature, such as [104], which describe a method as well as a system to control tonal noise generated by a ducted-rotor. The method rely on the introduction of upstream or downstream flow distorsions to create an anti-sound opposite in phase with respect to the primary tonal noise. An acoustic signal from one or more microphone arrays provide information to adjust each circumferential modal component of the flow. Two methods for producing the distorsions are proposed. The devices are mounted in a

circumferential array on the duct wall and consist of either 1) nozzles actively exhausting or ingesting controlled amount of air or 2) rods with actively controlled protrusion into the flow.

As opposed to what is reported in previous literature, the current work uses much more harmonically pure obstructions, which allows the control of a tone without affecting to the other tones. The goal of this paper is to characterize the acoustic performance of the flow control obstructions presented in the companion paper [8] and to show that the obstruction designed to generate a low harmonic content rate is possible. In Section 7.3, some theoretical basis for the control of tonal noise radiated from axial fans are presented. An experimental assessment and a validation of the theoretical results of the rotor/obstruction interaction, discussed in the companion paper [8], are then given in Section 7.4. Control results are then presented in Section 7.5 for free field acoustic control, using a sinusoidal obstruction geometry to control the flow non-uniformity arising from stator/rotor interaction. The approach is also validated for the control of the acoustic radiation in a duct, for different loading, using another experimental setup in Section 7.6. Finally, the aerodynamic performance of the fan is experimentally evaluated with the flow control obstruction in Section 7.7.

7.3 Control of tonal noise using flow obstruction

An insight on the tonal noise from subsonic fans is first presented as the basis of the flow obstruction control approach. Tonal noise is first related to the periodic unsteady lift acting by the rotating blades on the fluid. The approach used in this paper is the one proposed by Blake [4], where the radiated noise in free field is related to the unsteady lift experienced by the blades. Furthermore, this model is well adapted to the Sears description of the unsteady lift. This section also details and justifies the approximation of the acoustic radiation in Section 6.3 of the companion paper [8].

7.3.1 Tonal noise from subsonic fans

The rotor is considered as an array of rotating surfaces. When the fan tip Mach number is subsonic, as is the case for automotive engine cooling fans investigated in this paper, the monopolar thickness noise and the turbulent quadripolar terms can be neglected [4].

In order to examine the acoustic radiation of axial fans, it is convenient to use the polar coordinate system (R, θ, y_3) to describe the sources on the blades and the spherical coordinate system (r, φ, α) to describe the acoustic free field, as shown in Fig. 7.1. Both coordinate system origins are located at the center of the rotor.

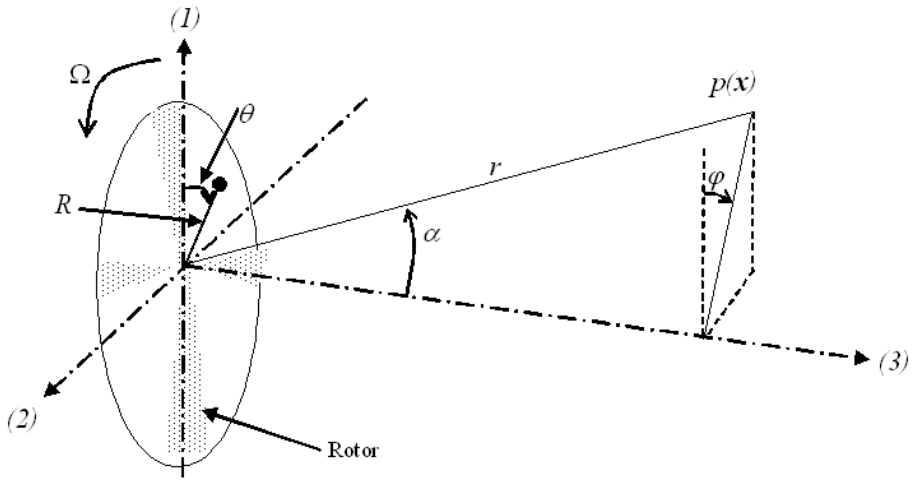

Figure 7.1 Sound radiation from a fan (Coordinate systems)

Following Blake [4], the lift per unit span on the blades $F'(R,t)$ is calculated by integrating the instantaneous pressure differential across the rotor $F''(R,\theta_b,t)$ along the chord ($-C/2R < \theta_b < C/2R$). For a circumferentially periodic inflow disturbance composed of wavelengths $2\pi R/\mathrm{w}$ (where $\mathrm{w} =]-\infty;+\infty[$ is the Fourier circumferential harmonic order of the disturbance), the circumferential and radial distribution of the fluctuating lift on the rotor blades in a frame rotating with the rotor can be expressed as follows :

$$\frac{dL(R,\theta,t)}{dR} = \sum_{b=0}^{B-1} \sum_{\mathrm{w}=-\infty}^{\mathrm{w}=+\infty} \frac{d\tilde{L}(\mathrm{w},R)}{dR} e^{-i\mathrm{w}\Omega t} e^{i\mathrm{w}\theta} \delta(\theta - b\frac{2\pi}{B}) \tag{7.1}$$

where the index b refers to the blades and the index w refers to the circumferential harmonic order of the lift, B is the number of blades and Ω is the rotation speed of the rotor in rad.s^{-1}. Eq. (7.1) represents a series of B line forces spaced at regular intervals $2\pi/B$ around the circumferential direction. As opposed to what was presented by Blake [4], the phase of the lift along the span (due to the sweep of the blade or the incident gust) is taken into account in the term $\frac{d\tilde{L}(\mathrm{w},R)}{dR}$. This term is defined in the Eq. (6.3) of the companion paper [8], which relates the circumferential harmonic decomposition of the inflow velocity normal to the blade chord to the unsteady lift per unit span.

Blake obtained the sound pressure $p(\mathbf{x},t)$, radiated by B blades at location $\mathbf{x} = (r,\varphi,\alpha)$ (see Fig. 7.1), by integrating (over the span) the product of the lift per unit span $\frac{d\tilde{L}(\mathrm{w},R)}{dR}$ projected over circumferential mode w and the appropriate Green function for rotating dipolar sources in free field. The far field approximation ($r \gg R$) is given by :

$$p(\mathbf{x},t) = \sum_{m=-\infty}^{\infty} \sum_{\mathrm{w}=-\infty}^{\infty} \left[P(\mathbf{x},\omega)\right]_{\mathrm{w},m} e^{-imB\Omega t} \tag{7.2}$$

with :

$$\begin{aligned}\left[P(\mathbf{x},\omega)\right]_{\mathrm{w},m} &= \underbrace{\frac{-ik_0 B e^{ik_0 r}}{4\pi r} e^{-i(mB-\mathrm{w})(\pi/2-\varphi)} \delta(\omega - mB\Omega)}_{\text{Acoustic wave propagation}} \times \int_{R_H}^{R_T} \underbrace{J_{mB-\mathrm{w}}(k_0 R \sin\alpha)}_{\text{Bessel function term}} \\ &\times \underbrace{\frac{d\tilde{L}(\mathrm{w},R)}{dR}}_{\text{Unsteady lift per unit span}} \times \Big[\underbrace{\cos\gamma\cos\alpha}_{\substack{\text{Axial forces}\\ \text{contribution}}} + \underbrace{\frac{mB-\mathrm{w}}{k_0 R}\sin\gamma}_{\substack{\text{Tangential forces}\\ \text{contribution}}} \Big] \quad dR \end{aligned} \tag{7.3}$$

The first summation of Eq. (7.2) represents the combination of multiple tones at angular frequencies $\omega = mB\Omega$. The second summation represents the decomposition of the lift over circumferential harmonics w. In Eq. (7.3), the first term describes the propagation of the acoustic waves, which have a wavenumber $k_0 = \omega/c_0$ (where c_0 is the speed of sound) and rotate at a circumferential phase velocity equal to $\frac{mB}{mB-\mathrm{w}}\Omega$. In the integration over the radius (from the hub radius R_H to tip radius R_T), the Bessel function term refers to the ability of a circumferential mode w to radiate sound at the harmonic of rank m of the blade passage frequency $B\Omega$. The term $\frac{d\tilde{L}(\mathrm{w},R)}{dR}$ is the contribution of the circumferential mode w to the lift per unit span acting at a radius R. The terms in brackets weight the relative importance of axial and tangential forces, which are function of the pitch angle γ.

To obtain the Eq. (6.2) of the companion paper [8] from Eq. (7.3), the fan effective area is reduced to an equivalent distribution of dipoles distributed along a mean radius of the fan $R_m = 0.7 \times R_T$ [4]. This approximation is expected to be accurate if the spatial extent of the fluctuating pressures on the rotor surface is less than a wavelength of the sound generated [19]. It is important to keep the unsteady lift per unit span into the integral to take the sweep of the blade and the sweep of the gust into account along the span. Considering the above simplifications, Eq. (7.3) can be written :

$$\begin{aligned}\left[P(\mathbf{x},\omega)\right]_{\mathrm{w},m} &\approx \frac{-ik_0 B e^{ik_0 r}}{4\pi r} e^{-i(mB-\mathrm{w})(\pi/2-\varphi)} \delta(\omega - mB\Omega) \times J_{mB-\mathrm{w}}(k_0 R_m \sin\alpha) \\ &\times \tilde{L}(\mathrm{w}) \times \left[\cos\gamma\cos\alpha + \frac{mB-\mathrm{w}}{k_0 R_m}\sin\gamma\right] \end{aligned} \tag{7.4}$$

where $\tilde{L}(\mathrm{w})$ is the lift per unit span integrated along the span :

$$\tilde{L}(\mathrm{w}) = \int_{R_H}^{R_T} \frac{d\tilde{L}(\mathrm{w}, R)}{dR} dR \tag{7.5}$$

The unsteady lift generated by the proposed control obstructions has been calculated using Eq. (6.7) in the companion paper [8]. Note that the approximate Eq. (7.4) is exact and equivalent to Eq. (7.3) on the fan axis ($\alpha = 0$).

7.3.2 Principle of the passive adaptive control of tonal noise

From the Bessel function $J_{mB-\mathrm{w}}(k_0 R \sin\alpha)$ in Eqs. (7.3) and (7.4), it can be seen that the lift circumferential harmonic of order $\mathrm{w} = mB$ is the major contributor to the tonal noise at the frequency $mB\Omega$. Thus, controlling this particular mode can lead to large tonal noise reduction in the whole space. In practice, coincidence between w and mB is avoided by choosing a number of stator vanes different to the number of rotor blades for example. However, one can use this coincidence to control the tonal noise at frequency $mB\Omega$ by superimposing a secondary unsteady lift $\tilde{L}_s(\mathrm{w} = mB)$ of equal intensity but opposite in phase relative to the most radiating circumferential component $\tilde{L}_p(\mathrm{w} = mB)$ of the primary lift. As shown in the companion paper [8], such a secondary unsteady lift can be created by carefully adjusting flow control obstructions. Assuming that the primary and secondary inflow velocity field (thus the unsteady lift) can be linearly added, the total sound field $p_t(\mathbf{x}, t)$ is the sum of the primary sound field $p_p(\mathbf{x}, t)$ and the secondary sound field $p_s(\mathbf{x}, t)$:

$$\begin{aligned} p_t(\mathbf{x}, t) &= p_p(\mathbf{x}, t) + p_s(\mathbf{x}, t) \\ &= \sum_{m=-\infty}^{\infty} \sum_{\mathrm{w}=-\infty}^{\infty} \Big([P_p(\mathbf{x}, \omega)]_{\mathrm{w},m} + [P_s(\mathbf{x}, \omega)]_{\mathrm{w},m} \Big) e^{-imB\Omega t} \end{aligned} \tag{7.6}$$

The linear assumption will be verified experimentally in section 7.4 for the automotive fan under investigation. From Eqs. (7.2) and (7.4), the total sound field can be written as a function of the sum of the primary unsteady $\tilde{L}_p(\mathrm{w})$ lift and the secondary unsteady lift $\tilde{L}_s(\mathrm{w})$:

$$p_t(\mathbf{x}, t) = \sum_{m=-\infty}^{\infty} \sum_{\mathrm{w}=-\infty}^{\infty} [H]_{\mathrm{w},m} \big(\tilde{L}_p(\mathrm{w}) + \tilde{L}_s(\mathrm{w}) \big) e^{-imB\Omega t} \tag{7.7}$$

where $\tilde{L}_s(\mathrm{w} = mB) = -\tilde{L}_p(\mathrm{w} = mB)$ to control the acoustic radiation at frequency $mB\Omega$ and H is defined as follows :

$$[H]_{\mathrm{w},m} = \frac{-ik_0 B e^{ik_0 r}}{4\pi r} e^{-i(mB-\mathrm{w})(\pi/2-\varphi)} \delta(\omega - mB\Omega) \times J_{mB-\mathrm{w}}(k_0 R_m \sin\alpha) \times \left[\cos\gamma\cos\alpha + \frac{mB-\mathrm{w}}{k_0 R_m}\sin\gamma\right] \quad (7.8)$$

To illustrate this, first consider a non-uniform inflow entering a typical 6-bladed automotive fan rotating at 3000 RPM (R_m=10 cm and $\gamma = 20°$) leading to the spatial lift fluctuation shown in Fig. 7.2 (a) and the associated circumferential spectrum of the unsteady lift shown in Fig. 7.2 (b). The lift fluctuation presented in Fig. 7.2 can be typically caused by a wake of a cylinder or a stator vane impinging the blades. The corresponding primary acoustic radiation is shown in Fig. 7.2 (c) at the BPF. The rotor is centered at the origin of the radiation space and is contained in the (x_1, x_2) plane. Then, consider a system capable of generating a secondary unsteady lift of order $\mathrm{w} = mB = 6$ of equal intensity but opposite in phase with respect to the primary unsteady lift order $\mathrm{w} = mB = 6$ (Figs 7.3 (a) and 7.3 (b)). Fig. 7.3 (c) shows the axial dipolar radiation of the secondary unsteady lift mode. The superposition of the primary and the secondary unsteady lift leads to a cancellation of the component $\mathrm{w} = mB = 6$ of the total unsteady lift (Fig. 7.4 (b)). Fig. 7.4 (a) shows the total spatial fluctuation of the lift. The total unsteady lift leads to a global reduction of sound at the BPF (Fig. 7.4 (c)). In the case depicted here, a global attenuation of the acoustic sound power of 7.5 dB is achieved.

A solution to reduce the tonal noise from axial fans is thus to create the secondary interaction mode by adding an obstruction in the upstream or downstream flow field to create a secondary non-uniform flow interacting with the rotor. This secondary non-uniform flow creates a secondary unsteady lift radiating a secondary tonal noise opposite in phase with the primary tonal noise so that the resulting sound is reduced. Thus, the control is passive but the position of the obstruction must be adapted to adjust the magnitude and the phase of the secondary interaction mode in order to minimize the tonal acoustic radiation. The adjustment of the distance between the control obstruction and the rotor allows the secondary interaction mode magnitude to be adjusted while the adjustment of the angle of the control obstruction allows the secondary interaction mode phase to be adjusted. Moreover, to control the tonal noise without affecting upper harmonics, the secondary unsteady lift should ideally contain only one circumferential harmonic ($\mathrm{w} = mB$ to control the tonal noise at the frequency $mB\Omega$). In the companion paper [8], analytical tools are provided, based on the unsteady lift theory, to analyze the spectral content of unsteady lift generated by control obstructions, and select obstruction geometries capable of creating a secondary unsteady lift with a selective harmonic content.

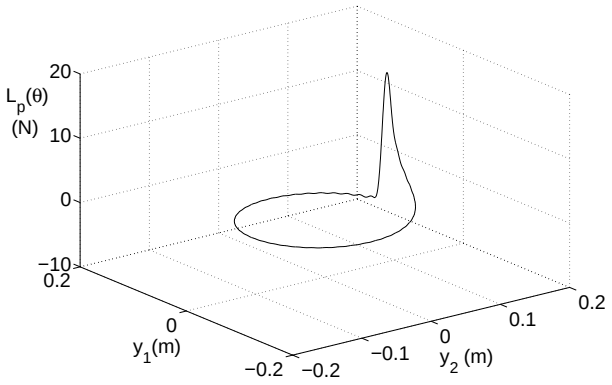

(a) Spatial primary lift

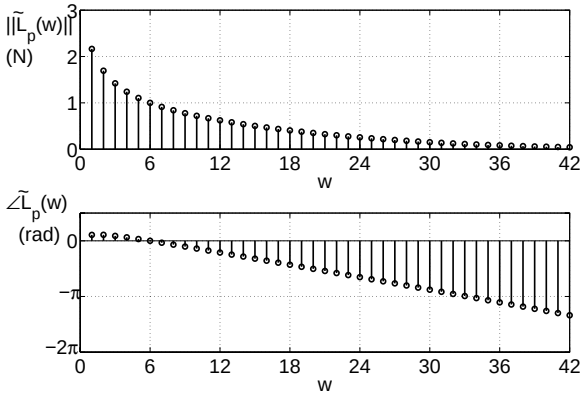

(b) Spectral primary lift

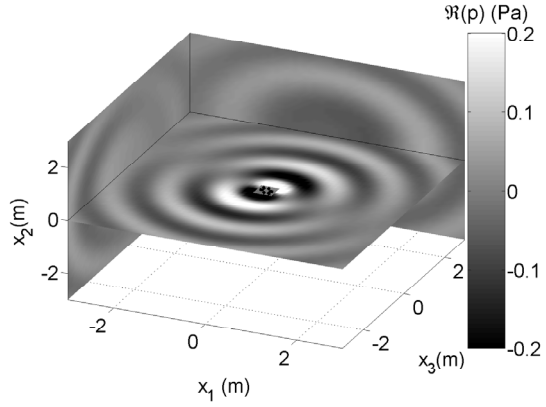

(c) Primary sound field at BPF

Figure 7.2 Primary unsteady lift and radiated sound field

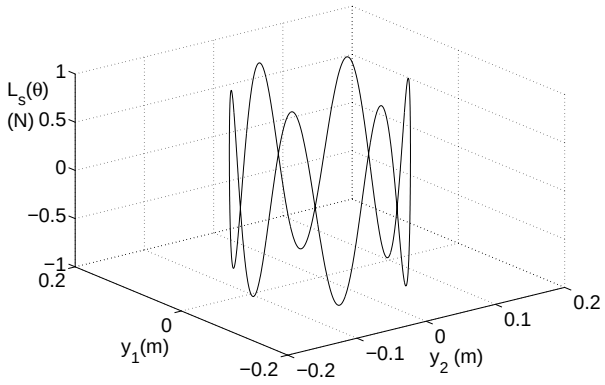

(a) Spatial secondary lift

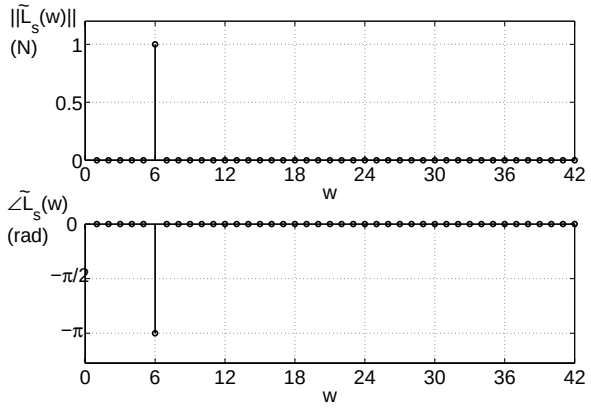

(b) Spectral secondary lift

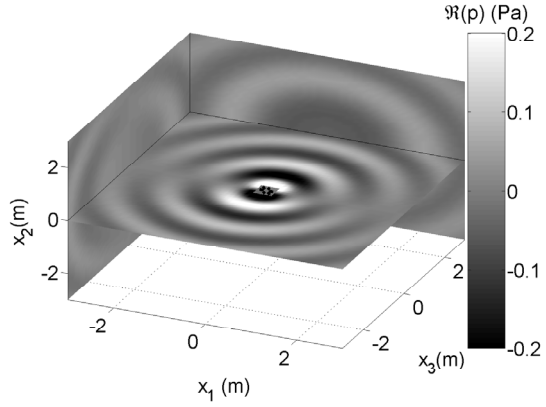

(c) Secondary sound field at BPF

Figure 7.3 Secondary unsteady lift and radiated sound field

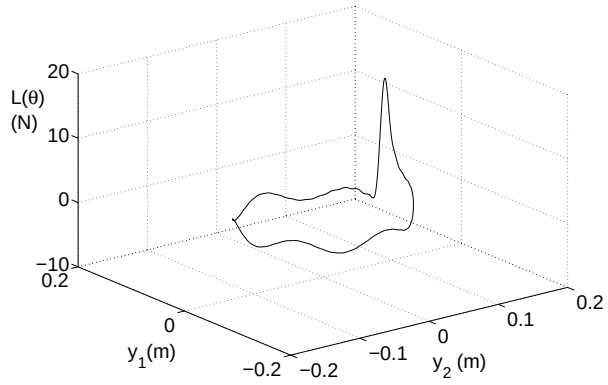

(a) Spatial resulting lift

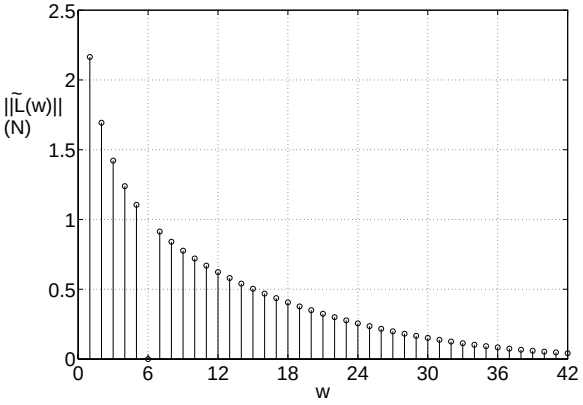

(b) Spectral resulting lift

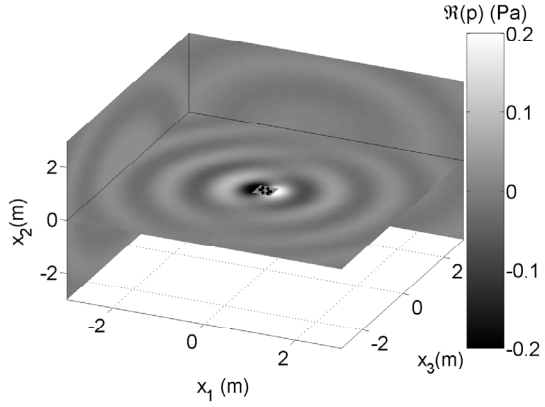

(c) Resulting sound field at BPF

Figure 7.4 Total unsteady lift and radiated sound field

7.3.3 Analysis of sound power attenuation resulting from flow control

This section is devoted to the estimation of the sound power attenuation of the BPF noise as a function of the number of cancelled circumferential components of the unsteady lift, the pitch angle of the fan, the rotational Mach number and the spectrum of the primary lift. The acoustic pressure $p(r, \alpha, \varphi)$ is defined in Eq. (7.2) for the primary sound field and in Eq. (7.6) for the total sound field with control of mode $\tilde{L}(\mathrm{w} = mB)$. The total sound power evaluated in the whole space is given by :

$$W = \frac{1}{2} \int_0^{\pi} \int_0^{2\pi} \frac{|p(r, \alpha, \varphi)|^2}{\rho_0 c_0} r^2 \sin\alpha d\varphi \, d\alpha \tag{7.9}$$

where ρ_0 is the mass density of air.

To calculate the sound power in the downstream half-space, the integration over α is calculated from 0 to $\pi/2$ and the sound power in the upstream half-space is calculated by integrating over α from $\pi/2$ to π. A typical automotive 6-bladed rotor with a mean radius of 10 cm is selected. The influence of the rotating speed and the pitch angle of the fan are analyzed in the simulation. Moreover the circumferential components $1 \leq \mathrm{w} \leq 42$ of the unsteady lift $\tilde{L}(\mathrm{w})$ are taken into account in the sound field predictions.

The total sound power W_t is calculated by inserting the total acoustic pressure defined in Eq. (7.6) into Eq. (7.9) and the primary sound power W_p is calculated by inserting the primary acoustic pressure defined in Eq. (7.2) into Eq. (7.9). Fig. 7.5 shows the sound power attenuation $10\log(W_p/W_t)$ at the BPF for different controlled modes as a function of the rotational Mach number $M_r = \frac{\Omega R_m}{c_0}$ and the pitch angle γ, when all the circumferential harmonics of the primary lift spectrum have a unitary amplitude (a Dirac in the circumferential spatial space).

The sound power attenuation at the BPF becomes larger as the number of controlled modes increases. At a rotational Mach number of $M_r = 0.1$, a gain of 12 dB can be obtained when controlling the orders w= 5, w= 6 and w= 7 of the primary unsteady lift ($\tilde{L}(5) = \tilde{L}_p(5) + \tilde{L}_s(5) = 0$, $\tilde{L}(6) = \tilde{L}_p(6) + \tilde{L}_s(6) = 0$ and $\tilde{L}(7) = \tilde{L}_p(7) + \tilde{L}_s(7) = 0$) in comparison to the control of the single component $\tilde{L}(6)$ ($\tilde{L}(6) = \tilde{L}_p(6) + \tilde{L}_s(6) = 0$).

The attenuations are larger at low rotational Mach number M_r since the importance of the circumferential orders $\mathrm{w} \neq B$ increases as the rotational Mach number increases, due to the Bessel function $J_{mB-\mathrm{w}}(k_0 R_m \sin\alpha) = J_{mB-\mathrm{w}}(mBM_r \sin\alpha)$ in Eq. (7.8). For a control of the single mode $\tilde{L}(6)$ and for a pitch angle of $\gamma = 30°$, the expected global sound power attenuations are respectively +5.2 dB and +1.3 dB for $M_r = 0.1$ and $M_r = 0.4$. The abscissa upper limit $M_r = 0.7$ almost satisfy the acoustic compacity condition since the acoustic wavelength ($\lambda =$

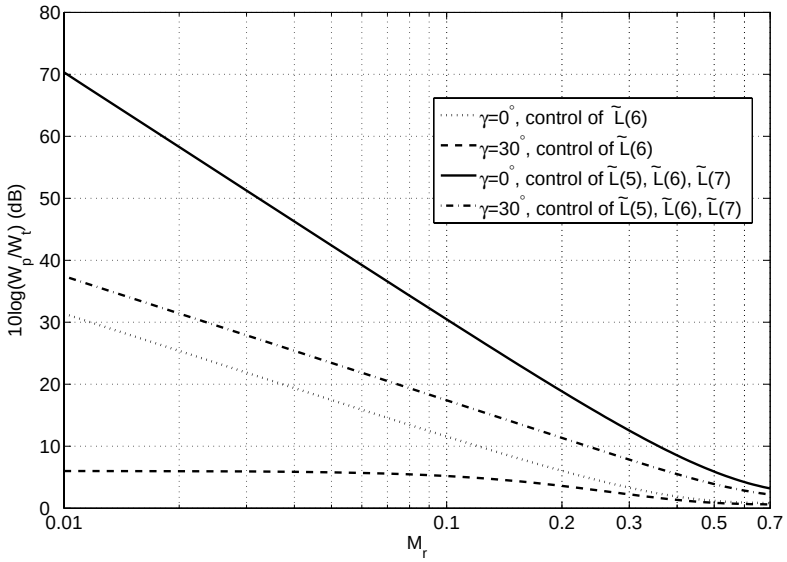

Figure 7.5 Total sound power attenuation of the BPF for a typical 6-bladed automotive axial fan. The imposed primary lift spectrum is unity for all the circumferential components

$\frac{2\pi R_m}{M_r B}$) associated to the sound wave generated at the BPF is 15 cm for the 6-bladed fan rotating with a mean radius R_m=10 cm.

The attenuation is larger for a rotor with a low pitch angle since tangential forces are theoretically zero for $\gamma = 0$. Indeed, when the pitch angle γ increases, the second term in brackets in Eq. (7.8) (which represents the contribution of tangential blade forces) increases relatively to the first term in brackets in Eq. (7.8) (which represents the contribution of axial blade forces), thus increasing the importance of unsteady lift circumferential orders w $\neq B$ in the radiated sound field relatively to the unsteady lift circumferential order w $= B$. Therefore, increasing the pitch angle of the blades requires to control more circumferential orders of the unsteady lift to keep the same level of attenuation.

Increasing the radius of the fan has the same effect as increasing the rotational Mach number (for a constant rotating speed Ω) upon the Bessel function $J_{mB-\mathrm{w}}(mBM_r \sin\alpha)$ in Eq. (7.8). Thus, the control is more effective for fans with a low radius.

When all the circumferential components of the primary lift spectrum is unity (as considered in Fig. 7.5), the upstream and downstream sound field are of equal magnitude but opposite in phase. In such a case, the cancellation of the dipolar radiation generated by the mode $\tilde{L}(6)$ leads to the same sound attenuation upstream and downstream. However, if the circumferential components of the primary lift spectrum are not equal, the acoustic radiation is not symmetric (except if $\gamma = 0°$). Since, in this case, the contribution of the mode $\tilde{L}(6)$ relatively to the

contribution of the modes $\tilde{L}(\mathrm{w} \neq 6)$ to the radiated sound power are not the same upstream and downstream, the attenuation may vary upstream and downstream when controlling the mode $\tilde{L}(6)$. For example, in the example given in Section 7.3.2, the upstream attenuation is 8.1 dB and the downstream attenuation is 7.2 dB.

For a typical automotive fan ($R_H = 6$ cm, $R_T = 14$ cm and $\gamma = 15°$) with a mean radius $R_m = 10$ cm, a global attenuation around +9 dB is expected when controlling the mode $\tilde{L}(6)$ of the actual primary lift spectrum of the fan which has been estimated by using an inverse aeroacoustic model [7]. Expected attenuations range from +13 dB for a fan rotating at 1000 RPM and a pitch angle of $\gamma = 10°$ to +5 dB for a fan rotating at 3000 RPM and a pitch angle of $\gamma = 30°$. Experimental results using the added triangular obstruction in the plane of the stator will be shown in section 7.5.

7.4 Experimental assessment of the rotor/ obstruction interaction

7.4.1 Experimental setup

An experimental setup has been used to demonstrate that the interaction between the rotor and the obstructions can generate noise and eventually destructively interfere with the primary noise arising from the stator/rotor interaction, depending on the position and orientation of the obstruction upstream the fan.

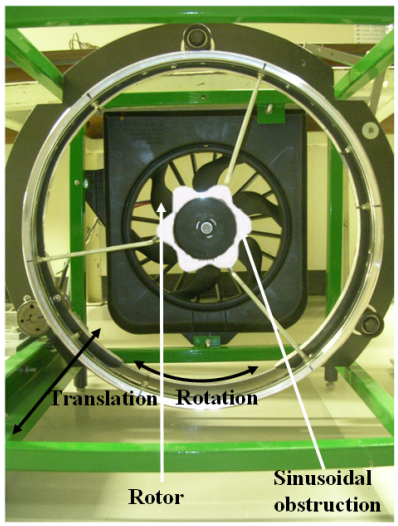

Figure 7.6 Experimental setup to study the acoustic radiation resulting from the rotor and the upstream obstruction.

Fig. 7.6 presents the experimental setup used to evaluate the acoustic radiation arising from

the interaction between the rotor and the control obstructions (a sinusoidal obstruction is used for illustration). An engine cooling unit (axial fan mounted in a shroud) is installed in a frame, downstream a positioning device allowing for the obstruction to be moved in the axial and angular directions. The fan has six regularly spaced blades and its rotational velocity is 2900 RPM, corresponding to a BPF at 290 Hz. The internal diameter of the fan is 12.5 cm while its external diameter is 30 cm. The 6-period sinusoidal obstruction shown in Fig. 7.6 is made of plexiglas and have an inner radius of R_1=5.5 cm and an outer radius of R_2 =7 cm.

Acoustic pressure measurements were performed in an anechoic room with and without control obstruction to extract the contribution of the obstruction to the total radiated acoustic pressure.

An upstream microphone (B&K type 4189 pre-polarized $1/2''$) was located on the fan axis at a distance of 2 m. The results are averaged over 20 sample blocks with a spectral resolution of 1 Hz between 0 and 2000 kHz. The experiments are conducted first without the radiator but with a small tape (2 cm×4 cm) between two stator vanes to slightly increase the non-uniformity of the flow ingested by the rotor.

7.4.2 Sound pressure level measurements

The acoustic pressure measurements were conducted at the BPF and its first three harmonics for 651 axial and angular locations of the sinusoidal, trapezoidal and cylindrical control obstructions (Fig. 7.7) presented in the companion paper [8]. In the following, z_s is the axial distance between the rotor and the control obstruction and θ_s is the angular position of the control obstruction. The control obstruction is translated by δ_{zs} =0.5 cm increments in the axial direction from z_s =13.5 cm to z_s =8.5 cm and by δ_{zs} =0.25 cm increments from z_s =8.25 cm to z_s =3.5 cm. The control obstruction is rotated by δ_{θ_s} =3° increments over a period of $2\pi/6$ for each axial position.

Fig. 7.8 shows the sound pressure level at BPF, 2×BPF, 3×BPF and 4×BPF (respectively in Figs. 7.8-a, 7.8-b, 7.8-c and 7.8-d) as a function of the axial distance and angular position of a 6-trapezoidal obstruction, for a small angle $\Theta = 10°$ of the trapezoids (see Fig. 7.7-a). Fig. 7.8 (a) shows that, to minimize the acoustic pressure level at the BPF, the optimal axial distance between the rotor and the control obstruction is z_s^{opt} =5.25 cm and the optimal angular position is about $\theta_s = 24°$. In this orientation, the circumferential harmonic of order 6 of the primary unsteady lift is out of phase with the circumferential harmonic of order 6 of the secondary unsteady lift. It can also be seen that, at BPF and for $24° + \frac{360°}{2\times6} = 54°$ orientation, the 6-trapezoidal obstruction creates a secondary acoustic field in phase with that created by the primary rotor/stator interaction.

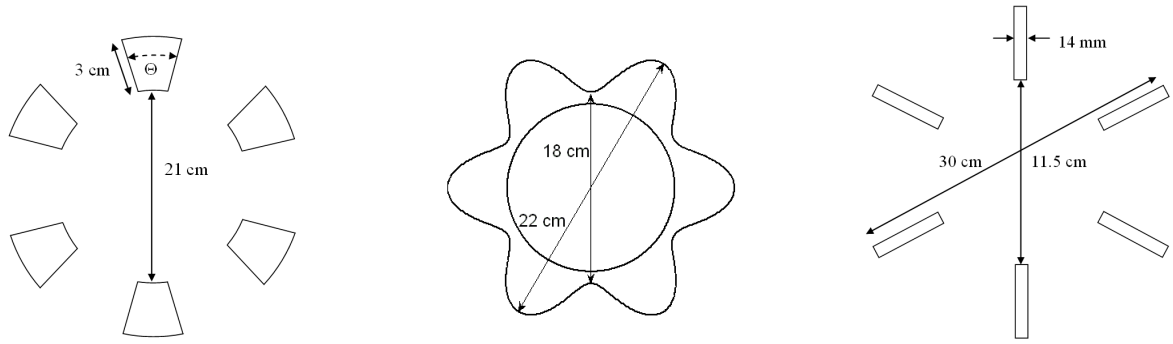

(a) Trapezoidal obstructions

(b) Sinusoidal obstructions

(c) Cylindrical obstruction

Figure 7.7 Geometries of the control obstructions

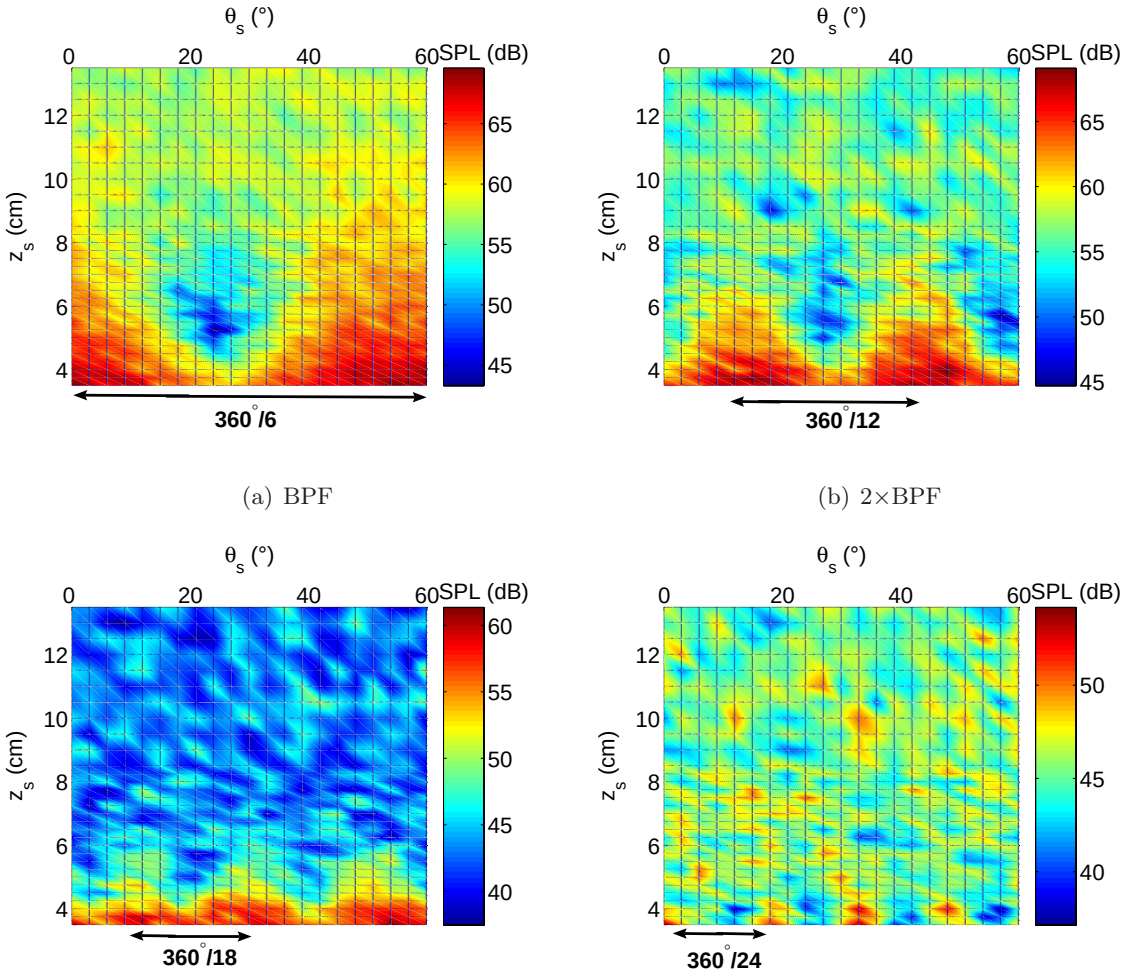

(a) BPF

(b) 2×BPF

(c) 3×BPF

(d) 4×BPF

Figure 7.8 Sound pressure level as a function of the control obstruction location - 6-trapezoidal obstruction ($\Theta = 10°$), leading to a high harmonic content rate

In Fig. 7.9, the sound pressure level is plotted as a function of the angular position of the control obstruction for the optimal axial distance. The primary acoustic pressure level is increased by about 6 dB when the primary unsteady lift and the secondary unsteady lift are in phase. It validates the assumption of the linear superposition of the two acoustic sound fields in Eq. (7.6). It has also been verified for all the obstructions shown in this paper. The evolution of the BPF tone as a function of the obstruction orientation is characteristic of an interference pattern.

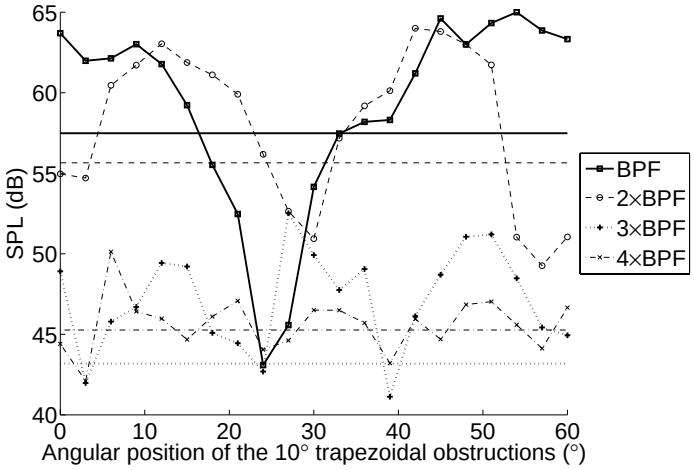

Figure 7.9 Sound pressure level produced by the $\Theta = 10°$ 6-trapezoidal obstruction at optimal axial location z_s^{opt}, measured by the upstream on-axis microphone.

As seen in Fig. 7.9 and in Figs. 7.8 (b), 7.8 (c) and 7.8 (d), the 6-trapezoidal obstruction also tends to affect the higher order harmonics. For example, in Fig. 7.8 (b), the acoustic pressure level measured for the harmonic $2 \times BPF$ varies with an angular period two times shorter than for BPF. The amplitude of the variation of the acoustic pressure level is also smaller than for BPF. As anticipated in the companion paper [8], these results confirm that a low angle Θ 6-trapezoidal obstruction has a non-negligible contribution to the circumferential order $w = 2B$ of the total unsteady lift, which radiates sound at the frequency 2×BPF. In Figs. 7.8 (c) and 7.8 (d), the acoustic pressure level measured for the harmonic $3 \times BPF$ and $4 \times BPF$ respectively vary with an angular period three times and four times shorter than for BPF, especially at low axial distance z_s. However, these higher harmonics of the BPF seem to be less affected by the 10° six-trapezoidal obstruction.

7.4.3 Validation of the theoretical results of part I - Unsteady lift generated by the control obstructions

An indirect estimation of the unsteady lift generated by the control obstructions, based on the sound pressure level measurements previously shown is proposed to validate the theoretical results of the companion paper [8].

Calculation

From Figs. 7.9 and 7.8, we can see that the $\Theta = 10°$ 6-trapezoidal obstruction affects the harmonics of the BPF (especially its first harmonic). It has also been shown analytically [8], that the circumferential order $\mathrm{w} = B$ is not the only circumferential order in the unsteady lift spectrum generated by obstructions. To compare the analytical prediction of the unsteady spectrum generated by the trapezoidal, sinusoidal and cylindrical obstructions, the ratios $\parallel \tilde{L}_s(B) \parallel / \parallel \tilde{L}_s(mB) \parallel$ are now indirectly estimated from the acoustic pressure level as a function of the control obstruction location, by manipulating Eq. (7.7) and Eq. (7.8).

Following Eq. (7.7), the acoustic pressure is obtained from the linear superposition of the primary and the secondary unsteady lift, respectively noted $\tilde{L}_p$ and $\tilde{L}_s$ due to the B-lobed sinusoidal obstruction [8]. Taking into account the dependance of the acoustic pressure and the secondary lift as a function of the location (z_s, θ_s) of the control obstruction, and by considering the particular case of the sound radiation in the axial direction $\mathbf{x} = (r, 0, 0)$, Eq. (7.7) can be written as follows in the frequency domain :

$$p(r,0,0,mB\Omega,z_s,\theta_s) = \sum_{m=-\infty}^{\infty} \sum_{\mathrm{w}=-\infty}^{\infty} \left[H(r,0,0;\omega)\right]_{\mathrm{w},m} \left(\tilde{L}_p(\mathrm{w}) + \tilde{L}_s(\mathrm{w},z_s,\theta_s)\right) \tag{7.10}$$

where $\tilde{L}_s(\mathrm{w} = B, z_s^{opt}, \theta_s^{opt}) = -\tilde{L}_p(\mathrm{w} = B)$ to cancel the acoustic radiation at the BPF ($B\Omega$) on the axis. The effect of the axial distance z_s (between the rotor and the control obstruction) on the wake width, thus on the unsteady lift spectrum $\tilde{L}_s(\mathrm{w}, z_s, \theta_s)$ and the related indicators, have not been taken into account in the analytical modelling presented in the companion paper [8]. As long as the wake can be considered Gaussian, it could be formally taken into account by writing the Gaussian width parameter as a function of z_s : $a(z_s)$.

In the axial direction ($\alpha = 0$) only the circumferential harmonic mB of the unsteady lift radiates sound at frequency $mB\Omega$ because only the 0^{th} order Bessel function in Eq. (7.3) takes a non-zero value when its argument is zero ($J_0(0) = 1$). Thus, in the axial direction, the radiation transfer function is reduced to :

$$\left[H(r,0,0;\omega)\right]_{\mathrm{w}=mB} = -\frac{imB^2\Omega}{4\pi r c_0}\cos\gamma \tag{7.11}$$

By writing the complex value of the unsteady lift in terms of magnitude and phase : $\tilde{L}_p(\mathrm{w}) = L_p(\mathrm{w})e^{i\mathrm{w}\theta_p^L(\mathrm{w})}$ and $\tilde{L}_s(\mathrm{w}, z_s, \theta_s) = L_s(\mathrm{w}, z_s)e^{i\mathrm{w}\theta_s^L(\mathrm{w},z_s,\theta_s)}$, where $L_p(\mathrm{w})$ and $L_s(\mathrm{w}, z_s)$ are respectively the magnitude of the circumferential component w of the primary and secondary lift and $\theta_p^L(\mathrm{w})$ and $\theta_s^L(\mathrm{w}, z_s, \theta_s)$ are respectively the phase of the circumferential component w of the

primary and secondary lift, the acoustic pressure at the harmonic m of the BPF as a function of the location of the control obstruction (z_s, θ_s) can be written as follows :

$$\begin{aligned} p_t(r,0,0,mB\Omega,z_s,\theta_s) &= p_p(r,0,0,mB\Omega) + p_s(r,0,0,mB\Omega,z_s,\theta_s) \\ &= -\frac{imB^2\Omega}{4\pi r c_0}\cos\gamma \times \left(L_p(mB)e^{imB\theta_p^L(mB)} + L_s(mB,z_s)e^{imB\theta_s^L(mB,z_s,\theta_s)}\right) \end{aligned} \tag{7.12}$$

The dependance of the secondary unsteady lift as a function of the axial distance z_s between the rotor and the control obstruction is formally taken into account in the magnitude $L_s(\mathrm{w}, z_s)$ and the phase $\theta_s^L(\mathrm{w}, z_s, \theta_s)$ of the unsteady lift. The phase of the secondary unsteady lift also depends on the angular location of the control obstruction θ_s in the following way : $\theta_s^L(\mathrm{w}, z_s, \theta_s) = \theta_s + \theta_s^L(\mathrm{w}, z_s, 0)$. The term $\theta_s^L(\mathrm{w}, z_s, 0)$ refers to the ability of the phase of the secondary unsteady lift to change as a function of z_s, due to swirl of the flow for example. No such effect has been observed for the obstructions used in this paper ($\theta_s^L(\mathrm{w}, z_s, 0) = \theta_s^L(\mathrm{w}, z_s^{opt}, 0)$), which is of practical interest when adjusting the position of the control obstruction (since, in this case, the change in magnitude and the change in phase of the secondary sound field are not coupled as a function of the axial distance z_s).

A particular case can be pointed out when the angular location of the control obstruction θ_s is chosen such that the primary and secondary unsteady lifts are in phase ($\theta_p^L(mB) = \theta_s^L(mB, z_s, \theta_s)$). In this case, the acoustic pressure is maximal and the absolute value of Eq. (7.12) leads to :

$$\| \, p_t(r,0,0,mB\Omega,z_s,\theta_p^L = \theta_s^L) \, \| = \frac{mB^2\Omega}{4\pi r c_0}\cos\gamma \times (L_p(mB) + L_s(mB,z_s)) \tag{7.13}$$

Moreover, the contribution of the primary lift $L_p(mB)$ can be estimated from the acoustic pressure measurement without the control obstruction, which can be formally calculated from Eq. (7.12) with $L_s = 0$:

$$L_p(mB) = \frac{4\pi r c_0}{mB^2\Omega\cos\gamma} \times \| \, p_p(r,0,0,mB\Omega) \, \| \tag{7.14}$$

Finally, the circumferential components $L_s(mB)$ of the secondary lift can be calculated by inserting Eq. (7.14) into Eq. (7.13) :

$$L_s(mB, z_s) = \frac{4\pi r c_0}{mB^2\Omega \cos\gamma} \times \left(\parallel p_t(r, 0, 0, mB\Omega, z_s, \theta_p^L = \theta_s^L) \parallel - \parallel p_p(r, 0, 0, mB\Omega) \parallel \right) \quad (7.15)$$

where $\parallel p_t(r, 0, 0; 1B\Omega, z_s, \theta_p^L = \theta_s^L) \parallel$ is the magnitude of the sound pressure in the axis when the primary and secondary lift are in phase, corresponding to approximative angular positions of the 10° trapezoidal obstruction $\theta_s = 24° + \frac{360\,°}{2\times 6} = 54°$ for $m = 1$, and about $\theta_s = 15°$ and $\theta_s = 45°$ for $m = 2$ in Fig. 7.9. The horizontal lines correspond to primary acoustic pressures $\parallel p_p(r, 0, 0; mB\Omega) \parallel$ without control obstruction.

In order to compare the estimated circumferential components of the secondary lift to the theoretical results of the companion paper [8], the following dimensionless ratios are calculated from Eq. (7.15) :

$$\frac{\parallel \tilde{L}_s(1B, z_s) \parallel}{\parallel \tilde{L}_s(mB, z_s) \parallel} = m \times \frac{\parallel p_t(r, 0, 0; 1B\Omega, z_s, \theta_p^L = \theta_s^L) \parallel - \parallel p_p(r, 0, 0; 1B\Omega) \parallel}{\parallel p_t(r, 0, 0; mB\Omega, z_s, \theta_p^L = \theta_s^L) \parallel - \parallel p_p(r, 0, 0; mB\Omega) \parallel} \quad (7.16)$$

Moreover, the harmonic content rate D is used to compare the ability of the various obstructions tested in this paper to control the fundamental of the circumferential unsteady lift spectrum without generating upper harmonics in both the unsteady lift spectrum and the acoustic spectrum. The harmonic content rate is defined as follows [8] :

$$D(z_s) = \sqrt{\frac{\sum_{m=2}^{m_{max}} \parallel \tilde{L}_s(mB, z_s) \parallel^2}{\sum_{m=1}^{m_{max}} \parallel \tilde{L}_s(mB, z_s) \parallel^2}} \times 100 \quad (7.17)$$

where $\tilde{L}_s(mB)$ is defined in Eq. (7.15).

The two harmonic content indicators (the ratios $\frac{\|\tilde{L}_s(\mathrm{w}=1B, z_s)\|}{\|\tilde{L}_s(\mathrm{w}=mB, z_s)\|}$ and the harmonic content rate $D(z_s)$) are estimated for several discretized axial distances $z_{s,i}$ between the rotor and the control obstruction, when the mB periodicity of the SPL at the harmonic $m\times$BPF as a function of the angular position of the control obstruction θ_s is clearly visible. In Fig. 7.8, the indicators are estimated from the optimal location $z_s^{opt} = 5.25$ cm to the nearest location z_{sN} =3.5 cm, where N is the number of discretized axial distance for which the two indicators are calculated. To provide a range of these estimators valid for various axial locations of the control obstructions (thus to control various magnitude of the primary sound pressure), they are averaged over the axial distances z_{sn}. Averaged values and standard deviations are calculated as follows :

$$D = \frac{1}{N}\sum_{n} D(z_{s,n}) \tag{7.18}$$

$$\sigma_D = \sqrt{\frac{1}{N}\sum_{n} (D(z_{s,n}) - D)^2} \tag{7.19}$$

$$\frac{\parallel \tilde{L}_s(\mathrm{w}=1B) \parallel}{\parallel \tilde{L}_s(\mathrm{w}=mB) \parallel} = \frac{1}{N}\sum_{n} \frac{\parallel \tilde{L}_s(\mathrm{w}=1B, z_{s,n}) \parallel}{\parallel \tilde{L}_s(\mathrm{w}=mB, z_{s,n}) \parallel} \tag{7.20}$$

$$\sigma_{\frac{\|\tilde{L}_s(\mathrm{w}=1B)\|}{\|\tilde{L}_s(\mathrm{w}=mB)\|}} = \sqrt{\frac{1}{N}\sum_{n} \left(\frac{\parallel \tilde{L}_s(\mathrm{w}=1B, z_{s,n}) \parallel}{\parallel \tilde{L}_s(\mathrm{w}=mB, z_{s,n}) \parallel} - \frac{\parallel \tilde{L}_s(\mathrm{w}=1B) \parallel}{\parallel \tilde{L}_s(\mathrm{w}=mB) \parallel} \right)^2} \tag{7.21}$$

In this paper, the indicators are presented as the averaged value D (or $\frac{\|\tilde{L}_s(\mathrm{w}=1B)\|}{\|\tilde{L}_s(\mathrm{w}=mB)\|}$) $\pm$ the standard deviation σ_D (or $\sigma_{\frac{\|\tilde{L}_s(\mathrm{w}=1B)\|}{\|\tilde{L}_s(\mathrm{w}=mB)\|}}$).

The first effect of the averaging over the axial distance z_s is to minimize the effect of random uncertainties on the two indicators. The second effect of the averaging over the axial distance z_s is to eventually average a deterministic variation of the wake width (as a function of z_s) generated by the obstruction upon the two indicators. Indeed, the wake disturbance velocity impinging the rotor blades can be sharper for low axial distance z_s [15], thus increasing the contribution of the circumferential harmonics contained in the unsteady lift spectrum. Thus $D(z_s)$ increases and $\frac{\|\tilde{L}_s(\mathrm{w}=1B,z_s)\|}{\|\tilde{L}_s(\mathrm{w}=mB,z_s)\|}$ decreases when decreasing z_s.

Effect of the wake width generated by 6-trapezoidal obstructions

Several trapezoidal obstruction angles $\Theta = [10°, 20°, 30°, 35°, 40°, 50°]$ were experimentally tested to verify the analytical prediction shown in Fig. 6.8 of the companion paper [8].

Since no anemometric measurements were carried out for the trapezoidal obstructions, the Gaussian width parameter $a = 0.5$ has been imposed in Fig. 7.10 to compare the measured values of the harmonic content rate $D(\%)$ and the ratio $\frac{\|\tilde{L}_s(\mathrm{w}=1B)\|}{\|\tilde{L}_s(\mathrm{w}=2B)\|}$ to the analytical predictions. The error bars correspond to $\pm$ one standard deviation around the averaged values of the harmonic content indicators, as explained in Section 7.4.3. The experimental estimations of the harmonic content rate and the ratio $\frac{\|\tilde{L}_s(\mathrm{w}=1B)\|}{\|\tilde{L}_s(\mathrm{w}=2B)\|}$ are in good agreement with the analytical predictions when imposing a Gaussian wake parameter $a_R = 0.5$ for the radial dependence of the inflow velocity magnitude in the analytical modelling, as shown in Eq. (6.18) of the companion paper. The radial wake width coefficient $a_R = 0.5$ was estimated from hot wire anemometer measurements

behind a sinusoidal obstruction. Since the radial extent of the trapezoidal obstructions used in this section is approximatively equal to the radial extent of the sinusoidal obstruction, $a_R = 0.5$ is expected to be accurate for trapezoidal obstructions. When no Gaussian distribution in the radial direction is included in the analytical model ($a_R \to \infty$), the differences are quite large but trends are similar to the experimental estimations of $D(\%)$ and the ratio $\frac{\|\tilde{L}_s(\mathrm{w}=1B)\|}{\|\tilde{L}_s(\mathrm{w}=2B)\|}$. It can be seen that the standard deviations associated to the ratios $\frac{\|\tilde{L}_s(\mathrm{w}=1B)\|}{\|\tilde{L}_s(\mathrm{w}=2B)\|}$ is high for the trapezoidal obstructions with a low harmonic content rate : for $\Theta = 35°$, the high standard deviation is due to the random uncertainties of the two indicators and for $\Theta = 40°$, the high standard deviation is associated to a monotonic decrease of the ratio $\frac{\|\tilde{L}_s(\mathrm{w}=1B,z_s)\|}{\|\tilde{L}_s(\mathrm{w}=2B,z_s)\|}$ as a function of z_s.

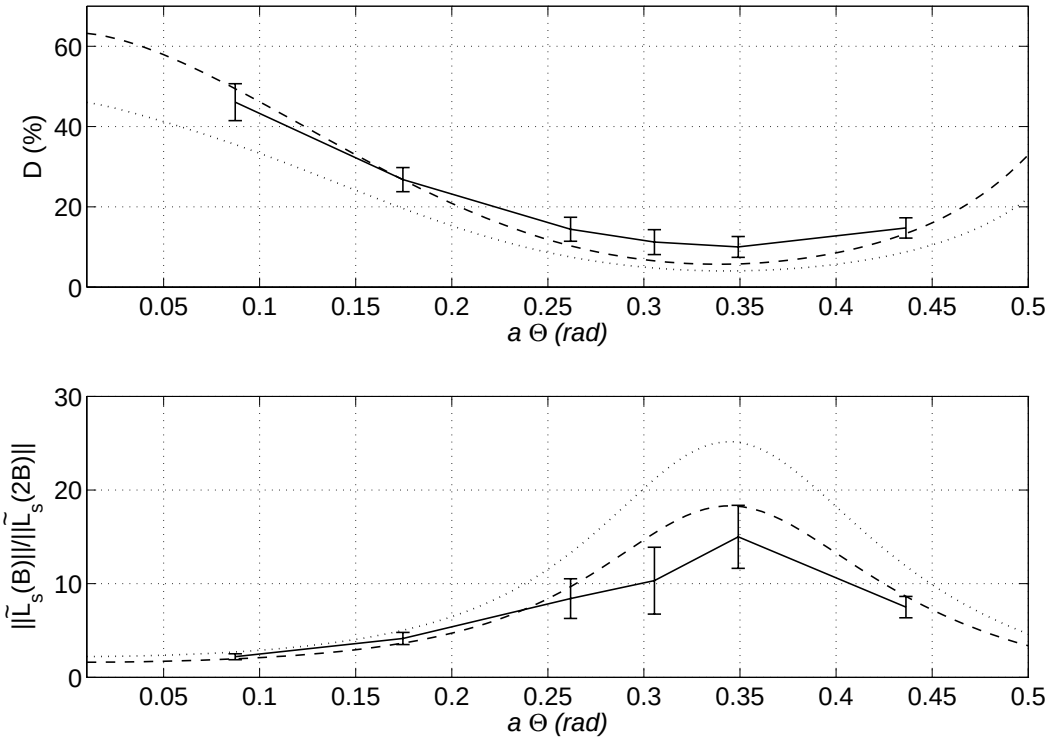

Figure 7.10 Harmonic content indicators, associated to the circumferential unsteady lift spectrum generated by 6-trapezoidal obstructions, as a function of the product $a\Theta$ for an actual automotive fan. Top : harmonic content rate $D(\%)$, bottom : ratio between the fundamental unsteady lift order and its first harmonic $\frac{\|\tilde{L}_s(\mathrm{w}=1B)\|}{\|\tilde{L}_s(\mathrm{w}=2B)\|}$. Solid line : estimated from acoustic pressure measurements by imposing $a = 0.5$, dashed line : analytically prediction $a_R = 0.5$, dotted line : analytically predicted $a_R \to \infty$.

The differences between the experimental estimations and the analytical predictions originate from several approximations in the analytical modelling, as explained in [8] and from uncertainties in the acoustic pressure measurements, especially the non-stationary part of the BPF tone and its harmonics. Another source of uncertainty in the measurement comes from the discretization

of the angular location θ_s of the control obstruction, which can lead to an under-estimation of $\| p_t(r, 0, 0; mB\Omega, z_s, \theta_p^L = \theta_s^L) \|$ so that the ratio defined in Eq. (7.16) is corrupted by uncertainties. The averaging effects over the axial distance z_s are included in the error bars, as explained in Section 7.4.3.

As anticipated analytically in [8], salient wakes generated by low width obstructions lead to a large harmonic content rate of the unsteady lift, thus leading to a risk of affecting the harmonics of the BPF. Better obstructions can be designed thanks to the analytical modelling presented in part I [8], to minimize the harmonic content rate of the unsteady lift. For example, the angles $\Theta = [30°, 35°, 40°, 50°]$ of the 6-trapezoidal obstruction lead to a low harmonic content rate. The angle $\Theta = 40°$ of the trapezoids provides the lowest harmonic content rate and the highest ratio between the fundamental of the unsteady lift spectrum and its first harmonic. The optimal angular wake width is $a\Theta = 0.5 \times 40° = 20°$. This angle is about 10° greater than the angular portion occupied by the blades at mid-span.

Harmonic content indicators for a sinusoidal obstruction

The estimated values of the ratios $\frac{\|\tilde{L}_s(\text{w}=1B)\|}{\|\tilde{L}_s(\text{w}=mB)\|}$ are given in Table 7.1 for $1 \leq m \leq 4$ for the sinusoidal obstruction shown in Fig. 7.7-b. As already explained in the companion paper [8], the energy contained in the first circumferential harmonic of the unsteady lift is non-negligible, but the upper harmonics decrease rapidly. The order of magnitude of the ratio $\frac{\|\tilde{L}_s(\text{w}=1B)\|}{\|\tilde{L}_s(\text{w}=mB)\|}$ estimated by indirect acoustical pressure measurements is similar to the analytical predictions. Apart from the approximations of the analytical modelling (e.g. only transversal gust are considered in the Sears theory), the differences between the analytical modelling and the experimental estimations of the indicators originate from the hot-wire measurements and from the gaussian approximation of the velocity profile generated by the sinusoidal obstruction, as explained in [8]. The uncertainties can also originate from uncertainties in the acoustic pressure measurements, i.e. from the non-stationary part of the acoustic radiation or from the discretization effect of the angular position of the control obstruction and from the averaging over z_s, as explained in section 7.4.3.

No value was experimentally estimated for the ratio $\frac{\|\tilde{L}_s(\text{w}=1B)\|}{\|\tilde{L}_s(\text{w}=4B)\|}$ since no periodicity of the acoustic pressure level as a function of the angular position of the sinusoidal obstruction θ_s was found for the third harmonic of the BPF ($m = 4$), even for low axial distance z_s between the rotor and the control obstruction.

Finally, the semi-analytical prediction of D =18.1% calculated in the companion paper [8] is in the range of the experimental estimation D =17.8% $\pm$ 2.8%. The term "semi"-analytical is used since the wake velocity profile has been measured behind the obstruction using a single hot wire anemometer. A gaussian approximation of the measured velocity profile has then been used as input data in the analytical model to estimate the circumferential spectrum of the unsteady

Tableau 7.1 Indirect estimation of the ratio $\frac{\|\tilde{L}_s(\text{w=}1B)\|}{\|\tilde{L}_s(\text{w=}mB)\|}$ from acoustical measurement in the axial direction for the sinusoidal obstruction

m	1	2	3	4
Estimated from acoustical pressure measurements	1	6.5 ± 1	35.0 ± 5.7	–
Calculated from the analytical model [8] and hot wire anemometer data	1	5.3	39.6	342

lift generated by the sinusoidal obstruction in the companion paper [8].

Harmonic content indicators for a 6-cylindrical obstructions

Finally, the cylindrical obstructions are tested to corroborate the analytical prediction of the re-scaled experiment of Polacsek *et al.* [103] described in the companion paper [8]. However, the diameter of the tested cylinders is slightly lower than the rescaled experiment of Polacsek *et al.* : 14 mm, which can slightly increase the harmonic content rate of the unsteady lift generated by the tested cylinders.

The ratios $\frac{\|\tilde{L}_s(\text{w=}1B)\|}{\|\tilde{L}_s(\text{w=}mB)\|}$ estimated from the acoustic pressure level measurements are shown in Table 7.2. The ratio $\frac{\|\tilde{L}_s(\text{w=}1B)\|}{\|\tilde{L}_s(\text{w=}2B)\|} = 2.8$ indicates that the cylinders have a non-negligible effect on the first harmonic of the BPF. The magnitude of the second harmonic of the circumferential spectral order of the unsteady lift is 13.1 times smaller than the fundamental order. The ratio $\frac{\|\tilde{L}_s(\text{w=}1B)\|}{\|\tilde{L}_s(\text{w=}4B)\|}$ could not be estimated from the sound pressure data.

Tableau 7.2 Indirect estimation of the ratio $\frac{\|\tilde{L}_s(\text{w=}1B)\|}{\|\tilde{L}_s(\text{w=}mB)\|}$ from acoustical measurement in the axial direction for the cylindrical obstructions

m	1	2	3	4
Estimated from acoustical pressure measurements	1	2.8 ± 0.2	13.1 ± 2.0	–
Calculated from the analytical model [8] ($a = 0.5$)	1	1.7	2.8	5.0
Calculated from the analytical model [8] ($a = 1$)	1	2.9	11.3	59.0

The experimentally estimated ratios $\frac{\|\tilde{L}_s(\text{w=}1B)\|}{\|\tilde{L}_s(\text{w=}mB)\|}$ are compared to the analytical prediction of ref. [8]. The prediction and measurement are in quite good agreement for a Gaussian wake width parameter $a = 1$ but large differences can be pointed out for $a = 0.5$. The harmonic content rate estimated from the acoustic pressure measurements is $D = 37.6\% \pm 2.3\%$, which is close to the analytically predicted value $D = 33.5\%$ for the large wake width parameter $a = 1$ but diverge

for $D = 58.6\%$, calculated from the analytical modelling by choosing $a = 0.5$. Thus, an a priori unexpected application of the method to estimate the harmonic content indicators is the indirect estimation of the Gaussian wake width characteristic, behind an obstruction in the flow field of a rotor, from acoustical pressure measurements using a single microphone in the axial direction and by varying the angular position of the obstruction.

7.5 Free-field control performance

The performance of the flow control obstruction approach is illustrated in acoustic free field conditions. Acoustic pressures are measured in both the upstream and downstream half-spaces. The acoustic directivity and sound power attenuations are presented in both the upstream and downstream half-space.

7.5.1 Experimental set-up

The experimental setup presented in Fig. 7.6 is now used to measure the far field acoustic directivity at BPF for the fan with and without control obstruction. The control is performed using the sinusoidal obstruction presented in Fig. 7.7-b. The sinusoidal obstruction is located upstream. Acoustic pressure measurements are performed in an anechoic room on 1.8 m radius hemispheres upstream and downstream the fan. The acoustic pressures are measured at 33 regularly spaced locations on each hemisphere. The directivity patterns are obtained for two flow conditions : i) flow non-homogeneity arising from the interaction between the rotor and the stator vanes, for which the optimal distance between the sinusoidal obstruction and the rotor is z_s =6 cm and ii) flow non-homogeneity arising from the interaction between the rotor, the stator and a triangular obstruction in order to increase flow non-homogeneity. The triangular obstruction was inserted between two vanes of the stator. This obstruction covers a 34° angular section and strongly interacts with the rotor. This obstruction tends to increase the amplitude of the BPF in the acoustic spectrum as it introduces energy in the low-order circumferential components of the unsteady lift [7]. For this flow condition, the optimal distance between the sinusoidal obstruction and the rotor is z_s =4.5 cm, which is lower than the optimal distance for controlling the weaker interaction between the rotor and the stator vanes.

7.5.2 Sound pressure spectrum without and with control obstruction

Fig. 7.11 presents the upstream and downstream sound pressure frequency spectra, at 1.8 m on the fan axis. The optimal upstream location of the sinusoidal obstruction was manually

chosen by adjusting the rotor/sinusoidal obstruction distance and its orientation. The control obstruction is effective at BPF but tends to slightly increase the broadband noise floor. At BPF, the attenuations are in the order of 10 to 20 dB for upstream and downstream on-axis sound pressure. The impact of the sinusoidal obstruction on sound radiation at BPF harmonics is small, which confirm the frequency selectivity of a sinusoidal obstruction. In Fig. 7.11, the increase in the broadband energy arises from vortex generated by the sharp edges of the obstruction which then impact the fan blades, producing random fluctuating forces. The broadband noise is only increased when the primary inflow is relatively clean, but when a radiator is installed in the upstream flow field, no amplification of the broadband noise is noted.

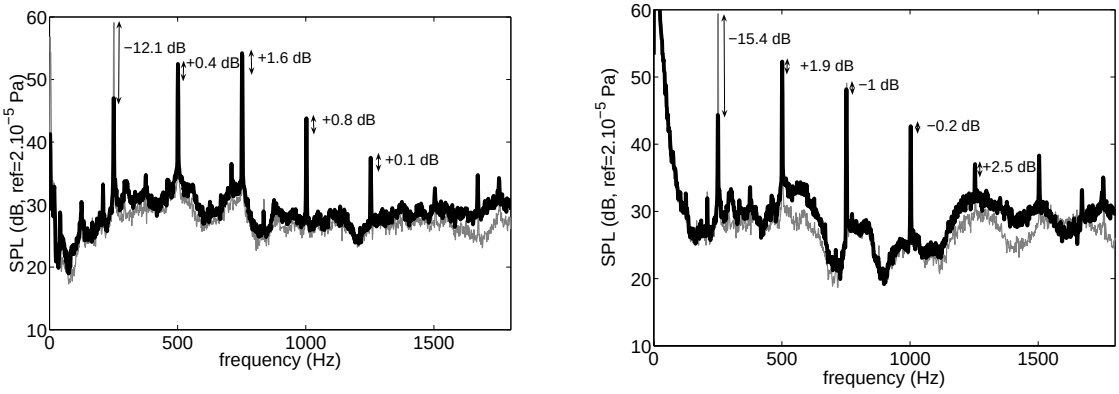

(a) Upstream microphone.

(b) Downstream microphone.

Figure 7.11 Sound pressure spectrum with (black thick line) and without sinusoidal flow obstruction (gray thin line) for the case of rotor/(stator and triangular obstruction) interaction, upstream (left) and downstream (right).

7.5.3 Sound power attenuation and acoustic directivity

The sound power attenuations are presented in Tables 7.3 and 7.4 for the case of rotor/(stator plus triangular obstruction) and the case of rotor/stator interaction, respectively.

At BPF, the sound power is attenuated by 7 dB in the upstream half-space and 2.6 dB in the downstream half-space when a triangular obstruction is added between two stator vanes, which generate a spatially highly primary non-uniform flow. The variation of sound power is negligible for the harmonics of the BPF, as noted in Fig. 7.11.

When no additional obstruction is added (case of rotor/stator interaction), the sound power attenuation is 8.4 dB in both the upstream and the downstream half-spaces. In this case, the flow is spatially slightly non-uniform. Sound power attenuation or amplification is negligible for the first three harmonics of the BPF.

Tableau 7.3 Acoustic power attenuation with an added triangular obstruction in the plane of the stator $10\log_{10}\left(\frac{W_p(m)}{W_t(m)}\right)$.

$m\times$BPF	1×BPF	2×BPF	3×BPF	4×BPF
Downstream	+7	-1.5	+0.9	-0.2
Upstream	+2.6	-0.7	-0.6	+0.1

Tableau 7.4 Acoustic power attenuation without triangular obstruction in the plane of the stator $10\log_{10}\left(\frac{W_p(m)}{W_t(m)}\right)$.

$m\times$BPF	1×BPF	2×BPF	3×BPF	4×BPF
Downstream	+8.4	0	-1.1	+0.4
Upstream	+8.4	-0.9	-0.6	0

As explained in Section 7.3.3, depending on the primary lift spectrum, the sound power attenuation is not the same in the upstream half-space and in the downstream half-space. we also experimentally observed that there is a trade-off between an optimal control in the downstream and in the upstream radiating half-spaces. This can be done by slightly adjusting the axial distance between the control obstruction and the rotor. An axial variation of about 1 cm can result in a maximal attenuation at the BPF in the downstream half-space or a maximal attenuation at the BPF in the upstream half-space. Intermediate axial positions allow for the tonal noise to be equally attenuated in both the downstream and the upstream half-space.

The acoustic directivity with and without control obstruction is presented in Fig. 7.12 for the case of rotor/(stator+triangular obstruction) interaction. It appears that an acoustic attenuation is obtained in the whole radiating space. The most radiating circumferential order $B = 6$ of the unsteady lift is effectively controlled, so that the attenuation is particularly large in the axial direction.

7.6 In-duct control performance

A ducted configuration was chosen to test the performance of the control obstruction for various loading conditions of the fan and for different acoustic boundary conditions. Acoustic measurements were carried out both in the upstream flow field (free field conditions) and in the downstream flow field (in-duct), while varying the loading of the fan.

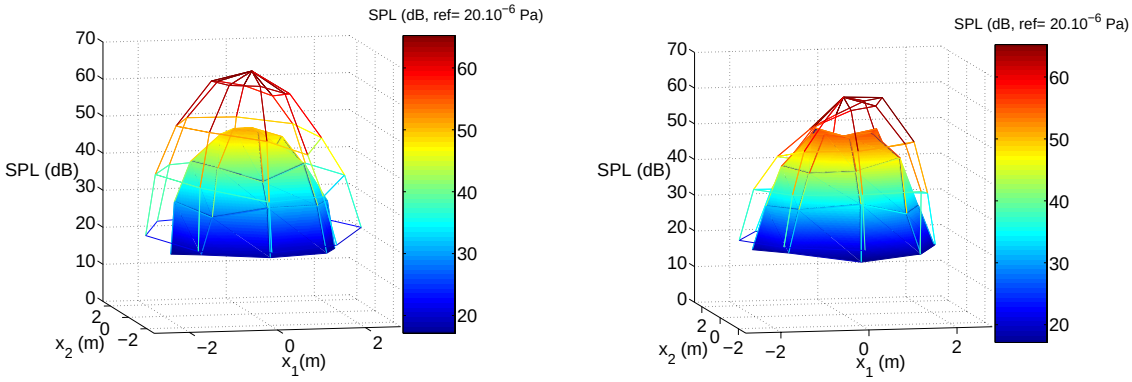

(a) Upstream directivity.

(b) Downstream directivity.

Figure 7.12 Upstream and downstream directivity at BPF in free field with an added triangular obstruction in the plane of the stator. Without sinusoidal control obstruction (lines) and with sinusoidal control obstruction (surfaces).

7.6.1 Experimental setup

The performance of the control approach for a ducted configuration is evaluated using the setup illustrated in Fig. 7.13. The fan is mounted on the radiator and the fan is itself inserted in a duct instrumented with a Pitot tube to measure static pressure and flow rate and a microphone inserted in a microphone nose cone to measure the downstream acoustic pressure. Another microphone is used to measure the upstream acoustic pressure. Mastic is used to ensure a tight seal between the fan shroud and the duct which has a 35.6 cm diameter. A damper is used to adjust the load applied on the fan. A flow rectifier grid is used to homogenize the flow downstream the fan to avoid the swirling of the flow and to homogenize the radial distribution of the flow velocity. The aerodynamic performance curves of the fan have been measured by varying the angular position α_{damp} of the in-duct damper. The acoustic pressure measurements were carried out for three damper positions : i) for a damper at $\alpha_{damp} = 0°$, for which the static pressure is minimum and the flow is maximum, ii) for a damper at $\alpha_{damp} = 50°$, for which the fan is at its maximum efficiency and iii) for a damper at $\alpha_{damp} = 30°$, which is an intermediate damper position.

A 4×8 cm rectangular piece of adhesive tape was bonded on the upstream side of the radiator at about 5 cm from the fan axis in order to enhance non-uniformity of the primary incoming flow and therefore increase tonal noise radiation. The radiated sound pressure with and without control obstruction has been measured for the chosen damper position for the three obstructions presented in Fig. 7.7 : i) a 6-sinusoidal obstruction, ii) a 6-trapezoidal obstructions and iii) a 12-trapezoidal obstruction.

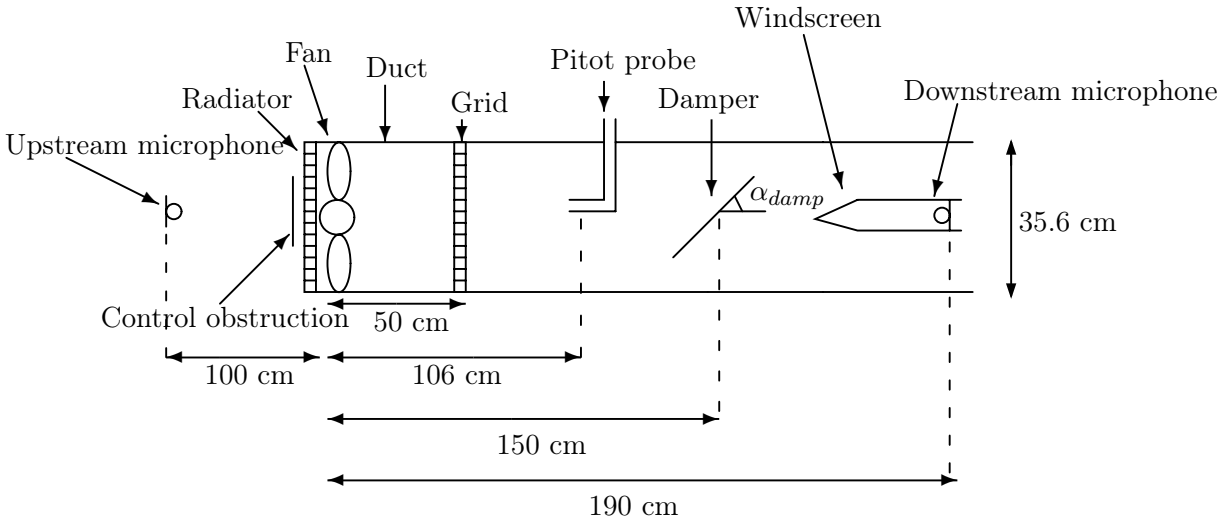

Figure 7.13 Experimental setup for the control performance evaluation in a duct.

Only the acoustic modes for which the rotational tip speed $\frac{mB-\mathrm{w}}{mB}\Omega R_T$ is supersonic can propagate in the duct [15]. For $m = 1$, i.e. at BPF=300 Hz, the circumferential mode order $\mathrm{w} = 6$ is the only mode that can propagate in the duct, and corresponds to an acoustic plane wave. For $m = 2$, i.e. at 2×BPF, the three circumferential mode orders $\mathrm{w} = 11, \mathrm{w} = 12$ and $\mathrm{w} = 13$ can propagate in the duct. The circumferential order $\mathrm{w} = 12$ propagates as a plane wave, while the circumferential orders $\mathrm{w} = 11$ and $\mathrm{w} = 13$ propagate with spiral wave fronts rotating in opposite directions. The relation between the w^{th} circumferential order of the unsteady lift and the in-duct radiated sound pressure at frequency m×BPF involves Bessel function of the first kind and of order $\mathrm{w}\pm mB$ [4] [15]. Thus, the radiated sound pressure due to the circumferential order $\mathrm{w} = 12$ of the unsteady lift is large compared to the radiated sound pressure due to the circumferential orders $\mathrm{w} = 11$ and $\mathrm{w} = 13$ (for the fan under investigation rotating at 3000 RPM). Thus, controlling the circumferential order $\mathrm{w} = 6$ and $\mathrm{w} = 12$ of the unsteady lift are sufficient to significantly reduce the in-duct acoustic radiation at frequencies BPF and 2×BPF respectively.

7.6.2 In-duct control results

Control with a 6-trapezoidal obstruction

To minimize the BPF tone, the optimal location of the 6-trapezoidal obstruction is closer to the fan for higher loads but the angular position is the same for the three tested loadings. For the highest load (damper at 50°), the obstruction is located on the radiator.

The acoustic pressure spectra measured by the upstream and downstream microphones with and without control obstruction are respectively presented in Figs. 7.14(a)(c)(e) and 7.14(b)(d)(f)

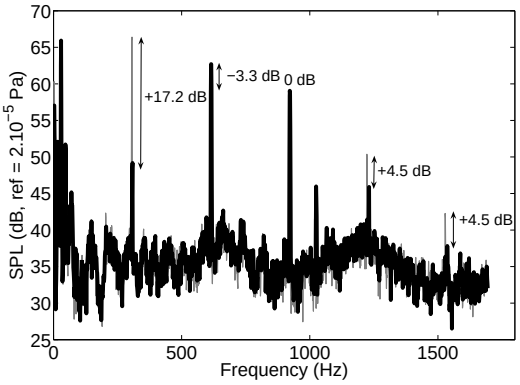

(a) Damper at 0° - Upstream microphone.

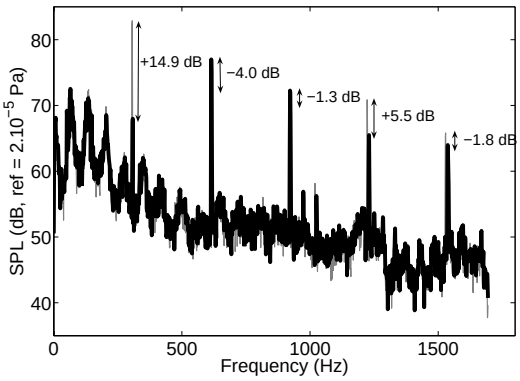

(b) Damper at 0° - Downstream microphone.

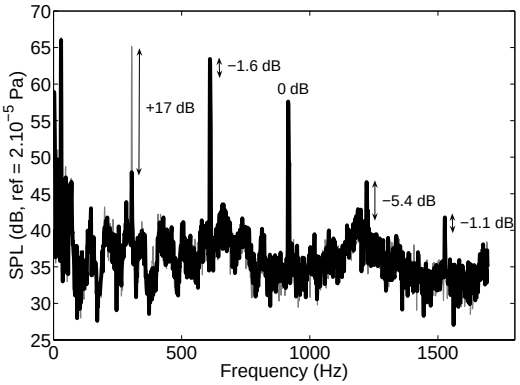

(c) Damper at 30° - Upstream microphone.

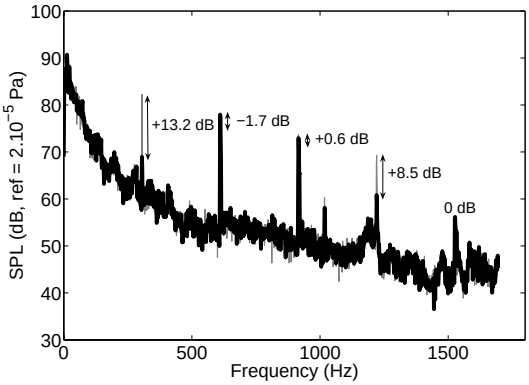

(d) Damper at 30° - Downstream microphone.

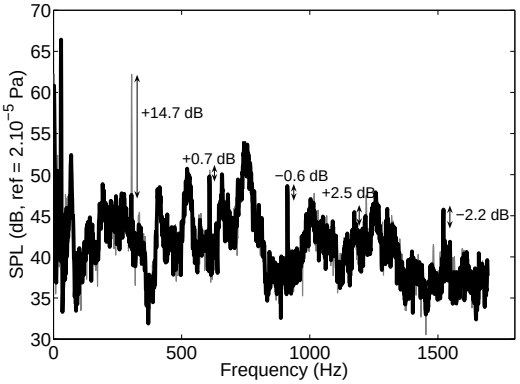

(e) Damper at 50° - Upstream microphone.

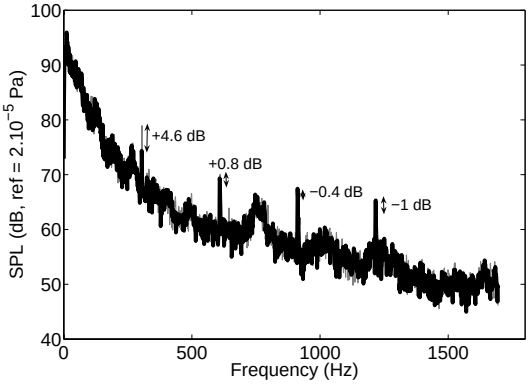

(f) Damper at 50° - Downstream microphone.

Figure 7.14 Spectrum of the sound pressure level measured by the downstream microphone with the 6-trapezoidal obstructions, with (thick black line) and without (thin gray line) control.

for three damper positions : 0°, 30° and 50°.

The fluctuation of the in-duct acoustic pressure level in the low frequency range (from 0 to 500 Hz) originates from the resonnance of the pipe close by the fan driver at one side and open at the other side. Moreover the increase of the spectrum broadband level for higher loads can be attributed to the vortex generated by the sharp edges of the damper, producing random fluctuating forces on it and radiating sound in the duct.

In agreement with the analytical modelling in part I [8] and the experiment in free field, the in duct control results generally show that the BPF tone can be attenuated without affecting its upper harmonics (Fig. 7.14). The few exceptions for which the harmonics of the BPF have been affected can be attributed to the non-stationary part of the acoustic pressure.

The results of Fig. 7.14 show that it is possible to control the BPF tone for various fan loading. However, the location of the control obstruction must be adapted to maintain a good attenuation. This illustrates the need for a controller to adjust the obstruction location in a changing environment.

Bi-harmonic control with a 6-trapezoidal obstruction and a 12-trapezoidal obstruction

Two control obstructions can be combined to control more than one multiple of the BPF. In order to demonstrate this, control results are presented using a $\Theta = 35°$ 6-trapezoidal obstruction and a $\Theta = 17°$ 12-trapezoidal obstruction simultaneously, aiming at the reduction of the 1×BPF and 2×BPF tones for a six-bladed fan. These results are obtained for a damper at 0°.

The optimal location of the 6-trapezoidal obstructions was first determined such that the BPF is reduced. The insertion of this first obstruction can lead to a slight modification of the sound pressure magnitude at harmonics of the BPF tone. The optimal location of the 12-trapezoidal obstruction was then determined in order to reduce the 2×BPF tone. The control of both frequencies is independent since the interaction between the 12-trapezoidal obstruction and the rotor does not generate the 6^{th} order of the unsteady lift.

The Fig. 7.15 presents the downstream and upstream spectrum of the sound pressure level with and without control. As can be seen in this figure, the attenuation at BPF is 19.3 dB upstream and 21.2 dB downstream. For the first harmonic of BPF, the attenuation is 7 dB upstream and 15.3 dB downstream. The higher harmonics are not significantly affected by the presence of the control obstructions. These results also demonstrate that the control using the obstructions is effective in both the upstream and downstream half-spaces.

Obstructions could be designed with $3B, 4B, 5B, ...$ lobes to control higher harmonics. Ho-

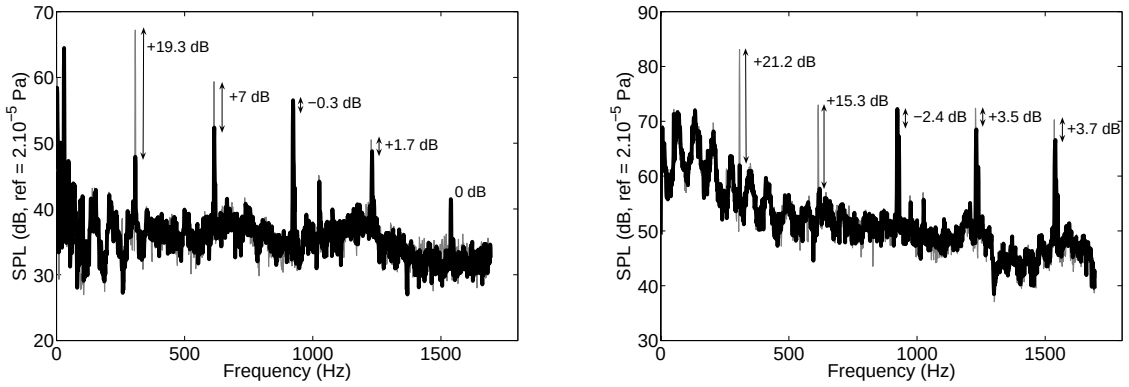

(a) Upstream microphone.

(b) Downstream microphone.

Figure 7.15 Bi-harmonic control ($BPF + 2 \times BPF$) using the 6-trapezoidal obstructions and the 12-trapezoidal obstructions simultaneously, with (thick black line) and without (thin gray line) control. The damper is at 0°.

wever, fan efficiency and overcrowding of the area in front of the fan might then become major concerns.

7.7 Aerodynamic performance of the fan with a control obstruction

7.7.1 Experimental setup

The impact of a trapezoidal obstruction (Fig. 7.7-a) and a sinusoidal obstruction (Fig. 7.7-b) on the aerodynamic performance of the fan is studied in this section. In order to evaluate this, the experimental facilities of Siemens VDO in London (Ontario, Canada), following the AMCA (Air Movement and Control Association) standard, was used. This setup is made of plenum chambers separated by grids and nozzles in order to allow precise pressure and flow measurement. The Fig. 7.16 presents an overview of the setup.

The fan is hermetically inserted between two chambers. The upstream chamber is at atmospheric pressure and the downstream chamber is completely sealed. A hatch located downstream the nozzles allows to adjust the load on the fan. A blower is used to measure the efficiency of the tested fan under forced flow condition, which allows to simulate the operation of an engine cooling fan on an automobile travelling at velocities up to 100 km/h.

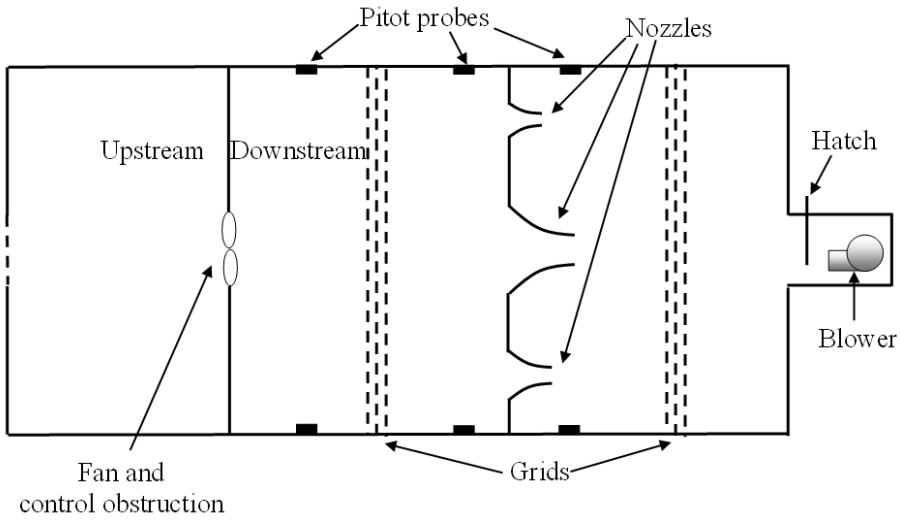

Figure 7.16 Experimental setup for the aerodynamic performance evaluation.

The efficiency of the fan is defined as :

$$\text{Efficiency} = \frac{\text{Static pressure (Pa)} \times \text{Flow } (\text{m}^3.\text{s}^{-1})}{\text{Input electrical power (W)}} \tag{7.22}$$

Thus, measurements of static pressure, flow and electrical power are required. The static pressure is measured with the help of Pitot tube located inside the downstream chamber. The flow is obtained from the pressure measured by the Pitot tubes using calibrated nozzles (from differential pressure measurements upstream and downstream the nozzles). Finally, the electrical power is estimated from voltage and current driving the fan under testing.

7.7.2 Impact of a control obstruction on the aerodynamic performance of the fan

The Fig. 7.17 presents the static pressure, the input electrical power and the efficiency as a function of the flow, for the fan with and without the sinusoidal obstruction located at the axial control location (4.3 cm from the rotor plane). The effect of the obstruction (the area of this obstruction is 121 cm^2 and the area of the rotor is 707 cm^2) seems almost negligible on the static pressure, the flow and the efficiency of the fan. Larger control obstructions have been tested. It has been shown that a sinusoidal obstruction with a larger area of 196 cm^2, located on the radiator (3 cm from the rotor plane) decreases the maximum efficiency from 25.8% to 24.7%.

Experiments on the fan without radiator also showed that the control obstruction has almost no effet on the fan efficiency, even for a low axial distance between the fan and a 196 cm^2 sinusoidal control obstruction. Moreover, 12-lobed obstruction (170 cm^2) and 6-trapezoidal obstructions (129 cm^2) similarly have also almost no effect on the fan efficiency.

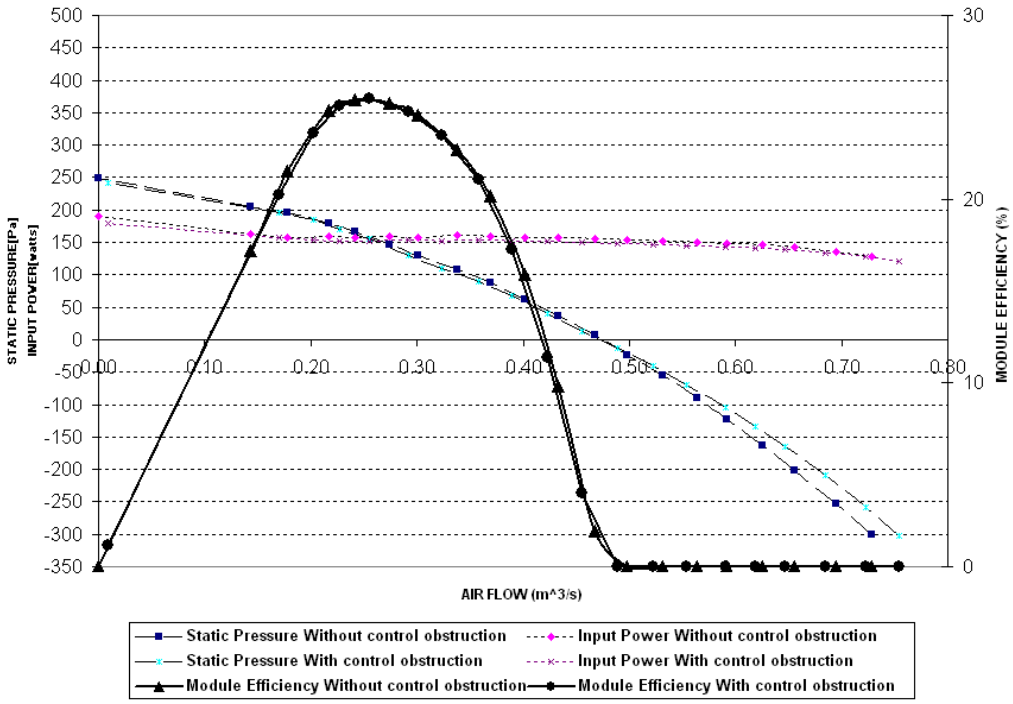

Figure 7.17 Aerodynamic performance curves for the fan with the sinusoidal obstruction.

7.8 Conclusion

A new passive adaptive approach has been proposed to reduce tonal noise from axial fan, by controlling the most radiating unsteady lift mode using flow control obstruction(s) with a low harmonic content rate. The flow control obstruction is located such that the secondary radiated noise is of equal magnitude but opposite in phase compared to the primary noise. The magnitude and phase of the secondary noise are respectively controlled by the axial distance between the rotor and the obstruction and the angular position of the control obstruction.

In the companion paper, we provided analytical tools to design the flow control obstructions in order for the blade unsteady lift generated by the rotor/control obstruction interaction to mainly contain the most radiating mode. It has been found that salient obstructions, such as low diameter rods, are not adapted to control a tone without affecting its harmonics; since the circumferential harmonic content of the associated unsteady lift is high. But it is possible to design trapezoidal or sinusoidal control obstructions such that the circumferential harmonic content of the unsteady lift is low. Thus, it is possible to control one tone without affecting its harmonics.

In this paper, we have validated the analytical model presented in the companion paper by indirect estimations of the harmonic content indicators from acoustic pressure measurements. Then, free field experiments have shown the ability of the sinusoidal obstruction to control the

BPF tone in the whole space. In-duct experiments have shown the ability for an appropriate angular portion of the trapezoidal obstructions ($\Theta = 35°$) to efficiently control the BPF for different loads. A biharmonic control have clearly demonstrated the ability of two control obstructions to attenuate the BPF and its harmonic (attenuation of sound pressure level up to 21 dB and 15 dB respectively). Moreover, the aerodynamic performances of the automotive fan used in this study are almost unaffected by the presence of the control obstruction.

The proposed approach is well adapted to acoustically compact fans, for which only one unsteady lift mode has a major contribution to the radiated noise at a single frequency. Increasing the rotation Mach number and/or the radius of the fan leads to an increase of the number of the radiating unsteady lift modes contributing the noise at a single frequency. It is possible to simultaneously reduce these other modes by adding several obstructions, circumferentially designed to contain the other radiating modes. In such a case, aerodynamic penalties could be of major concern. Therefore, the control approach is better adapted to small industrial chimney fans, PC fans, air conditioning fans, residential heat pump, automotive fans...

Further work involves implementing a feedback control system in order to automatically adjust the obstruction to its optimal solution ; and eventually to control the non-stationary part of the primary flow. A microphone or embedded sensors could be used to provide the error signal to be minimized. Further effort must also focuss on the optimization of aerodynamic shape of the flow control obstructions.

7.9 Acknowledgments

This work has been supported by the AUTO21 Network of Centres of Excellence (Canada) and Siemens VDO Automotive Inc. The authors wish to thank Sylvain Nadeau from Siemens Automotive Inc. and Marc Quiquerez for their collaboration to this research.

7.10 Nomenclature

a	circumferential Gaussian width parameter
a	radial Gaussian width parameter
B	number of blades
c_0	speed of sound, (m.s^{-1})
C	chord of the blade (m)
D	harmonic content rate (%)
F'	lift per unit span N.m^{-1}
$\mathbf{H}$	aeroacoustic transfer matrix (dimensionless)

i	imaginary number $\sqrt{-1}$
J_n	ordinary Bessel functions, nth order
k_0	acoustic wave-number, $k_0 = \omega/c_0$ (rad.m^{-1})
$\tilde{L}$	unsteady lift (N)
L	amplitude of the unsteady lift (N)
M_r	rotational Mach number $M_r = \Omega R/c_0$
N	number of discretized axial distance between the rotor and the obstruction
p	acoustic pressure (Pa)
R	radius (m)
R_m	mean radius $R_m = 0.7 \times R_T$ (m)
R_H, R_T	fan hub and tip radii (m)
t	time (s)
w	circumferential order
W	sound power (W)
$\mathbf{x}; r, \varphi, \alpha$	acoustic field point coordinate ; spherical coordinates
$\mathbf{y}; R, \theta, y_3$	acoustic source point coordinate ; cylindrical coordinates
z_s	axial distance between the rotor and the obstruction
θ	circumferential angle (rad)
θ_s	angular position of the control obstruction (rad)
θ_b	circumferential angle rotating with the blades (rad)
Θ	angle of the trapezoidal obstructions (°)
ρ_0	density of air (Kg.m^{-3})
σ	standard deviation
ω	angular frequency (rad.s^{-1})
Ω	angular velocity of the rotor (rad.s^{-1})

Subscripts and indices

b	blade index
m	acoustic frequency index
n	axial distance index
p	primary
s	secondary
t	total
T	tip

superscripts

L	lift
opt	optimal

7.11 Bilan

Dans ce dernier chapitre, les performances acoustiques des obstructions de contrôle ont été mesurées expérimentalement et ont validé le modèle utilisé au chapitre 6 pour calculer les taux de contenance harmonique. L'amplitude du bruit secondaire est contrôlée par la distance axiale entre le rotor et l'obstruction de contrôle ; et la phase du bruit secondaire est contrôlée par la position angulaire de l'obstruction de contrôle. L'actionnement des obstructions a été mis en oeuvre à l'aide de moteurs pas à pas permettant de les pivoter et de les translater pour minimiser manuellement la pression acoustique au(x) microphone(s) d'erreur. Une atténuation globale de puissance acoustique de 8 dB a été obtenue en champ libre à l'aide d'une obstruction sinusoïdale à six lobes sans régénération d'harmoniques d'ordres supérieurs. Des expériences de contrôle ont aussi montré l'efficacité de la méthode pour atténuer la FPP en conduit pour différentes conditions de charge. Un contrôle biharmonique a également permis d'obtenir des atténuations simultanées de niveau de pression acoustique aux microphones d'erreur de 19 dB en amont (semi-anéchoïque) et 21 dB en aval (en conduit) pour la FPP ainsi que 7 dB en amont et 15 dB en aval pour son premier harmonique. Finalement, des mesures dans une chambre répondant aux normes de l'AMCA (Air Movement and Control Association) ont montré que les obstructions proposées n'affectent quasiment pas l'efficacité du ventilateur. Les atténuations de puissance acoustique obtenues avec le contrôle passif adapté de l'écoulement sont du même ordre de grandeur que celle obtenues avec le contrôle actif acoustique.

Cette méthode de contrôle fait l'objet d'une demande de brevet ayant pour titre "Method and apparatus for controlling tonal noise from subsonic axial fans" (demande déposée auprès du bureau américain des brevets sous le numéro 60/805/944).

Une méthode de positionnement automatique des obstructions de contrôle est présentée dans l'annexe A.

CONCLUSION

Bilan des travaux

Malgré les efforts réalisés ces dernières décennies sur la réduction du bruit des ventilateurs, le bruit de raie demeure un problème quand l'écoulement traversant le rotor est non-uniforme. La revue de bibliographie a démontré certains manques sur l'estimation des sources de bruit de raie par modèle inverse ainsi que sur les stratégies de contrôle actif acoustique et de contrôle passif adaptatif de l'écoulement à l'aide d'obstructions.

Dans les chapitres 3 et 5, nous avons montré le potentiel des modèles inverses, basés sur les modèles analytiques similaires de Morse et Ingard et de Blake, et sur la méthode de régularisation de Tikhonov. Ces modèles inverses permettent en effet d'estimer les modes circonférentiels les plus rayonnants des forces instationnaires périodiques exercées sur les pales du rotor à partir de mesures de pression acoustique rayonnée en champ lointain. Les modes les moins rayonnants sont filtrés par la régularisation au profit d'une plus grande stabilité d'inversion. Les simulations menées au chapitre 3 ont tout d'abord permis d'étudier la sensibilité de l'inversion du modèle de Morse et Ingard par rapport aux divers paramètres de mesure du champ acoustique et par rapport au choix du paramètre de régularisation. Au chapitre 5, nous avons ensuite reconstruit expérimentalement les fluctuations circonférentielles périodiques de portance des pales du rotor et les vitesses d'écoulement traversant le rotor à partir du modèle de Blake. Nous avons aussi proposé une méthode graphique, basée sur l'association originale de la courbure de la courbe en L et de la condition de Picard, pour choisir le paramètre de régularisation. En plus de fournir une méthode sans contact d'estimation des sources de bruit de raie, les modèles inverses offrent un outil d'extrapolation du champ acoustique rayonné par un rotor à la FPP et ses harmoniques.

Dans le chapitre 4, nous avons développé une stratégie de contrôle actif du bruit de raies en champ libre. Pour un ventilateur de radiateur d'automobile, des simulations ont montré qu'un contrôle global des deux premières raies est possible avec un petit haut-parleur non-bafflé de directivité dipolaire situé devant le moyeu du ventilateur. L'implantation d'un contrôleur par anticipation FX-LMS monocanal a mené à des atténuations de niveau de pression acoustique de 28 dB et 18 dB au microphone d'erreur à la FPP et son premier harmonique respectivement. Un ventilateur possédant des directivités dipolaires à la FPP et ses harmoniques (rayonnement maximal dans l'axe) est très bien adapté à la configuration de contrôle proposée. Un moyen de

parvenir à cette directivité dipolaire est d'utiliser le même nombre d'aubes de stator et de pales de rotor [93]. De plus, l'utilisation d'un ventilateur à pales identiques et régulièrement espacées limite le nombre de raies à contrôler. La configuration géométrique "optimale" d'un ventilateur pour le contrôle actif du bruit de raie est donc à l'opposée des configurations classiques proposées pour son contrôle passif.

Dans les chapitres 6 et 7, une nouvelle approche de contrôle a été proposée. À l'aide d'obstructions introduites dans l'écoulement, il est possible de contrôler le mode circonférentiel de l'écoulement le plus rayonnant pour chaque raie . Les obstructions sont positionnées de sorte qu'elles génèrent une onde acoustique secondaire en opposition de phase avec l'onde acoustique primaire à contrôler. L'amplitude et la phase du bruit secondaire sont respectivement contrôlées par la distance axiale entre le rotor et les obstructions et la position angulaire des obstructions. Un modèle présenté au chapitre 6 a permis la conception d'obstructions capables d'atténuer une raie sans amplifications d'autres raies. Des obstructions trapézoïdales optimisées et des obstructions sinusoïdales permettent un contrôle harmoniquement beaucoup plus sélectif que les obstructions cylindriques trouvées dans la littérature. Dans le chapitre 7, par un contrôle biharmonique combinant deux séries d'obstructions, nous avons atténué simultanément le niveau de pression acoustique aux microphones d'erreur de 19 dB en amont (anéchoïque) et 21 dB en aval (en conduit) pour la FPP ainsi que 7 dB en amont et 15 dB en aval pour son premier harmonique. Des mesures ont finalement montré que l'impact des obstructions est mineur sur les performances aérauliques du ventilateur. Du point de vue de cette méthode, la configuration géométrique optimale du ventilateur est identique à celle issue du contrôle actif acoustique. L'utilisation d'un ventilateur à pales symétriques régulièrement espacées limite le nombre de raies à atténuer, donc le nombre d'obstructions de contrôle. Et un nombre d'aubes de stator identique au nombre de pales de rotor permet de privilégier les modes circonférentiels primaires contrôlables par les obstructions proposées dans cette thèse. Au chapitre 7, la méthode d'estimation du taux de contenance harmonique, à partir du pivotement des obstructions devant le ventilateur et de mesures de pressions acoustiques dans l'axe, présente aussi un intérêt pour estimer la largeur des sillages générés par les obstructions.

Les atténuations de puissance acoustique obtenues avec le contrôle passif de l'écoulement sont du même ordre de grandeur que celle obtenues avec le contrôle actif acoustique. Tandis que le contrôle actif réduit la conséquence acoustique des fluctuations de portance et nécessite une énergie continue d'activation, le contrôle passif adapté de l'écoulement réduit directement la source du bruit de raie et demande seulement un apport d'énergie lors du positionnement des obstructions. De plus, la méthode de contrôle de l'écoulement offre une alternative à privilégier pour des ventilateurs évoluant dans des conditions inhospitalières (pour l'usage d'un haut-parleur par exemple) et lorsque les niveaux acoustiques demandés excèdent les limites de puissance des haut-parleurs. Cette dernière technique de contrôle possède donc un bel avenir.

Les applications des méthodes de contrôle actif acoustique et passif adaptatif de l'écoulement

sont nombreuses dans le secteur automobile, de la climatisation et pour les ventilateurs acoustiquement compacts en général, en champ libre ou pour le contrôle des ondes planes en conduit. L'extension du contrôle passif adapté au cas des soufflantes de turboréacteurs demanderait une analyse plus détaillée de l'écoulement primaire et de la propagation des ondes acoustiques en conduit.

Perspectives

L'intégralité des travaux menés durant cette thèse ont fait appel à des modèles analytiques représentant de façon simple mais réaliste les phénomènes mis en jeu dans la génération, la propagation et le contrôle du bruit de raie. Quelques améliorations des modèles utilisés pour l'inversion et pour le contrôle du bruit de raie des rotors sont encore possibles analytiquement. Tout d'abord, un article récent de Huang [49] a, pour la première fois, introduit analytiquement les forces radiales instationnaires exercées sur les pales d'un rotor comme source de bruit de raie. Deuxièmement, des modèles analytiques sont disponibles pour la propagation du bruit de raie dans un conduit cylindrique [4] [15]. Un trop grand raffinement des modèles mènerait dans beaucoup de cas à des calculs compliqués, nécessitant des résolutions numériques coûteuses en temps de programmation et en temps de calcul.

En ce qui concerne le modèle inverse, une campagne de mesures anémométriques couvrant un tour complet de ventilateur permettrait de comparer les modes circonférentiels des vitesses d'écoulement mesurés à ceux estimés par le modèle inverse. Des mesures à fil chaud triple, similaires à celles réalisées par Morris *et al.* [39] permettraient aussi de distinguer les différentes composantes de la vitesse d'écoulement (axiale, radiale, tangentielle). Plusieurs points restent encore à éclaircir théoriquement sur les modèles inverses, notamment sur l'allure de la courbure de la courbe en L : des analyses plus approfondies de la décomposition en valeurs singulières et des facteurs de filtrage en fonction du rapport signal sur bruit sont quelques-unes des pistes à explorer.

Des améliorations peuvent aussi être apportées aux différentes stratégies de contrôle du bruit de raie étudiées durant cette thèse. Tout d'abord, en contrôle actif acoustique, la mise en œuvre de plusieurs sources secondaires et plusieurs capteurs d'erreur permettrait d'atténuer globalement les raies à des fréquences plus hautes [94]. De plus, en se basant sur des critères psychoacoustiques, la gêne auditive pourrait être diminuée en pondérant l'amplitude des différentes raies. L'utilisation d'un microphone d'erreur en champ proche permettrait aussi l'intégration du système de contrôle actif. En contrôle passif adaptatif de l'écoulement, l'intégration du système pourrait venir de capteurs de pression pariétale sur les pales du rotor, pour capter le signal de force à atténuer. Mais leur mise en œuvre pratique s'avère délicate, il faut donc chercher d'autres signaux d'erreur (acoustique, de force ou de vitesse d'écoulement) corrélés avec le bruit de raie

à atténuer. Le problème du contrôle passif adaptatif de l'écoulement n'est pas réglé non plus. Les premiers résultats obtenus par Kota [88] sur le positionnement automatique de cylindres montrent la difficulté de converger vers un minimum global de puissance acoustique. Des études préliminaires sur le positionnement automatique des obstructions proposées dans cette thèse, par contrôle optimal, sont très prometteuses (voir l'annexe A). Ces obstructions permettent d'utiliser des algorithmes de contrôle découplés qui ajustent la position d'une seule série d'obstructions pour atténuer une seule raie. L'efficacité des nouvelles méthodes de contrôle passe aussi par des géométries appropriées de ventilateurs. De futures expériences devraient être menées sur un ventilateur possédant autant d'aubes de stator que de pales de rotor (identiques et régulièrement espacées). Des obstructions profilées aérodynamiquement pourraient aussi limiter l'amplification du bruit large bande et limiter les pertes de performances aérauliques. Finalement, une optimisation plus approfondie (par algorithme génétique par exemple) de la géométrie des obstructions peut se baser sur le modèle analytique proposé au chapitre 6.

Enfin, la combinaison du modèle inverse et du contrôle passif adaptatif de l'écoulement ouvre de nouvelles perspectives pour la compréhension des mécanismes de génération du bruit de raie. Une antenne d'une trentaine de microphones permettrait, par modèle inverse, de déterminer le spectre de portance instationnaire généré pour différentes positions d'obstructions de contrôle et ainsi d'en apprendre plus sur les mécanismes d'interaction rotor/obstructions.

BIBLIOGRAPHIE

[1] Neise, W., Enghardt, L. (2003) *Technology approach to aero engine noise*, Aerospace Science and Technology, vol. 7, p. 352–363.

[2] Envia, E. (2002) *Fan noise reduction : An overview*, International Journal of Aeroacoustics, vol. 1, no 1, p. 43–44.

[3] Morse, P. M., Ingard, K. (1968) *Theoretical acoustics*, Princeton University Press, Princeton, NJ, USA.

[4] Blake, W.K. (1986) *Mechanics of Flow Induced Sound and Vibration, Vol. 2, Complex Flow Structure Interactions*, Academic Press Inc., 974 p.

[5] Gérard, A., Berry, A., Masson, P. (2005) *Active control of tonal noise from subsonic axial fan. part 1 : Reconstruction of aeroacoustic sources from far-field sound pressure*, Journal of Sound and Vibration, vol. 288, no 4-5, p. 1049–1075.

[6] Gérard, A., Berry, A., Masson, P. (2005) *Active control of tonal noise from subsonic axial fan. part 2 : Active control simulations and experiments in free field*, Journal of Sound and Vibration, vol. 288, no 4-5, p. 1077–1104.

[7] Gérard, A., Berry, A., Masson, P., Gervais, Y. (2006) *Evaluation of tonal aeroacoustic sources in subsonic fans using inverse models*, Accepté pour publication au Journal de l'American Institute of Aeronautics and Astronautics.

[8] Gérard, A., Berry, A., Masson, P., Gervais, Y. (2006) *Control of tonal noise from subsonic axial fans using flow control obstructions. part 1 : Interaction between the flow control obstructions and the rotor*, À soumettre au Journal of Sound and Vibration.

[9] Gérard, A., Berry, A., Masson, P., Gervais, Y. (2006) *Control of tonal noise from subsonic axial fans using flow control obstructions. part 2 : Acoustic performance of the control approach*, À soumettre au Journal of Sound and Vibration.

[10] Neise, W. (1992) *Review of Fan Noise Generation Mechanisms and Control Methods*, Fan Noise 92, 45-56 p.

[11] Zillmann, J., Maier, R., Bouty, E., Antoine, H., Just, W., Borchers, I., Enghardt, L., Tapken, U. (2001) *Control of Fan Noise Using Active Stators*, Internoise 2001, 30th International Congress on Noise Control Engineering.

[12] Waitz, I.A., Brookfield, J.M., Sell,J., Hayden, B.J. (1996) *Preliminary assessment of wake management strategies for reduction of turbomachinery fan noise*, Journal of Propulsion and Power, vol. 12, no 5, p. 958–966.

[13] Kota, V., Wright, M.C.M (2006) *Wake generator control of inlet flow to cancel flow distorsion noise*, Journal of Sound and Vibration, vol. 295, p. 94–113.

[14] Hansen, P.C. (1998) *Rank-Deficient and Discrete Ill-Posed Problems*, SIAM, Philadephia, 247 p.

[15] Goldstein, M.E. (1976) *Aeroacoustics*, McGraw-Hill International Book Company, 293 p.

[16] Ffowcs Williams, J.E., Hawkings, D.L. (1969) *Sound generated by turbulence and surfaces in arbitrary motion*, Phil. Trans. Roy. Soc. London, vol. A264, p. 321–342.

[17] Wright, S.E. (1969) *Sound radiation from a lifting rotor generated by asymmetric disk loading*, Journal of Sound and Vibration, vol. 9, no 2, p. 223–240.

[18] Tyler, J.M., Sofrin, T.G. (1994) *Axial flow compressor noise studies*, Transaction of the Society of Automotive Engineers, vol. 70, p. 309–332.

[19] Lowson, M.V. (1968) *Theoretical analysis of compressor noise*, Journal of the Acoustical Society of America, vol. 47, no 1, p. 371–385.

[20] Sears, W.R. (1941) *Some aspects of non-stationary airfoil theory and its practical application*, Journal of Aeronautic Science, vol. 8, p. 104–108.

[21] Gutin, L. (1936) *On the sound field of a rotating airscrew*, Zhurnal Tekhnicheskoi Fiziki, vol. 6, p. 899–909.

[22] Longhouse, R.E. (1976) *Noise mechanism separation and design considerations for low tip-speed axial flow fans*, Journal of Sound and Vibration, vol. 48, no 1, p. 461–474.

[23] Roger, M. (1996) *Modélisation du bruit de raies d'un fenestron d'hélicoptère en vol d'avancement*, Acta Acustica, vol. 82, p. 238–250.

[24] Fournier, F. (1988) *Mise au Point d'une Méthode de Calcul Adaptée au Bruit des Fenestrons d'Hélicoptères*, Thèse de doctorat, École Centrale de Lyon.

[25] Kemp, N.H., Sears, W.R. (1953) *Aerodynamic interference between moving blade rows*, Journal of Aeronautic Science, vol. 20, p. 585–598.

[26] Kemp, N.H., Sears, W.R. (1955) *The unsteady forces due to viscous wakes in turbomachines*, Journal of Aeronautic Science, vol. 22, p. 473–483.

[27] Amiet, R.K. (1974) *Compressibility effects in unsteady thin-airfoil theory*, American Institute of Aeronautics and Astronautics Journal, vol. 12, p. 252–255.

[28] Berhault, J.P. (1985) *Modélisation des sources aéro-hydrodynamiques de bruit dans les turbomachines*, La Houille Blanche, vol. 8, p. 679–695.

[29] Baude, P., Moreau, S., Stanciu, M., Aubert, S., Ferrand, P. (2001) *Unsteady Rotor-Stator Interactions in Automotive Engine Cooling Fan Systems*, Internet.

[30] Caro, S., Moreau, S., Roger, M. (2001) *Comparaison d'une Technique 2D de Type Sears avec un Calcul Instationnaire Direct pour le Calcul du Bruit de Raies d'un Ventilateur*, Colloque ventilateur 2001, Lyon, 1-7 p.

[31] Maloom, A., Kouidri, S., Rey, R. (2004) *Aeroacoustic evaluation of axial flow fans based on the unsteady pressure field on the blade surface*, Applied Acoustics, vol. 65, p. 367–384.

[32] Lee, J., Cho, K., Lee, S. (2000) *Application of acoustic analogy to automotive engine cooling fan noise prediction*, American Institute of Aeronautics and Astronautics Journal, vol. 38, no 6, p. 1095–1098.

[33] Dorney, D. (1996) *Numerical simulations of unsteady flow through an automotive radiator fan*, Journal of Propulsion and Power, vol. 12, no 2, p. 426–429.

[34] Sawyer, S., Nallasamy, M., Hixon, R., Dyson, R.W. (2004) *A computational aeroacoustic prediction of discrete-frequency rotor-stator interaction noise - a linear theory analysis*, Aeroacoustics, vol. 3, no 1, p. 67–86.

[35] Bakir, F. (1998) *Étude théorique et expérimentale des fluctuations de pression au passage d'un Étage axial de compression. application au bruit des ventilateurs*, Revue Française de Mécanique, vol. 4, p. 255–264.

[36] Korakianatis, T. (1992) *On the prediction of unsteady forces on gas turbine blades. part 1 : Description of the approach*, Transactions of the ASME, vol. 114, p. 114–122.

[37] Korakianatis, T. (1992) *On the prediction of unsteady forces on gas turbine blades. part 1 : Analysis of the results*, Transactions of the ASME, vol. 114, p. 123–131.

[38] Mugridge, B.D. (1975) *Axial flow fan noise caused by inlet flow distorsion*, Journal of the Acoustical Society of America, vol. 40, no 4, p. 497–512.

[39] Morris, S.C., Good, J.J., Foss, J.F. (1998) *Velocity measurements in the wake of an automotive cooling fan*, Experimental Thermal and Fluid Science, vol. 17, p. 100–106.

[40] Raffy, P., Lewy, S (1978) *Étude des sources de bruit de soufflantes subsoniques*, Entropie, vol. 82, p. 32–45.

[41] Staiger, M., Stetter, H., Rufer, L., Fabicki, M. (1996) *Periodic Response of Axial Fan Rotor Blades to Non-Uniform Inlet Flow Field*, International Gas Turbine and Aeroengine congress and Exhibition, Birmingham, UK.

[42] Akaike, S., Kikuyama, K. (1993) *Noise reduction of pressure type fans for automobile air conditioners*, Transactions of ASME, vol. 115, p. 216–220.

[43] Washburn, K.B., Lauchle, G.C. (1998) *Inlet flow conditions and tonal sound radiation from a subsonic fan*, Noise Control Engineering Journal, vol. 31, no 2, p. 101–110.

[44] Wong, Y.J. (2002) *Active Control of Fan Noise in a Duct*, Active 2002, Southampton, UK.

[45] Raffaitin, C., Roger, M., Rufer, L., Fabicki, M. (1994) *Caractérisation des sources de bruit aérodynamique sur un ventilateur centrifuge à flux axial*, Journal de Physique, vol. C5, no 4, p. 985–988.

[46] Carolus, T., Stremel, M. (2003) *Measurement of Surface Pressure Fluctuations - A Tool for Identifying Acoustic Sources in Fans*, Fan Noise, Senlis, France.

[47] Subramanian, S., Mueller, T.J. (1995) *An experimental study of propeller noise due to cyclic flow distortion*, Journal of Sound and Vibration, vol. 183, no 5, p. 907–923.

[48] Fournier, G. (1990) *Aéroacoustique et Hydroacoustique*, Techniques de l'ingénieur, Traité de Sciences Fondamentales, A 430.

[49] Huang, L. (2003) *Characterizing computer cooling fan noise*, Journal of the Acoustical Society of America, vol. 114, no 6, p. 3189–3200.

[50] Holste, F., Neise, W. (1992) *Experimental Determination of the Main Sources in a Propfan Model by Analysis of the Acoustic Spinning Modes in the Exit Plane*, DLR/AIAA 92-020138, 828-835 p.

[51] Holste, F. (1997) *An equivalent source method for calculation of the sound radiated from aircraft engines*, Journal of Soun and Vibration, vol. 203, no 4, p. 667–695.

[52] Bonnet, M. (2004) *Problèmes Inverses*, Cours du DEA Dynamique des Structures et Couplages, École Polytechnique, France.

[53] Hansen, P.C. (1993) *The use of the l-curve in the regularization of discrete ill-posed problem*, SIAM, Journal of Scientific Computing, vol. 14, no 6, p. 1487–1503.

[54] Johnston, P.R., Gulrajani, R.M. (2000) *Selecting the corner in the l-curve approach to tikhonov regularisation*, IEEE Transactions on Biomedical Engineering, vol. 47, no 9, p. 1293–1296.

[55] Johnston, P.R., Gulrajani, R.M. (2002) *An analysis of the zero-crossing method for choosing regularization parameters*, SIAM, Journal of Scientific Computing, vol. 24, no 2, p. 428–442.

[56] Oraintara, S., Karl, W.D., Castanon, D.A., Nguyen, T.Q. (2000) *A Method for Choosing the Regularization Parameter in Generalized Tikhonov Regularized Linear Inverse Problems*, IEEE International conference on Image Processing, Vancouver, Canada, 93-96 p.

[57] Nelson, P.A. (2001) *A review of some inverse problems in acoustics*, International Journal of Acoustics and Vibration, vol. 6, no 3, p. 118–134.

[58] Yoon, S.H., Nelson, P.A. (1998) *Reconstruction of Aeroacoustic Source Strength Distributions by Inverse Techniques*, AIAA-98-2339.

[59] Nelson, P.A., Yoon, S.H. (1999) *Estimation of acoustic source strength by inverse methods. part 1 : Conditionning of the inverse model*, Journal of Sound and Vibration, vol. 233, p. 643–668.

[60] Kim, Y., Nelson, P.A. (2003) *Spatial resolution limits for the reconstruction of acoustic source strength by inverse methods*, Journal of Sound and Vibration, vol. 265, p. 583–608.

[61] Gauthier, P.-A., Berry, A. (2005) *Sound-field reproduction in-room using optimal control techniques : Simulations in the frequency domain*, Journal of the Acoustical Society of America, vol. 117, no 2, p. 662–678.

[62] Kim, Y., Nelson, P.A. (2003) *Estimation of acoustic source strength within a cylindrical duct by inverse methods*, Journal of Sound and Vibration, vol. 275, p. 391–413.

[63] Schumacher, A., Hald, J., Rasmussen, K.B., Hansen, P.C. (2003) *Sound source reconstruction using inverse boundary element calculations*, Journal of the Acoustical Society of America, vol. 113, no 1, p. 114–127.

[64] Patrick, S.M., Atassi, H.M., Blake, W.K. (1994) *Inverse problems in unsteady aerodynamics and aeroacoustics*, ASME DE, vol. 75, p. 309–319.

[65] Grace, S.P., Atassi, H.M. (1996) *Inverse aeroacoustic problem for a streamlined body, part 1 : Basic formulation*, American Institute of Aeronautics and Astronautics Journal, vol. 34, p. 2233–2240.

[66] Grace, S.P., Atassi, H.M. (1996) *Inverse aeroacoustic problem for a streamlined body, part 2 : Accuracy of solutions*, American Institute of Aeronautics and Astronautics Journal, vol. 34, p. 2241–2246.

[67] Wood, T.V., Grace, S.M. (2000) *Inverse aeroacoustic problem for a rectangular wing*, American Institute of Aeronautics and Astronautics Journal, vol. 38, no 2, p. 203–210.

[68] Luo, J., Li, X.D. (2002) *An inverse aeroacoustic problem on rotor wake/stator interaction*, Journal of Sound and Vibration, vol. 254, p. 219–229.

[69] Li, X.D., Zhou, S. (1996) *Spatial transformation of the discrete sound field from a propeller*, American Institute of Aeronautics and Astronautics Journal, vol. 34, no 6, p. 1097–1102.

[70] Lewy, S. (2004) *Inverse Method Predicting Spinning Modes Radiated by a Ducted Fan from Free-Field Measurements*, 18^{th} International Congress on Acoustics, Kyoto, Japon.

[71] Maling, G.C. (1994) *Historical developments in the control of noise generated by small air moving devices*, Noise Control Engineering Journal, vol. 42, no 5, p. 159–169.

[72] Alizadeh, A., Belhabib, M. (1997) *Analyse aéroacoustique des ventilateurs de refroidissement pour l'automobile*, Ingénieur de l'Automobile, vol. 711.

[73] Fuller, C.R., Elliot, S., Nelson, P.A. (1996) *Active Control of Vibration*, Academic Press Limited, London, Great Britain.

[74] Nelson, P.A., Elliot, S. (1992) *Active Control of Sound*, Academic Press, London, 346 p.

[75] Elliot, S. (2001) *Signal Processing for Active Control*, Academic Press, London, 511 p.

[76] Eriksson, L.J., Allie, M.C, Bremigan, C.D., Gilbert, J.A. (1988) *Active Noise Control and Specifications for Fan Noise Problems*, Noise Con 88, Purdue University, USA.

[77] Yeung, Y.N., Yiu, P., Chow, W.K. (1996) *Active noise control : Evaluation in ventilation systems*, Building services engineering research and technology, p. 1991–1998.

[78] Kostek, T.M. (1997) *Combining Adaptive-Passive and Fully Active Noise Control in Ducts*, ASME Noise control and acoustics division.

[79] Besombes, M., Micheau, P. (1995) *Active Control Device Integrated in a Centrifugal Turbomachine : A Compact Solution for the Periodic Noise Control*, ACTIVE 1995, Newport Beach, USA, 263-274 p.

[80] Howard, H. (2004) *Experimental Results of Synchrophasing Two Axial Fans in a Duct*, ACTIVE 04, Williamsburg, Virginia, USA.

[81] Harada, I. (1979) *Blower-Noise Reducing Method by Phase Control*, Japanese Patent Number JP54062509.

[82] Thomas, R.H., Burdisso, R.A., Fuller, C.R., O'Brien, W.F. (1994) *Active control of fan noise from a turbofan engine*, American Institute of Aeronautics and Astronautics Journal, vol. 32, no 1, p. 23–30.

[83] Risi, J.D., Burdisso, R.A., Fuller, C.R. (1995) *Experimental demonstration of active flow control to reduce unsteady stator-rotor interaction*, Journal of the Acoustical Society of America, vol. 99, no 1, p. 408–416.

[84] Gerhold, C.H. (1997) *Active control of fan-generated noise*, American Institute of Aeronautics and Astronautics Journal, vol. 35, no 1, p. 17–22.

[85] Joseph, P., Nelson, P.A., Fisher, M.J. (1999) *Active control of fan tones radiated from turbofan engines. part 1 : External error sensors*, Journal of the Acoustical Society of America, vol. 106, no 2, p. 766–786.

[86] Joseph, P., Nelson, P.A., Fisher, M.J. (1999) *Active control of fan tones radiated from turbofan engines. part 2 : Induct error sensors*, Journal of the Acoustical Society of America, vol. 106, no 2, p. 766–786.

[87] Smith, J.P., Burdisso, R.A. (1999) *Active Control of Inlet Noise from a Turbofan Engine using Inlet Wavenumber Sensors*, AIAA 99-1808, 1-6 p.

[88] Kota, V. (2005) *Wake Generator Control of Flow Distorsion Induced Tonal Noise in Fans*, Thèse de doctorat, Université de Southampton.

[89] Wright, S.E., Atmoko, H. (2001) *Active control of environmental noise, iv : Performance of a fundamental free-field sound cancelling system*, Journal of Sound and Vibration, vol. 245, no 4, p. 581–609.

[90] Qiu, X., Hansen, H. (2000) *Secondary acoustic source types for active noise control in free field : Monopoles or multipoles*, Journal of Sound and Vibration, vol. 232, no 5, p. 1005–1009.

[91] Bschorr, O. (1992) *Reduction of propeller noise by active noise control*, DGLR/AIAA 92-02-156, vol. 919-923, p. 679–695.

[92] Quinlan, D.A. (1992) *Application of active control to axial flow fans*, Noise Control Engineering Journal, vol. 39, no 3, p. 95–101.

[93] Wang, J., Huang, L., Cheng, L. (2005) *A study of active tonal noise control for a small axial flow fan*, Journal of the Acoustical Society of America, vol. 117, no 2, p. 734–743.

[94] Gee, K.L., Sommerfeldt, S.D. (2004) *Application of theoretical modeling to multi-channel active control of cooling fan noise*, Journal of the Acoustical Society of America, vol. 115, no 1, p. 228–236.

[95] Lauchle, G.C., MacGillivray, J.R., Swanson, D.C (1997) *Active control of axial flow fan noise*, Journal of the Acoustical Society of America, vol. 101, no 1, p. 341–349.

[96] Piper, G.E., Watkins, J.M. (2005) *Active control of axial-flow fan noise using magnetic bearings*, Journal of Vibration and Control, vol. 11, no 9, p. 1221–1232.

[97] Kousen, K.A., Verdon, J.M. (1994) *Active control of wake/blade-row interaction noise*, American Institute of Aeronautics and Astronautics Journal, vol. 32, no 10, p. 1953–1960.

[98] Myers, S., Fleeter, S. (1999) *Dipole active control of wake-blade row interaction noise*, Journal of Propulsion, vol. 15, no 1, p. 31–37.

[99] Rao, N.M., Jinwei, F., Burdisso, R.A., Wing, F.Ng. (2001) *Experimental demonstration of active flow control to reduce unsteady stator-rotor interaction*, American Institute of Aeronautics and Astronautics Journal, vol. 39, no 3, p. 458–464.

[100] Neuhaus, L. (2003) *Active control of the aerodynamic performance and tonal noise of axial turbomachines*, Journal of Power and Energy, vol. 217, p. 375–383.

[101] Fournier, G., Huard, J., Pérucchini, J. (1994) *Noise Reduction of Fans by Control of Flow Distorsion*, Inter.noise 94, Yokohama, Japan.

[102] Nelson, P.A. (2000) *Active Techniques and Their Potential for Application in Aeroacoustics*, Keynote Lecture, 6th CEAS/AIAA Aeroacoustic Conference, Lahaina, Hawaï.

[103] Polacsek, C., Desbois-Lavergne, F. (2003) *Fan interaction noise reduction using a wake generator : Experiments and computational aeroacoustics*, Journal of Sound and Vibration, vol. 265, no 4, p. 725–743.

[104] Andersson, A.O. (1996) *Active Control of Tone Noise in Engine Ducts*, Patent No. : PCT/US95/09999 (WO 96/03585).

[105] Farrell, K.J. (2002) *Technique for Reducing Acoustic Radiation in Turbomachinery*, Patent No. : US 6,375,416.

[106] Jeon, W.H. (2003) *Overview of Numerical Analysis of Fan Noise*, Fan Noise 2003, Senlis, France.

[107] Yu, C., Li, X.D. (2003) *Feedforward control study on gust/cascade interaction noise*, Acta aeronautica et astronautica sinica, vol. 24, no 3, p. 237–241 (in chinese).

[108] Gérard, A., Berry, A., Masson, P. (2003) *Active Control of Automotive Fan Noise*, Fan Noise 2003, Senlis, France.

[109] Gérard, A., Tartarin, J., B. M., Gervais, Y. (2004) *An inverse aeroacoustic model for fans*, 10th AIAA/CEAS Aeroacoustic Conference - AIAA-2004-3036, Manchester, UK.

[110] Theodorsen, T. (1935) *General theory of aerodynamic instability and the mechanism of flutter*, N.A.C.A. Technical Report, vol. 435.

[111] Karman, T.V., Sears, W.R. (1938) *Airfoil theory for non-uniform motion*, Journal of the Aeronautical Sciences, vol. 5, no 10, p. 379–390.

[112] Horlock, J.H. (1968) *Fluctuating lift forces on aerofoils moving through tranverse and chordwise gusts*, Journal of Basic Engineering, Transactions of the ASME, vol. 90, p. 494–500.

[113] Filotas, L.T. (1969) *Theory of Airfoil Response in a Gusty Athmosphere. Part 1 : Aerodynamic Transfer Function*, University of Toronto, Institute of Aeronautics and Space, UTIAS, report 139.

[114] Mugridge, B.D. (1971) *Gust loading on a thin aerofoil*, The Aeronautical Quarterly, vol. 22, no 3, p. 301–310.

[115] Atassi, H.M. (1984) *The sears problem for a lifting airfoil revisited - new results*, Journal of Fluid Mechanics, vol. 141, p. 109–122.

[116] Namba, N. (1977) *Three-dimensional analysis of blade force and sound generation for an annular cascade in distorted flows*, Journal of Sound and Vibration, vol. 50, no 4, p. 479–508.

[117] Krishnappa, G. (1997) *Blade interaction noise from lift fans*, Journal of the Acoustical Society of America, vol. 51, no 5 Part 1, p. 1464–1470.

[118] Spiegel, M.R. (1968) *Mathematical Handbook of Formulas and Tables*, McGraw-Hill Book Company, N.Y., USA.

[119] Alauze, C. (1998) *Equilibrage actif des machines tournantes : application aux grandes lignes d'arbres*, Thèse de doctorat, INSA-Lyon.

[120] Dyer, S.W. (1999) *Adaptive optimal control of active balancing systems for high-speed rotating machinery*, Thèse de doctorat, Université du Michigan.

ANNEXE A

POSITIONNEMENT AUTOMATIQUE DES OBSTRUCTIONS DE CONTRÔLE : CONTRÔLE OPTIMAL

Des expériences en cours sur le contrôle passif adaptatif de l'écoulement montrent qu'une approche de contrôle analogue au contrôle actif de l'équilibrage dynamique est adéquate. Les travaux de Alauze [119] et de Dyer [120] offrent un formalisme tout à fait adapté au pilotage automatique des obstructions de contrôle.

A.1 Analogie avec l'équilibrage dynamique

L'équilibrage dynamique consiste en l'amélioration du comportement des machines tournantes, en réponses à des forces de balourd (forces générées par le déplacement du centre de masse du solide en rotation). Cet équilibrage dynamique consiste à engendrer un balourd "secondaire" d'égale amplitude mais en opposition de phase par rapport au balourd "primaire". Le principe en est proposé Figure A.1. Y sont présentés les vecteurs balourds B_1 et B_2 dans le plan de Nyquist, associé à deux mobiles de même masse se déplaçant dans un même plan, à une distance constante de l'axe du rotor. Chaque masse génère ainsi une force de balourd d'amplitude et de phase variables. Les balourds s'ajoutent vectoriellement. Les effets des 2 balourds s'annulent lorsque ceux-ci sont placés en opposition de phase.

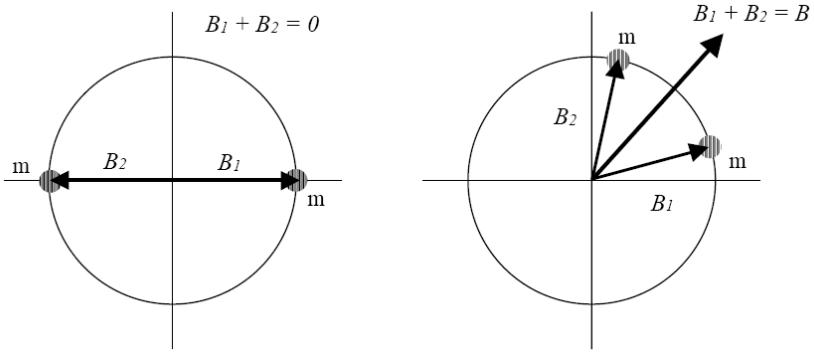

Figure A.1 Génération d'un balourd à partir de 2 masses (d'après [119])

Tableau A.1 Analogie avec l'équilibrage dynamique

Équilibrage dynamique de rotor	Contrôle passif de l'écoulement
Position de la masse	Position de l'obstruction de contrôle
Vecteur balourd	Vecteur pression acoustique

L'équilibrage nécessite donc trois étapes :

- La connaissance de l'état vibratoire du système par la mesure de l'amplitude et la phase des vibrations primaires synchronisées avec la rotation de l'arbre.

- La détermination du ou des balourds correcteurs à partir d'une méthode d'équilibrage (méthodes de coefficients d'influence par exemple).

- Le pilotage du positionnement du ou des masselottes de correction.

Le positionnement des obstructions de contrôle présente une profonde similitude avec les techniques d'équilibrage (Tableau A.1). On peut en effet représenter les pressions acoustiques primaire $p_p(mB\Omega)$ et secondaire $p_s(mB\Omega)$ (à la fréquence $mB\Omega$) de manière similaire aux balourds B_1 et B_2 de la Figure A.1. La position des obstructions de contrôle est similaire à la position des masselottes.

L'équilibrage dynamique actif consiste à adapter la position de masselottes de manière itérative. Leurs positions peuvent ainsi être adaptées pour compenser un balourd primaire qui évolue dans le temps (usure des paliers, variation de la vitesse de rotation, changement de chargement du rotor...). Le terme d'équilibrage dynamique **adaptatif** serait plus approprié dans la terminologie utilisée durant cette thèse. Le formalisme de contrôle utilisé par Dyer [120] sera adapté au positionnement automatique des obstructions de contrôle présentées dans ces travaux de doctorat. Dans cette annexe, nous présenterons seulement le positionnement initial des obstructions par contrôle optimal. Le passage à un contrôle adaptatif ne présente pas de difficultés formelles.

A.2 Contrôle optimal : Théorie

Les développements théoriques qui suivent, conformément à l'analogie présentée au paragraphe précédent, sont inspirés de [120].

A.2.1 Définition des coefficients d'influence

Les coefficients d'influence servent à exprimer l'influence de la portance sur la pression acoustique :

$$\begin{Bmatrix} p_1 \\ p_2 \\ \vdots \\ p_J \end{Bmatrix} = \begin{bmatrix} h_{11} & h_{12} & \cdots & h_{1I} \\ h_{21} & \ddots & & \vdots \\ \vdots & & \ddots & \vdots \\ h_{J1} & \cdots & \cdots & h_{JI} \end{bmatrix} \begin{Bmatrix} l_1 \\ l_2 \\ \vdots \\ l_I \end{Bmatrix} \tag{A.1}$$

où $\{P\}$ est le vecteur des pressions acoustiques mesurées en J points, $[H]$ est la matrice des coefficients d'influence (la dépendance des coefficients h_{ji} par rapport à la fréquence est sous-entendue) et $\{L\}$ est le vecteur des portances complexes générées par I obstructions.

Cas particulier 1 obstruction, 1 microphone dans l'axe

D'après l'Eq. (7.11), on a :

$$p = hl \tag{A.2}$$

avec

$$h = -\frac{imB^2\Omega}{4\pi r c_0}\cos\gamma \tag{A.3}$$

Remarque La relation entre $\{P\}$ et $\{L\}$ est linéaire. En revanche, il existe une relation non linéaire entre la position axiale des obstructions et les amplitudes des portances qu'elles génèrent :

$$l_i = \left(\frac{\alpha_i}{\sqrt{z_{si}}} + \frac{\beta_i}{z_{si}}\right) e^{i\theta_{li}} \tag{A.4}$$

où z_{si} est la distance rotor/obstruction i et θ_{li} est la phase de la portance secondaire l_i reliée à l'orientation angulaire $\theta_{si} = \theta_{li} - \theta_{cte,i}$ de l'obstruction i.

Au paragraphe *Prise en compte de la non linéarité de l'actionneur*, nous justifierons la relation A.4 et nous verrons comment prendre en compte cette non-linéarité dans le contrôleur.

A.2.2 Représentation de la portance secondaire

La portance secondaire l_i doit être ajustée pour annuler le signal d'erreur (fourni par le (ou les) microphone(s)). Sa représentation dans le plan complexe est présentée Figure A.2.

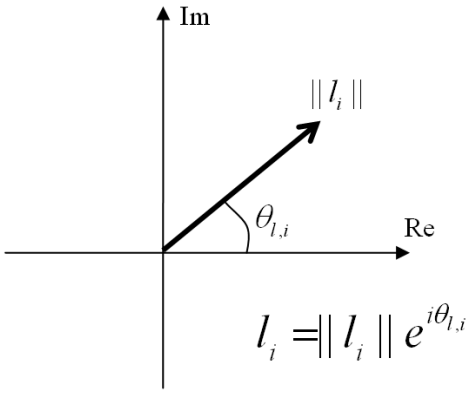

Figure A.2 Représentation de la portance secondaire dans le plan complexe

Les positions axiale z_{si} et angulaire θ_{si} de l'obstruction sont calculées en résolvant l'Eq. (A.4). Finalement, la commande est envoyée aux actionneurs pour positionner l'obstruction i.

A.2.3 Représentation du signal d'erreur

Pour obtenir un signal d'erreur synchronisé, le signal du microphone d'erreur est filtré et convolué avec le phaseur de rotation du rotor (Fig. A.3). Comme la phase de la pression acoustique est importante pour l'implémentation du contrôle, l'échantillonnage doit être synchronisé avec la vitesse de rotation en captant une référence fixe sur le rotor, avec un tachymètre par exemple.

Le phaseur synchronisé du signal d'erreur est présumé linéairement dépendant de toutes les perturbations synchronisées et des effets de correction active de portance (Fig. A.4).

d_i est la perturbation (en Pa) contribuant à l'erreur mesurée au microphone j à la fréquence ω.

L'erreur peut donc s'écrire :

$$\begin{Bmatrix} e_1 \\ e_2 \\ \vdots \\ e_J \end{Bmatrix} = \begin{bmatrix} h_{11} & h_{12} & \cdots & h_{1I} \\ h_{21} & \ddots & & \vdots \\ \vdots & & \ddots & \vdots \\ h_{J1} & \cdots & \cdots & h_{JI} \end{bmatrix} \begin{Bmatrix} l_1 \\ l_2 \\ \vdots \\ l_I \end{Bmatrix} + \begin{Bmatrix} d_1 \\ d_2 \\ \vdots \\ d_J \end{Bmatrix} \tag{A.5}$$

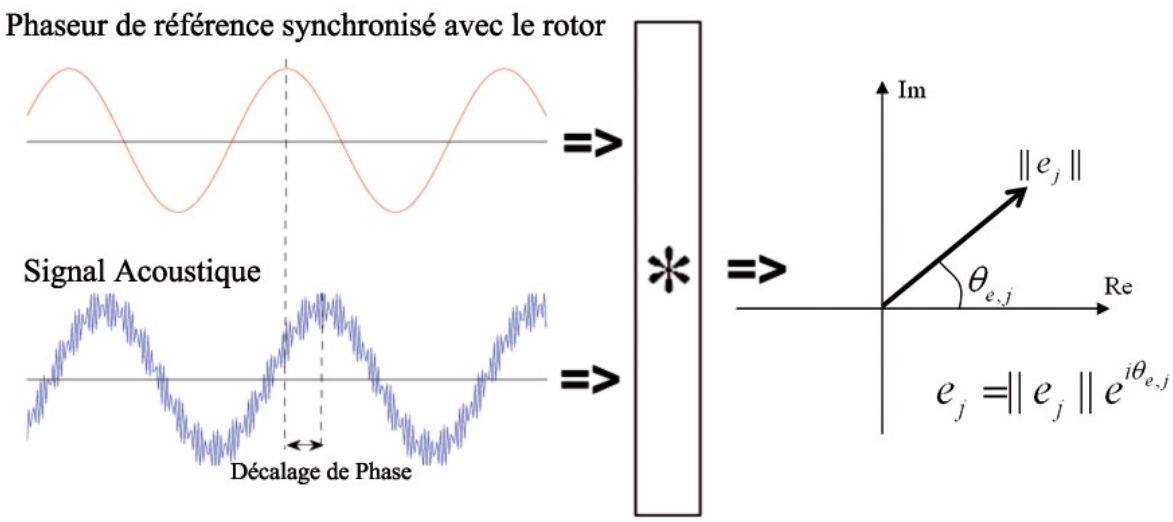

Figure A.3 Obtention du phaseur acoustique synchronisé

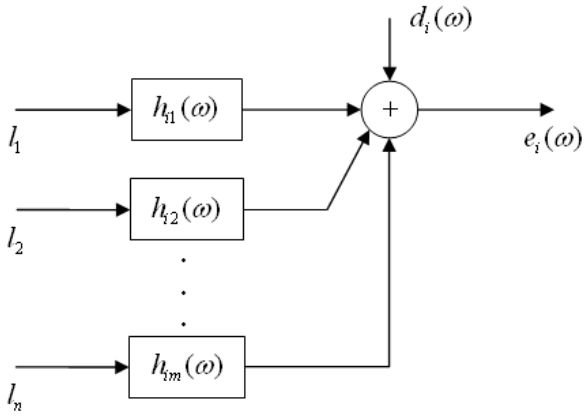

Figure A.4 Obtention du signal d'erreur

où J est le nombre de capteurs d'erreurs et I le nombre d'obstructions. L'Eq. (A.5) peut s'écrire sous forme matricielle de la manière suivante :

$$\{E\} = [H]\{L\} + \{D\} \tag{A.6}$$

A.2.4 Contrôle basé sur les coefficients d'influence

En émettant l'hypothèse que la matrice des coefficients d'influence ne varie pas significativement dans le temps et qu'elle peut être estimée correctement, nous pouvons formuler un système de positionnement actif classique.

Réécrivons l'Eq. (A.6) à l'itération k :

$$\{E\}_k = [H]\{L\}_k + \{D\} \tag{A.7}$$

En considérant $I = J$ (autant d'obstructions que de capteurs d'erreur), le contrôleur devrait envoyer une commande pour la portance secondaire $\{L\}_{k+1}$ qui annule le signal d'erreur à l'itération $k+1$, soit :

$$\{E\}_{k+1} = [H]\{L\}_{k+1} + \{D\} = \{0\} \tag{A.8}$$

Pour satisfaire l'Eq. (A.8), il faut que :

$$\{L\}_{k+1} = -[H]^{-1}\{D\} \tag{A.9}$$

Le vecteur de perturbation $\{D\}$ peut être mesuré directement lors de l'étape d'initialisation (sans obstruction) ; il s'agit de la mesure des pressions acoustiques primaires aux microphones d'erreurs. Il faut s'assurer que le vecteur de perturbation ne change pas plus vite que le passage d'une itération de contrôle à la suivante. En considérant une perturbation constante, les données issues de la précédente itération peuvent être utilisées dans l'Eq. (A.7) pour estimer le vecteur de perturbation {D} en présence d'une obstruction :

$$\{D\} = \{E\}_k - [H]\{L\}_k \tag{A.10}$$

En substituant l'Eq. (A.10) dans (A.8), nous trouvons le vecteur de portance qui annule théoriquement l'erreur $\{E\}_{k+1}$:

$$[H]\{L\}_{k+1} = [H]\{L\}_k - \{E\}_k \tag{A.11}$$

d'où

$$\{L\}_{k+1} = \{L\}_k - [H]^{-1}\{E\}_k \tag{A.12}$$

En pratique, l'erreur $\{E\}_{k+1}$ ne sera pas exactement égale à 0, et plusieurs itérations sont nécessaires pour sa minimisation.

A.2.5 Schéma bloc

Dans le cas d'une matrice d'influence $[H]$ carrée et non singulière, le contrôle peut être représenté en schéma bloc comme proposé sur Fig. A.5.

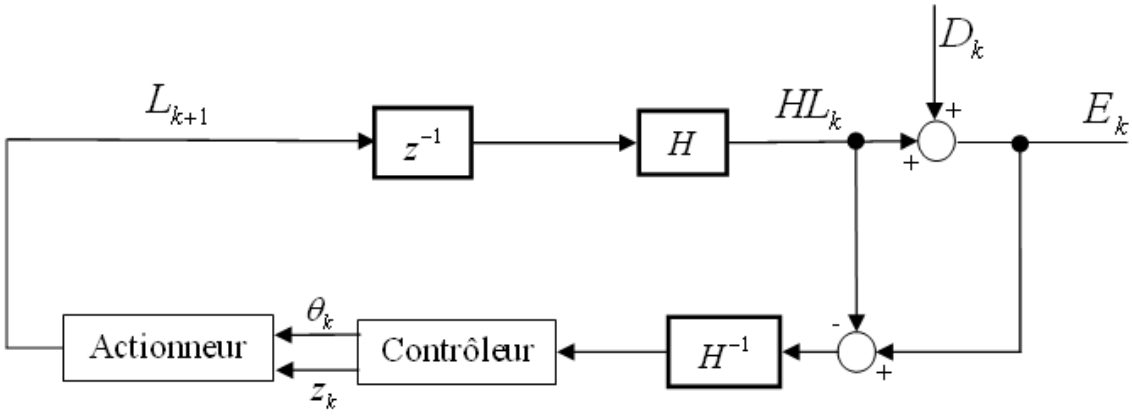

Figure A.5 Schéma-bloc du contrôle automatisé

Comme dans ce schéma la matrice des coefficients d'influence ne change pas, son inversion peut juste être réalisée une seule fois. Il reste uniquement des produits matriciels à effectuer.

En pratique, $[H]$ doit être estimée. Son estimée $[\hat{H}]$, obtenue analytiquement (Eq. (A.3) pour le cas 1 microphone d'erreur, 1 obstruction) ou expérimentalement, est utilisée dans l'Eq. (A.12).

A.2.6 Prise en compte de la non linéarité de l'actionneur

Le schéma de contrôle (Figure A.5) montre le contrôleur linéaire qui calcule la portance à $\{L\}_{k+1}$. A partir de la portance $\{L\}_{k+1}$, il faut déterminer les vecteurs de positions axiales $\{Z_s\}$ et angulaires $\{\Theta_s\}$ des I obstructions.

À partir des mesures de surfaces d'erreur (Fig. 7.8-a pour le cas de la série de 6 obstructions trapézoïdales d'angles $\Theta = 10°$) et de l'Eq. (7.15), il est possible de trouver une relation entre la portance générée par l'obstruction i et sa position axiale z_{si}. La combinaison linéaire de deux

fonctions permet une approximation correcte de la portance générée par l'obstruction i en fonction de sa position axiale z_{si}. La première de ces fonctions représente une interaction potentielle en α/z_s et la seconde représente une interaction de sillage visqueux en $\beta/\sqrt{z_s}$.

$$l_i = \left(\frac{\alpha_i}{\sqrt{z_{si}}} + \frac{\beta_i}{z_{si}} \right) e^{i\theta_{li}} \tag{A.13}$$

Assumons que la phase θ_{li} ne dépende pas de la distance z_{si} mais seulement de la position angulaire de l'obstruction θ_{si} telle que :

$$\theta_{li} = \theta_{cte,i} + \theta_{si} \tag{A.14}$$

La relation A.14 est valide pour les obstructions 6-périodiques utilisées tout au long de cette thèse.

Les paramètres α_i, β_i et $\theta_{cte,i}$ sont à déterminer expérimentalement pour chaque obstruction de contrôle. Une étape préliminaire d'identification est alors nécessaire.

Une regression non-linéaire, nous permet de calculer les paramètres α_i et β_i à partir de mesure de pression acoustique en champ libre dans l'axe du ventilateur pour plusieurs positions axiales de l'obstruction de contrôle i, possédant mB lobes pour le contrôle de la fréquence $\omega = mB\Omega$. Un moyen de gagner du temps lors du processus d'identification est de trouver la position angulaire de l'obstruction permettant de générer une pression acoustique secondaire en phase avec la pression acoustique primaire (voir les calculs de la section 7.4.3). Pour y parvenir, il suffit d'approcher l'obstruction de contrôle près du rotor et de trouver sa position angulaire qui maximise la pression acoustique totale. Il suffit ensuite d'utiliser la relation (7.15) pour calculer l'amplitude de la portance secondaire. La figure A.6 montre le résultat de la régression.

A.2.7 Calcul de la distance axiale rotor/obstruction z_{si}

La position axiale $\{z_{si}\}_{k+1}$ dépend uniquement de l'amplitude de la portance à l'itération $k+1$, soit

$$\|l_i^{k+1}\| = \frac{\alpha_i}{\sqrt{z_{si}^{k+1}}} + \frac{\beta_i}{z_{si}^{k+1}} \tag{A.15}$$

Posons $X_{si}^{k+1} = \sqrt{z_{si}^{k+1}}$, il vient :

$$\|l_i^{k+1}\|(X_{si}^{k+1})^2 - \alpha_i X_{si}^{k+1} - \beta_i = 0 \tag{A.16}$$

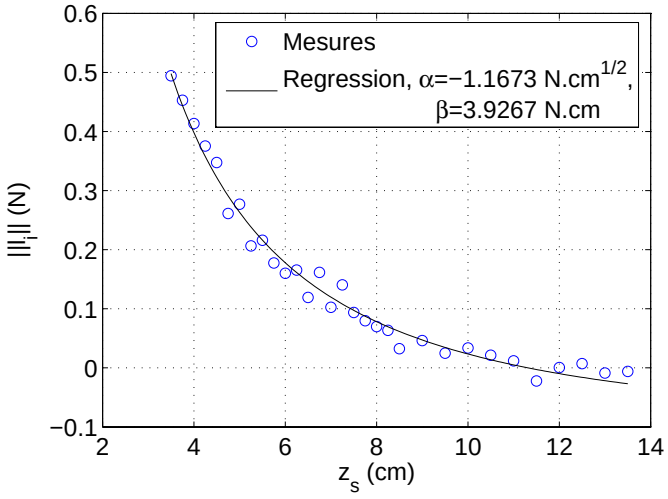

Figure A.6 Pression secondaire en fonction de la distance z_s - Série de 6 obstructions trapézoïdales d'angles 40°

On obtient donc une équation du second degré dont le discriminant est :

$$\Delta_i^{k+1} = \alpha_i^2 + 4\|l_i^{k+1}\|\beta_i \tag{A.17}$$

Les solutions sont de la forme :

$$z_{si}^{k+1} = \left(\frac{\alpha_i \pm \sqrt{\Delta_i^{k+1}}}{2\|l_i^{k+1}\|} \right)^2 \tag{A.18}$$

On choisit la solution qui a "le plus" de sens physique.

A.2.8 Calcul de l'angle de l'obstruction

À partir des Eq. (A.13) et (A.12), il vient :

$$\angle l_i^{k+1} = \theta_{li}^{k+1} \tag{A.19}$$

On en déduit la position angulaire de l'obstruction i à l'aide de l'Eq. (A.14) :

$$\theta_{si} = \theta_{li} - \theta_{cte,i} \bmod(2\pi) \tag{A.20}$$

A.3 Mise en oeuvre expérimentale

Dans cette section, nous proposons une mise en oeuvre expérimentale pour contrôler la FPP avec une série d'obstructions trapézoïdales optimisée pour ne pas régénérer d'harmoniques. Un seul microphone d'erreur est utilisé dans l'axe, en amont du ventilateur, dans des conditions anéchoïques.

Comme les grandeurs contrôlés sont les portances des pales du rotor, celles-ci sont utilisées comme variable de contrôle (par l'intermédiaire de la position axiale z_s et angulaire θ_s de l'obstruction). Par contre, les grandeurs mesurables sont les pressions acoustiques au microphone d'erreur. L'Eq. (A.2) fournit une relation linéaire entre ces deux grandeurs. Toutes les étapes qui suivent peuvent évidemment être menées en raisonnant uniquement en terme de pression acoustique.

A.3.1 Dispositif expérimental

Le dispositif expérimental (schématisé Fig A.7) utilise le même montage que celui de la Fig. 7.6. On ajoute cependant un tachymètre optique générant un signal synchronisé sur la fréquence de passage de pales. Ce dernier permet de fixer une référence de phase.

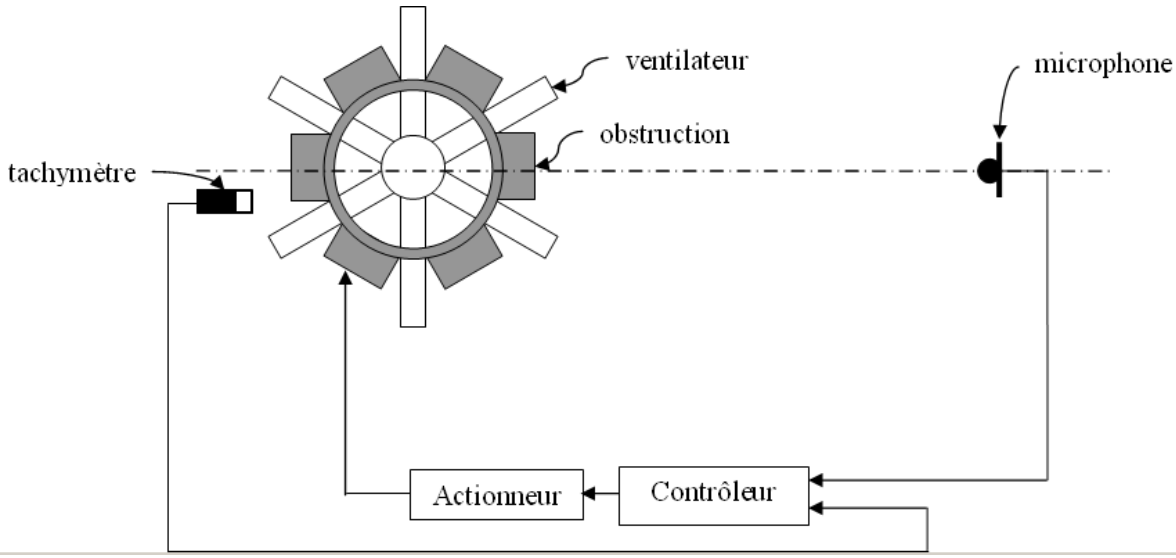

Figure A.7 Représentation schématique du dispositif de contrôle

A.3.2 Identification des lois de contrôle - Initialisation

La phase de contrôle à proprement parler doit être précédée d'une phase d'identification des lois liant z_s et θ_s aux quantités mesurables p_s et p_p, respectivement pressions acoustiques primaire (sans contrôle) et secondaire (uniquement dû à l'obstruction).

Étape 1 : Mesure du champ acoustique primaire On mesure premièrement l'amplitude $\|p_p\|$ et la phase θ_p de la pression acoustique primaire p_p (la perturbation d dans la terminologie du contrôle). Nous en déduisons l'amplitude $\|l_p\|$ et la phase θ_{lp} de la portance primaire par la relation (A.2). Cette étape est réalisée sans l'obstruction ou bien avec une obstruction suffisamment loin du rotor.

Étape 2 : Identification de θ_{cte} On fixe la position angulaire de l'obstruction θ_s et on la positionne à faible distance du rotor, de sorte que la pression acoustique primaire soit négligeable devant la pression acoustique secondaire (d'autres méthodes, comme la triangulation, doivent être suggérées pour éviter le positionnement de l'obstruction très près du rotor). La pression acoustique totale mesurée au microphone d'erreur fournit alors directement la pression acoustique secondaire p_s. Nous pouvons donc estimer la phase θ_{ls} de la portance secondaire (à partir de l'Eq. 7.15) en fonction de la position angulaire θ_s de l'obstruction. D'après l'Eq. (A.14), nous obtenons la constante θ_{cte} :

$$\theta_{cte} = \theta_l - \theta_s \tag{A.21}$$

Étape 3 : Identification de la loi $\|l_s\|(z_s)$ Les pressions acoustiques secondaire et primaire sont d'abord mises en phase. Ensuite nous faisons varier la position axiale z_s de l'obstruction. Conformément au calcul effectué au §A.2.7, nous pouvons obtenir une relation entre le module de la portance secondaire et la position axiale de l'obstruction z_s.

Étape 4 : Position initiale de l'obstruction La position de contrôle optimale est enfin calculée à partir de l'Eq. (A.12) et des relations identifiées lors des étapes précédentes.

On recherche donc :

$$\begin{cases} z_s \quad \text{tel que} \quad \|l_p\| = \|l_s\|(z_s) \\ \quad \text{et} \\ \theta_s \quad \text{tel que} \quad \theta_{lp} = -\theta_{ls}(\theta_s) \mod \frac{2\pi}{B} \end{cases}$$

Compte-tenu du caractère B-périodiques des obstructions de contrôle, θ_s est valable modulo $\frac{2\pi}{B}$.

L'obstruction de contrôle est alors mise à la position (z_s, θ_s), ce qui constitue la position initiale $k = 1$ de la boucle de contrôle.

A.3.3 Boucle de contrôle - Algorithmique

Le schéma de la Figure A.8 propose un représentation de l'itération de rang k ($k \geq 1$) de l'algorithme de contrôle. Celle-ci est schématisée dans le plan complexe sur la Figure A.9.

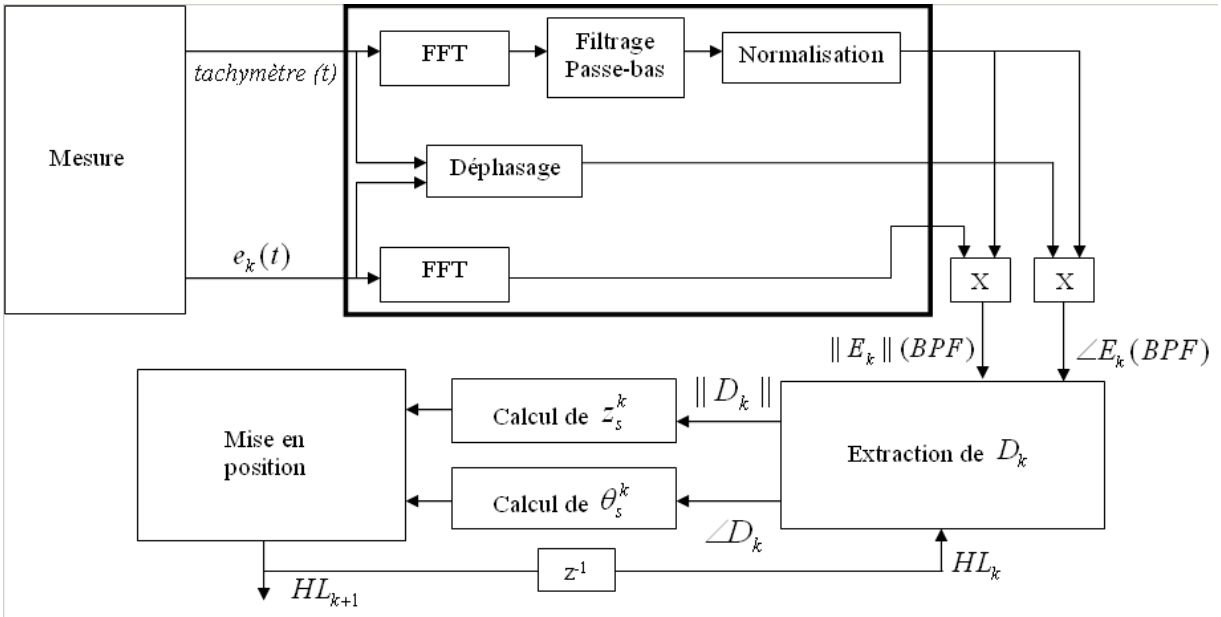

Figure A.8 Représentation schématique d'une itération $k \geq 1$ de l'algorithme de contrôle

Le filtrage du signal du tachymètre est réalisé à l'aide d'un filtre passe-bas de type Butterworth d'ordre et de fréquence de coupure réglables (par défaut, respectivement 5 et 350 Hz). L'amplitude du signal du tachymètre est également ramenée à 1 pour ne pas fausser les résultats lors de la convolution des signaux. Celle-ci se fait dans le domaine fréquentiel par produit des spectres : les informations de niveau de pression et de déphasage sont ensuite extraites par simple recherche du maximum dans les spectres obtenus après convolution.

A.4 Résultats préliminaires

La mise au point du programme et les premiers essais ont été conduits avec la série d'obstructions trapézoïdales de 40°.

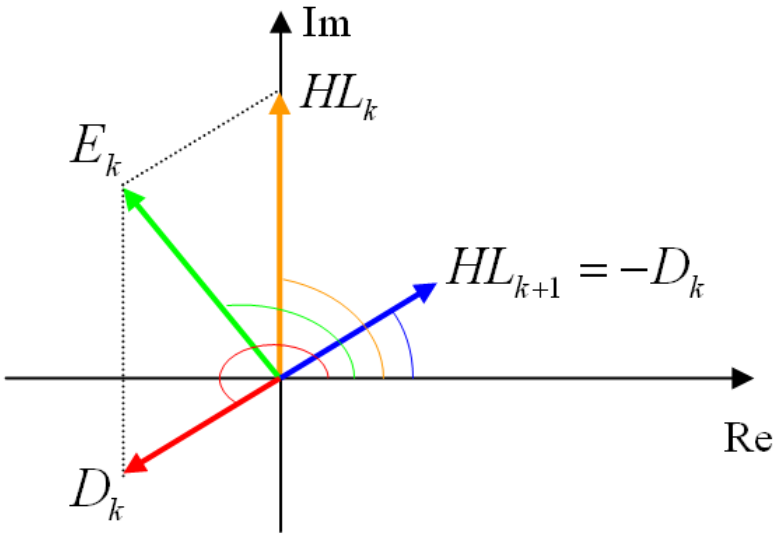

Figure A.9 Représentation d'une itération $k \geq 1$ de l'algorithme de contrôle dans le plan complexe

Malgré quelques difficultés liées à l'instationnarité de l'information de phase (nécessitant un nombre de moyennes important, environ 32), les premiers résultats ont été concluants, notamment le positionnement initial qui correspond assez bien à la position optimale "connue". L'étape d'identification préalable du chemin secondaire a nécessité une vingtaine de mesures (quelques minutes).

Le tableau A.2 propose les positions de l'obstruction et le signal d'erreur issus d'un test de l'algorithme. Une atténuation de pression acoustique de 10 dB à la FPP a été obtenu en 2 itérations. Cependant, le contrôle a commencé à diverger à partir de la quatrième itération à cause d'un problème de pilotage des moteurs.

k	θ_s^{k-1} (°)	z_s^{k-1} (cm)	$\|E_k\|$ (dB)
0	-	-	55.4
1	53	9,6	49
2	41	8,2	45,2
3	41	8,2	45

Tableau A.2 Exemple de résultats obtenus avec l'algorithme de contrôle - $SPL(p_p) = 55,4$ dB

Le temps a manqué cependant pour conduire des tests plus nombreux et plus longs permettant de régler le problème du pilotage et d'éprouver la bonne tenue de l'algorithme lors de modifications de l'écoulement primaire.

Pour mettre à l'épreuve l'algorithme et la stratégie de contrôle, il faudra donc conduire de nouvelles expériences, plus longues et présentant des modifications d'écoulement (en ajoutant un

obstacle en aval à une itération donnée par exemple).

Amélioration du contrôleur Nous pourrions introduire un paramètre de gain μ dans l'Eq. (A.12) pour améliorer la robustesse du contrôle par rapport aux erreurs d'estimations (analytiques ou expérimentales) de la matrice des coefficients d'influence $[H]$:

$$\{L\}_{k+1} = \{L\}_k - \mu[H]^{-1}\{E\}_k \tag{A.22}$$

De faibles valeurs du paramètre μ peuvent améliorer la stabilité du contrôle au détriment de la vitesse de convergence.